

ADVERTIMENT. L'accés als continguts d'aquesta tesi queda condicionat a l'acceptació de les condicions d'ús estableties per la següent llicència Creative Commons:  <https://creativecommons.org/licenses/?lang=ca>

ADVERTENCIA. El acceso a los contenidos de esta tesis queda condicionado a la aceptación de las condiciones de uso establecidas por la siguiente licencia Creative Commons:  <https://creativecommons.org/licenses/?lang=es>

WARNING. The access to the contents of this doctoral thesis is limited to the acceptance of the use conditions set by the following Creative Commons license:  <https://creativecommons.org/licenses/?lang=en>

DOCTORAL THESIS

PhD programme in Neurosciences

Preclinical Strategic Advances in the Therapeutic Landscape of Intracerebral Hemorrhagic Stroke

Alexia García Serran

Cellular and Molecular Neurobiology Group (CMN)

Institut d'Investigació en Ciències de la Salut Germans Trias i Pujol (IGTP)

Thesis directors:

Dr. Teresa Gasull Dalmau

Dr. Octavi Martí Sistac

Tutor:

Dr. Patrocinio Vergara Esteras

Institut de Neurociències (INc)
Universitat Autònoma de Barcelona (UAB)
Badalona 2025

This thesis has been developed in the Cellular and Molecular Neurobiology Group (CMN) from the Institut d'Investigació en Ciències de la Salut Germans Trias i Pujol (IGTP). The research was supported by grants from the Fondo de Investigaciones Sanitarias-Instituto de Salud Carlos III (PI21/01925, PI18/01813, PI19/00174, and PI24/00963), RICORS RD21/0006/0024 and RD24/0009/0015, and the Agency for Management of University and Research Grants (AGAUR) Catalan Research Group (2021SGR00925, 2019PROD00120), which may be co-financed by FEDER/FSE funds. The group also received funding from “la Caixa” (CI15-00009) from the European Institute of Innovation and Technology (EIT, PoC-2016-SPAIN-04), supported by the European Union’s Horizon 2020 research and innovation program, and the Fundación para la Innovación y la Prospectiva en Salud en España (FIPSE) program (3594-18).

INDEX

ABBREVIATIONS	1
Abstract	11
Resum	13
Resumen	15
INTRODUCTION	19
1. STROKE	21
1.1. Historical milestones	21
1.2. Definition, clinical signs and epidemiology	22
1.3. Stroke types.....	24
2. INTRACEREBRAL HEMORRHAGES	28
2.1. Specific epidemiology and costs	28
2.2. Neurological signs.....	28
2.3. Risk factors.....	29
2.3.1. <i>Non-modifiable risk factors</i>	29
2.3.2. <i>Modifiable risk factors</i>	30
2.4. Location.....	32
2.5. Neurological evaluation (scales)	33
2.6. ICH diagnostic requires imaging techniques.....	35
2.7. Complications in ICH	38
2.7.1. <i>Hematoma expansion</i>	38
2.7.2. <i>Peribematomal edema</i>	39
2.7.3. <i>Intraventricular hemorrhage</i>	40
2.7.4. <i>Other complications</i>	40
2.8. Pathophysiology	40
2.8.1. <i>Primary brain injury</i>	41
2.8.2. <i>Secondary brain injury</i>	42
2.8.2.1. Thrombin damage	42
2.8.2.2. Inflammation and immune system damage	43
2.8.2.3. Damage by erythrocytes' released products	45
2.8.3. <i>Iron and ferroptosis</i>	46
2.9. ICH treatment: clinical guidelines, clinical trials and preclinical treatments.....	49
2.9.1. <i>Current guideline for intracerebral hemorrhage</i>	49
2.9.2. <i>Clinical trials in ICH</i>	52
2.9.3. <i>Treatments in preclinical stages</i>	54

2.10. Animal models of ICH	56
2.10.1. <i>Rodents</i>	56
2.10.1.1. Rodent brain vasculature.....	58
2.10.1.2. Intracerebral hemorrhagic stroke models in rodents	59
2.10.2. <i>Large animals</i>	60
2.10.2.1. Swine vasculature.....	61
2.10.2.2. Intracerebral hemorrhagic stroke models in swine	63
2.11. Neurological evaluation in ICH stroke animal models.....	65
2.11.1. <i>Small animals</i>	66
2.11.1.1. Motor and sensorimotor tests	66
2.11.1.2. Cognitive and emotion-related tests.....	66
2.11.1.3. Sensory tests	66
2.11.2. <i>Large animals</i>	68
CONTEXTUALISATION AND JUSTIFICATION	71
HYPOTHESIS AND OBJECTIVES	75
MATERIALS AND METHODS	79
1. STUDY DESIGN.....	81
2. METHODS AND PROCEDURES.....	83
2.1. Experimental animals.....	83
2.2. Hypoxic/ischemic stroke model.....	83
2.3. Collagenase-induced intracerebral hemorrhagic stroke model.....	84
2.3.1. <i>bATf treatment protocol after the ICH mouse model</i>	85
2.4. Minimally invasive intracerebral hemorrhagic stroke model in pig	86
2.4.1. <i>Preoperative procedures</i>	86
2.4.2. <i>Neurointerventional procedure</i>	86
2.4.3. <i>Postoperative care, follow-up, and euthanasia</i>	88
2.5. Functional assays	89
2.5.1. <i>Tail bleeding test</i>	89
2.5.2. <i>Coagulation assays in human blood</i>	89
2.5.3. <i>Behavioral assessment</i>	90
2.5.4. <i>DeepLabCut, postprocessing and computational prediction models</i>	92
2.5.4.1. DeepLabCut for pose estimation and behavioral feature extraction	92
2.5.4.2. Post-Processing and feature extraction	94
2.5.4.3. Computational prediction models	95
2.6. Sample processing	95

2.6.1. <i>Plasma or serum collection</i>	95
2.6.2. <i>Brain collection</i>	96
2.7. Sample analysis	98
2.7.1. <i>Specific analysis of pig blood samples</i>	98
2.7.2. <i>Heme and hemoglobin concentrations</i>	98
2.7.3. <i>Gene expression analysis by RT-qPCR</i>	98
2.7.3.1. <i>RNA isolation</i>	98
2.7.3.2. <i>Reverse transcription</i>	100
2.7.3.3. <i>Quantitative PCR</i>	101
2.7.4. <i>Western Blot</i>	104
2.7.4.1. <i>SDS-polyacrylamide gel electrophoresis (SDS-PAGE)</i>	104
2.7.4.2. <i>Urea-polyacrylamide gel electrophoresis (U-PAGE)</i>	106
2.7.4.3. <i>Electroblotting</i>	107
2.7.4.4. <i>Immunodetection</i>	108
2.7.5. <i>TSAT assessment</i>	108
2.7.6. <i>Platelet Factor 4 detection by ELISA</i>	110
2.7.7. <i>Immunohistofluorescence</i>	110
2.7.8. <i>Antibodies</i>	111
2.8. Lesion quantification	113
2.8.1. <i>Ex vivo lesion quantification</i>	113
2.8.2. <i>MicroCT system, acquisition and reconstruction parameters</i>	115
2.8.2.1. <i>CT lesion quantification</i>	117
2.8.3. <i>Magnetic resonance imaging</i>	119
2.8.3.1. <i>MRI lesion quantification</i>	119
2.9. Distribution of the animals	120
2.10. Statistics	120
RESULTS	121
MANUSCRIPT I	123
MANUSCRIPT II	163
MANUSCRIPT III	197
DISCUSSION	223
1. Therapeutic efficacy of hATf in ICH: Unraveling mechanisms and therapeutic potential	225
2. Antiferroptotic mechanisms of hATf action: A novel pathway to neuroprotection.....	227

3. Challenges in lesion assessment and its relationship with the primacy of neurobiological outcome in ICH: Time to revisit preclinical functional endpoints.....	230
4. Automated computational behavioral assessment for enhanced preclinical stroke research: Pioneering objective and scalable endpoints.....	232
5. Developing a novel translational intracerebral hemorrhage model in swine: Bridging the translational gap.....	234
6. Conclusion and future directions: A strategic pathway for translational stroke research	236
CONCLUSIONS.....	239
REFERENCES.....	243
ANNEX.....	285
<i>Curriculum Vitae.....</i>	287

ABBREVIATIONS

4		ARRIVE	Animal Research: Reporting of <i>In Vivo</i> Experiments
4-HNE	4-Hydroxynonenal		
A		ASA	American Stroke Association
ACA	Anterior Cerebral Artery		
ACC	Accuracy	AST	Aspartate Aminotransferase
AComA	Anterior Communicating Artery	ATACH II	Antihypertensive Treatment of Acute Cerebral Hemorrhage Trial 2
ACSL4	Acyl-CoA Synthetase Long-chain family member 4	ATf	Apotransferrin
ADC	Apparent Diffusion Coefficient	AUC	Area Under the Curve
AHA	American Heart Association	AxT2*	Axial T2*-Weighted
		AxT2PostGd	Axial T2-Weighted Post-Gadolinium
AI	Artificial Intelligence	B	
AIFM2	Apoptosis Inducing Factor Family Member 2	BA	Basilar Artery
ALB	Albumin	BBB	Blood-Brain Barrier
ALP	Alkaline Phosphatase	BCA	Bicinchoninic Acid
ALT	Alanine Aminotransferase	Behavior	DEcoding behavior based on POsitional Tracking
ANOVA	Analysis of Variance	DEPOT	
APA	Ascending Pharyngeal Artery	BH4	Tetrahydrobiopterin

BLOC-ICH	BLOcking the Cytokine IL-1 in Intracerebral Hemorrhage Trial	CLEAR III	Clot Lysis: Evaluating Accelerated Resolution of Intraventricular haemorrhage Trial 3
BMI	Body Mass Index	CLH	Contralateral Hemisphere
BP	Blood Pressure	CMCiB	Comparative Medicine and Bioimage Centre of Catalonia
BSA	Bovine Serum Albumin	CNS	Central Nervous System
BUN	Urea Nitrogen	CoQ10	Coenzyme Q10
BV	Basilar Vein	COVID-19	Coronavirus Disease 2019
BVA	Brain Volume Affected	CoW	Circle of Willis
C		COX	Cyclooxygenase
C/CL	Contralateral	Cp	Crossing point
Ca	Calcium	CPSS	Cincinnati Prehospital Stroke Scale
CAA	Cerebral Amyloid Angiopathy	CRE	Creatinine
Casp2	Caspase 2	CRISPR	Clustered Regularly Interspaced Short Palindromic Repeats
CCA	Common Carotid Artery	CSF	Cerebrospinal Fluid
CCL2	Chemokine (C-C motif) ligand 2	CSVd	Cerebral Small Vessel Disease
CCR2	C-C chemokine receptor type 2		
cDNA	Complementary Deoxyribonucleic Acid		
CEEA	Animal Research Ethics Committee		
Cl	Chloride		

CTA	Computed Tomography Angiography	DTI	Diffusion Tensor Imaging
CT	Computed Tomography	DWI	Diffusion Weighted Imaging
Cu⁺	Cuprous Ion		
Cu²⁺	Cupric Iron	E	
CVT	Cerebral Venous Thrombosis	EDTA	Ethylenediaminetetraacetic Acid
CXCL16	Chemokine (C-X-C motif) ligand 16	EEG	Electroencephalogram
		ELISA	Enzyme-Linked Immunosorbent Assay
D		ENRICH	Early Minimally Invasive Removal of Intracerebral Hemorrhage Trial
DAMP	Damage-Associated Molecular Patterns		
DCT1	Divalent Cation Transporter 1	EVD	External Ventricular Drainage
DFO	Deferoxamine	EVT	Endovascular Thrombectomy
DIV	Days- <i>In-Vitro</i>		
DLC	DeepLabCut	F	
DMSO	Dimethyl Sulfoxide	- Fe	Iron removed
DMT1	Divalent Metal Transporter 1	+ Fe	Iron loaded
		F	French
DNA	Deoxyribonucleic Acid	FAST	Face, Arm, Speech,
DSA	Digital Subtraction Angiography		Time to call 911 scale
DSC	Dynamic Susceptibility Contrast	FAST trial	Factor Seven for Acute Hemorrhagic Stroke trial

FC paw	Contralateral Forepaw	GLOB	Globulin
Fe²⁺	Ferrous Iron	GLU	Glucose
Fe³⁺	Ferric Iron	GPX4	Glutathione-Dependent Hydroperoxidase 4
FI paw	Ipsilateral Forepaw	GSH	Glutathione
FL paw	Front Left Paw	GV	Vein of Galen
FLAIR	Fluid-Attenuated Inversion Recovery	H	
Fpaws	Distance Between Forepaws	H/I	Hypoxia/Ischemia
FR paw	Front Right Paw	hATf	Human Apotransferrin
FSBB	Flow-Sensitive Black Blood	Hb	Hemoglobin
FSP1	Ferroptosis Suppressor Protein 1	HCl	Hydrochloric Acid
FT	Ferritin	HC paw	Contralateral Hindpaw
G		hHTf	Human Holotransferrin
G	Gauge	HI paw	Ipsilateral Hindpaw
GAPDH	Glyceraldehyde-3-Phosphate Dehydrogenase	HL paw	Hind Left Paw
GATE-ICH	Glibenclamide Advantage in Treating Edema after Intracerebral Hemorrhage Trial	Hp	Haptoglobin
GCS	Glasgow Coma Scale	Hpaws	Distance Between Hindpaws
gDNA	Genomic DNA	Hpx	Hemopexin
		HR paw	Hind Right Paw
		HS	Hemorrhagic stroke
		HTf or diFe-Tf	Holotransferrin

I

I/IL	Ipsilateral
ICA	Internal Carotid Artery
ICH	Intracerebral Hemorrhage
ICP	Intracranial Pressure
ICV	Internal Cerebral Vein
ID	Integrated Density
i-DEF	Intracerebral Hemorrhage Deferoxamine Trial
IgG	Immunoglobulin G
IGTP	Germans Trias i Pujol Research Institute
IHC	Immunohistochemistry
IHF	Immunohistofluorescence
IJV	Internal Jugular Vein
IL-1β	Interleukin 1 β
IL-6	Interleukin 6
IM	Intramuscular
INTERACT I	Intensive Blood Pressure Reduction in Acute Cerebral Hemorrhage Trial 1

Intensive Blood Pressure Reduction in Acute Cerebral Hemorrhage Trial 2

Intensive Blood Pressure Reduction in Acute Cerebral Hemorrhage Trial 3

IRB Iron Removal Buffer
ISB Iron Saturation Buffer
IRDye Infrared Dye
IS Ischemic Stroke

ISS Inferior Sagittal Sinus
IV Intravenous
IVH Intraventricular Hemorrhages

K
KCl Potassium Chloride

L
LAPDD Los Angeles Prehospital Stroke Scale

LASSO Least Absolute Shrinkage and Selection Operator
LDL-C Low-Density Lipoprotein-Cholesterol

L-NAME	NG-Nitro-L-Arginine-Methyl Ester	mNSS	Modified Neurological Severity Score
lncRNA	Long Noncoding Ribonucleic Acid	MOPS	3-(N-morpholino)propanesulfonic Acid
M			
MAC	Membrane Attack Complex	MRI	Magnetic Resonance Imaging
MACH	Minocycline in Acute Cerebral Hemorrhage Trial	mRNA	Messenger Ribonucleic Acid
MAPK	Mitogen-Activated Protein Kinases	mRS	Modified Rankin Scale
MARS	Mouse Action Recognition System	MS	Mild Stroke
MCA	Middle Cerebral Artery	mTf	Mouse Transferrin
mFe or meFe-Tf	Monoferic Transferrin	mTORC1	Mechanistic Target of Rapamycin Complex I
		MTT assay	3-(4,5-Dimethylthiazol-2-yl)-2,5-Diphenyltetrazolium Bromide Colorimetric Assay
MIS	Minimally Invasive Surgery	N	
MISTIE III	Minimally Invasive Surgery Plus Recombinant Tissue Plasminogen Activator for Intracerebral Hemorrhage Evacuation Trial 3	N₂	Nitrogen
MMPs	Matrix Metalloproteinases	N₂O	Nitric Oxide
		NaCl	Sodium Chloride
		NAD(P)H	Nicotinamide Adenine Dinucleotide Phosphate
		NCCT	Non-Contrasted Computed Tomography

NDS	Neurological Deficit Scoring	NRT	No-Reverse Transcription
NeuN	Fox-3, Rbfox3, or Hex- a-ribonucleotide Binding Protein-3	NS	No Stroke
NETs	Neutrophil Extracellular Traps	NTC	No Template Control
NF-κB	Nuclear Factor Kappa B	O	
NIHSS	National Institutes of Health Stroke Scale	O₂	Oxygen
NIE	Neurological Impair- ment Equivalence	OCT	Optimal Cutting Tem- perature control
NLRP3	NOD-, LRR- and Pyrin domain-containing Pro- tein 3	OD	Optical Density
NMDA	N-methyl-D-Aspartate	P	
NPV	Negative Predicted Val- ues	P1	First Segment of the Posterior Cerebral Ar- tery
Nramp2	Natural Resistance-As- sociated Macrophage Protein 2	PARs	Protease-Activated Re- ceptors
NRD	Normalized Relative Difference	PBS	Phosphate-Buffered Sa- line
NRF2	Nuclear Factor Erythroid 2-Related Factor 2	PCA	Posterior Cerebral Ar- tery
		PCBP2	Poly(rC)-Binding Pro- tein 2
		PComA	Posterior Communica- ting Artery
		PF4	Platlet Factor 4
		PHE	Perihematomal Edema

PMSF	Phenylmethanesulfonyl Fluoride	Intracerebral Hemorrhage Trial
PPV	Positive Predictive Values	RIPA RadioImmunoPrecipitation Assay
proCasp2	ProCaspase 2	RM <i>Rete Mirabile</i>
PVDF	Polyvinylidene Fluoride	RMSE Root Mean Square Error
PVH	Periventricular Hemorrhage	RNA Ribonucleic Acid
Q		ROC Receiver Operating Characteristic
QASC	Quality in Acute Stroke Care	ROI Region of Interest
qPCR	Quantitative Polymerase Chain Reaction	ROS Reactive Oxygen Species
R		ROSIER Recognition of Stroke in the Emergency Room scale
R²	Coefficient of determination	RTA Radical-Trapping Antioxidants
RAINS	Rapid, Intensive, and Sustained Blood Pressure Reduction Trial	rtPA Recombinant Tissue Plasminogen Activator
rFVIIa	Recombinant Factor VIIa	S S Stroke
RICH	Remote Ischemic Conditioning on Functional Outcomes in Patients With Supratentorial	S1PR Sphingosine-1-Phosphate Receptor
		SAPNS Self-Assembly Peptide Nanofibrous Scaffold

SBI	Secondary Brain Injury	STAIR	Stroke Therapy Academic Industry Roundtable
SD	Standard Deviation		
SDS	Sodium Dodecyl Sulphate	STATIC	Statins for Neuroprotection in Spontaneous Intracerebral Hemorrhage Trial
SDS-PAGE	Sodium Dodecyl Sulphate Polyacrylamide Gel Electrophoresis		
SE	Sensitivity	STICH	International Surgical Trial in Intracerebral Hemorrhage Trial
SEM	Standard Error of the Mean	STICH II	International Surgical Trial in Intracerebral Hemorrhage Trial 2
SiS	Sigmoid Sinus		
SimBA	Simple Behavioral Analysis	STOP-IT	The Spot Sign for Predicting and Treating ICH Growth Study Trial
SLC3a2	Solute Carrier Family 3 Member 2		
SLC11a2	Solute Carrier Family 11 Member 2	STOP-MSU	Stopping Intracerebral Haemorrhage with Tranexamic Acid for Hyperacute Onset Presentation including Mobile Stroke Units Trial
SLEAP	Social LEAP Estimates Animal Poses		
SP	Specificity	StS	Straight Sinus
SPOTLIGHT	"Spot Sign" Selection of Intracerebral Hemorrhage to Guide Hemostatic Therapy Trial	SWI	Susceptibility-Weighted Imaging
SS	Severe Stroke		
SSS	Superior Sagittal Sinus		

T		
TAT	Thrombin-AntiThrombin	TOAST Trial of Org 10172 in Acute Stroke Treatment
TBHQ	Tert-Butylhydroquinone	TP Total Protein
TBIL	Total Bilirubin	tPA Tissue-type Plasminogen Activator
TBE	Tris-borate-EDTA	TR Tape Removal
TBS	Tris-buffered saline	Tregs Regulatory T cells
Tf	Transferrin	Tris Tris(hydroxymethyl)aminomethane
TfR	Transferrin Receptor	TS Transverse Sinus
TGF-β	Transforming Growth Factor-beta	TSAT Percentage of Transferrin Saturation
Th17	T helper 17	TSV Thalamostriate Veins
TICH-NOAC	Tranexamic Acid for Intracerebral Hemorrhage in Patients on Non-Vitamin K Antagonist Oral Anticoagulants Trial	TTC 2,3,5-Triphenyltetrazolium Chloride
TLR	Toll-Like Receptors	TXA Tranexamic Acid
TLR2	Toll-Like Receptor 2	U
TLR4	Toll-Like Receptor 4	
TNF-α	Tumor Necrosis Factor- α	U-PAGE Precast 6% TBE Urea Gels
TNFR	Tumor Necrosis Factor Receptor	W
		WB Western Blot
		WHO World Health Organization
		X
		xCT x_c^- System

Abstract

Intracerebral hemorrhage (ICH) is a form of stroke caused by bleeding into the brain parenchyma following blood vessel rupture. It is associated with high mortality and morbidity and, unlike ischemic stroke (IS), still lacks an approved, curative treatment despite several promising preclinical candidates. While IS therapies aim to restore blood flow by resolving vascular blockages, ICH management is focused on blood pressure control and preventing hematoma expansion. Critically, no approved therapy addresses the secondary injury caused by clot breakdown products, despite several candidates have been identified in preclinical studies.

One factor contributing to poor translation may be the use of preclinical models with limited predictive value. Rodent models, although useful in early-stage research, have lissencephalic brains and different gray-white matter architecture compared to humans. In contrast, large animals (e.g. pigs) provide a more suitable model that would help overcome critical shortcomings in ICH preclinical research.

A core focus of this thesis work is the evaluation of human apotransferrin (hATf) as a therapeutic for ICH. hATf significantly improved sensorimotor performance at early time points in mice without affecting hematoma size, edema, or coagulation. hATf rapidly reduced plasma transferrin saturation (TSAT) within 24 hours, accumulated in the injured brain, and reduced oxidative stress (4-HNE). These effects were independent of canonical ferroptosis pathways (GPX4/xCT or FSP1). Instead, hATf preserved the iron chaperone PCBP2, decreased expression of TfR1 (a hallmark ferroptosis marker), and blocked caspase-2 activation, indicating combined antiferroptotic and anti-apoptotic action.

Notably, hATf reduced TSAT and improved neurological outcomes more rapidly than previously described for deferoxamine, which has shown a delayed effect on TSAT and only modest benefits in the iDEF and TANDEM trials. hATf's demonstrated safety and efficacy in both ICH and ischemic rodent models support its potential as a broadly applicable stroke therapy.

This study also highlights that in ICH, functional recovery rather than hematoma volume is the most relevant and reliable preclinical endpoint. To improve its evaluation, an automated

DeepLabCut-based motion tracking tool was developed to analyze the neurobehavioral performance of mice in the adhesive tape removal test. This system provided a sensitive, objective assessment of neurobehavioral deficits and accurately classified stroke severity in both ischemic and hemorrhagic models. The tool is currently being adapted for pig studies to enhance translational value.

To further bridge the gap between preclinical and clinical research, a novel, minimally invasive swine ICH model was developed using autologous injection of blood, avoiding surgical trauma. Although the study pig population should be expanded, early MRI imaging and biomarker shifts validated the model's relevance.

Together with prior work, this thesis builds a compelling case for hATf as a rapid-acting, multi-target stroke therapy. Its efficacy in both stroke types supports its potential as a pre-hospital intervention.

Resum

L'hemorràgia intracerebral (ICH) és una forma d'ictus causada per un sagnat al parènquima cerebral arran de la ruptura d'un vas sanguini. S'associa a una elevada mortalitat i morbiditat i, a diferència de l'ictus isquèmic (IS), encara no disposa d'un tractament curatiu específic i aprovat, malgrat l'existència de diversos candidats prometedors en fase preclínica. Mentre que les teràpies per l'IS busquen restaurar el flux sanguini resolent les obstruccions vasculars, el tractament de la ICH se centra en el control de la pressió arterial i la prevenció de l'expansió de l'hematoma. És especialment crític que no hi ha cap teràpia aprovada que abordi el dany secundari causat pels productes de degradació del coàgul, tot i a ver-se trobat diverses molècules candidates en estudis preclínics.

Un dels factors que podria contribuir a aquesta mala traducció clínica és l'ús de models preclínics amb valor predictiu limitat. Els models en rosegadors, tot i ser útils en les fases inicials de la investigació, tenen cervells lisencèfals i una arquitectura de substància grisa i blanca diferent de la dels humans. En canvi, els animals grans (p. ex. el porc) ofereixen un model més adequat per superar mancances crítiques de la recerca preclínica sobre la ICH.

Un dels punts centrals d'aquest treball de tesi és l'avaluació de l'apotransferrina humana (hATf) com a teràpia per a l'ICH. Aquesta, va millorar significativament el rendiment sensoriomotor en ratolins a temps curts, sense afectar la mida de l'hematoma, l'edema ni la coagulació. L'hATf va reduir ràpidament la saturació de transferrina plasmàtica (TSAT) en menys de 24 hores, es va acumular al cervell lesionat i va disminuir l'estrès oxidatiu (4-HNE). Aquests efectes van ser independents de les vies canòniques de ferroptosi (GPX4/xCT o FSP1). En lloc d'això, l'hATf va preservar la xaperona del ferro PCBP2, va disminuir l'expressió del receptor de transferrina TfR1 (un marcador característic de ferroptosi), i va bloquejar l'activació de la caspasa-2, indicant una acció combinada antiferroptòtica i antiapoptòtica.

És destacable que l'hATf va reduir la TSAT i va millorar els resultats neurològics de manera més ràpida que el descrit prèviament per la deferoxamina, la qual ha mostrat un efecte retardat sobre la TSAT i beneficis modestos en els assaigs iDEF i TANDEM. La seguretat i

eficàcia demostrades de l'hATf en models rosegadors de ICH com d'ictus isquèmic donen suport al seu potencial com a teràpia aplicable per l'ictus.

Aquest estudi també posa de manifest que, en el context de l'ICH, la recuperació funcional, i no el volum de l'hematoma, és el criteri preclínic més rellevant i fiable. Per tal de millorar la seva evaluació, es va desenvolupar una eina automatitzada de seguiment del moviment basada en DeepLabCut per analitzar el comportament neurofuncional dels ratolins en la prova de retirada de cinta adhesiva. Aquest sistema va permetre una evaluació sensible i objectiva dels dèficits neuroconductuals i va classificar amb precisió la gravetat de l'ictus tant en models isquèmics com hemorràgics. Actualment, l'eina s'està adaptant per a estudis amb porcs, per tal d'incrementar el valor traslacional.

Per tal de reduir encara més la distància entre la recerca preclínica i clínica, es va desenvolupar un nou model porc de ICH mínimament invasiu mitjançant injecció autòloga de sang, evitant així el trauma quirúrgic. Tot i que cal ampliar la població de porcs de l'estudi, les primeres imatges per ressonància magnètica i els canvis en biomarcadors van validar la rellevància del model.

Juntament amb treballs previs, aquesta tesi construeix un argument sólid a favor de l'hATf com a teràpia per a l'ictus de múltiples dianes i acció ràpida. La seva eficàcia demostrada en ambdós tipus d'ictus reforça el seu potencial com a intervenció prehospitalària.

Resumen

La hemorragia intracerebral (ICH) es una forma de ictus causada por sangrado en el parénquima cerebral tras la ruptura de un vaso sanguíneo. Se asocia con una alta mortalidad y morbilidad y, a diferencia del ictus isquémico (IS), todavía carece de un tratamiento curativo aprobado y específico, a pesar de la existencia de varios candidatos prometedores en estudios preclínicos. Mientras que las terapias para el IS buscan restaurar el flujo sanguíneo resolviendo obstrucciones vasculares, el manejo de la ICH se centra en el control de la presión arterial y a la prevención de la expansión del hematoma. De forma crítica, no existe ninguna terapia aprobada que aborde el daño secundario causado por los productos de degradación del coágulo, a pesar de haberse encontrado moléculas candidatas en estudios preclínicos.

Uno de los factores que contribuyen a esta mala traducción clínica podría ser el uso de modelos preclínicos con valor predictivo limitado. Los modelos en roedores, aunque útiles en fases tempranas de investigación, tienen cerebros lisencefálicos y una arquitectura de sustancia gris y blanca distinta a la de los humanos. En contraste, los animales grandes (p. ej. el cerdo) representan un modelo más adecuado que ayudaría a superar deficiencias críticas en la investigación preclínica de la ICH.

Un foco central de este trabajo de tesis es la evaluación de la apotransferrina humana (hATf) como tratamiento para la ICH. La cual mejoró significativamente el rendimiento sensoriomotor en puntos de tiempo tempranos en ratones, sin afectar el tamaño del hematoma, el edema ni la coagulación. La hATf redujo rápidamente la saturación de transferrina plasmática (TSAT) en menos de 24 horas, se acumuló en el cerebro lesionado y redujo el estrés oxidativo (4-HNE). Estos efectos fueron independientes de las vías canónicas de ferroptosis (GPX4/xCT o FSP1). En su lugar, la hATf preservó la chaperona de hierro PCBP2, disminuyó la expresión del receptor de transferrina TfR1 (marcador característico de la ferroptosis), y bloqueó la activación de caspasa-2, lo que indica una acción combinada antiferroptótica y antiapoptótica.

De forma notable, la hATf redujo la TSAT y mejoró los resultados neurológicos de manera más rápida que la deferoxamina, la cual ha mostrado un efecto retardado sobre la TSAT y beneficios modestos en los ensayos iDEF y TANDEM. La seguridad y eficacia demostradas

de hATf en modelos de ICH y de isquemia cerebral en roedores respaldan su potencial como terapia aplicable para el ictus.

Este estudio también resalta que, en la ICH, la recuperación funcional, y no el volumen del hematoma, es el criterio preclínico más relevante y fiable. Para mejorar su evaluación, se desarrolló una herramienta automatizada de seguimiento de movimiento basada en DeepLabCut, utilizada para analizar el rendimiento neuroconductual de los ratones en la prueba de retirada de cinta adhesiva. Este sistema proporcionó una evaluación sensible y objetiva de los déficits neuroconductuales y clasificó con precisión la gravedad del ictus en modelos isquémicos y hemorrágicos. Actualmente, esta herramienta está siendo adaptada para estudios en cerdos con el fin de aumentar su valor traslacional.

Para acercar aún más la investigación preclínica a la clínica, se desarrolló un modelo porcino novedoso y mínimamente invasivo de ICH mediante inyección autóloga de sangre, evitando el trauma quirúrgico. Aunque la población del estudio de cerdo debe ampliarse, las primeras imágenes por resonancia magnética y los cambios en biomarcadores validaron la relevancia del modelo.

Junto con trabajos previos, esta tesis construye un caso convincente para la hATf como una terapia multiblanco de acción rápida para el ictus. Su eficacia demostrada en ambos tipos de ictus respalda su potencial como intervención en fase prehospitalaria.

INTRODUCTION

Introduction

1. STROKE

1.1. Historical milestones

The term “stroke” was first used in a medical context during the 19th - 20th century (Storey and Pols, 2010). In the past, physicians used the term “apoplexy”, which was present in Hippocrates's writings, to describe a catastrophic illness that caused a sudden loss of consciousness and often resulted in death (Clarke, 1963; Schutta and Howe, 2006). The term “apoplexy” envelops various conditions or illnesses, including some cases that probably referred to strokes.

It was not until the arrival of anatomists in the 17th century that the association between apoplexy and cerebral hemorrhages, as well as other causes like tumors and cerebral abscesses, began to be recognized (Schutta and Howe, 2006; Sacco *et al.*, 2013). Over time, apoplexy came to be primarily understood as a vascular disease and was further classified in two types: *sanguinea* (hemorrhagic) and *ischaemica* (ischemic) (Storey and Pols, 2010).

Towards the end of the 19th century and the beginning of the 20th, there was a growing interest in the study of vascular anatomy and, more specifically, the relationship between clinical syndromes and regions affected by stroke. As insights of stroke advanced and new technologies emerged, clinicians began to speculate about the pathological mechanisms underlying stroke and explore new therapeutic and diagnostic options (Storey and Pols, 2010).

Today, we understand stroke as a critical medical emergency that annually affects millions of individuals, resulting from a disruption of blood flow within the brain. It is triggered by either arterial blockage or the rupture of an intracranial blood vessel, resulting in primary and secondary damage (Kathirvelu and Carmichael, 2015; Tejada Meza *et al.*, 2019; Martin *et al.*, 2025). The understanding of these damages is still far from complete.

Overall, the historical evolution of stroke as a medical term reflects the progress of medical knowledge, and this knowledge has provided new diagnostic techniques and available treatment options to address this serious condition. This thesis dissertation aims to contribute to deepening the understanding of intracerebral hemorrhagic stroke and to lay the foundations for exploring innovative therapeutic alternatives and new research models.

1.2. Definition, clinical signs and epidemiology

A stroke is classically defined by the World Health Organization (WHO) as the rapid development of clinical signs indicating focal (or global) disturbance of cerebral function that lasts more than 24 hours or leads to death, with no apparent cause other than of vascular origin ([WHO MONICA Project Principal Investigators, 1988](#)). The most prevalent indications of a stroke include sudden numbness or weakness in the face, arm, or leg, and primarily affects only one side of the body. Additionally, individuals experience other typical symptoms such as confusion, difficulties in speech or understanding, vision problems, walking impairments, dizziness, loss of balance, unexplained severe headaches, and lack of coordination ([WHO, 2021](#)).

The WHO's definition, which primarily relies on symptoms, is considered outdated by the American Heart Association (AHA) and the American Stroke Association (ASA) due to the advancements in the understanding of pathophysiology and its clinical implications. These organizations have released a consensus statement that provides definitions for different types of strokes based on factors such as nature, timing, and clinical recognition of stroke and its mimics (**Table 1.**) ([Sacco *et al.*, 2013](#)).

Table 1. Definition of stroke

Definition of stroke	
Ischemic stroke (IS)	Episode of neurological dysfunction caused by focal cerebral, spinal, or retinal infarction.
Intracerebral hemorrhage (ICH)	A focal collection of blood within the brain parenchyma or ventricular system that is not caused by trauma (this includes parenchymal hemorrhages after CNS infarction).
Stroke caused by ICH	Rapidly developing clinical signs of neurological dysfunction attributable to a focal collection of blood within the brain parenchyma or ventricular system that is not caused by trauma.
Silent cerebral hemorrhage	A focal collection of chronic blood products within the brain parenchyma, subarachnoid space, or ventricular system on neuroimaging or neuropathological examination that is not caused by trauma and without a history of acute neurological dysfunction attributable to the lesion.

Subarachnoid hemorrhage	Bleeding into the subarachnoid space (the space between the arachnoid membrane and the pia mater of the brain or spinal cord).
Stroke caused by subarachnoid hemorrhage	Rapidly developing signs of neurological dysfunction and/or headache because of bleeding into the subarachnoid space (the space between the arachnoid membrane and the pia mater of the brain or spinal cord), which is not caused by trauma.
Stroke caused by cerebral venous thrombosis	Infarction or hemorrhage in the brain, spinal cord, or retina because of thrombosis of a cerebral venous structure. Symptoms or signs caused by reversible edema without infarction or hemorrhage do not qualify as stroke.
Stroke, not otherwise specified	An episode of acute neurological dysfunction presumed to be caused by ischemia or hemorrhage, persisting ≥ 24 hours or until death, but without sufficient evidence to be classified as one of the above.

Extracted from: [\(Sacco *et al.*, 2013\)](#)

Stroke presents a health challenge, affecting millions of people across different regions. The global prevalence of all stroke subtypes in 2021 was 93.82 million cases. From these, 69.94 million were ischemic strokes (IS), 16.60 million were intracerebral hemorrhages (ICH) and 7.85 million cases were subarachnoid hemorrhages [\(Martin *et al.*, 2025\)](#). Stroke is ranked as the second leading cause of death and a leading cause of serious long-term disability, right behind ischemic cardiopathies [\(World Health Organization \(WHO\), 2020; GBD 2019 Stroke Collaborators, 2021\)](#).

Despite advances in the management and treatment of stroke over the years, between 1990 and 2019 there has been a 70% increase in the absolute number of stroke incidents [\(Martin *et al.*, 2025\)](#). When considering the average age of stroke patients, trends reveal an increase in cases among young adults and middle-aged people [\(Martin *et al.*, 2025\)](#). When considering age-specific incidence rates, females exhibit lower rates than males in middle-aged groups [\(Brea *et al.*, 2013; Martin *et al.*, 2025\)](#). Reinforcing this trend, a recent systematic review of epidemiological studies highlights that the incidence for cerebrovascular diseases tends to be lower in women compared to men in most of the studies [\(Purroy and Montalà, 2021\)](#).

Certain countries from the Eastern Europe experience higher stroke incidence and prevalence rates compared to other European subregions. The stroke burden is influenced by

demographic, environmental and genetic factors, lifestyle, as well as healthcare infrastructure (Prendes *et al.*, 2024).

Despite significant advancements in stroke management in Europe, the incidence of stroke is on the rise. In Spain, for instance, the incidence of stroke exceeds 100 cases per 100,000 persons a year. In fact, the Ibericus study reports an annual stroke incidence of 187 cases per 100,000 persons (Díaz-Guzmán *et al.*, 2012), while data from Spain's National Statistics Institute suggests a slightly higher annual incidence, estimated at around 252 cases per 100,000 persons (Brea *et al.*, 2013). Considering these numbers, stroke also imposes a significant economic burden (Brea *et al.*, 2013; Martin *et al.*, 2025).

Looking ahead, the concerning statistics associated with the occurrence and economic impact of stroke, both in Spain and globally, emphasize the urgency of novel therapies, advanced therapeutic strategies, innovative diagnostic tools, and rehabilitation strategies. These efforts aim to improve the quality of life of post-stroke patients.

1.3. Stroke types

Depending on the nature/underlying pathology of the stroke, we classify them into two types: ischemic and hemorrhagic stroke (Amarenco *et al.*, 2009).

The **ischemic stroke** (IS) is the most common type of stroke, being 87% of all stroke cases (Martin *et al.*, 2025). It is caused by a temporary or permanent reduction in the blood flow in one or multiple brain regions (Bonkhoff *et al.*, 2022). This reduction is mostly due to a clot/thrombus or a decrease in the blood supply (Figure 1.) (Campbell *et al.*, 2019). The extent of the damage depends on the duration of the obstruction, severity and localization (Deb, Sharma and Hassan, 2010).

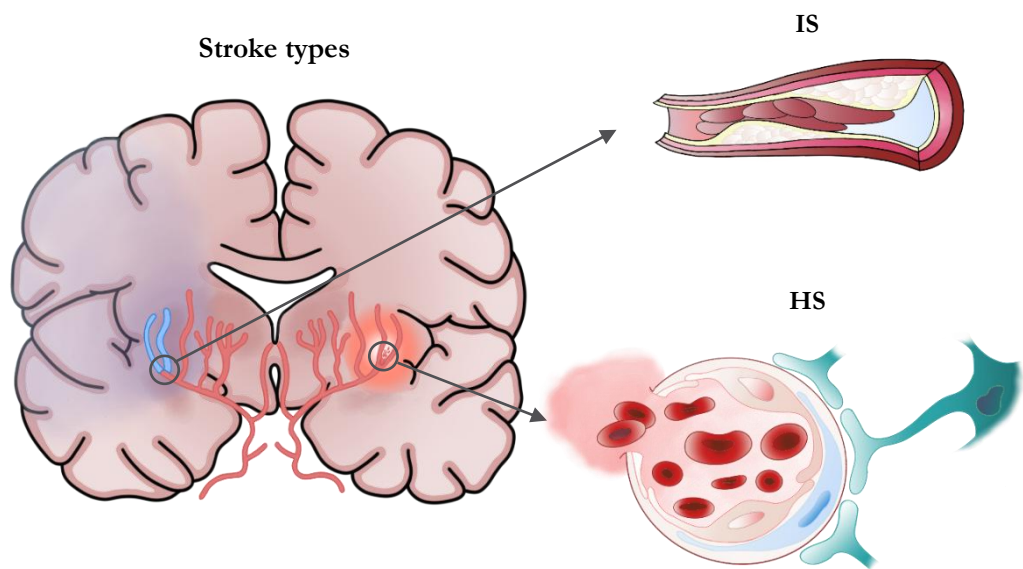


Figure 1. Schematic representation of a brain showing the pathophysiological differences in the mechanisms of two types of strokes: ischemic/IS (left side of the brain) and hemorrhagic/HS (right side of the brain). The ischemic stroke is associated with an occluded blood vessel, and the hemorrhagic stroke is characterized by a ruptured blood vessel, both shown by the arrow pointing to the blocked/broken vessel.

The classification of the ischemic stroke subtypes based on their etiology was established by the Trial of Org 10172 in Acute Stroke Treatment (TOAST) (Adams *et al.*, 1993). This categorization differentiates five subtypes of ischemic stroke:

- Large-artery atherosclerosis. This subtype involves an important stenosis or occlusion of a large artery or a branch cortical artery.
- Cardioembolism. It is a stroke subtype characterized by an arterial occlusion caused by an embolus originating in the heart.
- Small-artery occlusions (lacune). The ischemic stroke is produced because of the occlusion of brain arterioles, resulting in lesions with a diameter of less than 1.5 cm.
- Stroke of other determined etiology. Patients in this category have rare causes of stroke, such as systemic diseases like hematologic disorders or hypercoagulable states.
- Stroke of undetermined etiology. In this case, the cause of the stroke is not identified, or the patient exhibits two or more probable causes of stroke.

Hemorrhagic subtypes of **stroke** (HS), although being less common than ischemic strokes, are characterized by greater severity, worse prognosis, and higher mortality rates (Kathirvelu and Carmichael, 2015; Shoamanesh *et al.*, 2021). Cerebral hemorrhages within the central nervous system are classified as hemorrhagic stroke if they result from a blood vessel rupture (mainly arteries) into the surrounding brain areas (Figure 1.) (Fewel, Thompson and Hoff, 2003; Sacco *et al.*, 2013). These hemorrhages are classified in subtypes based on their location, which will determine the treatment, prognosis, etiology, complications and risk factors (Figure 2.):

- Intraparenchymal hemorrhage or intracerebral hemorrhage (ICH). ICH involves the extravasation of blood within the brain parenchyma or ventricular system (Martin *et al.*, 2025). In intraventricular hemorrhages (IVH) the blood is in the ventricular system or has extended to it, indicating a poor prognosis (Roh *et al.*, 2022).
- Subarachnoid hemorrhage. This type of hemorrhage takes place in the subarachnoid space (Seki *et al.*, 2016).
- Epidural hemorrhage. Blood accumulates between the skull and the dura mater and is usually associated with head trauma (Ng, Yeo and Seow, 2004; Aromatario *et al.*, 2021).
- Subdural hemorrhage. The hemorrhage is produced between the arachnoid and the dura mater, and is mainly due to head trauma (Aromatario *et al.*, 2021).

In addition to macrohemorrhages, we can find “microbleeds”, also known as silent cerebral hemorrhages or chronic small parenchymal hemorrhages. They share pathophysiology with macrohemorrhages and are frequently observed in patients with cerebral amyloid angiopathy and/or chronic hypertension. Despite their lack of immediate clinical manifestations, an elevated quantity of microbleeds is associated with cognitive decline and an increased risk of ICH (Sacco *et al.*, 2013).

Other causes that lead to the appearance of hemorrhages in the brain involve the rupture of veins resulting from a thrombus-induced occlusion, known as cerebral venous thrombosis (CVT). CVT may involve intracranial venous sinuses, the deep venous system, and cortical veins (Sacco *et al.*, 2013).

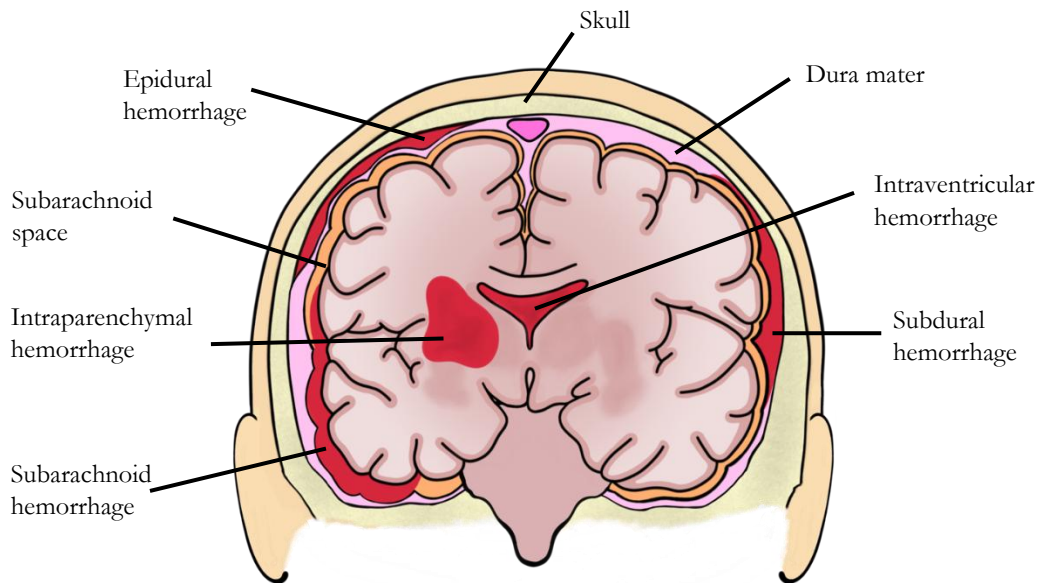


Figure 2. Coronal slice of a human head representing different types of hemorrhages in the brain or surrounding areas. The image shows the presence of hemorrhages at different locations: subarachnoid, epidural, subdural, intraparenchymal, and intraventricular. Each hemorrhage type is indicated in the corresponding regions, highlighting the diverse patterns of bleeding within the brain.

It is essential to differentiate between stroke types and discriminate from other neurological conditions that do not have a vascular origin but mimic the symptoms (e.g. stroke mimics). Not only for the different treatments that are applied according to the stroke subtype, but also to implement preventive strategies in order to reduce the risk of recurrent strokes, as well as for conducting research and clinical trials. There are several tissue injury mechanisms involved in stroke damage, and knowing them is crucial to develop neuroprotective and diagnostic strategies (Deb, Sharma and Hassan, 2010).

This thesis focuses on the hemorrhagic stroke type, specifically in the non-traumatic intracerebral hemorrhagic subtype.

2. INTRACEREBRAL HEMORRHAGES

Intracerebral hemorrhages (ICH) are bleeds into the brain parenchyma, either with or without communication into the ventricular system, due to the rupture of an intracranial vessel (Sacco *et al.*, 2013; Sheth, 2022). ICH is mainly caused by hypertension (which produces structural damage to the small arteries and arterioles), followed by others such as cerebral amyloid angiopathy (CAA), aneurysms or arteriovenous malformations rupture, ICH resulting from anticoagulation therapy, tumors, and hemorrhagic transformations of ischemic stroke among others (Ziai and Carhuapoma, 2018; Sheth, 2022; Ohashi *et al.*, 2023).

2.1. Specific epidemiology and costs

Among all stroke cases, intracerebral hemorrhages represent around 10% of all strokes (van Asch *et al.*, 2010; Martin *et al.*, 2025). It seems to have higher incidence rates in the elderly, in Eastern countries such as Japan, and in black and hispanic populations in the United States (Magid-Bernstein *et al.*, 2022; Martin *et al.*, 2025).

Characterized as the deadliest form of acute stroke with a 30-40% mortality rate in early stages, survivors are frequently left with long-term functional impairment with a high risk of recurrent hospitalization (Yousufuddin *et al.*, 2020; Greenberg *et al.*, 2022).

This condition has an important economic impact on healthcare systems, not only direct costs such as hospitalization, drugs, and rehabilitation but also indirect costs. These ones exceed the direct costs and include those associated with informal caregivers, reduction in work capacity, and both permanent and temporary incapacity (Navarrete-Navarro *et al.*, 2007). Indeed, in the United States, only the average accumulated direct costs per patient during the first three years after an ICH are approximately 48,000 \$ (Yousufuddin *et al.*, 2020); in Spain, the costs are around 12,000 € (Navarrete-Navarro *et al.*, 2007).

2.2. Neurological signs

Intracerebral hemorrhages produce sudden, not instantaneous, focal neurological signs that develop over minutes. The manifestation of these signs depends on the location and the extension of the hemorrhage. In general, ICH produces decreased level of consciousness, headaches, nausea and/or vomiting (Montaño, Hanley and Hemphill, 2021). Some authors

have specified the clinical signs depending on the location of the hemorrhage (**Table 2.**) ([Qureshi et al., 2001](#); [Sheth, 2022](#)):

Table 2. Potential neurological signs depend on the hemorrhage location

Brain location	Neurological signs
Upper brain stem and arousal nuclei	Depressed level of consciousness.
Ventricles	Headache and vomiting (if the ventricular hemorrhage is combined with hydrocephalus, it can cause stupor).
Basal ganglia	Hemiplegia and sensory-motor deficits in the non-damaged side (contralateral). Gaze preference to the damaged side (ipsilateral).
Thalamus	Hemiplegia and hemisensory loss (contralateral sensory-motor deficits), and eye signs such as downward and inward deviation, miotic pupils and “wrong-way” eyes with gaze preference to the contralateral side.
Cerebral hemispheres (lobes)	Hemiparesis and hemisensory loss, seizures, aphasia, neglect, hemianopia and gaze preference to the ipsilateral side.
Brain stem (pons)	Impaired level of consciousness, contralateral motor deficits, cranial nerve palsies, facial weakness, dysarthria, pinpoint (but reactive) pupils, absent or impaired horizontal gaze, ocular bobbing and coma.
Cerebellum (dentate nucleus)	Nystagmus, vertigo, vomiting, dysmetria and limb ataxia.
Fourth ventricle	Stupor or coma.

Extracted from: ([Qureshi et al., 2001](#); [Passero et al., 2002](#); [Sheth, 2022](#))

2.3. Risk factors

The identification of risk factors that underlie these hemorrhages is important in order to reduce the incidence and prevalence of ICH as well as to improve the prognosis, management and diagnosis of the patients.

2.3.1. Non-modifiable risk factors

The incidence of ICH varies according to age, sex, race, circadian and circannual patterns, environmental factors, and the prevalence of cerebral amyloid angiopathy ([Ariesen et al., 2003](#); [Fewel, Thompson and Hoff, 2003](#); [van Asch et al., 2010](#); [Garg et al., 2019](#); [Martin et al., 2025](#)).

Elevated ICH risk has been associated with advanced **age, race, and ethnicity**, with Asian countries and black individuals in the United States presenting a higher incidence compared to white individuals (Qureshi *et al.*, 2001; Ariesen *et al.*, 2003; Fewel, Thompson and Hoff, 2003; van Asch *et al.*, 2010; Martin *et al.*, 2025).

As previously mentioned, **cerebral amyloid angiopathy** (CAA) is an important risk factor for ICH, particularly prevalent in aged people (van Asch *et al.*, 2010). In CAA, β -amyloid protein is deposited in arteries, arterioles, and capillaries of the cortex, leptomeninges, and cerebellum, causing mainly lobar hemorrhages (Fewel, Thompson and Hoff, 2003; An, Kim and Yoon, 2017). Autosomal-dominant types of CAA and the presence of $\epsilon 2$ and $\epsilon 4$ alleles in the gene encoding apolipoprotein E are associated with recurrent hemorrhages (O'Donnell *et al.*, 2010; Greenberg *et al.*, 2022).

Temporal factors such as **circadian and circannual patterns**, alongside **environmental elements** like pollution, CO₂, and noise levels, are related to ICH incidence due to their effect on blood pressure. For instance, a peak in the ICH incidence in winter has been proposed to be a result of differences in barometric pressures that affect arterial distensibility (Fewel, Thompson and Hoff, 2003; Poon, Bell and Al-Shahi Salman, 2015; Garg *et al.*, 2019).

2.3.2. Modifiable risk factors

Among the different ICH modifiable risk factors, **hypertension** is the most important one (Fewel, Thompson and Hoff, 2003; Greenberg *et al.*, 2022). Chronic hypertension induces degenerative changes in blood vessels, reducing arterial compliance and increasing the chances of an ICH, particularly in both lobar and small deep areas supplied by small perforating vessels and their bifurcations (Qureshi *et al.*, 2001; Hemphill *et al.*, 2015). These changes result in lipohyalinosis, Charcot-Bouchard aneurysms, atrophy and fragmentation of smooth muscle, granular or vesicular cellular degeneration, and fibrinoid necrosis (Qureshi, Mendelow and Hanley, 2009; Magid-Bernstein *et al.*, 2022).

Hypertension is not only associated with a higher risk of recurrent stroke but also with a high hazard ratio for ICH mortality compared to ischemic stroke (Martin *et al.*, 2025). Effective control of hypertension has been shown to improve ICH incidence, highlighting the importance of blood pressure management in ICH patients (Qureshi *et al.*, 2001; Fewel, Thompson and Hoff, 2003; Martin *et al.*, 2025).

Anticoagulant treatment (Fewel, Thompson and Hoff, 2003; An, Kim and Yoon, 2017; Gulati *et al.*, 2018; Greenberg *et al.*, 2022), **coagulopathies, COVID-19, and antiplatelet therapy** (An, Kim and Yoon, 2017; Magid-Bernstein *et al.*, 2022), especially in elderly patients (Fewel, Thompson and Hoff, 2003), increase the risk of ICH. In fact, the use of warfarin and newer generations of anticoagulant agents have been correlated with an increased risk of fatal outcomes following ICH. Other **drugs**, such as sympathomimetics or cocaine, are also associated with an increased ICH risk (Fewel, Thompson and Hoff, 2003; An, Kim and Yoon, 2017; Magid-Bernstein *et al.*, 2022).

Total cholesterol is inversely associated with ICH risk (Segal *et al.*, 1999; Fewel, Thompson and Hoff, 2003; O'Donnell *et al.*, 2010; Martin *et al.*, 2025). Actually, low triglyceride levels and the use of low-density lipoprotein-cholesterol (LDL-C)-lowering drugs have been assessed to increase the risk of ICH (Sturgeon *et al.*, 2007; Martin *et al.*, 2025). Low cholesterol levels result in a weakened arterial endothelium that can be easily broken, producing hemorrhages and a slower repair after the incident (Sturgeon *et al.*, 2007).

The association between **alcohol consumption, smoking**, and increased ICH risk remains unclear (Martini *et al.*, 2012; Carlsson *et al.*, 2019). High alcohol consumption has been linked to increasing the risk of ICH (Qureshi *et al.*, 2001; O'Donnell *et al.*, 2010, 2016; Poon, Bell and Al-Shahi Salman, 2015; An, Kim and Yoon, 2017) affecting the integrity of cerebral vessels, probably by inducing hypertension (Gorelick, 1987; Klatsky, Armstrong and Friedman, 1989) and/or impairing the coagulation (Qureshi *et al.*, 2001). However, this relationship has not been found across all studies (Sturgeon *et al.*, 2007; Martini *et al.*, 2012).

In contrast, the association between smoking and ICH risk is weaker than that with alcohol (Fewel, Thompson and Hoff, 2003; O'Donnell *et al.*, 2010), and in some studies, it has not been associated at all (Martini *et al.*, 2012; Sallinen *et al.*, 2020).

There are **other risk factors** related to ICH, including prior ICH, ischemic stroke, imaging biomarkers (microbleeds) (An, Kim and Yoon, 2017; Greenberg *et al.*, 2022), as well as late menopause and gestational hypertension (Martin *et al.*, 2025). However, inconsistencies persist in the associations between ICH risk and physical inactivity, body mass index (BMI), and diabetes, requiring further research (Fewel, Thompson and Hoff, 2003; O'Donnell *et al.*, 2010, 2016; Poon, Bell and Al-Shahi Salman, 2015; Greenberg *et al.*, 2022).

2.4. Location

Intracerebral hemorrhages typically originate from the anterior, middle, posterior cerebral, or basilar arteries (Qureshi, Mendelow and Hanley, 2009), thus producing bleeding mainly in the lobes of the brain, basal ganglia, thalamus, brain stem, and cerebellum (Qureshi *et al.*, 2001; Qureshi, Mendelow and Hanley, 2009). Some authors have specified arteries as the source of bleeding depending on the location of the hemorrhage (Figure 3.) (Qureshi *et al.*, 2001; Fewel, Thompson and Hoff, 2003):

- In the **cerebral lobes** the blood arises from penetrating cortical branches of the anterior, middle, or posterior cerebral arteries.
- **Basal ganglia** hemorrhages originate from the ascending lenticulostriate branches of the middle cerebral artery.
- In **thalamic** hemorrhages, the blood comes from ascending thalamogeniculate branches of the posterior cerebral artery.
- In **brain stem** hemorrhages, which are commonly produced in the pons, the blood arrives from paramedian branches of the basilar artery.
- **Cerebellar** hemorrhages result from the rupture of penetrating branches of the posterior inferior, anterior inferior, or superior cerebral arteries.

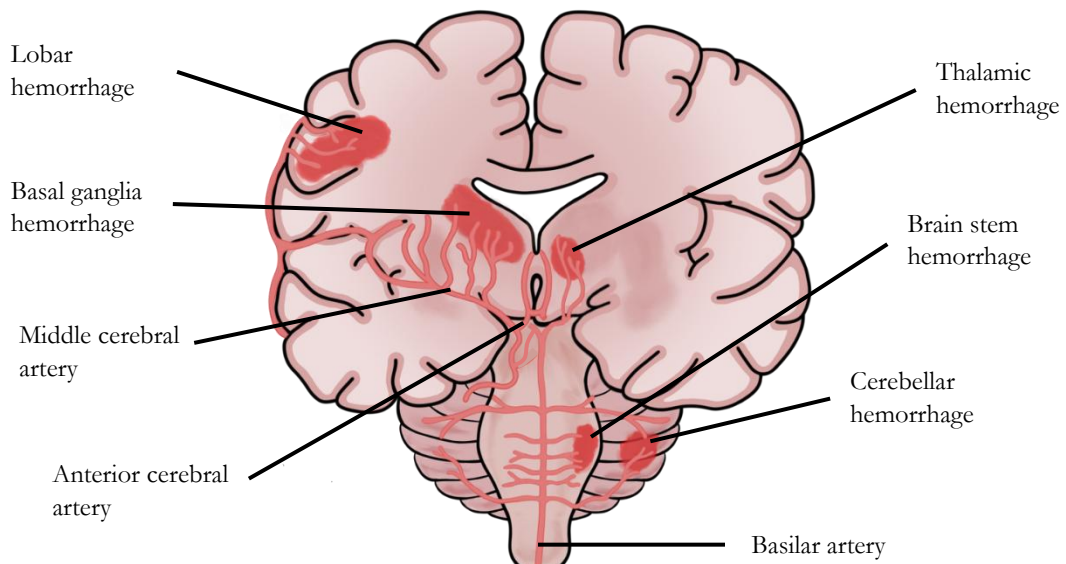


Figure 3. Coronal slice of a human brain highlighting various types of intracerebral hemorrhages. The image shows hemorrhages located in different regions, including, the basal ganglia, thalamus, lobar areas, brain stem, and cerebellum.

Accurate diagnosis and location of ICH requires imaging techniques such as computed tomography (CT) scan, magnetic resonance imaging (MRI), and angiography (Greenberg *et al.*, 2022).

2.5. Neurological evaluation (scales)

The neurological signs and highest percentage of mortality resulting from an intracerebral hemorrhage depend on the location of the extravasated blood (Rindler *et al.*, 2020; Sheth, 2022). The presence of a decreased level of consciousness and scoring alterations on neurological scales strongly suggests the possibility of an ICH (Qureshi *et al.*, 2001). However, an accurate diagnosis requires an initial assessment, including a complete anamnesis, and physical and neurological examination as well as additional tests (Greenberg *et al.*, 2022).

Complementary examinations such as laboratory assessments, electrocardiography, and thorax radiography play an important role in the diagnosis. Nevertheless, for diagnostic confirmation and differentiation between ischemic and hemorrhagic stroke, brain imaging using rapid CT scan or MRI is essential (Greenberg *et al.*, 2022).

The neurological examination of patients is accompanied by neurological scales to simplify the neurological evaluation and to facilitate communication among clinicians. However, there is currently no available scale capable of discriminating ICH from other stroke types without neuroimaging (Hemphill *et al.*, 2015).

Prehospital tools for ICH diagnosis are very limited, and it is not clear if it is better to use scales that incorporate severity instead of just stroke presence. Currently, prehospital scales, such as FAST (Face, Arm, Speech, Time to call 911 Scale), LAPDD (Los Angeles Prehospital Stroke Scale), CPSS (Cincinnati Prehospital Stroke Scale), and ROSIER (Recognition of Stroke in the Emergency Room Scale) are used for stroke patients but are not specifically made for ICH (Greenberg *et al.*, 2022). The decreased level of consciousness in ICH patients affects neurological scoring, guiding triage decisions and referral to appropriate care facilities (Qureshi *et al.*, 2001).

In the Emergency Department, one of the simplest and most widely used neurological assessment tools for ICH patients is the Intracerebral Hemorrhage score, which incorporates the Glasgow Coma Scale (GCS) (Sheth, 2022). Another scale that is also useful in ICH patients is the National Institutes of Health Stroke Scale (NIHSS), commonly used for ischemic stroke, although a limited level of consciousness could reduce its utility (Tables 3 and 4.) (Smith *et al.*, 2013; Greenberg *et al.*, 2022).

Table 3. Glasgow Coma Scale (GCS)

Domain	Response	Score
Eye opening	Spontaneous	4
	To speech	3
	To pain	2
	No opening	1
Verbal response	Oriented	5
	Confused patient	4
	Inappropriate response	3
	Incomprehensible response	2
	No response	1
Motor response	Obeying correctly	6
	Localize painful stimuli	5
	Response to the painful stimuli without localizing it	4
	Response with an abnormal flexion of the limbs	3
	Response with an abnormal extension of the limbs	2
	No motor response	1
Total		3-15

Extracted from: (Teasdale *et al.*, 1979)

Table 4. National Institutes of Health Stroke Scale (NIHSS)

Item	Name	Score
Conscious level	Alert	0
	No alert, response to minimum verbal stimuli	1
	No alert, response to repeated or painful stimuli	2
	Coma. Only reflexes or no responses	3
Questions (age and current month)	Both correct	0
	One correct	1
	None correct or coma	2
Motor commands (close and open eyes and hands)	Both correct	0
	One correct	1
	None correct or coma	2
Gaze	Normal	0
	Partial paresis	1
	Total paresis	2
Visual fields	Normal	0
	Partial hemianopsia	1
	Complete hemianopsia	2
	Blind	3

Facial paresis	Normal	0
	Minor paralysis (asymmetric smile)	1
	Partial paralysis	2
	Complete paralysis	3
Arms (both)	No drift	0
	Drift before 10 seconds	1
	Falls before 10 seconds	2
	No effort against gravity	3
	No movement	4
Legs (both)	No drift	0
	Drift before 5 seconds	1
	Falls before 5 seconds	2
	No effort against gravity	3
	No movement	4
Ataxia	No ataxia	0
	One limb	1
	Both limbs	2
Sensory	Normal	0
	Hypoesthesia. Mild sensory loss	1
	Anesthesia. Complete sensory loss	2
Language (words and drawings)	Normal	0
	Light or moderate aphasia	1
	Severe aphasia (misunderstanding)	2
	Mute or non-comprehension	3
Dysarthria	Normal	0
	Light or moderate	1
	Severe, unintelligible	2
Inattention/Extinction	No alterations	0
	Inattention or extinction in one modality	1
	Severe negligence or extinction in more than 1 modality	2

Extracted from: [\(Lyden *et al.*, 1994\)](#)

2.6. ICH diagnostic requires imaging techniques

In a prehospital environment, it is not possible to discriminate between the different types of strokes. Because of this, early recognition of stroke symptoms is important, as well as transport to an appropriate facility, and notification of the arrival of the stroke patient to ease the clinician-stroke response. An earlier diagnosis and immediate treatment will improve the patient's outcome ([Greenberg *et al.*, 2022](#)).

Imaging techniques are essential to diagnose ICH and to be able to differentiate between different types of strokes ([Greenberg *et al.*, 2022](#)). They play a crucial role in determining the cause of ICH, which determines the appropriate treatment to reduce the chances of ICH recurrence. They are also capable of spotting specific characteristics of the hemorrhage or its underlying pathology that could influence the prognosis and recovery of the patient ([Rindler *et al.*, 2020](#)).

Computed tomography scanning (CT) is the preferred method for ICH because of its widespread accessibility, fast obtention of results, and the capacity to quickly identify small hemorrhages (Fewel, Thompson and Hoff, 2003; Hemphill *et al.*, 2015; Greenberg *et al.*, 2022). CT scans are not only able to show the size and location of the hemorrhage, but also if the cause is due to vascular malformations or tumors. Using CT scans, clinicians are also able to identify complications that happen in an ICH, such as hemorrhage extension over time, blood drainage to the ventricles, or edema that affects actions addressed to patient stabilization and management (Fewel, Thompson and Hoff, 2003).

Some patients require emergency surgical procedures, and because of this, some hospitals use intraoperative CT scanners and C-arm cone-beam CTs. These can use digital subtraction angiography (DSA), which characterizes the direction and rate of intracranial blood flow and is useful in populations with a risk of macrovascular pathology. When DSA is not available, intraoperative 3D rotational fluoroscopy after the injection of contrast can be used (Rindler *et al.*, 2020).

The intracerebral hemorrhage in a CT scan is presented as a hyperdense area of 30 to 80 Hounsfield units in the brain parenchyma (Fewel, Thompson and Hoff, 2003). ICH volume and location are crucial in the prognosis of the patient; for instance, hemorrhages that are deep in the brain, in the brainstem or larger than 30 mL, are linked to higher mortality rates (Rindler *et al.*, 2020). The CT scan allows us to determine the volume of the hemorrhage directly using software or by using the formula ABC/2 or the simplified ABC/2 (sABC/2) (Kwak, Kadoya and Suzuki, 1983; Kothari *et al.*, 1996; Qureshi *et al.*, 2001).

The accuracy of both methods varies depending on the size and shape of the ICH. In larger or irregularly shaped hemorrhages, both methods are inaccurate, overestimating or underestimating the ICH volume (Khan *et al.*, 2017; Oge *et al.*, 2021).

The sABC/2 formula is easier and quicker, and it is commonly used in clinical studies and screening programs; however overestimates the ICH size (Oge *et al.*, 2021). If rapid estimation is a priority and overestimation is acceptable in clinics, sABC/2 is useful. If a more accurate volume estimation is crucial, careful considerations about which method should be used is essential.

CT angiography (CTA) is a fast and non-invasive technique to evaluate cerebral vascularization, which allows us to assess vascular abnormalities that result in secondary ICH (Qureshi *et al.*, 2001; Sheth, 2022).

Magnetic resonance Imaging (MRI) is another imaging method to diagnose ICH. MRI allows us to assess changes in white matter, cavernous malformations, lacunar infarcts, venous thrombosis, hemorrhagic transformations, and small vessel diseases such as CAA, among others (Greenberg *et al.*, 2022). MRI helps date hemorrhages, as the hematoma appearance changes over time due to the release of the different components present in the extravasated blood (Rindler *et al.*, 2020). Depending on the MRI sequence, the visualization of the hemorrhage is different (Fewel, Thompson and Hoff, 2003). In hyperacute hemorrhages (0 up to 6 hours since the beginning of the bleeding) for instance, the signal is iso-intense for the T1 sequence, hyperintense in T2, and hypointense in the borders, and iso-intense in the nuclei in T2* sequences (**Table 5.**) (Fewel, Thompson and Hoff, 2003). Other MRI sequences (susceptibility-weighted imaging (SWI) for Siemens and flow-sensitive black blood (FSBB) for Canon) allow us to localize vascular lesions, and contrast administration helps us determine the location of secondary ICH (Qureshi *et al.*, 2001; Rindler *et al.*, 2020).

MRI angiography is also performed to assess underlying structural lesions such as vascular abnormalities and tumors (Hemphill *et al.*, 2015).

Table 5. Evolution of ICH intensity over time

Time after ICH	MRI signal intensity		
	T1 – Weighted	T2 – Weighted	T2*
Hyperacute (0 – 6 hours)	Isointense to hypointense	Hyperintense	Hypointense
Acute (6 hours – 3 days)	Isointense to hypointense	Hypointense	Hypointense
Early subacute (3 days – 1 week)	Hyperintense	Hypointense	Hypointense
Late subacute (1 week – 1 month)	Hyperintense	Hyperintense	Hypointense
Chronic (>1 month)	Hypointense	Hypointense	Hyperintense or iso-intense core with a hyperintense surrounding

Extracted from: (Fewel, Thompson and Hoff, 2003; Rindler *et al.*, 2020)

Cerebral arteriography is used for the diagnosis of the underlying neurovascular pathology (Fewel, Thompson and Hoff, 2003). This technique is employed when there is a clinical suspicion of subarachnoid or intraventricular hemorrhages, intracerebral calcifications, prominent vascular structures or specific locations, and/or when non-invasive radiological scans suggest a vascular origin of the ICH (Fewel, Thompson and Hoff, 2003). The location of the hemorrhage in deep structures, elderly patients, and hypertension history are factors to consider before performing angiography because, for instance, if the hemorrhage is located in thalamic structures and the patient is old and hypertense there is no benefit in the performance of a cerebral angiography (Fewel, Thompson and Hoff, 2003).

Summarizing, the use of imaging techniques provides diagnostic information about the ICH patient, as it identifies imaging features suggestive of complications (Greenberg *et al.*, 2022).

2.7. Complications in ICH

Among the most important complications of ICH, factors such as hematoma expansion, large hematoma volume (>30 mL), intraventricular hemorrhage extension, and hyperglycemia are major predictors of early mortality and poor outcome (Broderick *et al.*, 1993; Qureshi *et al.*, 1995, 2001; Balami and Buchan, 2012; Hemphill *et al.*, 2015; An, Kim and Yoon, 2017; Magid-Bernstein *et al.*, 2022; Sheth, 2022).

2.7.1. Hematoma expansion

Initial reports considered that the bleeding stopped fast because of clotting, but CT scans have shown that hematomas expand over time (Qureshi *et al.*, 2001; Magid-Bernstein *et al.*, 2022). In fact, 26% of the patients had hemorrhagic growth within one hour of the baseline CT, and 12% of the patients had a hemorrhagic growth between 1 to 20 hours after the baseline CT scan (Brott *et al.*, 1997). In general, hematoma expansion after 24 hours is rare (Kazui *et al.*, 1996).

Hematoma expansion occurs shortly after ICH in a considerable number of patients and is associated with poor outcomes, neurologic deterioration, and mortality. Also, it increasingly compresses nearby brain structures, leading to the well-known mass effect (Qureshi *et al.*, 2001; Greenberg *et al.*, 2022; Sheth, 2022).

Several radiological signs indicate the risk of ICH expansion. These include heterogeneous hematoma densities, irregular hematoma margins, and the presence of a “black & white” and “spot” sign. The black and white sign is defined as any spot sign (contrast within the hematoma detectable in contrast-enhanced CT or CTA) seen on a CTA scan that shows up inside or right next to a darker area on the matching non-contrast CT scan (Pensato *et al.*, 2025). These markers influence prognosis, patient monitoring, and clinical decision-making (Greenberg *et al.*, 2022; Magid-Bernstein *et al.*, 2022; Pensato *et al.*, 2025; Blacquiere *et al.* 2015). Routine serial CT scans at different post-stroke times can be useful for monitoring ICH progression (Hemphill *et al.*, 2015; Greenberg *et al.*, 2022).

Several factors have been associated with the assessment of hematoma enlargement such as early admission after symptom onset (shorter time between symptom onset and baseline CT), heavy alcohol consumption, irregularly shaped hematoma, decreased level of mental alertness, low fibrinogen level, anticoagulant use, and anemic patients (Fujii *et al.*, 1998; Greenberg *et al.*, 2022; Sheth, 2022).

Several clinical trials have been initiated to identify the most effective strategies for reducing mortality and improving outcomes in ICH patients by targeting hematoma expansion. Trials such as TICH-NOAC and STOP-MSU investigated the use of tranexamic acid to limit hematoma growth, but found no significant clinical benefit, nor in hematoma expansion, nor in clinical outcome (Polymeris *et al.*, 2023; Yassi *et al.*, 2024). The STOP-IT and SPOT-LIGHT trials evaluated the use of the spot sign tool and the recombinant factor VIIa (rFVIIa) as potential treatments for ICH without finding improvements in clinical outcomes or radiographically. Prospective trials including INTERACT II, ATACH II, JAMA2015, and RAINS have explored the effects of aggressive blood pressure reduction on hematoma expansion, resulting in contradictory results depending on the specific study (Brouwers and Greenberg, 2013).

2.7.2. Perihematomal edema

The edema is produced due to the presence of the hematoma (Qureshi *et al.*, 2001). The fluid is collected in the region around the extravasated blood, which can result in mass effect, increasing the intracranial pressure and the neurological impairment (Balami and Buchan, 2012).

2.7.3. Intraventricular hemorrhage

Intraventricular hemorrhage (IVH) expansion occurs in 21% of ICH patients (Balami and Buchan, 2012; Greenberg *et al.*, 2022; Magid-Bernstein *et al.*, 2022; Sheth, 2022). These hemorrhages often lead to hydrocephalus. Both IVH volume and hydrocephalus are independent predictors of mortality and poor prognosis after ICH and typically lead to a decreased level of awakening/consciousness and worse clinical outcomes (Hallevi *et al.*, 2009; Balami and Buchan, 2012; Greenberg *et al.*, 2022; Magid-Bernstein *et al.*, 2022). IVH results in a mechanical disruption, ventricular wall distention, and increased intracranial pressure, thus reducing the brain perfusion (Mayer, Thomas and Diamond, 1996; Mayfrank *et al.*, 1997; Hallevi *et al.*, 2009). In animal models, IVH has been shown to increase cerebrospinal fluid (CSF) production and subsequent posthemorrhagic hydrocephalus (Lolansen *et al.*, 2022). IVH is frequently diagnosed via CT or MRI, with CT being the key tool for early detection and rating the grade of IVH extent (Dastur and Yu, 2017).

Several trials have explored strategies to accelerate blood clearance from ventricles, such as the CLEAR III trial, which validated the use of very low-doses of thrombolytic drugs (Naff *et al.*, 2004) when combined with an external ventricular drainage (EVD) (Qureshi, Mendelow and Hanley, 2009; Hanley *et al.*, 2017; Magid-Bernstein *et al.*, 2022).

2.7.4. Other complications

Thrombotic events, such as pulmonary embolism or deep vein thrombosis, are also common and life-threatening complications that reduce rehabilitation and recovery of the ICH patient, and the incidence is approximately 7% in hospitals. In order to reduce the risk of these thrombotic events, it has been proposed the use of intermittent pneumatic compression devices, prophylaxis with low-molecular-weight or no fractionated heparin, or insertion of an inferior vena cava filter (Greenberg *et al.*, 2022). Early treatment of hematoma expansion, **hyperglycemia**, **fever**, and **impaired swallowing** reduces mortality, disability, and in-hospital time (Greenberg *et al.*, 2022).

2.8. Pathophysiology

The cerebral damage produced after the ICH is commonly classified into primary and secondary brain injury, both of which are interrelated yet differ pathophysiologically. The primary cerebral damage refers to the immediate events after the bleeding, such as tissue

disruption due to hematoma expansion and mass effect, defined as the pressure made by the hematoma on surrounding tissues, leading to displacement, compression, and potential neurological deficits. On the other hand, the secondary brain damage relates specifically to the activation of cellular and molecular mechanisms that are triggered by substances released by the hematoma that underlie cerebral damage due to ICH (**Figure 4.**) (Qureshi *et al.*, 2001; Keep, Hua and Xi, 2012; Mracsko and Veltkamp, 2014; Magid-Bernstein *et al.*, 2022).

2.8.1. Primary brain injury

As mentioned, the primary brain injury occurs after the onset of the bleeding and is mainly due to the tissue disruption, defined as mechanical cell alterations, including neurons, that cause the release of excitotoxic neurotransmitters such as glutamate (Qureshi *et al.*, 2003). These changes are the result of brain structures' compression and blood deposition in the brain parenchyma, leading to an increase in the intracranial pressure (ICP) and causing mass effect (Mracsko and Veltkamp, 2014). In some cases, the increase in the ICP can lead to brain structure herniation, compromising the arterial perfusion (Herweh *et al.*, 2007).

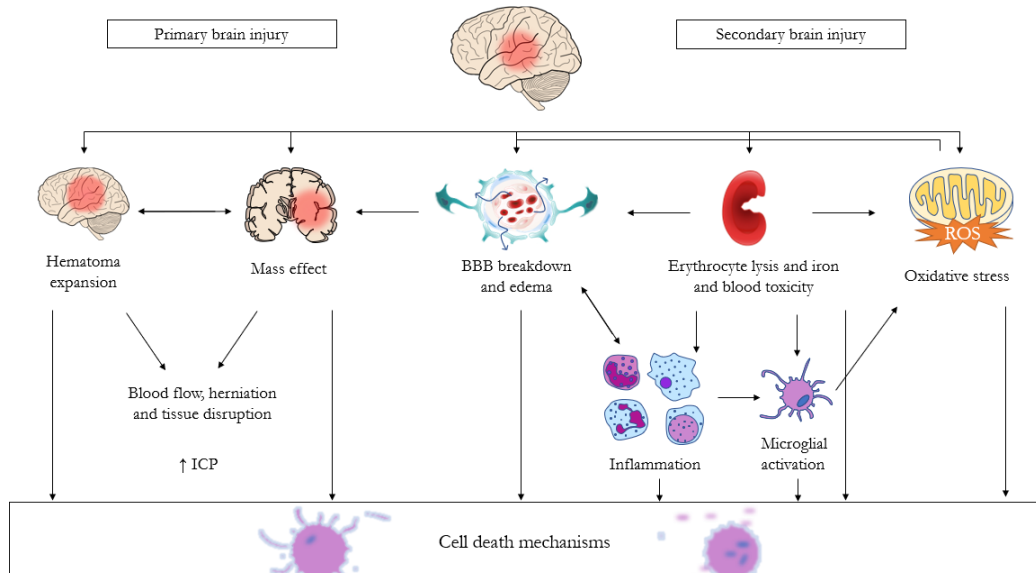


Figure 4. General schema of primary and secondary brain injury mechanisms in intracerebral hemorrhage (ICH). Primary brain injury results from hematoma expansion and mass effect, leading to increased intracranial pressure (ICP) and tissue disruption. Secondary brain injury involves blood-brain barrier (BBB) breakdown, edema, oxidative stress, and erythrocyte lysis, contributing to inflammation and microglial activation. These cascades ultimately drive cell/neuronal death mechanisms. ROS: reactive oxygen species.

Modified from (Magid-Bernstein *et al.*, 2022)

There is no consensus on the time-course development of the perihematomal edema (PHE) around the hemorrhagic area after the ICH. Historically, the PHE has been considered a prognostic factor in the outcome of ICH patients, as it can increase both ICP and mass effect (Qureshi *et al.*, 2001; Xi, Keep and Hoff, 2006). However, its relationship with the clinical outcome is not completely clear (Arima *et al.*, 2009; Venkatasubramanian *et al.*, 2011). In the first hours, the PHE is characterized by a hyperactive phase due to the disruption of the blood-brain barrier (BBB) and the diffusion of blood and serum proteins into the brain parenchyma. In the following days, the edema expands as a result of thrombin release, iron-induced damage, and inflammation, reaching its maximum volume between 1 and 2 weeks post-ICH. Afterward, the volume of edema gradually decreases (Mracsko and Veltkamp, 2014; Chen *et al.*, 2021; Magid-Bernstein *et al.*, 2022; Krishnan *et al.*, 2023).

2.8.2. Secondary brain injury

The secondary brain injury (SBI) occurs as a consequence of the complex and adverse mechanisms activated after the ICH, including oxidative stress pathways, intense inflammatory responses, excess iron in the brain parenchyma, microglial activation, and excitotoxicity. The breakdown of the erythrocytes in the brain parenchyma and the molecules released during their rupture, together with coagulation factors, complement components, and immunoglobulins, contribute to this secondary brain injury that is not yet fully understood (Qureshi *et al.*, 2001; Aronowski and Zhao, 2011; Keep, Hua and Xi, 2012; Mracsko and Veltkamp, 2014; Zhou *et al.*, 2014; Magid-Bernstein *et al.*, 2022; Alsbrook *et al.*, 2023). Some of these molecules related to ICH secondary damage are explained in the following sections.

2.8.2.1. Thrombin damage

Thrombin, a serine protease generated through activation of the coagulation cascade, plays a central role in mediating SBI following ICH. Upon vascular rupture, high concentrations of thrombin are rapidly produced in the brain parenchyma, where they exert predominantly neurotoxic effects (Tao *et al.*, 2024). Thrombin activates protease-activated receptors (PARs), particularly PAR-1 and PAR-4, on neurons, astrocytes, microglia, and endothelial cells, triggering a cascade of pathological responses that include BBB disruption, neuroinflammation, and neuronal apoptosis (Tao *et al.*, 2024; Shao, Tu and Shao, 2019). These effects are mediated by activation of downstream signaling pathways such as mitogen-activated protein kinases (MAPKs), nuclear factor kappa B (NF- κ B), and the NOD-, LRR- and pyrin domain-

containing protein 3 (NLRP3) inflammasome, leading to increased expression of proinflammatory cytokines (e.g., tumor necrosis factor- α (TNF- α), interleukin 1 β (IL-1 β)) and matrix metalloproteinases (MMP), which further compromise BBB integrity (Tao *et al.*, 2024).

In experimental models, direct intracerebral injection of thrombin induces brain edema, microglial activation, and neuronal loss, closely replicating features of SBI seen in ICH (Zheng *et al.*, 2016; Wan *et al.*, 2016; Krenzlin *et al.*, 2020). Thrombin also enhances excitotoxicity by potentiating N-methyl-D-Aspartate (NMDA) receptor function, promoting calcium influx and oxidative stress in neurons (Gingrich *et al.*, 2000). Clinically, elevated thrombin activity and thrombin-antithrombin (TAT) complex levels in the cerebrospinal fluid of ICH patients are associated with worse neurological outcomes, suggesting thrombin as a biomarker of injury severity (Krenzlin *et al.*, 2020). Although thrombin is essential for hemostasis, its pathological signaling post-ICH has prompted investigation of therapeutic strategies aimed at selective thrombin inhibition or downstream blockade (e.g., PAR-1 antagonists). Preclinical studies using direct thrombin inhibitors such as hirudin and argatroban demonstrate reduced edema and improved neurological function without significantly increasing rebleeding risk when administered appropriately (Hua *et al.*, 2009; Tao *et al.*, 2024).

2.8.2.2. Inflammation and immune system damage

Secondary brain injury is also mediated by neuroinflammation and immune responses triggered by blood extravasation into the brain parenchyma. Toll-like receptors (TLRs), particularly TLR2 and TLR4, are crucial pattern recognition receptors that detect damage-associated molecular patterns (DAMPs) such as hemoglobin, heme, and thrombin released after ICH. Their activation initiates intracellular signaling cascades that culminate in NF- κ B translocation to the nucleus, driving the transcription of pro-inflammatory cytokines including interleukin-1 β (IL-1 β), TNF- α , and interleukin-6 (IL-6) (Zhou *et al.*, 2014; Dasari, Bonsack and Sukumari-Ramesh, 2021). NF- κ B is therefore a master regulator of inflammation post-ICH, linking TLR activation to downstream immune responses and contributing to BBB disruption, edema formation, and neuronal apoptosis (Zhou *et al.*, 2014). Pharmacological inhibition of TLR4 or NF- κ B signaling reduces neuroinflammation and improves functional outcomes in animal models (Teng *et al.*, 2009).

Resident microglia, together with infiltrating peripheal macrophages, also play a central role in the inflammatory response in the brain after ICH. These cells rapidly respond to

hemorrhagic injury by exhibiting phenotypic plasticity, adopting either a pro-inflammatory M1 phenotype, characterized by the release of cytokines and reactive oxygen species (ROS), which exacerbate neuronal injury and vascular permeability (Gong *et al.*, 2025), or an anti-inflammatory M2 phenotype, which promoted hematoma resolution and tissue repair (Jiao *et al.*, 2023; Zhang *et al.*, 2023).

M1 microglia are typically activated in the acute phase after ICH and secrete pro-inflammatory cytokines such as TNF- α , IL-6, IL-1 β , and IL-12, along with chemokines like CCL2 (chemokine (C-C motif) ligand 2). In contrast, M2 microglia contribute to tissue repair by promoting the phagocytosis of cellular debris and misfolded proteins, supporting extracellular matrix remodelling, and releasing neurotrophic factors that enhance neuronal survival (Gao *et al.*, 2023).

Astrocytes also become reactive, differentiating into neurotoxic A1 or neuroprotective A2 phenotypes, with A1 astrocytes releasing matrix MMPs that further degrade BBB integrity (Gong *et al.*, 2025; Liddelow *et al.*, 2017). The inflammasome, activated by DAMPs including thrombin and hemoglobin breakdown products, mediates caspase-1-dependent maturation of IL-1 β and IL-18, amplifying the inflammatory response (Zhou *et al.*, 2014). Inhibitors of NLRP3 have demonstrated efficacy in reducing edema and improving neurological recovery in preclinical ICH models (Zhang *et al.*, 2024).

The complement system, a key component of innate immunity, is activated following ICH and contributes to SBI by opsonizing erythrocytes and cell debris, recruiting immune cells, and promoting inflammation via anaphylatoxins such as C3a and C5a (Ducruet *et al.*, 2009). Complement activation exacerbates neuronal damage and BBB disruption, while complement inhibition attenuates brain edema and improves neurological function in rodent hemorrhagic stroke models (Holste *et al.*, 2021).

Peripheral immune cells, including neutrophils and monocytes, infiltrate the perihematomal brain region. Neutrophils release myeloperoxidase, MMP-9, and form neutrophil extracellular traps (NETs), worsening BBB damage and edema (Zhou *et al.*, 2014). Monocytes recruited via C-C chemokine receptor type 2 (CCR2) differentiate into macrophages that contribute both to inflammatory damage and tissue repair (Zhou *et al.*, 2014; Dasari, Bonsack and Sukumari-Ramesh, 2021). Adaptive immune cells, notably CD4+ T helper 17 (Th17)

cells, secrete IL-17 which aggravates neuroinflammation and BBB breakdown, while regulatory T cells (Tregs) counterbalance inflammation through IL-10 and transforming growth factor-beta (TGF- β) production (Zhou *et al.*, 2014). Modulation of lymphocyte trafficking via agents such as fingolimod reduces lymphocyte infiltration and ameliorates outcomes after ICH (Wan *et al.*, 2023).

Systemic inflammatory responses are also implicated in ICH prognosis. Elevated circulating cytokines (IL-6, TNF- α) and increased neutrophil-to-lymphocyte ratios correlate with hematoma expansion, perihematomal edema, and worse clinical outcomes (Gong *et al.*, 2025). These peripheral immune parameters reflect the interplay between central neuroinflammation and systemic immune activation and may serve as biomarkers or therapeutic targets.

Given the complex role of inflammation in ICH pathophysiology involving TLR-mediated NF- κ B activation, inflammasome signaling, complement cascade engagement, and diverse immune cell infiltrations, the immune system represents a promising therapeutic target. However, the dual nature of microglia requires strategies that not only suppress harmful inflammation but also promote healing responses. Several agents, such as minocycline, siRNA targeting chemokine (C-X-C motif) ligand 16 (CXCL16), and sinomenine, have shown potential in preclinical studies by promoting M2 polarization while inhibiting the M1 phenotype (Dinc and Ardic, 2025).

2.8.2.3. Damage by erythrocytes' released products

The molecules released by the damaged or lysed red blood cells worsen the injury produced by the ICH by increasing oxidative stress, lipid peroxidation, and inflammation. Oxidative stress and lipid peroxidation play a crucial role in secondary brain injury caused by intracerebral hemorrhage (Mrakko and Veltkamp, 2014; Zhou *et al.*, 2014). As erythrocytes break down, inflammatory cells are recruited, and hemoglobin (Hb) is released. The Hb is then degraded into heme group and iron. These products generate free radicals and ROS, producing neuronal membrane damage, deoxyribonucleic acid (DNA) disruption, and triggering a range of responses that result in different cell death mechanisms (Zhou *et al.*, 2014), such as apoptosis, necrosis, ferroptosis, and autophagy, among others (Wan, Ren and Wang, 2019). Recent evidence suggests that the released heme group and iron are among the primary causes of brain damage produced by ICH (Zille *et al.*, 2017). However, the brain has protective mechanisms that can be activated after ICH and erythrocyte lysis, the most

important one being the Hb-scavenging molecule haptoglobin (Hp) and the heme scavenging system hemopexin (Hpx), the role of these molecules in ICH has been reviewed (DeGregorio-Rocasolano, Martí-Sistac and Gasull, 2019).

Among the different cell death mechanisms, ferroptosis is an iron-driven programmed cell death characterized by the excessive accumulation of lipid peroxides, which causes significant damage to plasma membranes (Dixon *et al.*, 2012; DeGregorio-Rocasolano *et al.*, 2018; DeGregorio-Rocasolano, Martí-Sistac and Gasull, 2019; Dixon and Olzmann, 2024). Ferroptosis is a cell death mechanism that has generated a renewed interest, since it can be activated and regulated in many ways depending on the cell type and the triggering factors, and provides several molecular targets for intervention (Dixon and Olzmann, 2024).

Since the neurons have a large amount of membrane, and membranes are very rich in lipids, the brain is particularly susceptible to lipid peroxidation and free radicals damage (Duan *et al.*, 2016; DeGregorio-Rocasolano, Martí-Sistac and Gasull, 2019). This vulnerability worsens with the accumulation of iron released from hemoglobin degradation after an ICH. Iron, by catalyzing the formation of hydroxyl radicals through the Fenton reaction, increases the oxidative stress and damages the lipid structures of neurons/brain cells (Dixon *et al.*, 2012; DeGregorio-Rocasolano, Martí-Sistac and Gasull, 2019).

Of note, this iron-induced ferroptosis is a mechanism of cell death common to both ischemic and hemorrhagic stroke types (Figure 5.).

2.8.3. Iron and ferroptosis

Iron, in the form of ferric iron (Fe^{3+}), is transported and distributed by transferrin (Tf), a protein that is abundant in blood. When iron is bound to transferrin, it does not participate in redox activities. Tf is present in the blood in different isoforms depending on the number of iron atoms it transports: transferrin loaded with two iron atoms (diferric or holotransferrin, HTf), transferrin with one iron atom (monoferric, mFe), and iron-free transferrin (apoferic or apotransferrin, ATf). The amount of free (ATf) and iron-loaded transferrin is presented as the percentage of transferrin saturation (TSAT), which is approximately 30% in humans (DeGregorio-Rocasolano *et al.*, 2018).

Iron reaches the brain through systemic circulation mainly bound to Tf, and its levels in systemic blood depend on diet, intestinal absorption, and the release of iron from hepatic and macrophagic stores (DeGregorio-Rocasolano, Martí-Sistac and Gasull, 2019). The entry of iron in the brain is finely regulated by the BBB (DeGregorio-Rocasolano, Martí-Sistac and Gasull, 2019). Iron bound to Tf circulates until it binds to transferrin receptors (TfR) located in cellular membranes, with TfR-Tf being the main entry route for iron into neurons (Figure 5.) (DeGregorio-Rocasolano *et al.*, 2018; DeGregorio-Rocasolano, Martí-Sistac and Gasull, 2019). Tf binds to its receptor in the cell membrane and is internalized by endocytosis mainly in the form of HTf, as this form has a higher affinity for the receptor than ATf (DeGregorio-Rocasolano, Martí-Sistac and Gasull, 2019). Once inside the cell, in the acidic environment of the endosome, ferric iron (Fe^{3+}) is converted to ferrous iron (Fe^{2+}) before being translocated into the cytosol through metal-transporting proteins such as the divalent

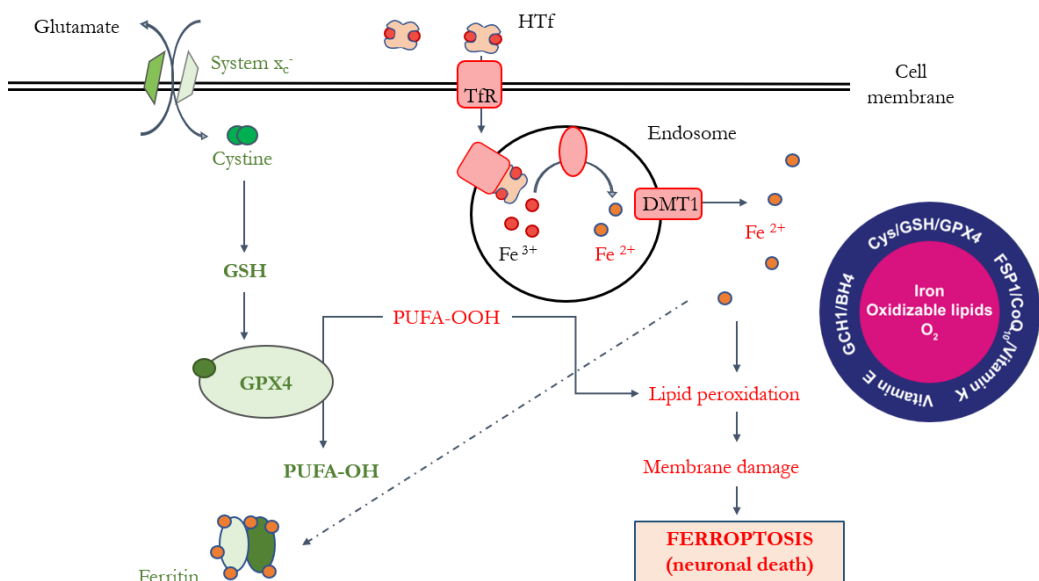


Figure 5. Lipid peroxidation and iron are central mediators of ferroptosis. Via transferrin receptor (TfR), transferrin-bound iron enters to the cell, increasing intracellular iron levels and promoting lipid peroxidation, ultimately leading to ferroptosis. Neuroprotection against ferroptosis is primarily mediated by antioxidant molecules. The most prominent are listed in the deep blue circle of the image, with two concentric circles at the right of the figure, with glutathione peroxidase 4 (GPX4) being the most extensively studied antioxidant. The function of GPX4 (in green on the left of the image requires glutathione (GSH) as a cofactor that indeed requires cell cystine imported through the system x_c^-/xCT cystine/glutamate antiporter. Abbreviations: GSH-dependent hydroperoxidase 4 (GPX4), hydroxylated polyunsaturated fatty acids (PUFA-OH), hydroperoxide polyunsaturated fatty acids (PUFA-OOH), transferrin receptor (TfR), divalent metal transporter 1 (DMT1), tetrahydrobiopterin (BH4) and ferroptosis suppressor protein 1 (FSP1).

metal transporter 1 (DMT1) also called solute carrier family 11 member 2 (SLC11A2) (Berndt *et al.*, 2024).

Following the rupture of the brain vessels and disruption of the BBB in hemorrhage, the iron is released from hemoglobin and accumulates in the brain tissue after an ICH. This process leads to an increase in intracellular iron, which, in turn, induces the expression of intracellular iron-storing proteins, such as ferritin (FT) or iron chaperones like poly(rC)-binding proteins (PCBPs) (DeGregorio-Rocasolano *et al.*, 2018; DeGregorio-Rocasolano, Martí-Sistac and Gasull, 2019). However, the iron storage capacity is rapidly exceeded in an ICH, and free iron catalyzes ROS formation, causing severe oxidative damage to neurons'/brain cells membranes, proteins, and DNA, ultimately leading to ferroptosis (Figure 5.) (Zhou *et al.*, 2014; DeGregorio-Rocasolano *et al.*, 2018; Gaasch *et al.*, 2007).

TfR has been proposed as a new ferroptosis marker and the TfR-Tf-iron pathway identified as a common mechanism in brain injury in both ischemic and hemorrhagic stroke (Zille *et al.*, 2017; DeGregorio-Rocasolano *et al.*, 2018; DeGregorio-Rocasolano, Martí-Sistac and Gasull, 2019; T. Liu *et al.*, 2021; Tang *et al.*, 2021; Berndt *et al.*, 2024). In fact, blocking the receptor protects from excitotoxic/ferroptotic/oxidative damage after ischemic stroke (DeGregorio-Rocasolano *et al.*, 2018).

One of the most studied antioxidant molecules, pivotal to prevent ferroptosis, is glutathione (GSH)-dependent hydroperoxidase 4 (GPX4), a selenoenzyme that normally protects cells against lipid peroxidation (Friedmann Angeli *et al.*, 2014; Yang *et al.*, 2014; Dixon and Olzmann, 2024). GPX4 catalyzes the reduction of lipid peroxides to non-damaging lipid alcohols, using GSH as a cofactor. Without GPX4, lipid peroxides accumulate, leading to ferroptosis (Yang *et al.*, 2014). GSH synthesis primarily depends on the xCT transporter, a cystine/glutamate antiporter that exchanges cystine and glutamate through the cell membrane. Cystine, inside the cell, is then converted to cysteine, which is used for GSH synthesis. Inhibition of the xCT system leads to reduced intracellular cystine levels, and therefore GSH, resulting in an increased susceptibility to ferroptosis (Dixon *et al.*, 2012).

In parallel, other mechanisms limit lipid peroxidation either using radical-trapping antioxidants (RTAs), such as α -tocopherol (the most active form of vitamin E), tetrahydrobiopterin (BH4), or ferroptosis suppressors such as the ferroptosis suppressor protein 1 (FSP1)

(Dixon and Olzmann, 2024). FSP1 and BH4 are key molecules in ferroptosis suppression, acting independently or in conjunction with GPX4 (Doll *et al.*, 2019; Berndt *et al.*, 2024). These molecules generate reduced forms of coenzyme Q10 (CoQ₁₀), and FSP1 also generates reduced forms of vitamin K, both of which have RTA activity (Berndt *et al.*, 2024; Dixon and Olzmann, 2024). FSP1 reduces hydroxyl lipid radicals through a mechanism that is not dependent on GSH, providing an alternative protective route when GPX4 is inhibited or GSH levels are low (Doll *et al.*, 2019).

Recently, acyl-CoA synthetase long-chain family member 4 (ACSL4), the tumor suppressor p53 pathway, mechanistic target of rapamycin complex I (mTORC1) pathway, NAD(P)H, and nuclear factor erythroid 2-related factor 2 (Nrf2) have been related to ferroptosis (Berndt *et al.*, 2024; Dixon and Olzmann, 2024).

2.9. ICH treatment: clinical guidelines, clinical trials and pre-clinical treatments

While in ischemic stroke recombinant tissue-type plasminogen activator (rtPA), and endovascular thrombectomy (EVT) are the gold standard treatments in eligible patients, ICH is still in search of effective curative treatments. The rapid identification of the type of stroke in a given patient is pivotal since thrombolysis with rtPA and EVT are to be used in a subset of ischemic stroke patients only, and contraindicated in ICH patients.

The ICH guideline (Greenberg *et al.*, 2022) provide a framework for clinical ICH management, focusing on control of blood pressure (BP), pyrexia and hyperglycemia, as well as anticoagulant treatment reversal, and to use surgical interventions when adequate. In addition to these guidelines, new treatment protocols and therapies are being developed and tested in clinical trials.

2.9.1. Current guideline for intracerebral hemorrhage

The 2022 Guideline for the Management of Patients With Spontaneous Intracerebral Hemorrhage is a current and comprehensive update of a prior guideline, published by the American Heart Association (AHA) and the American Stroke Association (ASA) in 2015 (Hemphill *et al.*, 2015). This guideline is specifically focused on spontaneous ICH; its main goal is to offer evidence-based guidance using available clinical trial data and published

research for the diagnosis, treatment, rehabilitation, and prevention of hemorrhagic stroke. Additionally, it aims to optimize clinical decision-making in order to improve functional outcomes and reduce mortality in patients with ICH (Greenberg *et al.*, 2022).

One of the important topics covered in this guideline is the importance of early stroke recognition and type identification, emphasizing the importance of education among healthcare professionals, the general population and relatives of ICH patients (Greenberg *et al.*, 2022). Furthermore, it highlights the need to transfer patients to specialized centers when the initial healthcare center does not have the necessary facilities to manage stroke patients (Abid *et al.*, 2013; Parry-Jones *et al.*, 2019).

Early stroke recognition allows early treatment initiation, including fever control, hyperglycemia management, and swallowing assessment (Middleton *et al.*, 2011; Greenberg *et al.*, 2022). The QASC (ACTRN12608000563369) and INTERACT III (NCT03209258) trials demonstrated that the early multimodal interventions and multidisciplinary team care significantly reduce hospital length of stay, mortality, and the degree of disability in ICH patients (Middleton *et al.*, 2011, 2017; Ma *et al.*, 2023).

An early ICH diagnosis is a key point in the management of intracerebral hemorrhage (Ruff *et al.*, 2024). CT and MRI are fast imaging techniques that help identify the cause of bleeding and differentiate between hemorrhagic and ischemic strokes in patients with stroke-like symptoms (Kidwell *et al.*, 2004; Lummel *et al.*, 2012; Charidimou *et al.*, 2017). Follow-up imaging studies are essential to evaluate hematoma expansion, hydrocephalus, and perihematoma edema (Brott *et al.*, 1997; Greenberg *et al.*, 2022).

The treatment of ICH has to be individualized based on the patient's preexisting conditions, particularly anticoagulant or antiplatelet use (Ruff *et al.*, 2024). Anticoagulant therapy should be discontinued immediately, with reversal agents administered if blood anticoagulant levels are clinically significant (Hanger *et al.*, 2013). The impact of antiplatelet therapy on prognosis remains uncertain (Feldman *et al.*, 2019; Schmidt *et al.*, 2019; Mengel *et al.*, 2020). However, in emergency craniotomies for hematoma evacuation, platelet transfusion has demonstrated benefits in reducing postoperative hemorrhagic volume (Li *et al.*, 2013; Ruff *et al.*, 2024).

Blood pressure (BP) control is crucial in ICH management, as elevated BP contributes to hematoma expansion, worsens neurological deficits, and increases mortality and

dependency. Clinical trials, including INTRACT I (NCT00226096), INTERACT II (NCT00716079), and ATACH II (NCT01176565) demonstrated that intensive BP control for ICH is safe, feasible, and may improve functional outcomes (Anderson *et al.*, 2008, 2013; Qureshi *et al.*, 2018). In fact, the primary recommendation is to keep systolic blood pressure between 130-140 mmHg (Moullaali *et al.*, 2019; Greenberg *et al.*, 2022; Ruff *et al.*, 2024).

Other important aspects of ICH management include glycemic control, emphasizing the need to avoid both hyperglycemia and hypoglycemia (Passero *et al.*, 2002; Kim *et al.*, 2017). However, strict glycemic control increases the risk of hypoglycemia (Van den Berghe *et al.*, 2001; Oddo *et al.*, 2008; NICE-SUGAR Study Investigators *et al.*, 2009). Temperature management is also essential, as fever worsens functional outcomes (Iglesias-Rey *et al.*, 2018). While therapeutic hypothermia has been proposed to reduce perihematomal edema, no significant clinical benefit has been demonstrated (Greenberg *et al.*, 2022). Finally, antiepileptic treatment is recommended for patients with clinically evident seizures or epileptic activity detected by electroencephalogram (EEG) (Vespa *et al.*, 2003; Mehta *et al.*, 2018).

The efficacy and safety of surgical intervention in ICH patients depends on hematoma location, volume, and neurological status. For large hematomas with moderate GCS scores (5-12), surgical evacuation of the hematoma is recommended if accessible, as demonstrated in the clinical trials STICH (ISRCTN19976990), STICH II (ISRCTN22153967) and MISTIE III (NCT01827046) trials (Mendelow *et al.*, 2005, 2013; Hanley *et al.*, 2019), favoring minimally invasive surgery (MIS) over medical management alone (Xia *et al.*, 2018; Hanley *et al.*, 2019; G. Guo *et al.*, 2020). The ENRICH trial (NCT02880878) further supports MIS, showing reduced mortality compared to craniotomy when surgical evacuation is necessary (Akhigbe *et al.*, 2015; Scaggiante *et al.*, 2018; Xia *et al.*, 2018; G. Guo *et al.*, 2020; Sondag *et al.*, 2020; Pradilla *et al.*, 2024). However, the effectiveness of craniotomy for supratentorial hematomas remains uncertain (Mendelow *et al.*, 2005, 2013; Gregson *et al.*, 2012; G. Guo *et al.*, 2020; Sondag *et al.*, 2020), though it is a lifesaving in cases of severe neurological deterioration (Mendelow *et al.*, 2013; Bhaskar *et al.*, 2017; Sondag *et al.*, 2020).

For cerebellar hemorrhages with brainstem compression and/or hydrocephalus, surgical evacuation is recommended to reduce mortality (Witsch *et al.*, 2013; Kuramatsu *et al.*, 2019; Singh *et al.*, 2020). Furthermore, in patients in coma with massive supratentorial ICH, midline shift, and increased intracranial pressure, decompressive craniotomy has been shown to

lower mortality rates (Fung *et al.*, 2012; Heuts *et al.*, 2013; Yao *et al.*, 2018; Gildersleeve *et al.*, 2019; Iwuchukwu *et al.*, 2020).

The management of hemorrhagic stroke requires a multidisciplinary approach, emphasizing education for both healthcare professionals and patients to facilitate early recognition and reduce ICH recurrence (Greenberg *et al.*, 2022).

2.9.2. Clinical trials in ICH

The vast majority of the clinical trials focus on testing measures of medical and surgical management of ICH. However, some recent studies have tested additional strategies to reduce brain damage after the bleeding. These include reducing iron toxicity, enhancing hematoma clearance, and controlling perihematomal swelling and inflammation. Early-phase trials have already begun investigating some of these strategies.

Given the role of hematoma-derived toxins in secondary brain injury, several trials have investigated the hematoma clearance. Trials such as the CLEAR III (NCT00784134), which assessed intraventricular alteplase administration in IVH patients (Hanley *et al.*, 2017), and the FAST trial (NCT00127283), which tested the use of rFVIIa to reduce the hematoma growth and improve patient survival (Mayer *et al.*, 2008), concluded that there was no survival benefit in its use without improving functional outcomes, although it improved clot resolution. TICH-NOAC (NCT02866838) and STOP-MSU (NCT03385928) evaluated the use of tranexamic acid (TXA), an antifibrinolytic agent, for limiting the hematoma expansion in ICH. Both studies found that TXA did not reduce the hematoma growth nor improve the functional outcomes in ICH patients (Polymeris *et al.*, 2023; Yassi *et al.*, 2024).

Similarly, the i-DEF trial (NCT02175225) investigated the effects of deferoxamine (DFO) in ICH patients, confirming its safety. Although no significant improvements were observed in the primary analysis (90 days), a post-hoc analysis found a potential benefit in functional outcome up to 6 months after ICH (Selim *et al.*, 2019; Foster *et al.*, 2022).

Other recent trials investigating novel treatments targeting secondary brain injury (SBI) have started but have not yielded promising results (see some examples in **Table 6**).

Table 6. Clinical trials of new ICH treatments

Treatment	Mechanism of action	Clinical trial number	Status	Outcome	Ref
Ciraparantag	Binds to anti-coagulants	NCT04593784 AMAG-977-213	Ongoing	-	-
Mesenchymal Stem cells	-	NCT03371329	Completed	The administration of the stem cells is safe	(Durand <i>et al.</i> , 2023)
Minocycline (MACH)	Antibacterial and anti-inflammatory	NCT01805895	Completed	The drug is safe but should not be used in critically ill patients	(Fouda <i>et al.</i> , 2017)
Remote ischemic conditioning (RICH)	-	NCT03930940	Completed	No differences were found regarding functional outcome	(Wenbo <i>et al.</i> , 2025)
Anakinra (BLOC-ICH)	Recombinant IL-1 receptor antagonist	NCT03737344	Completed	The treatment is safe, but the trial lacked of power to test the effects of edema	(Parry-Jones <i>et al.</i> , 2023)
Celecoxib	COX-2 inhibitor	NCT03741530	Ongoing	-	-
Glibenclamide (GATE-ICH)	Antidiabetic drug	NCT03741530	Completed	Glibenclamide did not improve functional outcome and could result in hypoglycemia	(Zhao <i>et al.</i> , 2022)
Atorvastatin (STATIC)	Anti-inflammatory and antioxidant	NCT04857632	Ongoing	-	(Gao <i>et al.</i> , 2024)
Conivaptan	Vasopressin inhibitor	NCT03000283	Completed	The drug is safe	(Corry <i>et al.</i> , 2020)
DFO (i-DEF)	Iron chelator intermediate dose	NCT02175225	Completed	The drug is safe and improve outcomes > 90 days	(Selim <i>et al.</i> , 2019; Foster <i>et al.</i> , 2022)
DFO (HI-DEF)	Iron chelator high dose	NCT01662895	Completed	Discontinued for adverse effects	(Yeatts <i>et al.</i> , 2013)

Modified from: (Chiang, Tsai and Tsai, 2024)

2.9.3. Treatments in preclinical stages

Preclinical research testing of experimental treatments with the potential to help attenuate SBI in ICH has produced encouraging evidence for treatments that target BBB disruption, iron overload, inflammation, and reactive oxygen species. These are able to reduce hematoma expansion or increase the speed of hematoma resolution, or multi-component treatments that are multi-target, multi-pathway. Some of the most promising have evolved into clinical trials currently ongoing or to be performed in the near future.

Probably because in the East Asian countries such as China, Japan, and Korea, ICH accounts for at least 20-30% of all strokes, a large amount of preclinical studies have been published by Chinese/Japanese researchers using Chinese medicine extracts/herb formulas or medicinal herb-derived compounds used traditionally to treat ICH. Most of them are multi-component, multi-target, multi-pathway mixtures that provide some benefit (Sun *et al.*, 2025; Li *et al.*, 2024; Q. Guo *et al.*, 2020; Feng *et al.*, 2023; Wu *et al.*, 2021; Lai *et al.*, 2019; Zhou *et al.*, 2021; Zeng *et al.*, 2020; King *et al.*, 2011). Other mixtures of compounds, e.g., cerebrolysin, ameliorate SBI in ICH (Yang *et al.*, 2016).

Besides these far East studies, the specific compounds tested so far preclinically as treatments for ICH and reported in the literature can be grouped in the following categories:

Preventers of BBB disruption, hematoma preventers, and hematoma aspiration

The early hematoma reducer 17 β -estradiol has been shown to prevent BBB disruption and to improve neurological deficits (Zheng *et al.*, 2015). The initial arterial rupture and chemokines activation have a role in the mechanisms of damage (F. Guo *et al.*, 2020), and the antifibrinolytic agent CM352, administered early after ICH (1 hour), was efficient in reducing hematoma expansion (Rodríguez *et al.*, 2017) and was associated with benefit. Also, it has been shown that aspiration of the hematoma after an experimental ICH model improves functional outcome and reduces neuronal loss (Hu *et al.*, 2025).

Neuroprotective molecules

A number of molecules, such as the glycoprotein osteopontin (Gong *et al.*, 2018), the vaso-protector angiopoietin-like 4 (Qiu *et al.*, 2018), COA-Cl, a novel synthesized adenosine analog (Lu *et al.*, 2016), apelin-13 (Bao *et al.*, 2016), or statins (Karki *et al.*, 2009), have been found beneficial in ICH through reducing inflammation, edema, and/or neuronal death.

Antioxidant compounds

Nuclear factor erythroid 2-related factor 2 (Nrf2) activators (Chen-Roetling and Regan, 2017), tert-butylhydroquinone (TBHQ) (Sukumari-Ramesh and Alleyne, 2016), or edavarone, with or without hypothermia (Zhou, Chen and Zhang, 2009; Nakamura *et al.*, 2007; Li *et al.*, 2025; Zhu, Liu and Sun, 2015), have been reported protective in ICH by improving barrier function, attenuating edema, inflammation, neuronal loss and/or neurological deficits. Also, GSH/glutathione improves the prognosis of mice with ICH by attenuating neurological impairment, decreasing neural damage, and inhibiting apoptosis, through the up-regulation of mitochondrial oxidative respiration function. (Diao *et al.*, 2020).

Iron chelation or hemoglobin (Hb)-haptoglobin (Hp) targeting

Iron plays a critical toxic role in ICH, which can be reduced by the highly CNS-penetrant antibiotic minocycline, at least in part through the inhibition of metalloproteinase activity (Zou *et al.*, 2017; Y. Liu *et al.*, 2021; Xue and Yong, 2020). The iron chelators 2,2'-bipyridyl, deferasirox, and deferoxamine (DFO) have been demonstrated to have neuroprotective effects and to improve neurological outcome in animal models of ICH (Okauchi *et al.*, 2010; Auriat *et al.*, 2012; Wu *et al.*, 2012; Chen *et al.*, 2022; Cui *et al.*, 2015), even in aged rats (Hatakeyama *et al.*, 2013). Building on this concept of iron toxicity in ICH, it has been shown that Hb-induced hypohaptoglobinemia aggravates ICH-induced brain damage, while sulforaphane-induced increase in brain Hp reduces brain damage. In agreement with these findings, Hp deficiency worsens, whereas Hp overexpression alleviates ICH-induced brain injury (Zhao *et al.*, 2009).

Antiinflammatory treatments

The suppression of proinflammatory microglia (M1 phenotype) is neuroprotective in ICH (Rahman *et al.*, 2020; Ohnishi *et al.*, 2020). The thrombin inhibitor argatroban attenuates inflammation and edema without enlarging the hematoma in experimental ICH models (Kitaoka *et al.*, 2003; Nagatsuna *et al.*, 2005) and, unlike rtPA, it acts independently of the fibrinolytic system (Hamada and Matsuoka, 2000). The aforementioned antibiotic minocycline has also shown antioxidant activity and to inhibit proinflammatory signaling activity in ICH (Hamada and Matsuoka, 2000), although some studies have reported minimal benefit in this regard (Wang, 2010). Another class of immunomodulation arises from sphingosine-1-phosphate receptor (S1PR) modulators, such as fingolimod. These agents reduce T-cell

infiltration and BBB disruption, resulting in recovered behavioral outcomes (Xue and Yong, 2020). Prostaglandins and cyclooxygenase (COX) enzymes also play a role in secondary brain injury after ICH (Leclerc *et al.*, 2015; B. Chen *et al.*, 2019). The COX-2 inhibitor celecoxib reduces inflammation, prostaglandin synthesis, and brain edema, leading to better functional recovery (Chu *et al.*, 2004). Statins also exert neuroprotective antiinflammatory effects (Xue and Yong, 2020) through reducing leukocyte infiltration in preclinical ICH models (Keep, Hua and Xi, 2012; Xue and Yong, 2020). R-7050, a cell-permeable triazoloquinoxaline inhibitor of the tumor necrosis factor receptor (TNFR) complex, showed benefit after ICH in mice (King, Alleyne and Dhandapani, 2013).

Other approaches

The use of stem cells, small RNAs, exosomes, neurotropic factors, such as neuritin (Lu *et al.*, 2021), and nanoparticles are currently being investigated for the ICH treatment. While in its infancy, these approaches offer great promise for future clinical translation (Seyfried *et al.*, 2010; Zille *et al.*, 2022). For instance, intravenous (IV) administration of human adipose-derived stem cells ameliorates motor and cognitive function in an ICH mouse model (Kuramoto *et al.*, 2019).

In addition, several potentially repurposable treatments with anti-inflammatory, antioxidative, neuroprotective, or hematoma clearance effects have been tested and listed in a review by Crilly and colleagues in 2021 (Crilly *et al.*, 2021). Other approaches, such as self-assembly peptide nanofibrous scaffold (SAPNS), have been found to aid functional recovery (Zhang *et al.*, 2016).

2.10. Animal models of ICH

Preclinical research models are basic to study specific characteristics of a disease and perform clinical tests of new treatments. The choice of a model will mainly depend on the questions posed beforehand by the researchers, as well as the cost, opportunity, and the stage and scope of the research, among others.

2.10.1. Rodents

Rodents are the most commonly used species in animal research, and they are useful for initial *in vivo* testing of new therapeutic strategies. They are small, have good reproductive characteristics, and easily allow the application of new reproductive biotechnology

techniques, such as transgenesis, knock-out animals, and CRISPR, to develop new disease models. The lower body weight of small animals results in reduced drug quantities needed for dose-ranging and efficacy studies, thereby decreasing cost relative to studies in larger species at the same dosage (Bryda, 2013). Additionally, they are well-domesticated laboratory animals, easy to handle, and drugs can be administered in the required route (Domínguez-Oliva *et al.*, 2023).

Rodents have a great dissimilarity with humans regarding cerebral anatomy (Figure 6.), because their brains are lissencephalic, unlike the human brain, which is gyrencephalic, and they also have lower proportions of white matter (Melià-Sorolla *et al.*, 2020). Moreover, they are nocturnal animals, affecting their circadian cycle (which is the opposite of humans, who are active performing research and testing neurological deficits in the stroke models in the diurnal period), and their neural network structure and functionality differ from humans (Corbett *et al.*, 2017). It is also important to mention that most studies conducted on rodents are performed during the day, in young, healthy animals without comorbidities and with optimized diets, raised in controlled, pathogen-free environments (Lourbopoulos *et al.*, 2021).

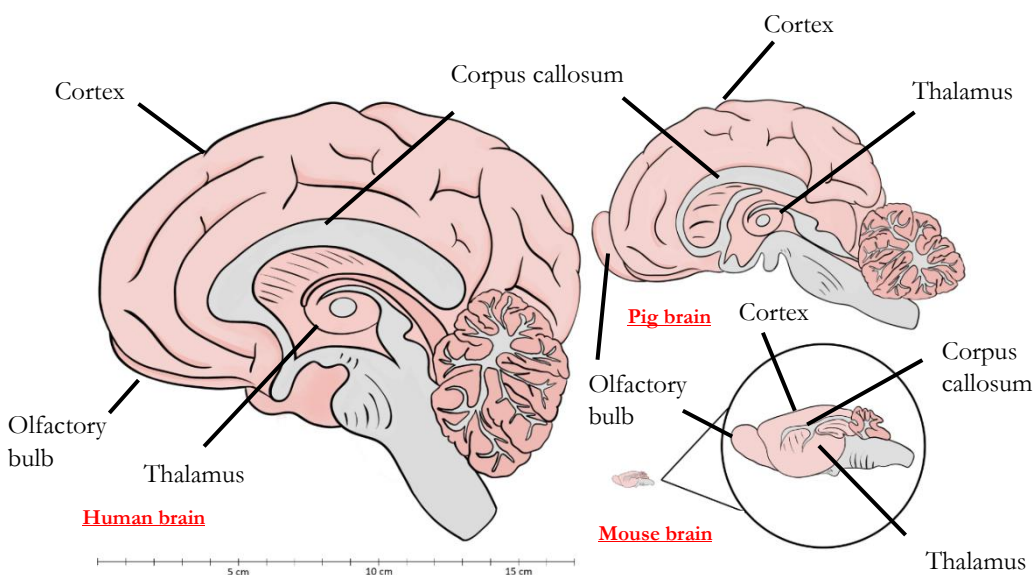


Figure 6. Sagittal cross-sections of the human, pig, and mouse brains, shown to scale, with an enlarged view of the mouse brain for clarity. The illustration compares structural differences among these species, highlighting the gyrencephalic nature of the human and pig brains, which exhibit greater cortical folding and a higher white-gray matter ratio. In contrast, the lissencephalic mouse brain has a smoother surface and a relatively higher proportion of gray matter, making it structurally distinct. The olfactory bulb is more developed in pigs and mice compared to humans.

2.10.1.1. Rodent brain vasculature

The circle of Willis (CoW) is an arterial ring/anastomosis at the base of the brain that supplies blood to both the brain and its surrounding structures, present in most vertebrates (Vrselja *et al.*, 2014). In humans, the CoW encompasses the anterior cerebral arteries (ACAs), which are connected by the anterior communicating artery (AComA), the internal carotid artery (ICAs), which branch into the middle cerebral arteries (MCAs), the posterior cerebral arteries (PCAs), which are connected by the posterior communicating arteries (PComA), and the basilar artery (BA), forming the arterial ring (Figure 7A.) (Ayre *et al.*, 2022).

In mice, the ICA bifurcates into the MCA, and it then continues as the ACA, which branches to the anterior communicating artery (AComA) until it becomes the olfactory artery. However, in several mouse strains, the PCAs do not connect to the BA, resulting in independent units of blood supply. This makes the CoW of the mouse an open circuit, in contrast to humans (Okuyama *et al.*, 2004). Additionally, numerous anatomic variants can be found

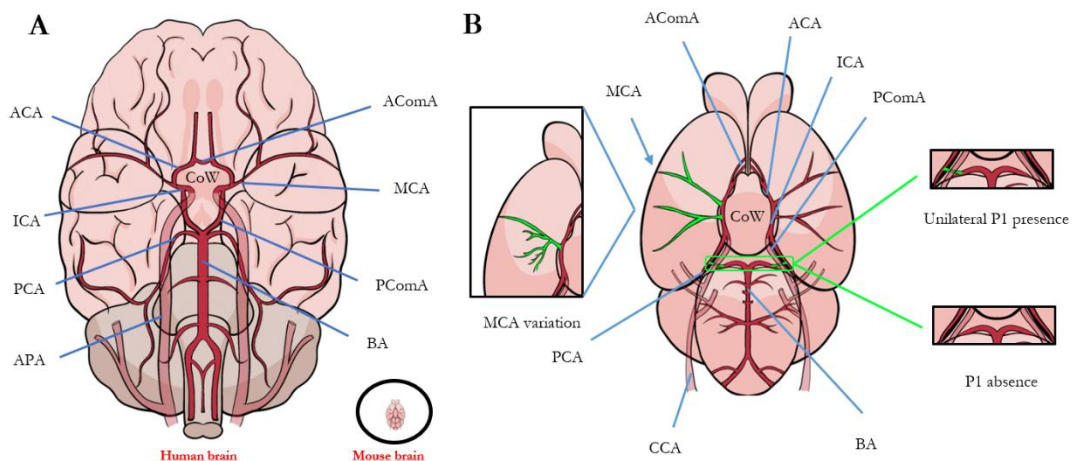


Figure 7. Ventral view of the human and mouse brains, illustrating the arterial vasculature. (A) The image is drawn to scale, with the mouse brain surrounded by a black circle (see magnified view of the mouse brain in B). Major cerebral arteries are depicted. The circle of Willis (CoW) is visible in both species. The mouse brain displays a more simplified arterial pattern compared to the human brain, which has a more complex and extensive vascular network. (B) Magnified ventral view of a mouse brain, highlighting common anatomical variants. (B, left) Variations in the middle cerebral artery (MCA in green, pointed with a blue arrow). (B, right top) Unilateral presence of the first segment of the posterior cerebral artery (P1 in green). (B, right bottom) Absence of the P1 segment. Abbreviations: anterior communicating artery (AComA), anterior cerebral artery (ACA), basilar artery (BA), internal cerebral Artery (ICA), posterior communicating artery (PComA), posterior cerebral artery (PCA), first segment of the PCA (P1), middle cerebral artery (MCA), ascending pharangeal artery (APA), common carotid artery (CCA).

(Figure 7B.). The most common variants include the absence or unilateral presence of the first segment of the posterior cerebral artery (P1) and variations in the MCA, such as accessory MCAs originating from the distal ICA (Qian *et al.*, 2018).

Regarding the mouse brain venous vasculature, important connections between intra- and extracranial veins are important drainage pathways in brain circulation (Mancini *et al.*, 2015). In both humans and mice, the superior sagittal sinus (SSS), inferior sagittal sinus (ISS), straight sinus (StS), vein of Galen (GV), internal cerebral vein (ICV), transverse sinus (TS), and sigmoid sinus (SiS) are present.

2.10.1.2. Intracerebral hemorrhagic stroke models in rodents

Injection-based ICH models

Autologous blood or bacterial collagenase-specific intracerebral injections are the most commonly used methods to induce ICH in rodents. Both models require craniotomy and allow researchers to induce hemorrhages at the desired location while controlling the speed and size of the hematoma (Mracsko and Veltkamp, 2014). These models require invasive procedures.

- **The autologous blood model** involves the production of a hematoma by using a stereotaxic frame to inject freshly-obtained arterial blood, usually from the femoral artery of the same animal, into the brain parenchyma (Bullock *et al.*, 1984).
- **The intracerebral injection of bacterial collagenase model** dissolves the basal lamina of adjacent blood vessels, resulting in continuous bleeding for up to several hours (MacLellan *et al.*, 2008; Da Silva-Candal *et al.*, 2015).

The human condition typically results from the spontaneous rupture of an intracerebral artery, and this differs from the two previous models (Mracsko and Veltkamp, 2014).

Other ICH models

- **Spontaneous models.** Although less commonly used, spontaneous ICH models have been described to encompass several characteristics of human ICH or to mimic hemorrhage development (Bai, Liu and Wang, 2020; Withers *et al.*, 2020). In

these models, the hemorrhage location and size cannot be controlled (Withers *et al.*, 2020).

- Hypertension-induced models. These models spontaneously generate microhemorrhages, petechial hemorrhages, and larger hemorrhages in the cerebellum. Hypertension is produced experimentally by using deoxycorticosterone acetate salts, angiotensin, or by genetic modifications (Ogata *et al.*, 1982; Iida *et al.*, 2005; Wakisaka *et al.*, 2010; De Silva and Faraci, 2023).
- CAA models. Developed due to mutations in a region of the amyloid precursor protein gene. The hemorrhages appear in old animals with this mutation (Winkler *et al.*, 2001; Herzog *et al.*, 2004).
- Cerebral small vessel disease (CSVD) models. Induced by mutating isoforms of the collagen type IV gene (Jeanne, Jorgensen and Gould, 2015).
- **Periventricular/intraventricular hemorrhages (PVH/IVH).** More common in premature infants due to the high blood supply required for developing neurons, and having incompletely formed blood vessels (Whitelaw, 2012). In PVH/IVH animal models, the injection of glycerol (Conner *et al.*, 1983) or phenylephrine (Goddard *et al.*, 1980) produces intracranial hypotension or hypertension, respectively, leading to IVH hemorrhages. Other approaches involve autologous blood injection directly in the ventricles or the periventricular tissue (Xue and Del Bigio, 2003).
- To study specific ICH parameters, such as the mass effect, **microballoon insertion models** are used. These simulate the hematoma expansion effect by increasing the intracranial pressure and reducing the cerebral blood flow in the ipsilateral hemisphere (Sinar *et al.*, 1987). To study the secondary brain injury caused by thrombin released from the initial hematoma, **thrombin injection models** are used (Xue and Del Bigio, 2001).

2.10.2. Large animals

To improve the translationality of preclinical findings, new humanized stroke models have been developed in large animals and non-human primates (Combs *et al.*, 1990; Watanabe *et al.*, 2007; Boltze *et al.*, 2008; Rink *et al.*, 2008; Cook and Tymianski, 2012; Golubczyk *et al.*, 2020; Kaiser and West, 2020; Castaño *et al.*, 2023). Most of these animals have gyrencephalic brains with vascular anatomy similar to humans (Figure 6 and Figure 8.) (Wagner *et al.*,

1996; Küker *et al.*, 2000; Mun-Bryce *et al.*, 2001; Rohde *et al.*, 2001; Zhu *et al.*, 2013; Gerhardson *et al.*, 2020; Withers *et al.*, 2020; Castaño *et al.*, 2023).

The advantage of modeling ICH in large animals lies in their larger size, with a higher percentage of white matter (Melià-Sorolla *et al.*, 2020; Withers *et al.*, 2020) and structurally more human-like brains (Kaiser and West, 2020; Melià-Sorolla *et al.*, 2020). A variety of species, such as pigs, sheep, non-human primates, cats, and dogs, have been used to establish ICH models. However, due to social concerns, research costs, and availability issues, the last three are used much less frequently (Wagner *et al.*, 1996; Küker *et al.*, 2000; Mun-Bryce *et al.*, 2001; Rohde *et al.*, 2001; Zhu *et al.*, 2013; Liu *et al.*, 2014; An *et al.*, 2015; Dai *et al.*, 2018; Boltze *et al.*, 2019; Gerhardson *et al.*, 2020; Withers *et al.*, 2020). The use of farm animals like sheep and pigs raises fewer concerns than the use of non-human primates, and their use is crucial for understanding the pathophysiology of stroke.

Most large-animals ICH models are performed in pigs (Wagner *et al.*, 1996; Küker *et al.*, 2000; Mun-Bryce *et al.*, 2001; Rohde *et al.*, 2001; Zhu *et al.*, 2013; Gerhardson *et al.*, 2020; Withers *et al.*, 2020). The advantages of porcine models over ovine models focus on the pre-surgical preparation of the animal. Ruminants produce a large amount of saliva and have a high risk of regurgitation, necessitating esophageal, as well as tracheal intubation, and positioning their head downwards (Seddighi and Doherty, 2016). Additionally, there are increasing numbers of successful transgenic pig models for metabolic, neurodegenerative, and genetic diseases (Adam *et al.*, 2007; Renner *et al.*, 2010; Yu *et al.*, 2016; Perleberg, Kind and Schnieke, 2018; Andersen *et al.*, 2022; Wei *et al.*, 2022; Slijkhuis *et al.*, 2024).

These large animal models are much more expensive than rodent models. It also requires specialized personnel for their handling, control, and review, as well as appropriate facilities for their housing. Moreover, most large animals (including pigs) have a network of small arteries at the base of the brain, before the internal carotid artery, called the *rete mirabile* (RM), which prevents reaching the CoW through catheters (Figure 8.) (Melià-Sorolla *et al.*, 2020; Castaño *et al.*, 2023).

2.10.2.1. Swine vasculature

Pigs are animals that possess significant similarities with humans and are the most used model for experimental surgery and the development of medical devices, especially for

research in vascular diseases, transplants, and xenotransplants (Tanaka and Kobayashi, 2006). Additionally, pigs have interesting brain characteristics and broad social acceptance to be used in research. Domestic pig breeds are among the most commonly used in experimentation, with juvenile animals reaching a weight of 40-50 kg. The use of adult mini-pigs, weighing around 40 kg, enables long-term studies, including those involving geriatric animals. Due to their tendency to form individualized relationships, it is essential to acclimate these animals to routine procedures and ensure they receive sufficient environmental enrichment.

Being large animals, pigs allow the use of the same multimodal imaging techniques used in humans, as well as repeated and substantial biological sampling. This enables the longitudinal study of imaging and blood biomarkers (Melià-Sorolla *et al.*, 2020; Castaño *et al.*, 2023). Recently, new porcine models have been developed with comorbidities and pathologies found in human patients (Melià-Sorolla *et al.*, 2020; Castaño *et al.*, 2023).

The brain and vascular anatomy of the pigs are comparable to humans (Scheulin *et al.*, 2021). The main difference is the RM, a network of small arteries connecting the ascending

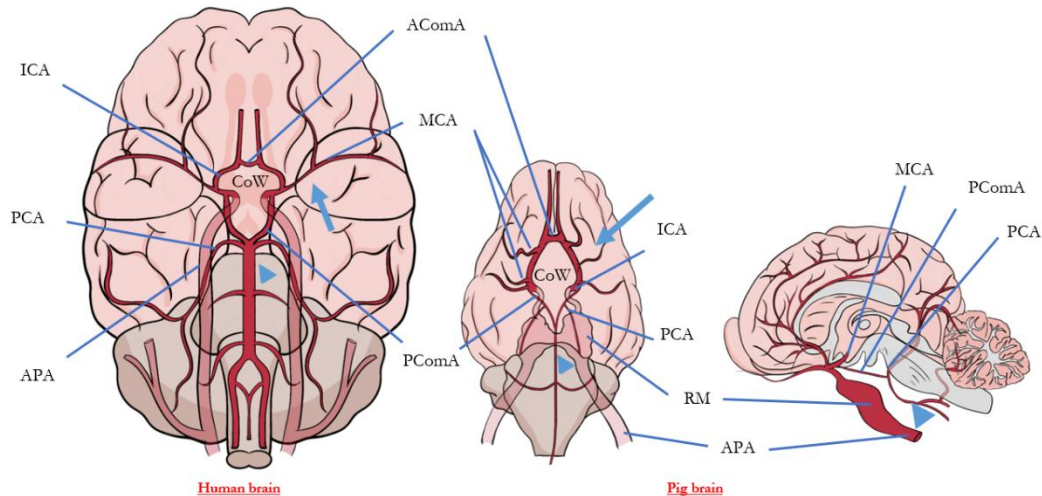


Figure 8. View of the human (ventral) and pig (ventral and sagittal) brains, illustrating the arterial vasculature (in red). Major cerebral arteries are depicted. The circle of Willis (CoW) is visible in both species. The *rete mirabile* (RM) is present in the pig vasculature in contrast to the human. The basilar artery (BA, blue arrowhead) is thinner in pigs, and the anterior brain circulation in pigs (anterior communicating artery, AComA) is very important in contrast to humans. Normally, in pigs, several middle cerebral arteries (MCAs) are present (see blue arrow; differences in the number of MCAs in the right and left hemispheres are also described). Abbreviations: internal cerebral artery (ICA), posterior communicating artery (PComA), posterior cerebral artery (PCA), ascending pharyngeal artery (APA).

pharyngeal artery (APA) and the ICA, present in farm animals like pigs, sheep, and goats, but not in humans, dogs, or cats (Melià-Sorolla *et al.*, 2020) (Figure 8.). Other subtle differences include the presence of multiple branches of the MCA in pigs, the formation of the ICA by the convergence of arterioles from the RM, and the proportional size difference of the BA and AComA compared to other arteries in the CoW. Additionally, the CoW is consistently complete in pigs, meaning there are almost no variations between individuals of the same breed, whereas variations are common in humans (e.g. hypoplasia, aplasia, and duplication) (Unpublished results by our lab).

At the venous level, there is much less information available. However, pigs also appear to share the main structures of cerebral venous circulation with humans. Few researchers have explored the intricate cerebral venous system in pigs. In fact, only Fries in 1992, Wang in 2010, and Pasarikovski in 2020 have successfully accessed and described common structures with humans via angiography, such as the SSS, StS, TS, and SiS (Figure 9.) (Fries *et al.*, 1992; Wang *et al.*, 2010; Christopher R. Pasarikovski *et al.*, 2020).

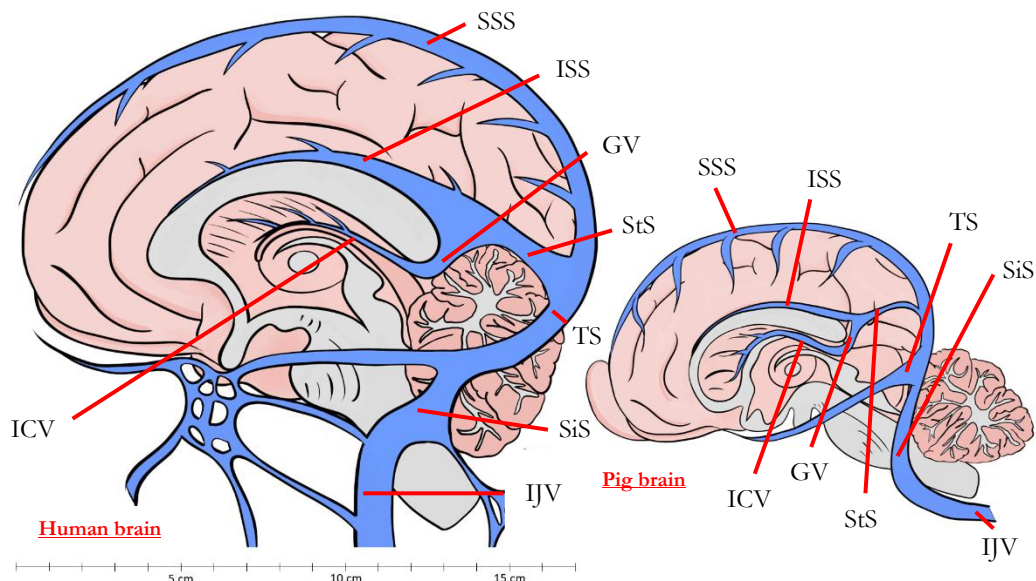


Figure 9. Sagittal cross-sections of the human and pig brains and venous system (depicted in blue). The illustration compares the cerebral venous vasculature of both species. Abbreviations: superior sagittal sinus (SSS), inferior sagittal sinus (ISS), straight sinus (StS), vein of Galen (GV), internal cerebral vein (ICV), transverse sinus (TS), sigmoid sinus (SiS), internal jugular vein (IJV).

2.10.2.2. Intracerebral hemorrhagic stroke models in swine

Most large animal ICH models are generally very invasive procedures that require specialized personnel, a stereotaxic frame, and typically involve intracerebral injection of autologous

blood or collagenase via craniotomy (**Table 7.**) (Wagner *et al.*, 1996; Küker *et al.*, 2000; Mun-Bryce *et al.*, 2001; Rohde *et al.*, 2001; Zhu *et al.*, 2013; Gerhardson *et al.*, 2020), although other models do exist (Aviv *et al.*, 2014; Xu *et al.*, 2015). The procedure to develop these models is very similar to that described in rodents, with some modifications for the autologous blood injection model (Küker *et al.*, 2000; Rohde *et al.*, 2001; Zhu *et al.*, 2013).

- **Autologous blood injection model.** Similar to small animal models, this involves an intracerebral injection of autologous blood (Wagner *et al.*, 1996; Gerhardson *et al.*, 2020). However, due to the larger volume of blood to be injected, there is a significant risk of reflux, leading to slight modifications in the procedure, such as a double injection (Zhu *et al.*, 2013), balloon dilation along with double injection (Rohde *et al.*, 2001), or balloon dilation with a single injection (Küker *et al.*, 2000). This model has been performed in various animal species, including cats, rabbits, dogs, monkeys, and pigs (Andaluz, Zuccarello and Wagner, 2002).
- **Intracerebral collagenase injection model.** As in small animal models, collagenase is injected intracerebrally (Mun-Bryce *et al.*, 2001). This model has been used in various large animal species, including pigs, dogs, monkeys, and rabbits (Mun-Bryce *et al.*, 2001; Liu *et al.*, 2014; An *et al.*, 2015; Dai *et al.*, 2018).

Table 7. List of pig-ICH stroke models available in the literature

Approach	Method	Target	Ad-vantages	Disad-vantages	Ref
Craniotomy	MRI-guided focused ultrasound	Brain parenchyma	Reproducible	Invasive	(Xu <i>et al.</i> , 2015)
	Collagenase injection	Brain parenchyma	Reproducible	Invasive and only used in juvenile pigs	(Mun-Bryce <i>et al.</i> , 2001)
	Single blood injection	Brain parenchyma	Reproducible	Invasive	(Gerhardson <i>et al.</i> , 2020)

Cranial burr hole	Double blood injection	Brain parenchyma	Reproducible	Invasive	(Zhu <i>et al.</i> , 2013)
	Balloon catheter dilation and double blood injection	Brain parenchyma	Reproducible	Invasive	(Rohde <i>et al.</i> , 2001)
	Balloon catheter dilation and single blood injection	Brain parenchyma	Reproducible	Invasive	(Küker <i>et al.</i> , 2000)
	Single blood injection	Ventricles and brain parenchyma	Reproducible	Invasive	(Wagner <i>et al.</i> , 1996)

Extracted from: (Melià-Sorolla *et al.*, 2020)

2.11. Neurological evaluation in ICH stroke animal models

Intracerebral hemorrhage leads to specific neurological symptoms that develop within minutes. Symptoms vary widely, ranging from stupor or coma to seizures, nystagmus, gaze preference, sensory-motor deficits, and contralateral motor deficits. These symptoms need to be measured to assess the degree of neurological deterioration.

To better understand stroke, its pathophysiology, and to develop new drugs or therapeutic strategies that improve the lives of stroke patients, animal models are currently necessary. After stroke induction in animal models, they exhibit neurobehavioral and sensorimotor deficits similar to those seen in humans (Grabowski, Brundin and Johansson, 1993; Perleberg, Kind and Schnieke, 2018). Therefore, it is crucial to use the most appropriate neurological tests to evaluate the extent of neurological impairment. When selecting these tests, factors such as the location of the injury, the duration of the experiment, and the specific interventions applied must be considered, along with the expected improvements based on the treatment being tested. For instance, if a treatment is anticipated to improve learning

and memory impairments, cognitive function tests should be used in addition to other sensorimotor tests.

2.11.1. Small animals

Rodents are widely used as animal models for studying stroke, and choosing the right tests is essential for effective translational research. Generally, these tests are classified into motor and sensorimotor, cognitive and emotion-related, and sensory tests.

2.11.1.1. Motor and sensorimotor tests

They measure changes in the animal's ability to perform tasks that require the integration of sensory input and motor output.

Similar to human assessments, different **scoring systems** have been developed to assess the functional outcome in animal models of stroke, such as the modified neurological severity score (mNSS), Garcia's test, and the neurological deficit scoring (NDS) scale. The main disadvantages of these scoring systems are their subjective component, their difficulty in conducting them, and their limited utility for long-term studies ([Balkaya et al., 2018](#); [Ruan and Yao, 2020](#); [Fang et al., 2023](#)).

Apart from the neuroscores, **other motor and sensorimotor tests** are frequently performed. These are generally more objective than scoring systems, but a significant disadvantage is that they often require both animal and researcher training (**Table 8.**) ([Balkaya, 2018](#)).

2.11.1.2. Cognitive and emotion-related tests

These tests are designed to assess emotional and behavioral changes, such as anxiety, depression-like behavior, and stress response, as well as cognitive functions like learning, memory, attention, and decision-making (**Table 8.**) ([Schaar, Brenneman and Savitz, 2010](#); [Ruan and Yao, 2020](#); [Fang et al., 2023](#)).

2.11.1.3. Sensory tests

Sensory tests are not commonly used to evaluate neurological impairments in stroke models but are valuable for identifying increased sensitivity to pain, such as mechanical allodynia, mechanical hyperalgesia, cold hyperalgesia, and thermal hyperalgesia ([Fang et al., 2023](#)).

Table 8. Most common behavioral tests and their objectives

Behavioral test	Purpose	Ref
Motor and sensorimotor tests	Neurological severity scores (mNSS)	(Zhao <i>et al.</i> , 2017; Lin <i>et al.</i> , 2018; Qiu <i>et al.</i> , 2018; Liang <i>et al.</i> , 2019; Li <i>et al.</i> , 2020; Yu <i>et al.</i> , 2020)
	Garcia's test	(Yu <i>et al.</i> , 2017; Yang, X. Zhang, <i>et al.</i> , 2018; Lu <i>et al.</i> , 2019; S. Chen <i>et al.</i> , 2019; Ding <i>et al.</i> , 2020)
	Neurological deficit scoring (NDS) scale	(Leclerc <i>et al.</i> , 2015, 2018, 2019; Williamson and Colbourne, 2017; Sosa, De Souza and Mello-Carpes, 2018; Bao <i>et al.</i> , 2020)
	Modified ranking scale (mRS) score	(Kinder, Baker and West, 2019; Spellicy <i>et al.</i> , 2020; Scheulin <i>et al.</i> , 2021)
	Adhesive tape removal test	(MacLellan <i>et al.</i> , 2008; Min <i>et al.</i> , 2016; Alim <i>et al.</i> , 2019; Xu <i>et al.</i> , 2020; García-Serran <i>et al.</i> , 2023)
	Pole test	(Masuda <i>et al.</i> , 2010)
	Rotarod test	(Glushakov <i>et al.</i> , 2013; Yu <i>et al.</i> , 2017; Zhao <i>et al.</i> , 2017; Lin <i>et al.</i> , 2018; Qiu <i>et al.</i> , 2018; Sosa, De Souza and Mello-Carpes, 2018; Yang, X. Zhang, <i>et al.</i> , 2018; Hayashi <i>et al.</i> , 2020)
	Corner test	(Ni <i>et al.</i> , 2016; Yu <i>et al.</i> , 2017; Li <i>et al.</i> , 2017, 2019, 2020; Qiu <i>et al.</i> , 2018; Alim <i>et al.</i> , 2019; B. Chen <i>et al.</i> , 2019; S. Chen <i>et al.</i> , 2019; Tan <i>et al.</i> , 2019; Jing <i>et al.</i> , 2019; Lu <i>et al.</i> , 2019; Bao <i>et al.</i> , 2020; Han <i>et al.</i> , 2021b)
	Cylinder test	(Ni <i>et al.</i> , 2016; Chang <i>et al.</i> , 2020; Diaz Diaz <i>et al.</i> , 2020; Xu <i>et al.</i> , 2020)

	Beam walking test	Assesses sensorimotor coordination.	(Yang, X. Zhang, <i>et al.</i> , 2018; W. Chen <i>et al.</i> , 2019; Hayashi <i>et al.</i> , 2020)
	Grid walking (foot-fault) test	Assesses sensorimotor skills, motor coordination, and difficulties with placing during movement.	(Yu <i>et al.</i> , 2017, 2020; Diaz Diaz <i>et al.</i> , 2020; Xu <i>et al.</i> , 2020)
	Limb placing/vibrissae-evoked test	Assesses the coordination of fore and hindlimb movements and proprioceptive input.	(Yu <i>et al.</i> , 2017; B. Chen <i>et al.</i> , 2019; Li <i>et al.</i> , 2019; Lu <i>et al.</i> , 2019; S. Chen <i>et al.</i> , 2019; Bao <i>et al.</i> , 2020; Chang <i>et al.</i> , 2020)
	Montoya's staircase test	Assess the reaching abilities, grasping capabilities, preference for one side, and separate use of forelimbs (sensorimotor test generally performed in rats).	(Williamson <i>et al.</i> , 2019)
	Hanging test	Assess various elements of mobility.	(Diaz Diaz <i>et al.</i> , 2020; Han <i>et al.</i> , 2021b)
Cognitive and emotion-related tests	Open field test	Assess general coordination.	(Glushakov <i>et al.</i> , 2013; Sosa, De Souza and Mello-Carpes, 2018; Yang, X. Zhang, <i>et al.</i> , 2018)
	Morris water maze test	Assesses cognitive abilities for spatial learning and memory.	(Chen <i>et al.</i> , 2020; Ding <i>et al.</i> , 2020; Xu <i>et al.</i> , 2021)
	Sucrose test	Assess depression-like symptoms.	(Yang, K. Zhang, <i>et al.</i> , 2018)
	Forced swim test		(Yang, K. Zhang, <i>et al.</i> , 2018)
	New object recognition test		(Zhu <i>et al.</i> , 2014)

Table adapted from: (Schaar, Brenneman and Savitz, 2010; Balkaya *et al.*, 2018)

2.11.2. Large animals

Large gyrencephalic animal stroke models are recommended by the STAIR to improve the translationability of the results (Stroke Therapy Academic Industry Roundtable (STAIR), 1999). The assessment of motor impairment, and the performance of functional tasks are widely used to evaluate the outcome and severity of the lesion (Duberstein *et al.*, 2014; Baker *et al.*, 2019; Kinder, Baker and West, 2019; Kinder, Baker, Howarth, *et al.*, 2019; Kinder, Baker, Wang, *et al.*, 2019; Scheulin *et al.*, 2021; Kaiser *et al.*, 2022; Jeon *et al.*, 2023; Sun *et al.*, 2024). In contrast to rodents, large animals are not that handy, and the neurological/functional outcome assessment can be challenging. Most of the neurological assessments in large animals are focused on scales (Table 9.) that evaluate features such as consciousness, motor function, sensory function, head position gaze, hemianopia, and circling.

Table 9. Modified Rankin Scale (mRS) score

Deficits	Points
No symptoms.	0
The animal is able to perform normal activities, although some neurological deficits can be found.	1
Slight disability can be found but the animal can eat without assistance.	2
Moderate deficits (such as facial paralysis). Assistance for eating and drinking is necessary but can walk without help.	3
Moderate-severe disability (circling, head pressing, unable to stand). Unable to perform normal activities without assistance.	4
Severe deficits. The animals need constant attention and aids.	5
Dead.	6

Extracted from: (Spellicy *et al.*, 2020)

Apart from the neurological scales, in swine, gait assessments using video recordings are especially popular (Baker *et al.*, 2019; Kinder, Baker and West, 2019; Kinder, Baker, Howerth, *et al.*, 2019; Kinder, Baker, Wang, *et al.*, 2019; Kaiser *et al.*, 2022; Taha *et al.*, 2022; Jeon *et al.*, 2023; Sun *et al.*, 2024).

Here is a description of some of the most commonly used tests in large animals:

- **Gait analysis** is a walkway mattress system associated with a software evaluation of swing time, stance time, step and stride length, step velocity, stance time and pressure parameters (Duberstein *et al.*, 2014; Kinder, Baker and West, 2019; Kinder, Baker, Howerth, *et al.*, 2019; Kinder, Baker, Wang, *et al.*, 2019; Scheulin *et al.*, 2021).
 - Step length: distance between the hoof prints of the front or hind hooves (right and left) during gait cycle.
 - Stride length: distance between the hoof prints of the same foot during gait cycle.
 - Velocity: mean speed of the animal during gait cycle.
 - Cadence: strides (complete cycles of movement of the legs) performed by the animal in a minute.
 - Swing: the time during which the limb of the animal is not in contact with the ground, it is expressed as a percentage of the total gait cycle.

- Stance: the time during which the limb of the animal is in contact with the ground, it is expressed as a percentage of the total gait cycle.
- Pressure parameters: percentage of weight distribution across the paws of the animal during movement.
- **Open field** ([Kinder, Baker and West, 2019](#); [Kinder, Baker, Howerth, *et al.*, 2019](#); [Scheulin *et al.*, 2021](#)) test consists of tracking the movement of the animal for 10 minutes in a controlled pen using software. Different parameters are extracted from it, such as the distance travelled, the average velocity, and the movement duration. In this test, stroked animals move a shorter distance.
- **Modified ranking scale (mRS) score** ([Kinder, Baker and West, 2019](#); [Spellicy *et al.*, 2020](#); [Scheulin *et al.*, 2021](#)) from 0 to 6 (death). As in rodents, they are used to assess neurological deficits according to the researcher's criteria.
- **New/Novel object recognition test** measures the functional outcome of pigs. In this test, pigs are placed in a pen with two similar objects. After several minutes, one of these objects is replaced with a new one. A video tracking software records the pig's speed, time spent in the area near each object, and distance traveled ([Kaiser *et al.*, 2021](#)).
- **Social recognition test**, although is not a common test performed in large animal stroke models, assesses social memory, anxiety, and exploration tendencies ([Souza *et al.*, 2006](#)). In this test, the pig is exposed to a new object and an unfamiliar pig. After a break, the new object is replaced by another unfamiliar pig, making the first unfamiliar pig familiar. The pig is expected to spend more time with the unfamiliar pig than with the new object or the familiar pig. As in the new object recognition test, this process is recorded by a software tracking system.

The use of software tracking systems in these video-recorded tests opens the door for integrating machine-deep learning techniques, which helps to reduce researcher subjectivity, to standardize procedures, and to provide a more objective and comprehensive understanding of large animal behavior ([Hakansson and Jensen, 2023](#); [Wei *et al.*, 2023](#)).

The background of the image is a complex, abstract composition. It features several overlapping circles in various colors like pink, yellow, and light blue. In the lower-left quadrant, there is a stylized illustration of a pig's head and neck. In the lower-right quadrant, there is a detailed illustration of a human brain with various colored regions. The overall style is modern and artistic, with a focus on organic and geometric forms.

CONTEXTUALISATION AND JUSTIFICATION

Contextualisation

Intracerebral hemorrhage (ICH) is one of the most severe forms of stroke, accounting for approximately 10–15% of all strokes and associated with significantly higher morbidity and mortality rates compared to ischemic stroke. Despite advances in stroke research, current therapeutic strategies for ICH are primarily supportive rather than curative. Understanding the pathophysiological mechanisms driving neuronal death and secondary brain injury following ICH is critical for identifying novel therapeutic targets and improving patient outcomes.

Our laboratory is particularly interested in identifying the specific deleterious mechanisms that are common to all strokes. This approach will provide a common intervention target for both stroke types, ischemic and hemorrhagic. Once these common targets have been identified, the opportunity arises to develop therapies beneficial for both ischemic and hemorrhagic stroke patients, by allowing an early administration, before the differential diagnosis between ischemic or hemorrhagic stroke is confirmed. As in stroke “time is brain”, our approach holds significant clinical value.

Among the mechanisms under investigation, the accumulation of excess iron in the brain following both ischemic and hemorrhagic stroke has emerged as a critical contributor to injury. Clinical trials such as i-DEF and TANDEM have demonstrated the potential benefit of the iron chelator deferoxamine in patients with either ischemic stroke or ICH. However, as the use of deferoxamine has intrinsic limitations, other approaches to target this excess iron are needed.

This dissertation aims to address several critical aspects of ICH pathophysiology and potential treatment strategies, focusing on the treatment with apotransferrin. Our research group has already published that apotransferrin is neuroprotective for ischemic stroke in rodents, appears to be superior to deferoxamine, and is currently being tested in our laboratory in a preclinical study in an ischemic stroke model in swine. The results of this thesis are presented as a compendium of 3 publication-styled manuscripts: one of them has already been published in a D1 journal, the second one is currently submitted, and the third one is presented in a short communication format (we are currently in the process to increase the number of swine in the study).

- The **first manuscript** explores the role of iron in neuronal death mechanisms in ICH and evaluates the safety and efficacy of apotransferrin treatment in improving the neurological outcome. Confirming its effectiveness in a preclinical model would potentially expand the number of patients eligible for this early treatment (an Annex with post-publication obtained relevant results of ICH growth has been included).
- The **second manuscript** introduces a more objective and standardized tool for evaluating stroke outcomes in preclinical research, indicating that neurological impairment correlates with the infarct size in ischemic stroke but not with the volume of hemorrhage in ICH preclinical models. According to this particularity of the ICH models, the development of predictive and objective algorithms to refine the assessment of neurological impairment providing more precise, objective, and unbiased systems is a must.
- The **third manuscript** describes the establishment of a minimally invasive ICH model in pigs. We designed this model to overcome some of the serious limitations of existing ICH in large animal models, eliminating the need for greatly invasive craniotomies that alter intracranial pressure and affect translational validity. Although rodent models have traditionally been and are still a cornerstone of pre-clinical stroke research, as they are very useful for initial testing of new therapeutic drugs, their translational limitations have resulted in a high failure rate of preclinical promising therapies when tested in clinical trials. In particular, ICH models in rodents often fail to replicate human pathophysiological features, such as intracranial pressure dynamics and brain complexity, i.e. simpler brain structure and lower white-to-gray matter ratio than those of humans. For these reasons, developing and validating stroke models in pigs, whose gyrencephalic brains more closely resemble the human brain, is of crucial importance for improving translational success.

The background of the slide is a vibrant, abstract collage. It features several concentric, multi-colored circles in shades of yellow, orange, pink, and purple. Interspersed among these circles are various scientific and organic motifs: a molecular structure with a central hexagon and surrounding spheres, a brain-like cell with pink and yellow regions, a DNA helix, and a pig's head in profile. The overall aesthetic is a blend of scientific precision and organic complexity.

HYPOTHESIS AND OBJECTIVES

Hypothesis

Hypothesis I

Apotransferrin (ATf) treatment, administered as a single intravenous bolus, will reduce neurological impairment induced by intracerebral hemorrhage (ICH) in mice. The ICH will be induced via intrastratial stereotaxic injection of collagenase, and neurological impairment will be evaluated using mouse-validated neurobehavioral tests.

Hypothesis II

The neuroprotective effect of ATf is mediated by modulation of brain molecules involved in iron homeostasis and ferroptosis rather than reducing the hematoma size. Identification of these molecular changes will reveal novel therapeutic targets for ICH.

Hypothesis III

Application of the open-source, machine learning-based tracking software DeepLabCut to video recordings of validated neurobehavioral and neurological tests for assessing stroke-induced impairments in mice will enhance the quality and reproducibility of preclinical stroke research by enabling automated, objective evaluations of neurological deficits and recovery.

Hypothesis IV

A novel pig model of ICH induced via an endovascular approach can be established to minimize invasiveness, more accurately recapitulate human ICH pathology, and reduce confounding factors such as parenchymal damage caused by more invasive methods. Validation of ATf therapy in this large animal model is essential prior to undergoing clinical studies.

Hypothesis V

This new endovascular ICH pig model will facilitate investigation of specific pathophysiological questions, including the effects of parenchymal hematoma on systemic coagulation and the impact of hematoma-derived iron release into systemic circulation, while avoiding confounding variables.

Objectives

Objective I

To determine the effect of ATf, previously demonstrated as protective by reducing ischemic infarct size and neurological impairment in ischemic stroke in mice, when tested in a preclinical ICH stroke rodent model.

Objective II

To study how the iron- and ferroptosis-related molecules that are altered during the ICH stroke are modulated with the specific treatment with ATf in order to identify new intervention targets.

Objective III

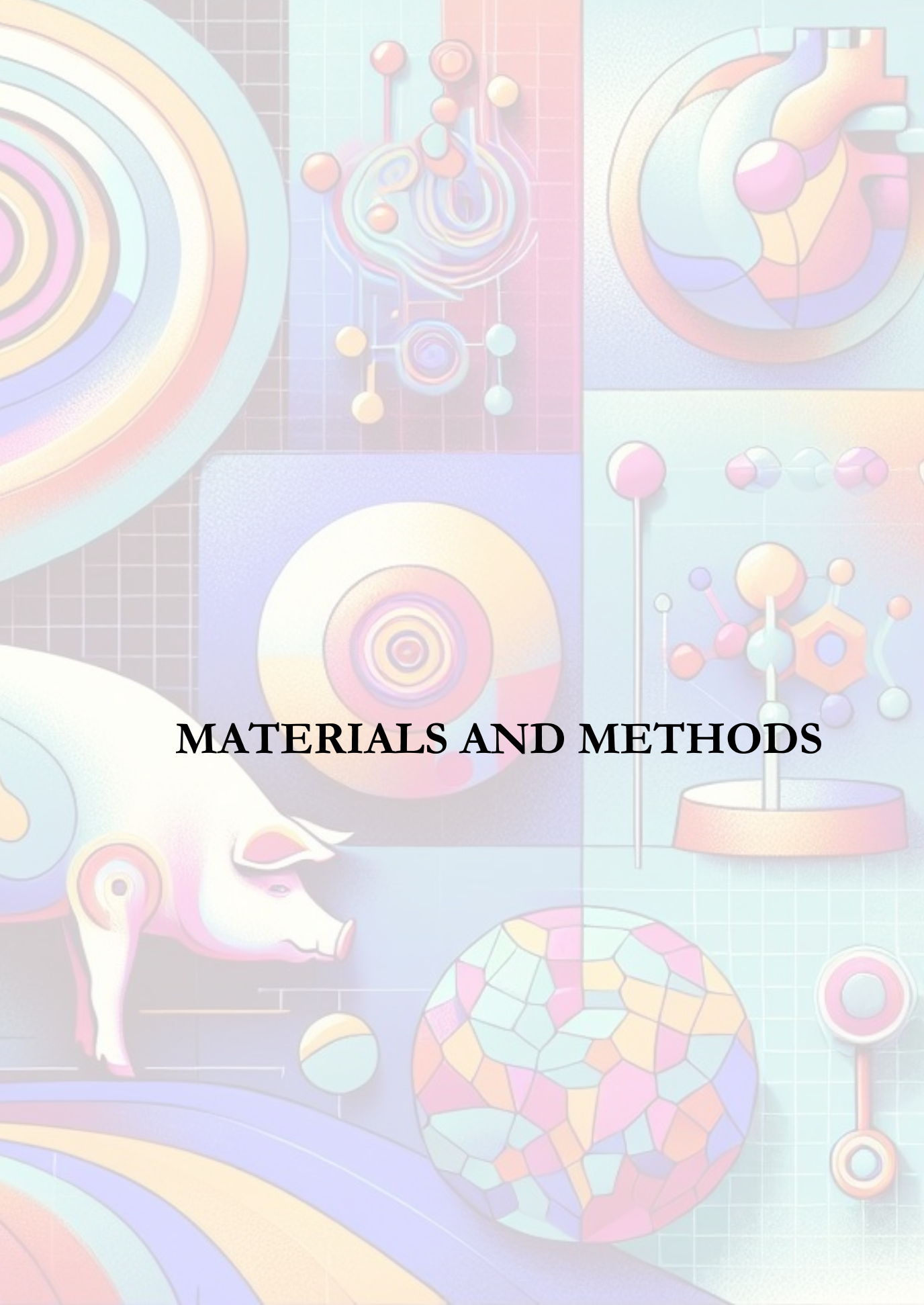
To determine the effect of ATf treatment on the volume of ICH or on coagulation/clotting time.

Objective IV

To develop an automated machine learning model capable of predicting individual outcomes in mice subjected to experimental stroke using only a single neurobehavioral test.

Objective V

To establish a minimally invasive hemorrhagic stroke model in pigs, as close as possible to the human ICH scenarios, and to study pathophysiological mechanisms related to coagulation, and iron-related molecules in serum and brain parenchyma.

The background of the image is a complex, abstract collage. It features several large, overlapping circles in various colors (yellow, orange, pink, purple, blue) of different sizes. Interspersed among these are various scientific and organic motifs: a detailed molecular structure with spheres and connecting lines; a stylized brain or cell with a pink-to-white gradient; a molecular model with spheres and connecting rods; a pig's head in profile; and a circular diagram with a grid pattern. There are also some smaller, isolated shapes like a red and yellow ring and a blue and white sphere.

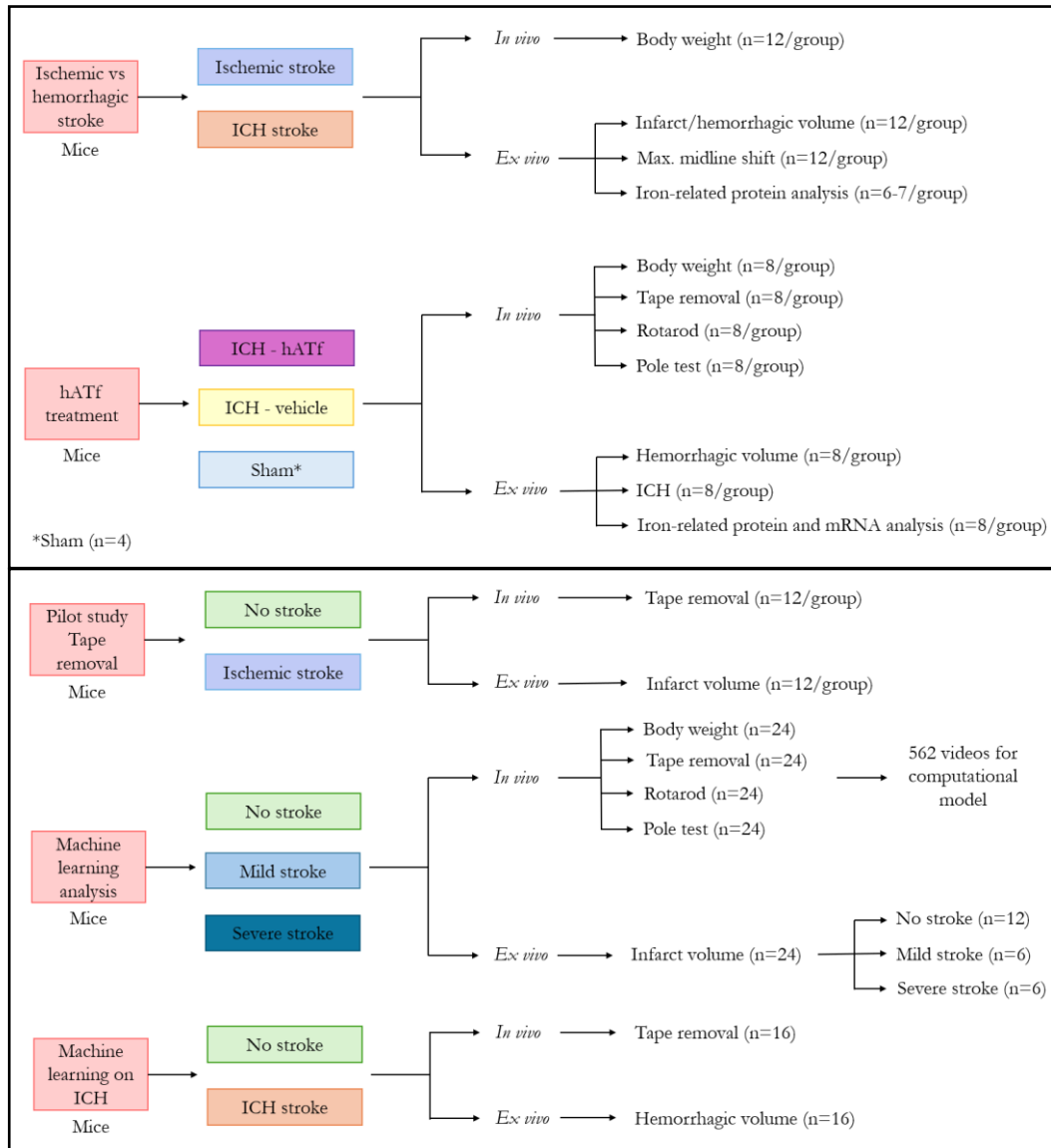
MATERIALS AND METHODS

Materials and methods

1. STUDY DESIGN

To address the aims of this thesis, three independent research studies were conducted, each of which is presented in **Manuscripts I** through **III**.

Animals were divided into different experimental groups based on the specific purpose of each study. An overview of the animal groups, the techniques employed, and the corresponding goals are provided in **Figure 10**.



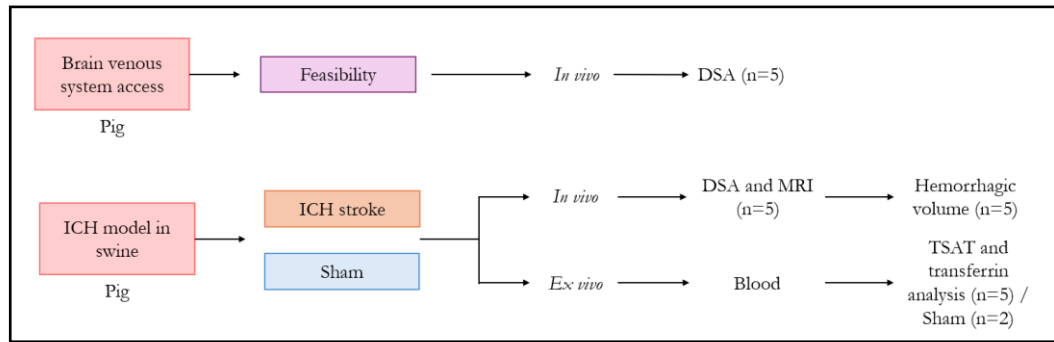


Figure 10. Overview diagram of the studies presented as manuscripts in this thesis. The diagram illustrates the study groups (highlighted in colored boxes) along with the number of subjects in each group. Each of the three main studies is represented by a separate box, summarizing the methods used and their specific objectives, which are shown in pink boxes at the beginning of each scheme. Abbreviations: digital subtraction angiography (DSA), intracerebral hemorrhage (ICH), human apotransferrin (hATf), immunohistofluorescence (IHF), messenger ribonucleic acid (mRNA), magnetic resonance imaging (MRI) and percentage of transferrin saturation (TSAT).

2. METHODS AND PROCEDURES

2.1. Experimental animals

The mouse models used were 9-week-old male C57BL/6J mice obtained from Charles River Laboratories (Saint-Germain-Nuelles, France). Animals were maintained under controlled, standardized environmental conditions, including regulated temperature, humidity, and a 12-hour light/dark cycle, environmental (such as tissue paper and tunnels for mice; and rubber balls, hanging ropes, chains, or chewable toys for pigs) and social enrichment. Food and water were available without restriction.

For the new pig ICH model, 3-month-old Duroc × Landrace pigs (castrated males and females), with a mean body weight of 40.1 ± 3.3 kg, were sourced from Mir Ramadera (Tona, Spain). Upon arrival at the Comparative Medicine and Bioimage Centre of Catalonia (CMCiB), the animals underwent an acclimatization period of at least one week in a controlled environment.

All procedures received ethical approval from both the Germans Trias i Pujol Research Institute Animal Ethics Committee and the Generalitat de Catalunya (Authorization numbers for mouse models: references 11131, 11182; Authorization numbers for pig model: 10671) and adhered strictly to EU Directive 2010/63/EU. Randomization was used to allocate animals to experimental groups, and the investigator was blinded to treatment conditions throughout the experiments. Experiments were performed in compliance with Animal Research: Reporting of *In Vivo* Experiments (ARRIVE) guidelines and the 3Rs principle (Replacement, Reduction and Refinement). Housing and procedures were carried out at the CMCiB.

2.2. Hypoxic/ischemic stroke model

A hypoxic-ischemic (H/I) stroke model involving unilateral transient cerebral ischemia was implemented based on a protocol modified from Guan *et al.* (Guan *et al.*, 1993). Animals were anesthetized with isoflurane (4% induction, 1.5% maintenance; Zoetis Inc.; Parsippany, NJ, USA) using a 30:70 mix of oxygen (O₂) and nitrous oxide (N₂O). The right common

carotid artery (CCA) was transiently ligated using sterile 5-0 silk suture material (Ethicon, LLC.; San Lorenzo, Puerto Rico).

After recovery and a 2-hour rest period with unrestricted food and water, animals were transferred to a hypoxia chamber pre-warmed to 35.5°C, where they inhaled a humidified 8% O₂/92% nitrogen (N₂) mixture for 20 minutes at an airflow rate of 1 L/min. The CCA occlusion was then reversed under isoflurane anesthesia (using the same concentrations as before), and blood flow restoration was visually confirmed. The skin incision was closed using a simple interrupted 4-0 silk non-absorbable suture (Silkam; B.Braun; Rubí, Spain) (**Figure 11**).

This procedure induces ischemic injury in the ipsilateral hemisphere and results in motor deficits contralateral to the lesion.

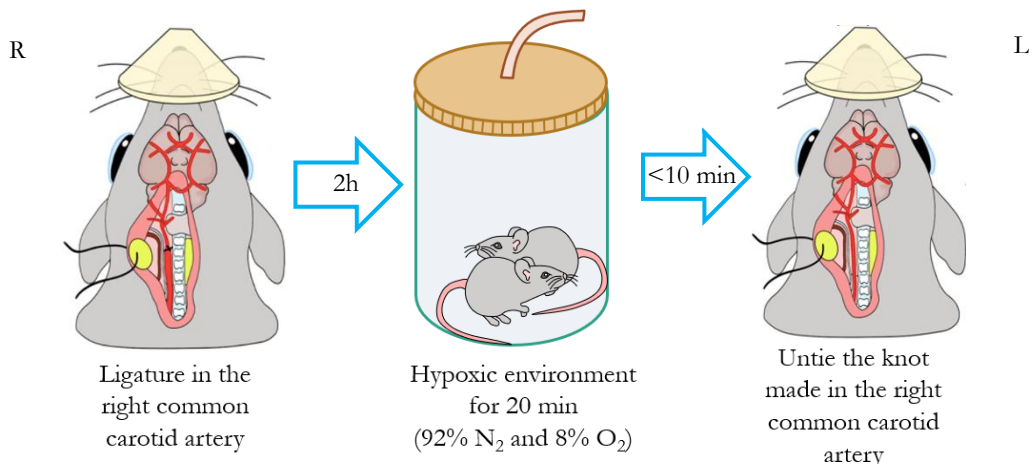


Figure 11. Schematic representation of the hypoxic/ischemic model. First, the common carotid artery (CCA) is exposed and transiently ligated. After two hours of recovery, the animals are placed in a hypoxic environment for 20 minutes with a gas mixture of 92% nitrogen (N₂) and 8% oxygen (O₂). After this period, the CCA ligature is released, and restoration of the blood flow is verified *de visu*.

2.3. Collagenase-induced intracerebral hemorrhagic stroke model

For hemorrhagic stroke induction, a collagenase-based model adapted from Klebe *et al.* (Klebe *et al.*, 2018) was used. Under isoflurane anesthesia (4% induction, 1.5% maintenance; using a 30:70 mix of O₂ and N₂O), mice were secured in a stereotactic frame (Model 940 Small animal; Kopf instruments; Tujunga, CA, USA), using ear bars and a face mask. The

animals are then shaved, and the skull was exposed and perforated. Subsequently, 0.06 units of *Clostridium histolyticum* type VII-S collagenase (Sigma-Aldrich; Saint Louis, MO, USA) in 0.4 μ L sterile saline was infused into the right striatum using a microinjection system (Model UMP3T-A; Kopf Instruments) and a NanoFil 26G syringe (World Precision Instruments; Sarasota, FL, USA). Injection coordinates were set at 0.5 mm anterior, 1.7 mm lateral, and 3.0 mm depth relative to Bregma (Figure 12.). Infusion proceeded at 200 nL/min, and the needle remained *in situ* for 10 minutes post-injection while isofluorane was reduced to 1% for this period of time. Withdrawal was made at a controlled speed of 1 mm/min to avoid reflux, and the burr hole was sealed with bone wax (Bone Wax; B.Braun). Then, the skin wound was sutured using a simple interrupted 4-0 silk non-absorbable suture. Sham-operated controls underwent the same procedure without the collagenase; only sterile saline was injected.

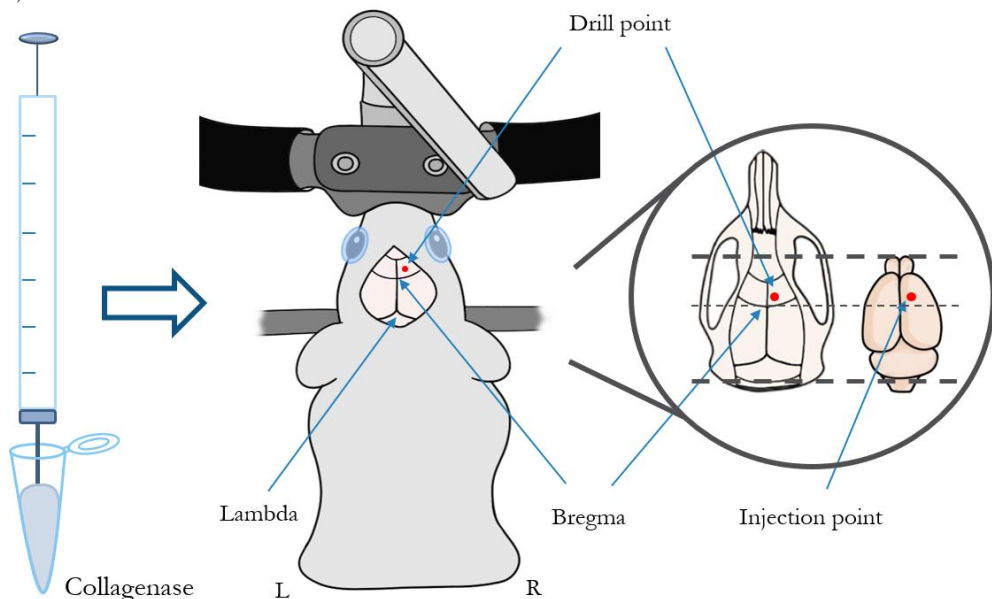


Figure 12. Schematic representation of the collagenase-induced hemorrhagic stroke model. A total of 0.06 units of *Clostridium histolyticum* type VII-S collagenase, diluted in 0.4 μ L sterile saline, is injected intracerebrally into the striatum. The injection is performed using the following Bregma coordinates: 0.5 mm anterior, 1.7 mm lateral, and 3.0 mm in depth.

2.3.1. hATf treatment protocol after the ICH mouse model

Human apotransferrin (hATf; Sigma-Aldrich) was selected to differentiate it from murine endogenous transferrin. Treatment with hATf was made by diluting it in sterile saline and injecting it intravenously (IV), at a dose of 230 mg/kg, 40 minutes post-collagenase injection.

Animals were randomly divided into two treatment groups ($n = 8$ per group): one received hATf and the other sterile saline.

2.4. Minimally invasive intracerebral hemorrhagic stroke model in pig

2.4.1. Preoperative procedures

Preoperative protocols followed the methodology outlined by Castaño *et al.* ([Castaño *et al.*, 2023](#)). Before neurointervention, pigs were fasted for 12 hours. Anesthesia was induced via intramuscular injection of atropine (0.04 mg/kg; B.Braun), dexmedetomidine (0.03 mg/kg; Orion Corporation; Espoo, Finland), ketamine (3 mg/kg; VetViva Richter GmbH; Wels, Austria), buprenorphine (0.01 mg/kg; Ecuphar; Sant Cugat del Vallès, Spain), and midazolam (0.3 mg/kg; Normon; Tres Cantos, Spain). Once sedation was achieved, the animals received corneal protection with ophthalmic ointment, an intramuscular injection of tulathromycin (2.5 mg/kg; Zoetis Inc.), and intravenous administration of propofol (1 mg/kg; Zoetis Inc.). For analgesia, a dermal fentanyl patch (2 μ g/kg/h; Johnson & Johnson Innovative Medicine; Beerse, Belgium) was applied.

Tracheal intubation (tubes of 6-6.5 mm Ø) was facilitated using lidocaine spray (Inibsa Dental; Lliçà de Vall, Spain), and anesthesia was maintained with 1.5–2% isoflurane administered through a closed mechanical ventilation system. Continuous intravenous fluid therapy with sterile saline solution was provided at a rate of 100 mL/h. Once anesthetized, the animals were transferred to either the neurointerventional or magnetic resonance imaging (MRI) suite for the procedure.

2.4.2. Neurointerventional procedure

In the angiography room, animals were positioned supine. To prevent thrombus formation during the intervention, a bolus of physiological saline containing 3,000 units of heparin was administered. Under ultrasound guidance, 7F sheath introducers (Prelude® Sheath Introducer PRO-7F-11-035MT; Merit Medical; South Jordan, UT, USA) were placed in both the right femoral vein and left femoral artery.

Real-time vascular imaging was conducted using a Canon Alphenix monoplane angiography system (Canon Medical Systems Corporation; Ōtarawa, Tochigi, Japan) at 3 frames per

second. A 7F Envoy Guide Catheter (778-256-00; Codman; Integra LifeSciences; Princeton, NJ, USA) was advanced into the left ascending pharyngeal artery until reaching the *rete mirabile* entrance. Simultaneously, a second 7F Envoy Guide Catheter was introduced into the right internal jugular vein using a Terumo Glidewire (Radifocus™ Guide Wire M Standard RF*GA35183M; Terumo Corporation; Shibuya, Tokio, Japan).

To visualize the venous anatomy and the junction between the internal jugular vein (IJV) and the sigmoid sinus (SiS), iodine-based contrast agent (Iodixanol; Visipaque™ 320 mg/mL; GE Healthcare; Chicago, IL, USA) was injected through both catheters. Using a Stryker Synchro2 Guidewire (Synchro2® Standard; 2641; Stryker Corporation; Kalamazoo, MI, USA) and a Terumo Headway Duo Microcatheter (Headway Duo! Microcatheter MC162156S; Terumo Corporation), access to the brain's venous system was achieved via navigation through the transverse sinus (TS), straight sinus (StS), vein of Galen (GV), internal cerebral veins (ICV), and thalamostriate veins (TSV).

Once the target site in the right cerebral hemisphere was reached, venous perforation was performed. Iodine contrast was subsequently injected to confirm extravasation. Then, 1.5 mL of autologous arterial blood was slowly infused through the microcatheter at a rate of 0.5 mL/min to induce a controlled hemorrhage (**Figure 13.**).

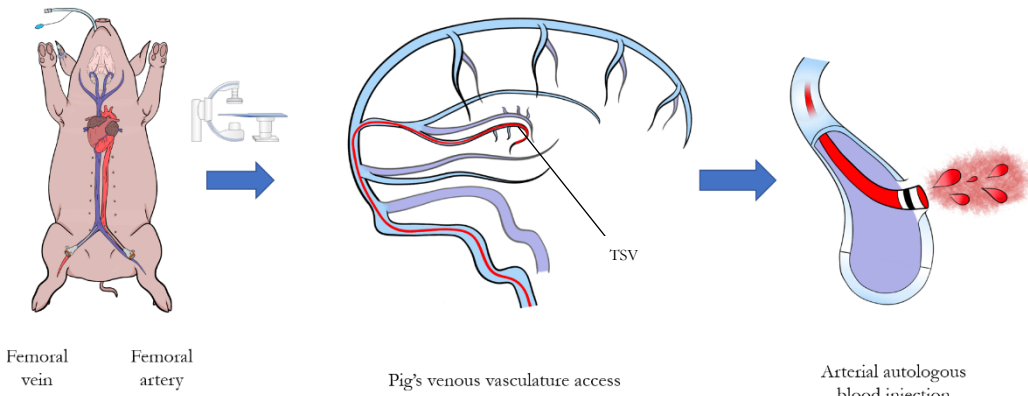


Figure 13. Schematic overview of the neurointerventional procedure for inducing intracerebral hemorrhage in the swine model. The pig is positioned supine within a C-arm angiography suite. Two 7F vascular sheaths are inserted into the right femoral vein (blue), allowing catheter navigation through the vertebral venous system. Under fluoroscopic guidance, the catheters are advanced to the thalamostriate vein (TSV). Once the target vein is reached, it is mechanically ruptured using a microcatheter, followed by the controlled injection of 1.5 mL of autologous arterial blood to induce hemorrhage.

After the ICH-induction, all catheters were carefully withdrawn, and a final rotational angiography scan was conducted. This allowed the reconstruction of both extracranial and intracranial vasculature using Vitrea® Advanced Visualization software (Canon Medical Systems Corporation). Manual pressure was applied to the femoral artery for 30 minutes to ensure hemostasis before the animals were moved out of the vascular radiology suite.

A separate cohort of four pigs was assigned to the sham group. These animals underwent identical preparatory and anesthetic protocols as those in the experimental group but did not receive the intracerebral hemorrhage induction. They were maintained under general anesthesia for a total of five hours to replicate the procedural duration of the experimental intervention.

2.4.3. Postoperative care, follow-up, and euthanasia

Upon completion of the neurointerventional and MRI procedures, general anesthesia was reversed using an intramuscular injection of atipamezole (0.1 mg/kg; Antisedan; Zoetis Inc.). Animals were continuously monitored for vital signs, including heart rate, respiratory rate, reflexes, and body temperature, until fully stabilized. Once the swallowing and palpebral reflexes returned, pigs were extubated and transferred back to their housing units, where they were observed under continuous video surveillance during the first night.

To support thermoregulation, thermal foil blankets were used initially, followed by the installation of heat lamps positioned 1.5 meters above the pens. Animals had unrestricted access to food and water once they regained consciousness. In some cases, intravenous levetiracetam (10 mg/kg; Normon) was administered every 12 hours as a prophylactic anti-convulsant.

At the end of the experimental period, animals were euthanized using an intravenous injection of sodium pentobarbital (200 mg/kg; Dolethal; Vetoquinol; Madrid, Spain).

2.5. Functional assays

2.5.1. Tail bleeding test

To evaluate the coagulation effects of hATf, a tail bleeding assay was conducted in nine C57BL/6J male mice (hATf n = 4; vehicle n = 5). Animals were anesthetized as described in **Section 2.2.** and received an IV injection of hATf at a dose of 230 mg/kg. Ten minutes after administration, the distal tail tip was excised and immersed in 37°C saline. Bleeding duration was recorded as the duration until complete hemostasis ([Denis *et al.*, 1998](#)). Vehicle animals are injected with the same volume of sterile saline (**Figure 14.**).

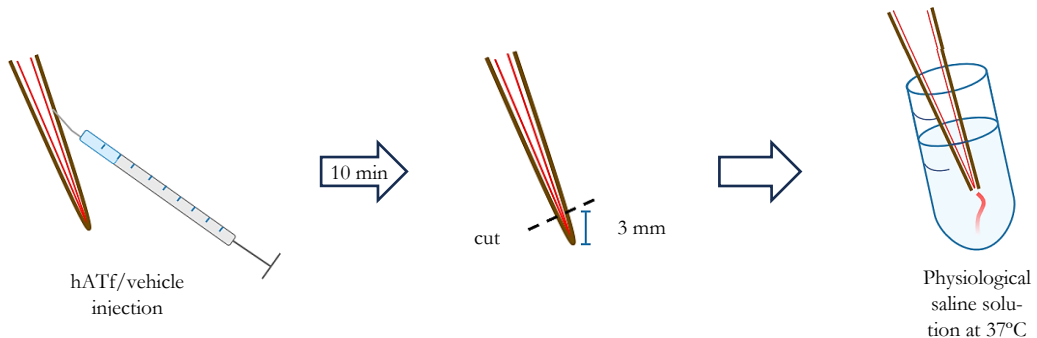


Figure 14. Overview of the tail bleeding test to assess coagulation effects of the human apotransferrin (hATf).

2.5.2. Coagulation assays in human blood

To simulate *in vivo* exposure of the hATf in blood in the collagenase-induced ICH mice model, *ex vivo* coagulation assays were conducted using freshly collected human plasma. Plasma was treated with one of the following: hATf or human holotransferrin (hHTf) (both at 50 mg/mL from Sigma-Aldrich) or sterile saline solution (vehicle). Equal concentrations and volumes were matched to reflect therapeutic exposure levels in the mouse model.

Human blood samples were collected from healthy adult donors into 1.8 mL BD™ Vacutainer™ Citrate Tubes (Thermo Fisher Scientific; Waltham, USA) and processed within 1 hour of collection to isolate plasma.

All coagulation assays (e.g., prothrombin time, activated partial thromboplastin time, thrombin time) were performed under standardized clinical laboratory conditions by the Hematology service of the Germans Trias i Pujol Hospital (Badalona, Spain).

2.5.3. Behavioral assessment

Mice were weighed daily and subjected to a battery of behavioral tests. In the first manuscript, neurological performance was measured using the pole, rotarod, and adhesive tape removal tests (**Figure 15.**), whereas in the second manuscript, it was measured by the tail hanging, rotarod, and adhesive tape removal tests. All of the tests are described below. All behavioral tests were performed at 24-, 48-, and 72-hours post-ICH, and mice were pre-trained for 2–3 days prior to stroke induction to ensure familiarity with the procedures.

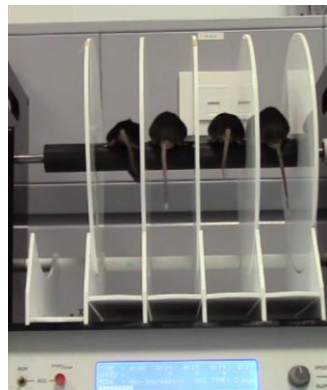
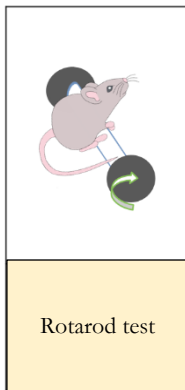
Pre-training in behavioral tests is essential because it reduces stress, improves task performance and ensures more reliable data. It helps mice get familiar with the environment and procedures, which minimize variability, providing more interpretable results. Pretraining standardizes baseline performance, allowing researchers to detect real experimental effects.

- The **rotarod test** involved an accelerating rod (Rota Rod LE8200; Harvard Apparatus; Holliston, USA), which increased speed from 4 to 40 revolutions per minute. Latency to fall was measured and averaged across three trials per time point, with rest intervals of 5 to 10 minutes between trials (**Figure 15A.**).
- In the **pole test**, mice were placed facing upwards on top of a vertical pole (55 cm height, 1 cm diameter), and the time to turn around and descend was recorded (**Figure 15B.**).
- In the **adhesive tape removal test**, mice were placed inside a transparent open-top box with a square base of 25 × 25 cm and a height of 30 cm. Small circular adhesive tapes, measuring 6 mm in diameter, were alternately applied to the pads of each forepaw, both ipsilateral and contralateral to the lesioned hemisphere. Two metrics were recorded: the detection time (latency to first notice the tape) and the removal time (TR time), defined as the time taken for the animal to actively remove the tape, typically by biting or pulling it off.

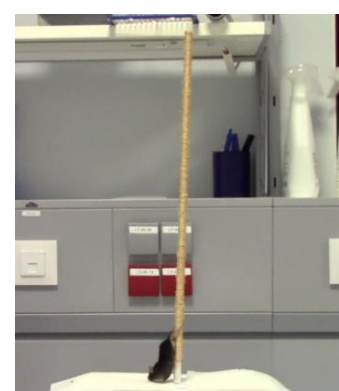
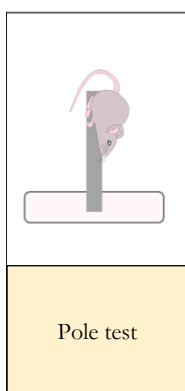
Each session was video recorded from beneath the transparent box using a smartphone controlled by a smartwatch, oriented orthogonally to the center of the box (**Figure 15C and 16A.**). Videos captured for each forepaw were independently analyzed and scored by two trained investigators. Typically, two daily sessions were recorded per paw, ending once the adhesive tape was removed, though some videos continued for up to 200 seconds to accommodate longer response times.

- In the **tail hanging test**, mice were suspended by their tails, and the first lateral bending direction was recorded over 20-30 trials to minimize variability.

A



B



C

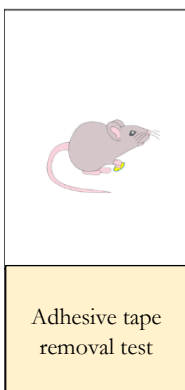


Figure 15. Overview of some of the neurobehavioral tests performed: (A) rotarod test, (B) pole test, and (C) adhesive tape removal test.

Neurological function in pigs was assessed daily post-intervention by a certified veterinarian using an adapted version of the NIHSS score (**Table 10**). A maximum score of 5 was defined as a humane endpoint criterion. Short video recordings were taken twice daily to monitor behavior.

Table 10. Neurological score system and welfare assessment score

Score	Description
0	Normal behavior.
1	Slight neurologic symptomatology such as ataxia (i.e., uncoordinated or unskilled movements), nystagmus, tremors, repeated head shaking, imping, etc., without problems in performing common activities.
2	Slight disability with level 1 symptoms, plus others such as circling (i.e. repetitive and unilateral and ipsilateral circular motion when walking) and head pressing against walls.
3	Moderate disability with level 2 symptoms, plus either convulsions or standing, or swallowing difficulties.
4	Moderate to severe disability with level 3 symptoms plus prolonged prostration, weight loss, or dehydration symptoms.
5	Severe disability with level 4 symptoms plus total prostration, unresponsiveness or comatose, anorexia or incontinence.
6	Dead.

2.5.4. DeepLabCut, postprocessing and computational prediction models

This segment of the study also contributed to several undergraduate thesis projects (“Treballs de Final de Grau”) conducted by students from Universitat Politècnica de Catalunya and Universitat de Barcelona.

2.5.4.1. DeepLabCut for pose estimation and behavioral feature extraction

Video footage of the adhesive tape removal tests was analyzed using DeepLabCut (DLC) for pose estimation, implemented in a Python 3.8 Anaconda environment (Anaconda; Austin, TX, USA). Prior to analysis, video files were preprocessed by resizing to 900 x 900 pixels, masking the outer box area, and trimming to the first frame in which the mouse’s body parts were fully visible, thereby excluding any frames with the researcher’s hand (**Figure 16C**).

Frame selection for manual annotation was guided by k-means clustering, and eight body landmarks along with the adhesive tape were labeled (**Figure 16B**). A label at the tail midpoint was finally excluded due to poor tracking consistency. The position of the adhesive

tape was annotated during both attachment and post-removal periods. Manual quality control was performed on DLC's initial automated outputs to correct mislabeling, and additional complex motion scenarios were incorporated to enhance model robustness. Each model training session consisted of 200,000 iterations with an 80/20 split between training and validation datasets. Training proceeded iteratively until the network achieved satisfactory performance metrics.

The final trained network was then applied to the full set of video recording to extract body part coordinates and their corresponding confidence scores for each frame. To facilitate spatial calibration, a separate DLC model was trained to identify the boundaries of the test chamber, enabling conversion from pixel-based to centimeter-based measurements.

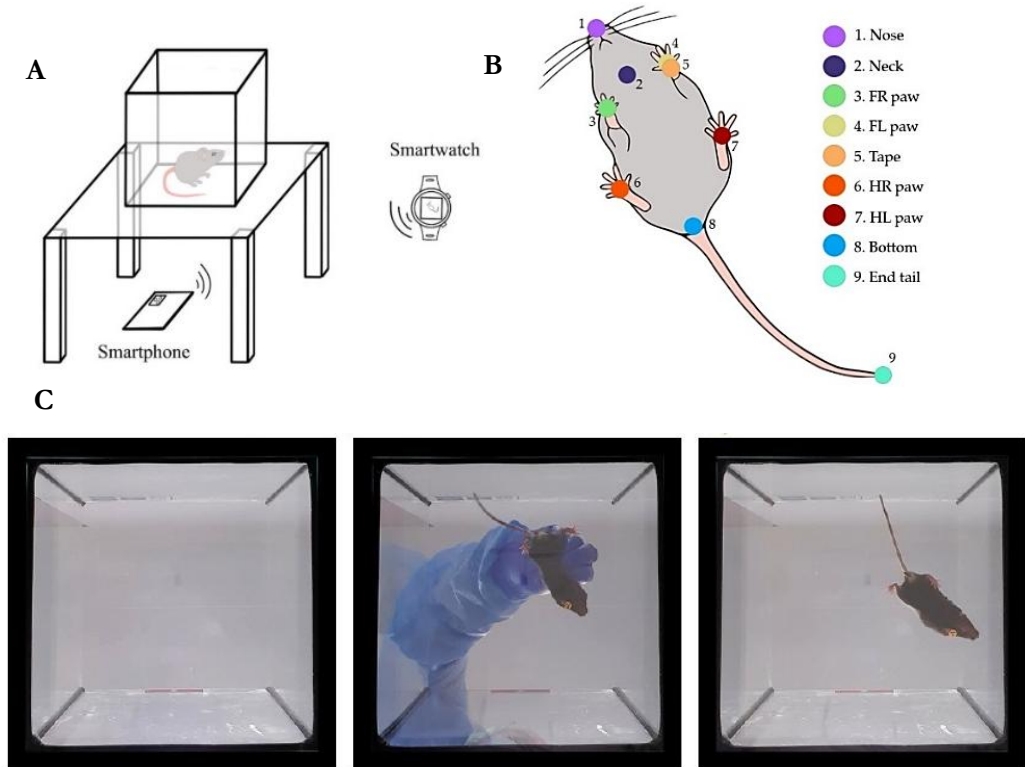


Figure 16. Automated setup and analysis pipeline for the tape removal test in mice. **(A)** Schematic representation in a transparent box, while their behavior during the tape removal test was recorded using a smartphone controlled remotely via a smartwatch. **(B)** Illustration of the anatomical body parts selected for labeling in the DeepLabCut project used for pose estimation and behavioral tracking. **(C)** Example of automated frame processing showing background removal outside the test box and identification of the frame in which the researcher's arm is no longer visible.

Finally, to assess labeling accuracy, a single random frame from each video was visually inspected by two independent reviewers who confirmed whether the predicted label positions aligned correctly with anatomical landmarks.

2.5.4.2. Post-Processing and feature extraction

The output data generated from DLC were further processed and analyzed using MATLAB R2022b (MathWorks; Portola Valley, CA, USA) and R version 4.2.2 (R Foundation; Vienna, Austria). Initially, DLC-generated coordinate points with confidence scores below 0.95 were excluded and replaced through linear interpolation to maintain data continuity. Following this, paw labels were reassigned, distinguishing left/right and fore/hind limbs, based on their positions relative to the nose and the bottom of the mouse's body in each frame. In parallel, the tail midpoint was computationally estimated using the coordinates of the tail base and tip, employing image-based algorithms to approximate this location for subsequent kinematic analysis.

To facilitate spatial quantification, all coordinate values were converted from pixel units to centimetres using the known dimensions of the testing chamber and the vertex positions of the box, which were also detected using DLC. With this transformation, pairwise distances between specific anatomical landmarks were calculated for each frame. Videos in which more than 10% of the frames showed implausible body part distances, for instance, exceeding biologically feasible thresholds, were excluded from downstream analyses to ensure data integrity.

One key metric extracted from the pose data was the time to remove the tape (TR time), which was algorithmically determined based on the trajectories and velocities of the tape, nose, and forepaws (see script [01_Features/tapeRemovalTime.m](#) in the [GitHub repository](#)). To validate this automatic method, TR times were compared to manually assessed values from trained behavioral researchers. Algorithm-derived values that fell within ± 2 seconds of the visual scores were considered accurate. All code used in data processing and behavioral feature extraction is openly accessible via the GitHub repository: https://github.com/nmrcadeb/DeepLabCut_to_predict_stroke_on_mice.

2.5.4.3. Computational prediction models

Two distinct computational models were developed to predict behavioral outcomes: one for the classification of stroke occurrence and another for the estimation of stroke severity, based on the percentage of brain volume affected (BVA). Behavioral variables were analyzed independently at each post-H/I time point (24, 48, and 72 hours), with only post-stroke data used for model training. Feature selection was performed using the least absolute shrinkage and selection operator (LASSO) regression. Logistic LASSO was employed for binary classification of stroke presence, while linear LASSO was used for continuous prediction of BVA.

Each LASSO regression was repeated 200 times using 5-fold cross-validation to ensure robustness and avoid overfitting. Predictor variables that were selected in more than 75% of these iterations were retained in the final models. Model performance was evaluated by training on randomly selected 80% subsets of animals and predicting outcomes on the remaining 20%. This process was repeated across 300 iterations to account for variability across training/test splits.

For the classification model, performance was assessed using specificity (SP), sensitivity (SE), accuracy (ACC), and both positive and negative predictive values (PPV and NPV). The regression model for stroke severity was evaluated using the coefficient of determination (R^2), adjusted R^2 , and root mean square error (RMSE), providing a comprehensive assessment of its predictive accuracy.

2.6. Sample processing

2.6.1. Plasma or serum collection

In the mouse models, blood was drawn at three time points: baseline (pre-surgery), post-injection, and 24 hours post-ICH from the submandibular vein. Plasma samples were obtained using ethylenediaminetetraacetic acid (EDTA)-K or lithium heparin-coated tubes (Microvette CB 300 EDTA or Microvette CB 300 lithium heparin; Sarstedt; Nümbrecht, Germany).

In the pig model, samples were drawn from the cranial vena cava at several time points: pre-intervention, and at 1 hour, 4 hours, 24 hours, 1 week, and 2 weeks post-ICH. For the sham

pigs, blood samples were collected at two specific time points: one hour prior to the onset of anesthesia (baseline) and at 4.5 hours, corresponding to the one-hour post-ICH time point in the experimental group.

Swine blood collection was performed with an 18 G needle inserted into the supraclavicular region of the cranial vena cava. Approximately 10 mL of blood was collected into two types of BD Vacutainer tubes (Becton Dickinson; Franklin Lakes, NJ, USA): SST II Advanced tubes for serum and K2-EDTA tubes for plasma.

For plasma collection, EDTA tubes, containing blood samples, were inverted to mix and then centrifuged at $2,500 \times g$ for 15 minutes at room temperature using an NF-400 benchtop centrifuge (Nüve, Ankara, Turkey). The supernatant was transferred to a new tube, centrifuged again under the same conditions, and the final plasma supernatant was aliquoted (0.5-1 mL) and stored at -80°C.

For serum preparation, blood samples in SST II Advanced tubes were left at room temperature for at least 30 minutes to allow clot formation, followed by centrifugation at $2,500 \times g$ for 15 minutes using the NF-400 benchtop centrifuge. The resulting serum was aliquoted and stored at -80°C.

2.6.2. Brain collection

Brain collection and sampling of the mice was performed at day 3 post-treatment. Mice were euthanized via cervical dislocation, and brains were rapidly extracted and sectioned into 2 mm-thick coronal sections using a brain coronal matrix (Harvard Apparatus; Massachusetts, USA). Both hemispheres and sides of each slice were photographed using a Samsung Note 10+ smartphone (Samsung; Suwon, South Korea) for infarct/hemorrhage quantification as described in **Section 2.8.1**.

For molecular analyses (real-time-quantitative polymerase chain reaction (RT-qPCR) and Western Blot (WB)), the third rostro-caudal 2 mm-slice, corresponding to peak lesion area, was bisected along the midline. Tissue was immediately snap-frozen in liquid nitrogen in Eppendorf tubes (Eppendorf; Hamburg, Germany), then lyophilized for 24 hours at -20 °C and 0.008 mbar using a freeze dryer (B.Braun; Melsungen, Germany), smashed until a fine powder was obtained, and finally stored at -80°C until use. This workflow ensured standardized and reproducible tissue collection while minimizing selection bias.

For immunohistofluorescence (IHF), the adjacent second rostro-caudal-2 mm slice (S2) was conserved in optimal cutting temperature compound (OCT; Sakura Finetek; Barcelona, Spain) and stored at -80°C. Cryosectioning was performed using a Leica CM1950 cryostat (Leica Biosystems; Nussloch, Germany), generating 15 μ m-thick sections mounted on Polysine® adhesion microscope slides (Menzel Gläser; Thermo Fisher Scientific). Sections were stored at -20°C until staining (**Figure 17**).

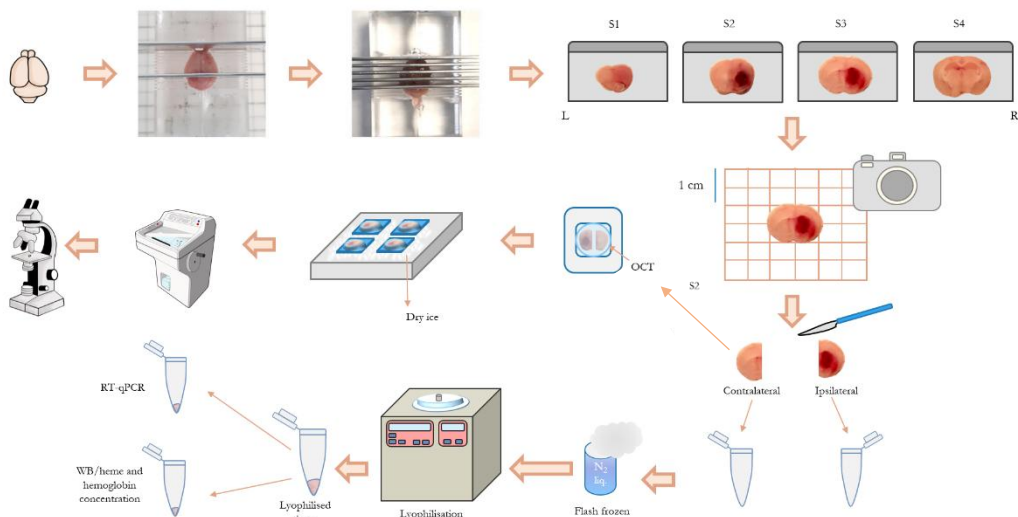


Figure 17. Overview of sample collection of the various *ex vivo* techniques following brain extraction. Abbreviations: Slice 1, 2, 3, and 4 (S1, S2, S3, and S4, respectively), optimal cutting temperature compound (OCT), real-time-quantitative polymerase chain reaction (RT-qPCR), and Western Blot (WB).

Fresh pig brains were placed in a brain slicer matrix and cut into 5 mm-thick coronal sections using a steel blade. These brain sections were then photographed using a Samsung Note 10+ smartphone. Next, the brain slices were fixed in a 4% paraformaldehyde solution (Thermo Fisher Scientific) prepared in 1X PBS and stored at 4°C for 1-5 days. After fixation, the hemispheres were separated and further divided to ensure the tissue fragments could fit on a standard microscope slide. Then, tissue fragments were gradually incubated in increasing concentrations of sucrose (Sigma-Aldrich) in 1X PBS (up to 30%) at 4°C for cryoprotection. Once the samples had fully sunk in the solution, they were carefully blotted dry using filter paper, transferred into embedding moulds, and embedded in OCT compound. For cryopreservation, the samples were snap-frozen by immersing them for 30 seconds in nitrogen-chilled isopentane (2-Methylbutane; Sigma-Aldrich). The frozen tissue blocks were stored at -80°C until further analysis.

2.7. Sample analysis

2.7.1. Specific analysis of pig blood samples

Blood samples were collected at five time points: before intervention, 1-hour post-hemorrhage induction, and at 24 hours, 7 days, and 14 days post-ICH. Samples were analyzed to assess systemic physiology and hematological profiles, including glucose, calcium, albumin, total protein, globulins, and various electrolytes. Hematological analyses included complete blood counts, hematocrit, hemoglobin, platelet counts, and leukocyte levels. Liver and kidney function markers, alanine aminotransferase (ALT), aspartate aminotransferase (AST), alkaline phosphatase (ALP), total bilirubin (TBIL), and blood urea nitrogen (BUN), were also evaluated.

2.7.2. Heme and hemoglobin concentrations

For biochemical assessment, mouse lyophilized brain tissue, standardized by packing an approximate equivalent amount of 1 mg of protein using the cut tip of a 1 mL pipette tip, was reconstituted in radioimmunoprecipitation assay (RIPA) buffer, composed of 20 mM Tris-Cl (pH 7.6), 137 mM NaCl, 2.6 mM KCl, 1% NP-40, 0.5% sodium deoxycholate, 0.1% SDS, 1X Complete EDTA-free protease inhibitor cocktail, and 1 mM PMSF (all reagents from Sigma-Aldrich). Protein concentration in the sample was determined using the Pierce™ bicinchoninic acid (BCA) protein assay kit (Thermo Fisher Scientific). Results were expressed as μ mol of analyte/g of total protein (see **Section 2.7.4.1.**).

From these reconstituted samples, hemoglobin and heme concentrations were measured using colorimetric assays according to the manufacturer's protocols: the QuantiChrom Heme Assay Kit (<https://bioassaysys.com/wp-content/uploads/DIHM.pdf>) and QuantiChrom Hemoglobin Assay Kit (<https://bioassaysys.com/wp-content/uploads/DIHIB.pdf>) (BioAssay Systems; Hayward, CA, USA).

2.7.3. Gene expression analysis by RT-qPCR

2.7.3.1. RNA isolation

Total ribonucleic acid (RNA) was isolated using the miRNeasy tissue/cells advanced mini kit (Qiagen; Hilden, Germany); all the specific materials (e.g., buffers, columns) were provided by the kit. Lyophilized brain tissues (corresponding to approximately 1 mg of protein)

from the ipsilateral and contralateral hemispheres were rehydrated separately in 450 μ L of the RLT buffer, supplemented with 0.01% β -mercaptoethanol. Homogenization was achieved by repeatedly passing the lysate through a 21G needle at least five times to ensure complete cell disruption and RNA release. Then, centrifuge the lysate for 5 min at maximum speed in the NF-400 benchtop centrifuge and collect the supernatant.

To remove genomic deoxyribonucleic acid (gDNA), 140 μ L of buffer AL was added to the supernatant and mixed thoroughly. The mixture was incubated at room temperature for 3 minutes, then loaded onto a gDNA eliminator spin column placed in a 2 mL collection tube. The column was centrifuged at 8,000 \times g for 30 seconds in the benchtop centrifuge and discarded once the flow-through was collected, ensuring that no liquid remained on the column membrane.

The resulting flow-through was transferred to a new 1.5 mL Eppendorf tube. To precipitate protein and other inhibitors, 20 μ L of buffer RPP was added. Samples were vortexed vigorously for at least 20 seconds and incubated at room temperature for 3 minutes. After centrifugation at 12,000 \times g for 3 minutes in the benchtop centrifuge, the supernatant was transferred to a new tube.

The volume of the sample was estimated, and isopropanol (1 volume) was added and mixed thoroughly. The solution was then loaded onto a RNeasy mini spin column placed in a 2 mL collection tube and centrifuged at 8,000 \times g for 15 seconds in the benchtop centrifuge. For samples exceeding 700 μ L, multiple loading steps were performed using the same column, discarding the flow-through between spins.

Subsequently, 700 μ L of buffer RWT were added to the column. The column was centrifuged for 15 seconds at 8,000 \times g, and the flow-through discarded. This step was repeated using 500 μ L of buffer RPE, followed by centrifugation under the same conditions. Finally, 500 μ L of 80% ethanol were pipetted, and the column was centrifuged for 2 minutes at 8,000 \times g.

The column was transferred to a new 2 mL collection tube and centrifuged at full speed for 1 minute. It was then placed in a fresh 1.5 mL collection tube, and RNA was eluted by applying 30 μ L of RNase-free water (Sigma-Aldrich) directly to the center of the membrane.

After a 1-minute incubation at room temperature, the column was centrifuged for 1 minute at full speed. RNA concentration and purity were assessed using a NanoDrop ND-1000 spectrophotometer (NanoDrop; Thermo Fisher Scientific).

Complementary DNA (cDNA) was synthesized using the QuantiTect reverse transcription kit (Qiagen), which includes a gDNA elimination step. All reactions were performed on ice unless otherwise specified.

To eliminate residual gDNA, RNA samples were adjusted to contain 500 ng of RNA in a final volume of 12 μ L using RNase-free water. To each reaction, 2 μ L of 7 \times gDNA wipeout buffer was added, yielding a total reaction volume of 14 μ L (**Table 11**). Samples were gently mixed and kept on ice.

Table 11. gDNA elimination

Component	Volume/reaction
gDNA wipeout buffer, 7 \times	2 μ L
Sample RNA	Volume of 500ng RNA
RNase-free water	Rest
Total volume	14 μL

Samples were incubated in a thermocycler at 42 °C for 2 minutes to allow gDNA digestion, then cooled to 4 °C and kept on ice for immediate reverse transcription.

2.7.3.2. Reverse transcription

A reverse transcription master mix (**Table 12**) was then prepared on ice for cDNA synthesis, except RNA, and scaled for the number of samples with an additional 10% volume to account for pipetting error.

Table 12. Reverse transcription master mix

Component	Volume/reaction	Volume for 5 reactions (+10%)
Quantiscript Reverse Transcriptase	1 μ L	5.5 μ L
Quantiscript RT Buffer, 5 \times	4 μ L	22 μ L
RT primer mix	1 μ L	5.5 μ L
Total volume	6 μL	33 μL

For the no-reverse transcription (NRT) control, reverse transcriptase was replaced with 1 μ L of RNase-free water (**Table 13.**):

Table 13. NRT control

Component	Volume/reaction
RNase-free water	1 μ L
Quantiscript RT buffer, 5x	4 μ L
RT primer mix	1 μ L
Total volume	6 μL

Each purified RNA sample received 6 μ L of the corresponding master mix (or NRT control mix), resulting in a final reaction volume of 20 μ L. Samples were gently mixed and kept on ice.

Reverse transcription was carried out at 42 °C for 15 minutes, followed by enzyme inactivation at 95 °C for 3 minutes, and finally cooled at 4°C. At the end, 80 μ L of RNase-free water was added to each tube to bring the final cDNA volume to 100 μ L. Samples were stored at -20 °C until further use.

2.7.3.3. Quantitative PCR

The resulting cDNA and negative control were subjected to qPCR. The cDNA was combined with LightCycler® 480 SYBR Green I master mix (Roche Applied Science; Penzberg, Germany) and gene-specific PrimeTime® qPCR mouse primers (Integrated DNA Technologies; Coralville, IA, USA) (**Table 14.**). All reagents and samples were briefly centrifuged before use to ensure contents were collected at the bottom of the tubes.

Table 14. PCR reaction mix

Component	Volume/reaction
SYBR Green I master mix, 2x	10 μ L
RNase-free water	8 μ L
Primers, 20x	1 μ L
Total volume	19 μL

A PCR master mix was prepared on ice for each primer pair and for all samples, including triplicates (technical replicates) and appropriate controls (Universal Reference, NRT, and no template control (NTC)).

A total of 19 μ L of the reaction mix was dispensed into each well of a LightCycler® 480 96-well multiwell plate, kept on ice. Then, 1 μ L of cDNA sample was added per well. Samples were mixed gently by pipetting up and down. The plate was sealed with LightCycler® 480 sealing foil and centrifuged at 1,000 \times g for 1 minute to eliminate air bubbles. Plates were stored on ice or at 4 °C until thermal cycling.

The qPCR was performed on a Roche LightCycler 480 I (Roche Applied Science) instrument using the following cycling conditions: initial denaturation at 95 °C for 5 minutes, followed by 45 cycles of 95 °C for 10 seconds, 60 °C for 10 seconds, and 72 °C for 10 seconds.

All reactions were run in triplicate. A melting curve analysis was performed to verify amplification specificity. No-template controls, substituting cDNA with RNase-free water, and positive controls using universal mouse reference RNA (Invitrogen; Waltham, MA, USA) were included in the assay.

Relative gene expression was quantified using the $\Delta\Delta C_p$ (crossing point) method, with glyceraldehyde-3-phosphate dehydrogenase (GAPDH) used as the internal reference mRNA. Primer sequences are provided in **Table 15**.

$\Delta\Delta C_p$ method:

- Calculate the mean C_p for the different technical replicates.
- Calculate ΔC_p :

$$\Delta C_p = C_p(\text{gene of interest}) - C_p(\text{Housekeeping})$$

- Calculate $\Delta\Delta C_p$:

$$\Delta\Delta C_p = \Delta C_p(\text{treatment}) - \Delta C_p(\text{control})$$

- Calculate Fold change:

$$\text{Fold change} = 2^{-\Delta\Delta C_p}$$

Table 15. Commercially available pre-designed qPCR primers from IDT

Gene	Protein	IDT name	Forward Primer	Reverse Primer
Aifm2	Ferroptosis suppressor protein 1 (FSP1)	Mm.PT.58.30983091	5'-GAC-CTTCTCATCTCCACAAAGC-3'	5'-GCCTCTCTTCCACAGTTAAC-3'
Ftl1	Ferritin light chain 1	Mm.PT.58.32413506.g	5'-GACTTAGAG-CAGCGCCTTG-3'	5'-GAAGCGAG-TACAGTGG-GAATC-3'
Gapdh	Glyceraldehyde-3-phosphate dehydrogenase	Mm.PT.39a.1	5'-AATGGTGAAGGTCGGTGTG-3'	5'-GTGGAGTCAT-ACTG-GAACATGTAG-3'
Gpx4	Glutathione peroxidase 4	Mm.PT.58.5454337	5'-CACTGTG-GAAATGGATGAAA GTC-3'	5'-CGCAGCCGTTCTTATCAATG-3'
Pcbp2	Poly(rC)-binding protein 2	Mm.PT.58.7663496	5'-CATTCCACAGCCAGATTGAC-3'	5'-CATGA-GAAGTAGTT-GAGCAGATG-3'
Slc11a2	Divalent metal transporter 1 (DMT1)	Mm.PT.58.16122997	5'-GCTTGCATCTTGCTGAAGTATG-3'	5'-CATGTCAGAAC-CAATGATTGCC-3'
Slc3a2	Solute carrier family 3 member 2	Mm.PT.58.41156435	5'-ACCTCAC-TCCCAACTACCA-3'	5'-CATTCATCAGCTTCCCACATC-3'
Trf	Transferrin	Mm.PT.58.23794874	5'-AGATAGAG-TGTGAGTCAG-CAGA-3'	5'-TCTCGTAG-TACTCTGCCATGA-3'
Tfrc	Transferrin receptor	Mm.PT.39a.22214833.g	5'-TCAA-GCCAGATCAG-CATTCTC-3'	5'-AGCCAG-TTTCATCTCCACATG-3'

Extracted from: ([García-Serran *et al.*, 2023](#))

2.7.4. Western Blot

2.7.4.1. SDS-polyacrylamide gel electrophoresis (SDS-PAGE)

Sodium dodecyl sulfate-polyacrylamide gel electrophoresis (SDS-PAGE), followed by Western blotting, is used to identify specific proteins using antibodies, after separating them based on their molecular weight.

SDS is a strong anionic detergent that denatures proteins. This is due to proteins binding to SDS within their hydrophobic regions and resulting in them becoming negatively charged. This allows SDS-highly negatively charged protein complexes to migrate directionally through the polyacrylamide gel under an electric field. In denaturing SDS-PAGE, protein migration is determined by molecular weight, not intrinsic electrical charge.

Brain protein homogenate preparation

Protein homogenates were prepared from lyophilized brain samples (see **Section 2.6.2.**), reconstructed at 4°C in RIPA buffer (20 mM Tris-Cl (pH 7.6), 137 mM NaCl, 2.6 mM KCl 1% NP-40, 0.5% sodium deoxycholate, 0.1% SDS, 1x complete EDTA-free protease inhibitor cocktail, 1 mM PMSF; all from Sigma-Aldrich). These protein homogenates were collected into microcentrifuge tubes, passed 7 times through a 23 G needle, and incubated on ice for 30 minutes. Lysates were then centrifuged at 12,000 \times g at 4°C for 15 minutes. The supernatant was carefully collected and transferred to new labeled microcentrifuge tubes. A 7 μ l aliquot was used for protein quantification. All aliquots were stored at -20°C until further analysis.

Protein concentration determination

Total protein concentration was determined using the BCA protein assay kit. This assay relies on biuret reaction: proteins reduce Cu²⁺ to Cu⁺, which then forms a purple complex by chelating bicinchoninic acid (BCA). This complex absorbs at 562 nm, and the absorbance correlates linearly with protein concentration across a defined. This allows the creation of a standard curve and the interpolation of absorbance values from the samples to determine their protein concentration.

Bovine serum albumin (BSA; Sigma-Aldrich) was used to prepare a standard curve with final concentrations of 2.0, 1.0, 0.5, 0.25, 0.125, and 0.0625 mg/mL. A blank with 1X only phosphate-buffered saline (PBS; provided by IGTP) was included.

For each sample, 2 μ L of each protein homogenate was diluted with 23 μ L of PBS, resulting in a total volume of 25 μ L. Duplicate 25 μ L aliquots of both standards and diluted samples were pipetted into a 96-well microplate. Then, 200 μ L of BCA working reagent (prepared at a 50:1 ratio of reagent A to reagent B provided in the kit) were added to each well. The plate was then covered and incubated at 37 °C for 30 minutes.

Absorbance was measured at 562 nm using a Varioskan® Flash microplate reader (Thermo Fisher Scientific). A standard curve was generated by plotting the average absorbance of the BSA standards versus their known concentrations (mg/mL). The protein concentration of each sample was determined by interpolating the corresponding absorbance value on the standard curve. Finally, the resulting concentration (in mg/mL) was corrected for the initial dilution by dividing by the dilution factor (12.5 \times).

Sample preparation

Brain protein homogenates were thawed on ice, and the volume required to load 30 μ g of protein per sample was taken and mixed with 4x Laemmli Sample Buffer (Bio-Rad Laboratories Inc.; Hercules, CA, USA), 2.5% 2-mercaptoethanol (Bio-Rad Laboratories Inc.) and deionized water to a final volume of 15 μ L. The mixtures were incubated at 95°C for 5 minutes to denature the proteins.

Plasma samples were diluted 1:15. Based on previous measurements, the expected endogenous concentration of transferrin in mouse plasma is similar to the one found in rat plasma (3.8 μ g/ μ L). After dilution, the final Tf concentration was estimated at 0.253 μ g/ μ L, which is approximately 0.5 μ g of transferrin per well.

Protein electrophoresis

Thirty μ g of total protein from brain homogenates or 0.26 μ L of plasma were loaded onto NuPAGE™ Midi 10% Bis-Tris (Invitrogen). Additionally, 2.5 μ L of precision plus protein™ dual color standards (Bio-Rad laboratories Inc.) were loaded at both the beginning and end of each gel to verify protein molecular weights. Polypeptides were separated by

electrophoresis using MOPS-SDS running buffer (50 mM MOPS, 50 mM Tris-Base, 0.1% SDS, 1 mM EDTA; pH 7.7; from Sigma-Aldrich) using an X-Cell4™ superlock midi gel system chamber (Thermo Fisher Scientific) at 200 V for 45 minutes. Upon completion, gels were removed and equilibrated in 1X Tris-glycine transfer buffer (27 mM Tris, 192 mM glycine, pH 8.3, with 20% methanol) for 15 minutes and then electroblotted (see **Section 2.7.4.3.**)

2.7.4.2. Urea-polyacrylamide gel electrophoresis (U-PAGE)

To determine transferrin saturation in plasma or serum samples, we developed a method for analysing the iron isoforms of transferrin by combining the urea-polyacrylamide gel electrophoresis (U-PAGE), based on the technique by Makey and Seal ([Makey and Seal, 1976](#)), with Western immunoblotting. This method separates transferrin obtained from serum or cell culture samples into the ATf form, two monoferric forms, and the diferric form based on their electrophoretic mobilities in U-PAGE gels.

Standards preparation

Human apotransferrin (hATf) and diferric holotransferrin (hHTf) (Sigma-Aldrich) were used as electrophoretic standards to identify transferrin isoforms. Because commercial mouse- and pig-specific standards are unavailable, we prepared apo- and holo-forms from the respective species' plasma or serum.

To prepare mouse-specific ATf and HTf standards, transferrin is either depleted of iron or fully saturated. In order to generate HTf, we followed a procedure described by Nagaoka *et al.* in 2000 with minor modifications ([Nagaoka and Maitani, 2000](#)). Five µL of plasma or serum were diluted in 10 mM Tris-HCl (pH 7.5) containing 25 mM sodium bicarbonate. A fresh Fe-citrate solution (25 mM) was added in either equimolar or 2:1 Fe:Tf ratios. The solution was mixed and incubated at room temperature for 1 hour to ensure full Fe-binding. The resulting mouse- and pig-ATf preparations were aliquoted and stored at -20°C until electrophoretic analysis.

To prepare apotransferrin, iron release is promoted. For this, plasma or serum samples were incubated in fresh iron removal buffer (IRB; 50 mM sodium acetate and 5 mM EDTA, pH 4.9; all reagents from Sigma-Aldrich) for 1 hour at room temperature, following the protocol

of Byrne and Mason (Byrne and Mason, 2009). Aliquots of the resulting ATf were also stored at -20°C until use.

U-PAGE Electrophoresis

Precast 6% TBE urea gels (U-PAGE; Invitrogen) were loaded with 0.26 µL of either mouse plasma or pig serum samples. Transferrin iron- isoforms are separated by electrophoresis in Tris-borate-electrophoresis buffer (100 mM Tris, 10 mM boric acid, pH 8.3) at 150 V for 2 hours at 4°C in a SuperLock™ mini gel system chamber (Thermo Fisher Scientific). After electrophoresis, gels were removed and rinsed for 10 minutes in 0.05% SDS and prepared for electroblotting (see **Section 2.7.4.3.**)

2.7.4.3. Electroblotting

Immobilon®-FL PVDF membranes (Polyvinylidene fluoride; Millipore) were cut to fit the dimensions of the gel, and activated in methanol for 30 seconds, rinsed in water for 2 minutes, and equilibrated in transfer buffer. Filter paper and fiber pads were also equilibrated by soaking them in the same buffer. The transfer “sandwich” was assembled with the PVDF membranes positioned adjacent to the polyacrylamide gel and oriented toward the anode, flanked by thick blotting filter paper (Bio-Rad Laboratories Inc.) and fiber pads. Protein transfers were carried out at 100 V for 1 hour at 4°C using the Mini Trans-Blot® Module (Bio-Rad Laboratories Inc.). Membranes were air-dried for at least 40 minutes before further processing.

However, in serum pig samples, prior to immunodetection, total protein staining was employed as a loading control using the Revert™ 700 total protein stain kit (Li-COR Biosciences). The PVDF membrane was briefly immersed in methanol, rinsed in MiliQ water, and equilibrated in 1X Tris-buffered saline (TBS) for 5 minutes. The membrane was then stained for 5 minutes with Revert™ 700 solution, followed by two 30-second washes in the kit’s wash solution. After a final MiliQ rinse, the membrane was scanned at 700 nm using the Odyssey® CLx imaging system (Model 9120; Li-COR Biosciences), ensuring the membrane remained moist during scanning.

De-staining was performed by shaking in Revert™ 700 de-staining solution for up to 10 minutes, followed by rinsing in MiliQ water. Membranes were subsequently blocked and processed (see **Section 2.7.4.4.**).

2.7.4.4. Immunodetection

Dried PVDF membranes were briefly rehydrated in methanol, rinsed in MiliQ water, and equilibrated in 1X TBS. Membranes are blocked in Intercept® (TBS) blocking buffer (Li-COR Biosciences; Lincoln, NE, USA) for 1 hour at room temperature.

After blocking, membranes were incubated overnight at 4°C with target-specific primary antibodies diluted in blocking buffer. The following day, the membranes were washed three times for 5 minutes each in TBS-T (1X TBS with 0.1% Tween® 20; Sigma-Aldrich) and then incubated for 1 hour at room temperature in the dark with near-infrared-conjugated secondary antibodies diluted in blocking buffer (see **Table 16.** for antibody list). All steps from this point onward were conducted under light-protected conditions.

Commercial secondary antibodies are solid-phase adsorbed to ensure minimal cross-reaction with serum proteins from several species, but not with serum proteins from pig. We developed an *in-house* solid-phase pre-adsorption using pig serum blotted onto PVDF membranes (retaining membrane). This method captures and retains antibodies that might cross-react with pig immunoglobulins. Before incubating with the membrane of interest (with the pig samples), secondary antibodies diluted in blocking buffer are incubated for 1 hour with the "retaining membrane."

After the incubation with the secondary antibody, membranes were washed again (three times for 5 minutes with TBS-T), rinsed in 1X TBS to remove residual detergent, and air-dried prior to imaging. Membranes are allowed to air-dry before imaging. Fluorescence was detected using the Odyssey® CLx imaging system at 800 nm. Band intensity was quantified using Image Studio Lite software (version 5.2; Li-COR Biosciences), measuring the integrated density of each band after subtracting background OD.

2.7.5. TSAT assessment

Baseline transferrin saturation (TSAT) levels were measured prior to intracerebral hemorrhage induction to confirm that mice exhibited physiologically relevant TSAT levels, consistent with typical human levels (<40%). Following stroke induction, TSAT was measured at 24, 48, and 72 hours post-ICH. For pig samples, TSAT measurements were taken at baseline, 1 hour, 4 hours, 24 hours, 1 week, and 2 weeks post-ICH.

Quantification of TSAT in the serum pig samples or plasma mice samples was determined using the OD obtained from the U-PAGE/WB bands (visualized on PVDF-LF membranes) and the formula used by Agarwal (Agarwal *et al.*, 2004):

$$TSAT (\%) = \frac{\left(\frac{1}{2} \times mFe\ Tf\ OD + diFe\ Tf\ OD\right) \times 100}{ATf\ OD + mFe\ Tf\ OD + diFe\ Tf\ OD}$$

However, in the experiment from **Manuscript I**, mice, after receiving IV exogenous human apotransferrin, the mixture of mouse and human iron-loaded transferrin forms present in the mouse blood determines a new transferrin saturation index that we named total TSAT. We used a modification of the Agarwal formula (previously used by DeGregorio-Rocasolano *et al.* (DeGregorio-Rocasolano *et al.*, 2018)) to calculate total TSAT in these samples using concentrations instead of OD as follows:

$$TSAT (\%) = \frac{\left(\frac{1}{2} \times \text{total } mFe\ Tf + \text{total } diFe\ Tf\right) \times 100}{\text{total } ATf + \text{total } mFe\ Tf + \text{total } diFe\ Tf}$$

Where:

- Total ATf is the concentration of mouse apotransferrin + concentration of human apotransferrin
- Total mFe Tf is the concentration of mouse monoferric transferrin + concentration of human monoferric transferrin
- Total diFe Tf is the concentration of mouse diferric transferrin + concentration of human diferric transferrin

Concentrations in the formula were obtained using:

1. The mean concentration of mouse endogenous transferrin was 5.4 mg/mL (determined in previous experiments of the group). The human transferrin concentration in blood was 3.4 mg/mL, because 230 mg/kg were injected into the mice.
2. The OD of each one of the mouse transferrin iron isoforms and each one of the human transferrin iron isoforms present in a given sample, loaded in a U-PAGE/WB.

2.7.6. Platelet Factor 4 detection by ELISA

The detection of pig platelet factor 4 (PF4) was made using pig plasma samples by enzyme-linked immunosorbent assay (ELISA) following manufacturer instructions (MBS2701434, 96 Tests; MyBiosource Inc.; San Diego, CA, USA).

2.7.7. Immunohistofluorescence

Frozen pig and mouse brain tissues were cryosectioned into 15 μ m-thick slices using a Leica CM1950 cryostat (Leica Biosystems; Deer Park, TX, USA) and mounted onto poly-L-lysine-coated glass slides (Menzel-Gläser Polysine slides; Thermo Fisher Scientific).

The tissue sections were first left at room temperature to adhere properly to the slides and then stored at -20°C until further processing. Prior to staining, slides were equilibrated to room temperature for 15 minutes, followed by heating at 50°C for 30 minutes, and then returned to room temperature for an additional 15 minutes. Tissue fixation was carried out by incubating the slides in 4% paraformaldehyde in PBS (Thermo Fisher Scientific) for 20 minutes. Rehydration was performed through a graded ethanol series (100%, 95%, 70%, 50%) with brief 30-second immersions, followed by rinsing in 1X PBS.

To permeabilize the tissue, sections were washed three times for 5 minutes each in 0.25% Triton X-100 (Prolabo; Paris, France) prepared in 1X PBS. Antigen retrieval was then achieved by heating the slides in citrate buffer (pH 6; Sigma-Aldrich) at 95°C for 20 minutes. After cooling, the sections were washed three times in 20 mM glycine (Thermo Fisher Scientific) in 1X PBS. Blocking was performed at room temperature for 1 hour using a solution containing 3% (w/v) BSA (Sigma-Aldrich); 5% normal donkey serum (Sigma-Aldrich); and 0.25% Triton X-100 in 1X PBS. This was followed by a single 5-minute wash in 20 mM glycine before incubating the sections overnight at 4°C with primary antibodies diluted in a buffer containing 0.025% Triton X-100 and 3% normal donkey serum in PBS (200 μ L/slide).

After primary antibody incubation, the sections were washed three times in 20 mM glycine before being exposed to secondary antibodies for 2 hours at room temperature in the dark (see **Table 16.** for antibodies list). Post-secondary incubation, slides were washed three times with 1X PBS, then counterstained with Hoechst 33342 (0.4 μ g/mL in 1X PBS; Invitrogen; Waltham, MA, USA) for 10 minutes to visualize cell nuclei. Following three additional washes with 20 mM glycine were performed. Then, the sections were dehydrated via a graded

ethanol series (50%, 70%, 90% and 100%, 30 seconds each), and coverslips were applied using FluoromountTM mounting medium (Sigma-Aldrich). Coverslips were sealed with clear nail polish to preserve the aqueous mounting.

For broader visualization, in the mouse samples, neuronal nuclei (NeuN) immunohistochemistry was performed on brain sections and analyzed using the Odyssey imaging system using infrared secondary antibodies listed in **Table 16**. Slices were incubated with anti-NeuN primary antibody followed by a near-infrared-conjugated secondary antibody compatible with Odyssey Imaging. Areas lacking NeuN staining, particularly those overlapping with hematoma sites, were indicative of neuronal loss. Cortical regions surrounding the hematoma, identified using anatomical references such as the *corpus callosum* and lateral ventricles, were examined for peri-infarct damage. In these regions, 4-hydroxynonenal (4-HNE) immunoreactivity was evaluated specifically within NeuN-positive neurons across serial sections.

After the broader visualization, in mouse slides, fluorescence imaging was performed on an AxioObserver Z1 microscope (Carl Zeiss; Oberkochen, Germany) at the IGTP Microscopy Platform Core Facility, with a 40x/1.3 plan objective and using the secondary antibodies coupled with widefield fluorophores (Alexa FluorTM; listed in **Table 16**), and image analysis was carried out using ImageJ software. These images were then used for quantification.

For pig slides, images were acquired using the ZEISS Axioscan 7 (Carl Zeiss Microscopy GmbH; Jena, Germany) equipped with a 20x/0.8 objective. Fluorophores were excited with LED-modules and excitation and emission filters isolated the fluorescence bands.

2.7.8. Antibodies

The primary and secondary antibodies utilized for IHF and WB are listed below (**Table 16**):

Table 16. List of antibodies used by experimental method

Primary antibody	Dilution	Method	RRID/Ref.	Company
Mouse anti-transferrin receptor (H68.4) (TfR)	1:1,000	WB	AB_2533029	Thermo Fisher Scientific (Waltham, MA, USA)
Mouse anti-glyceraldehyde-3-phosphate dehydrogenase (GAPDH)	1:2,000	WB	AB_2536381	

Materials and Methods

Rabbit anti-ferritin light chain	1:1,000	WB	AB_1523609	Abcam (Cambridge, UK)
Rabbit anti-glutathione peroxidase 4 (GPX4)	1:2,000	WB	AB_10973901	
Rabbit anti-4-hydroxynonenal (4-HNE)	1:100	Mouse IHF	AB_722490	
Goat anti-mouse transferrin (mTf)	1:1,000	WB	AB_1147328	Novus Biologicals (Centennial, CO, USA)
Rabbit anti-xCT complex (SLC7A11 subunit - solute carrier family 7 member 11)	1:1,000	WB	AB_2239445	
Mouse anti-neuronal nuclei (NeuN)	1:100	Mouse and pig IHF	AB_2298772	Sigma-Aldrich (Saint Louis, MO, USA)
Mouse anti-NRAMP 2 (G-5), so called divalent metal transporter 1 (DMT1)	1:200	WB	AB_10610255	Santa Cruz Biotechnology (Dallas, TX, USA)
Mouse anti-human transferrin (Tf) (GMA-099)	1:250	WB	Lot#109052B	Green Mountain Antibodies (Burlington, VT, USA)
Rabbit anti-rat Tf	1:150 / 1:50	WB/pig IHF	Cat#55729	Cappel, ICN Pharmaceuticals (Costa Mesa, CA, USA)
Rabbit anti-pig ferritin (FTH)	1:50	Pig IHF	ABIN7440041	Antibodies online (Limerick Township, PA, USA)

Seconday antibody	Dilution	Method	RRID	Company
IRDye-800CW donkey anti-mouse	1:25,000	WB/IHF	AB_2716622	Li-COR Bioscience (Lincoln, NE, USA)
IRDye-680RD donkey anti-rabbit	1:15,000	WB/IHF	AB_2716687	
IRDye-680RD donkey anti-goat)	1:10,000	WB	AB_2650427	
Donkey anti-rabbit IgG (H+L) Alexa Fluor TM 555	1:500	Mouse IHF	AB_162543	Thermo Fisher Scientific (Waltham, MA, USA)
Donkey anti-mouse IgG (H+L) Alexa Fluor TM 555	1:500	Mouse IHF	AB_141607	
Donkey anti-mouse IgG (H+L) Alexa Fluor TM 647 (A-31571)	1:500	Pig IHF	AB_162542	
Donkey anti-rabbit IgG (H+L) Alexa Fluor TM 488 (A-21206)	1:500	Pig IHF	AB_2535792	

Extracted and modified from: ([García-Serran *et al.*, 2023](#))

2.8. Lesion quantification

In mice models, at 72 hours post-treatment, infarct and hemorrhage volumes were quantified. However, hemorrhage extension was measured via MicroCT system at 0.5, 1.5, 5, and 24 hours after ICH-collagenase-induced. In hemorrhagic pigs, hemorrhage volumes were measured at 4 hours, 24- or 2-weeks post-ICH via MRI.

2.8.1. *Ex vivo* lesion quantification

For infarct quantification, fresh brains were obtained as in **Section 2.6.2.** and were coronally sectioned into 2 mm-thick slices and incubated in 1% 2,3,5-triphenyltetrazolium chloride (TTC) (Sigma-Aldrich) prepared in PBS at 37°C for 11 minutes. TTC reacts with active mitochondrial enzymes, staining viable tissue red, while infarcted areas remain white ([Beder-son *et al.*, 1986](#)) (**Figure 18A.**).

Digital photographs of the serial slices were taken. From each image we measured the area of infarcted tissue (white), the area corresponding to the ipsilateral hemisphere (Ipsi) and the area corresponding to the contralateral hemisphere (Contra) using ImageJ software (version 1.53; Wayne Rasband, NIH; Bethesda, MD, USA).

Conversely, hemorrhagic volume was assessed in unstained brain sections. Digital photographs of the serial slices were taken. From each image we manually outlined the blood-filled regions as well as the area corresponding to the Ipsi and the area corresponding to the Contra. These areas were analyzed using the ImageJ software following established protocols (Zhang *et al.*, 2022) (Figure 18D.).

For each section, the infarct/hemorrhagic (lesion) area, the total area of the ipsilateral, and the contralateral and were determined in mm^2 , and the volume was calculated in mm^3 by considering section thickness. The final lesion volume (mm^3) resulted from the sum of the lesion volumes of all sections corrected by the ratio of the total volume of the contralateral hemisphere to that of the ipsilateral one; that is, corrected by edema. The final lesion volume results are given as % of the ipsilateral hemisphere (Figure 18D.).

The edema was determined as a percentage of the subtraction of ipsilateral hemisphere volume from the of the contralateral one divided by the addition of both volumes.

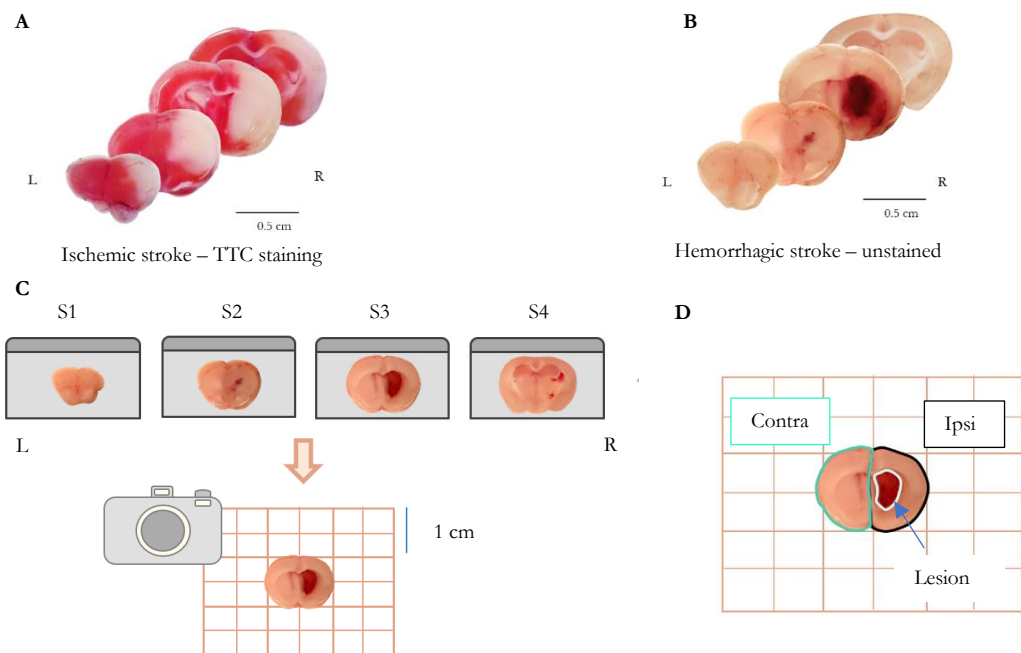


Figure 18. Brain slicing for stroke models and stroke volume measurement. (A) 2-mm-thick coronal slices of an ischemic mouse brain stained with 1% 2,3,5-triphenyltetrazolium chloride (TTC). (B) 2-mm-thick coronal slices of a hemorrhagic stroke mouse brain, unstained. (C) Schematic representation of the slices of the brain after slicing and the matrix used for positioning. (D) Illustration of the manual delineation of the brain hemispheres (ipsilateral, Ipsi and contralateral, Contra) and the stroked area (lesion). Abbreviations: Section 1, 2, 3, and 4 (S1, S2, S3, and S4, respectively).

2.8.2. MicroCT system, acquisition and reconstruction parameters

Hematoma progression was monitored using *in vivo* MicroCT imaging (SkyScan 1076; Bruker; Kontich, Belgium) with the administration of the contrast agent Viscover Ex-iTronTM nano 12000 (Viscover; Berlin, Germany) (Figure 19.). Imaging revealed hematoma stabilization within the first five hours following induction. For MicroCT acquisition, mice were anesthetized with isofluorane (4% for induction, 1.5% for maintenance) delivered in oxygen at a flow rate of 1 L/min.

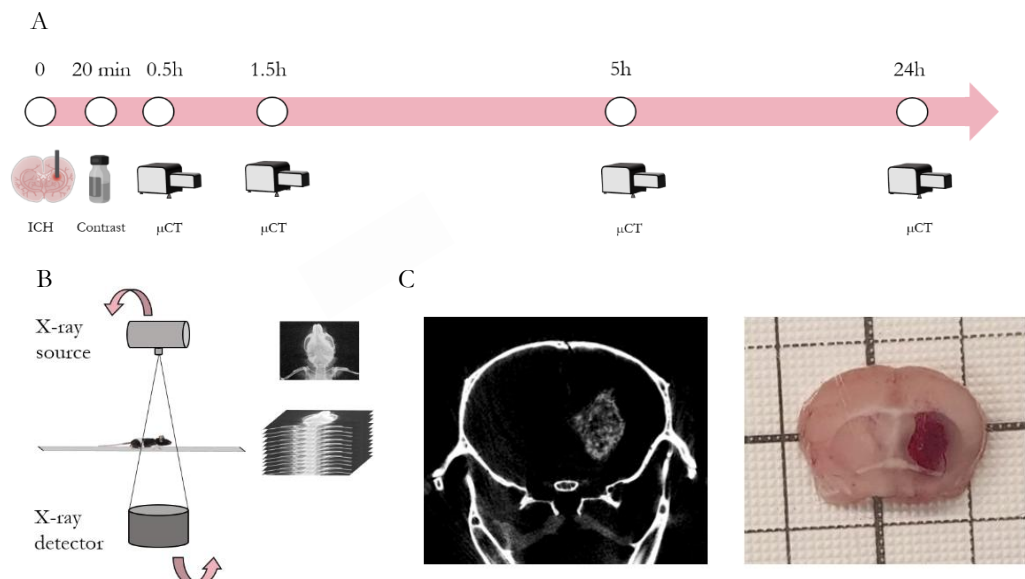


Figure 19. (A) Diagram of the assessment of hemorrhagic growth expansion in the collagenase-induced ICH model. (B) Schematic representation of the function of the MicroCT. (C, left) reconstructed images obtained and (C, right) sliced brain corresponding to the reconstructed image.

Specific parameters of the MicroCT system, acquisition and reconstruction are specified in Table 17.

Table 17. MicroCT specific parameters

System	
Parameter	Value
Scanner	Skyscan1076
Instrument SN	09H02068
Hardware	C
Secure mode	OFF
Software	Version 3.2 (build 1)
Home Directory	C:\Skyscan
Tube	Hamamatsu 100/250

Materials and Methods

Camera	Princeton Instruments (Trenton, NJ, USA)
Camera Pixel Size (μm)	12.32
Camera X/Y Ratio	1.0067
Acquisition	
Parameter	Value
Source Voltage (kV)	59
Source Current (μA)	167
Filter	No filter
Object to Source (mm)	121.000
Camera to Source (mm)	165.000
Number Of Files	494
Number Of Rows	1336
Number Of Columns	2000
Optical Axis (line)	650
Image Pixel Size (μm)	17.7700
Image Format	TIFF
Depth (bits)	16
Data Offset (bytes)	264
Horizontal overlap (pixel)	0
Camera horizontal position	Center
Visual Camera	ON
Screen LUT	0
Exposure (ms)	160
Rotation Step (deg)	0.400
Frame Averaging	On (4)
Scanning position	141.150 mm
Suggested beam-hardening correction	10
Suggested HU-Calibration	86,000
Number of connected scans	2
Number of lines to be reconstructed	703
Use 360 Rotation	NO
Rotation Direction	CC
Scanning Trajectory	ROUND
Type Of Motion	STEP AND SHOOT
Camera Offset	OFF
Scanning Start Angle	0.000
Scan duration	00:29:05
Reconstruction	
Parameter	Name
Reconstruction Program	NRecon (Micro Photonics; Allentown, PA, USA)
Program Version	Version: 1.7.0.4
Program Home Directory	C:\Skyscan
Reconstruction engine	NReconServer (Micro Photonics)
Engine version	Version: 1.7.0
Reconstruction from batch	No
Postalignment	-50.50 (this value can vary depending acquisition)
Reconstruction servers	I11073
Reconstruction mode	Standard
Dataset Origin	Skyscan1076
Section to Section Step	1
Sections Count	526

Result File Type	BMP
Result File Header Length (bytes)	1,134
Result Image Width (pixels)	2,000
Result Image Height (pixels)	2,000
Pixel Size (μm)	17.77462
Reconstruction Angular Range (deg)	197.60
Use 180+	OFF
Angular Step (deg)	0.4000
Smoothing	3
Smoothing kernel	0 (Asymmetrical boxcar)
Ring Artifact Correction	20
Draw Scales	ON
Object Bigger than FOV	ON
Reconstruction from ROI	OFF
Filter cutoff rel. to Nyquist freq. (%)	100
Filter type	0
Filter type description	Hamming (Alpha=0.54)
Undersampling factor	1
Threshold for defect pixel mask (%)	0
Beam Hardening Correction (%)	56
CS Static Rotation (deg)	0.00
Min for CS to Image Conversion	0.015986
Max for CS to Image Conversion	0.080390
HU Calibration	OFF
BMP LUT	0
Cone-beam Angle Horizontal (deg)	16.713697
Cone-beam Angle Vertical (deg)	11.208715

2.8.2.1. CT lesion quantification

The quantification of the CT lesion was performed using 3 different ways:

- Same as the *ex vivo* quantification (see **Section 2.8.1.**).
- Using the $s \frac{ABC}{2}$. In this formula, A is the biggest hemorrhagic diameter on the CT, B is the largest transverse diameter measured at 90° perpendicular to A, and C is the number of CT slices with hemorrhage multiplied by the slice thickness (**Figure 20.**) (Kwak, Kadoya and Suzuki, 1983).
- Using the $\frac{ABC}{2}$. Here, A and B are defined as in the $sABC/2$, however C not only considers the number of cuts on the CT where the hemorrhage is present, but also the size of the hemorrhage area in each cut. Depending on the percentage of the hemorrhagic area observed in the current slice compared to the largest hemorrhagic area noted it is counted as either a complete, half, or it is not considered as a hemorrhage slice. If a slice's hemorrhage area is

more than 75% of the largest hemorrhagic area, it is counted as one complete hemorrhage slice for C. If the area is around 25 to 75% of the largest hemorrhage, the slice is considered half a hemorrhage slice. And finally, if the area is less than 25% of the largest hemorrhage, the slide is not considered a hemorrhage slice in the calculation (**Figure 20C.**) (Kothari *et al.*, 1996).

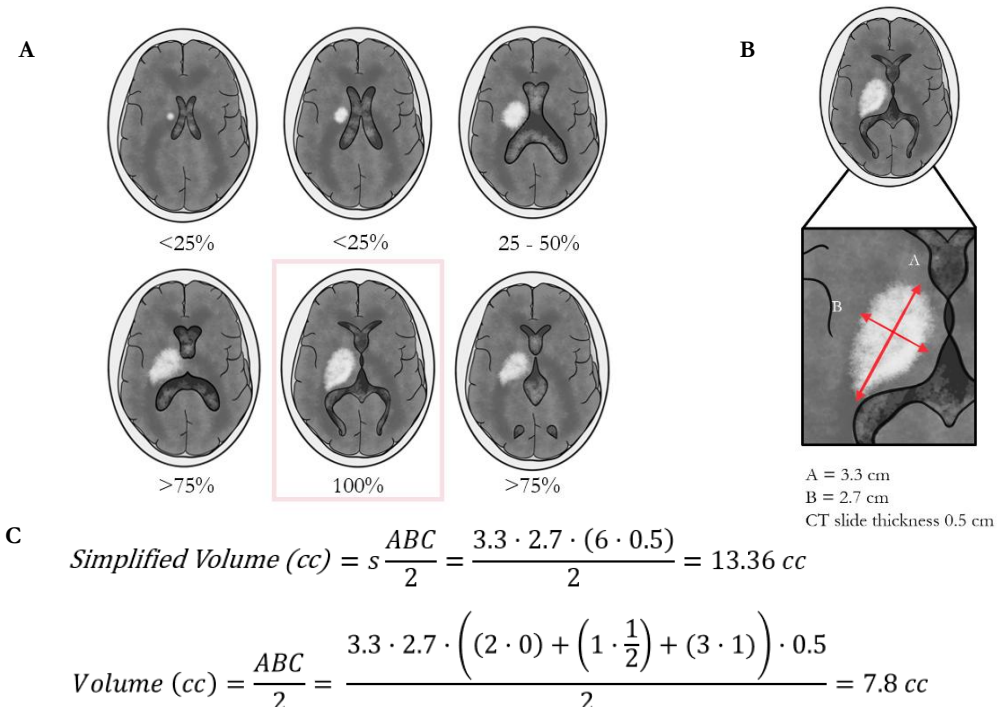


Figure 20. Schematic representation of the assessment and calculation of intracerebral hemorrhage (ICH) volume using drawn computed tomography (CT) brain cuts. **(A)** Dorsal views of different brain cuts as seen in a CT scan. A white area is present in the thalamus, representing a hemorrhage. Below each drawing there is a percentage indicating the relative size of the hemorrhage in comparison to the cut with the largest hemorrhage, which is marked with 100% and surrounded by a pink square. **(B)** Drawing of the cut with the largest hemorrhage, with an amplified view of the hemorrhage where two perpendicular red arrows are shown together with its measures. **(C)** Mathematical formulas used to calculate the ICH volume. The first formula is the simplified $sABC/2$ formula, where A is the largest hemorrhagic diameter, B is the largest transverse diameter perpendicular to A, and C is the number of CT slices with hemorrhage multiplied by the slice thickness. The second formula is the $ABC/2$ formula, where A and B are defined in the same way, but C takes into account both the number of slices with hemorrhage and the size of the hemorrhagic area in each slice. The slice is categorized based on the proportion of the hemorrhagic area observed compared to the largest hemorrhage, classifying it as either full (1 when is higher than 75%), partial (1/2 when is between 25 and 75%), or not considered (0 when is less than 25%) as a hemorrhage slice. A numerical example is provided in both, demonstrating how the ICH volume is measured using the data from part A and B of the figure.

2.8.3. Magnetic resonance imaging

MRI scans were performed using a Vantage Galan 3T scanner (Canon Medical Systems). The initial imaging session took place 90 minutes after hemorrhage induction, with follow-up scans at 24 hours, 1 week, and 2 weeks post-ICH for animals with lobar hemorrhages. The MRI protocol included sequences such as T2*-weighted imaging (T2*), diffusion tensor imaging (DTI), 3D flow-sensitive black blood imaging (FSBB), fluid-attenuated inversion recovery (FLAIR), and apparent diffusion coefficient (ADC) mapping (**Table 18**).

T2*-weighted images were utilized for the measurement of hemorrhagic volume using 3D Slicer software v5.6.1 (<https://www.slicer.org/>). Additionally, diffusion-weighted imaging (DWI) and DTI maps were generated from the DTI sequence using Olea Sphere 3.0-SP22 (Olea Medical; La Ciotat, France) software.

Table 18. MRI sequences and specifications

Sequence	FOV (mm)	Matrix (mm)	TR (ms)	TE (ms)	TI (ms)	Flip angle	Slice thickness (mm)	In-plane resolution (mm)
T1w	100x171	176x304	700	9	-	70	3	0.28x0.28
T2w (axial)	100x170	224x384	5300	105	-	90	3	0.22x0.22
FLAIR	100x170	128x192	8000	120	2200	90	3	0.39x0.39
T2*	100x170	240x256	600	12	-	20	3	0.21x0.21
DTI	170x105	80x168	6799	90	-	90	2	0.51x0.51
FSBB	100x169	144x240	39	30	-	10	1	0.35x0.35
3D TOF	155x155	256x256	23	3.9	-	15	0.6	0.30x0.30

2.8.3.1. MRI lesion quantification

Hemorrhage lesion volume was quantified using axial T2*-weighted MRI DICOM images analyzed in 3D Slicer. Hypointense regions representing hemorrhages were manually delineated in all the supratentorial planes for the scans acquired at 90 minutes and 24 hours after stroke, as well as hyperintense/hypointense regions observed at 2 weeks after ICH induction. Volumes were expressed in milliliters (mL) and as a percentage of the ipsilateral hemisphere. *Ex vivo* volume measurements were performed as described in **Section 2.8.1**, and also expressed as a percentage of total brain volume for comparison with MRI-based estimates.

2.9. Distribution of the animals

For the **first manuscript**, animals were randomized before distributing them in the experimental groups.

Animals in the **second manuscript** were classified based on post-mortem stroke size analysis using TTC staining. Mice were categorized into either a stroke (S) or no stroke (NS) group depending on the presence or absence of an infarct. Subsequently, mice within the stroke group were further subdivided into mild stroke (MS) or severe stroke (SS) based on infarct volume. An infarct involving less than 28% of the affected brain hemisphere was classified as mild, whereas an infarct equal to or exceeding this threshold was classified as severe.

2.10. Statistics

For the **first manuscript**, all statistical evaluations were performed using GraphPad Prism 9 (Dotmatics; Boston, MA, USA). Depending on the data distribution and comparison type, *t*-tests or one-way ANOVA (with Tukey's multiple comparisons) were applied. Normality was verified; log transformations were used when needed. Statistical significance was set at $p<0.05$. Results are shown as mean \pm standard error of the mean (SEM).

For the **second**, both observationally and algorithmically derived data were analyzed using one-way ANOVA, with statistical significance set at $p<0.05$. LASSO regression was used for feature selection and model construction. All quantitative results are presented as means \pm SEM.

Finally, in the **third manuscript**, statistical analyses were conducted using GraphPad Prism version 10. For datasets involving multiple time point comparisons, repeated-measures two-way ANOVA was performed, followed by Tukey's post-hoc test where applicable. Statistical significance was defined as $p<0.05$. All quantitative data are presented as means \pm SEM.

RESULTS

MANUSCRIPT I

Targeting Pro-Oxidant Iron with Exogenously Administered Apo-transferrin Provides Benefits Associated with Changes in Crucial Cellular Iron Gate Protein TfR in a Model of Intracerebral Hemorrhagic Stroke in Mice

Antioxidants (Basel) (2023)

Antioxidants. 2023; 12(11):1945. DOI: [10.3390/antiox12111945](https://doi.org/10.3390/antiox12111945)

Article

Targeting Pro-Oxidant Iron with Exogenously Administered Apotransferrin Provides Benefits Associated with Changes in Crucial Cellular Iron Gate Protein TfR in a Model of Intracerebral Hemorrhagic Stroke in Mice

Alexia García-Serran ¹, Jesús Ordoño ¹, Núria DeGregorio-Rocasolano ¹, Marc Melià-Sorolla ¹, Karla Odendaal ^{1,2}, Octavi Martí-Sistac ^{1,3*} and Teresa Gasull ^{1*}

¹ Cellular and Molecular Neurobiology Research Group, Department of Neurosciences, Germans Trias i Pujol Research Institute, 08916 Badalona, Catalonia, Spain; agarciash@igtp.cat (A.G.-S.); jesus.ordono@imdea.org (J.O.); ndgregorio@igtp.cat (N.D.-R.); mmelia@igtp.cat (M.M.-S.); kk.o@btinternet.com (K.O.)

² School of Biosciences, University of Cardiff, Cardiff CF10 3AT, UK

³ Department of Cellular Biology, Physiology and Immunology, Universitat Autònoma de Barcelona, 08193 Bellaterra, Catalonia, Spain

* Correspondence: octavi.marti@ub.cat (O.M.-S.); tgasull@igtp.cat or teresagasull@yahoo.com (T.G.); Tel.: +34-93-0330-531 (T.G.)



Citation: García-Serran, A.; Ordoño, J.; DeGregorio-Rocasolano, N.; Melià-Sorolla, M.; Odendaal, K.; Martí-Sistac, O.; Gasull, T. Targeting Pro-Oxidant Iron with Exogenously Administered Apotransferrin Provides Benefits Associated with Changes in Crucial Cellular Iron Gate Protein TfR in a Model of Intracerebral Hemorrhagic Stroke in Mice. *Antioxidants* **2023**, *12*, 1945. <https://doi.org/10.3390/antiox12111945>

Academic Editors: Syed Shadab Raza and Johannes Boltze

Received: 13 August 2023

Revised: 29 September 2023

Accepted: 9 October 2023

Published: 31 October 2023



Copyright: © 2023 by the authors. Licensee MDPI, Basel, Switzerland. This article is an open access article distributed under the terms and conditions of the Creative Commons Attribution (CC BY) license (<https://creativecommons.org/licenses/by/4.0/>).

Abstract: We have previously demonstrated that the post-stroke administration of iron-free transferrin (apotransferrin, ATf) is beneficial in different models of ischemic stroke (IS) through the inhibition of the neuronal uptake of pro-oxidant iron. In the present study, we asked whether ATf is safe and also beneficial when given after the induction of intracerebral hemorrhage (ICH) in mice, and investigated the underlying mechanisms. We first compared the main iron actors in the brain of IS- or collagenase-induced ICH mice and then obtained insight into these iron-related proteins in ICH 72 h after the administration of ATf. The infarct size of the IS mice was double that of hemorrhage in ICH mice, but both groups showed similar body weight loss, edema, and increased ferritin and transferrin levels in the ipsilateral brain hemisphere. Although the administration of human ATf (hATf) to ICH mice did not alter the hemorrhage volume or levels of the classical ferroptosis GPX4/system xc⁺pathways, hATf induced better neurobehavioral performance, decreased 4-hydroxyynonenal levels and those of the second-generation ferroptosis marker transferrin receptor (TfR), and restored the mRNA levels of the recently recognized cytosolic iron chaperone poly(RC) binding protein 2. In addition, hATf treatment lowered the ICH-induced increase in both endogenous mouse transferrin mRNA levels and the activation of caspase-2. In conclusion, hATf treatment provides neurobehavioral benefits post-ICH associated with the modulation of iron/oxidative players.

Keywords: ischemic stroke; intracerebral hemorrhage; iron; oxidation; apotransferrin; mouse

1. Introduction

A global consensus exists throughout the literature reporting the detrimental effects of systemic iron overload in ischemic stroke, and the protective effect of iron chelators and the iron-binding protein apotransferrin (ATf) in ischemic stroke models [1–3] and ischemic stroke patients [4]. Moreover, iron chelators and Tf have been studied as neuroprotectors in hemorrhagic stroke models. Chen-Roetling *et al.* reported the protective effect of Tf in cortical neurons [5], and deferoxamine has been reported to be beneficial in hemorrhagic stroke patients [6,7]. In preclinical studies, our laboratory has shown that Tf, the iron-free form of transferrin (Tf), is a potent neuroprotective agent in ischemic stroke because it reduces the saturation of blood transferrin with iron (TSAT) and inhibits the entry of iron-Tf into the neurons [3].

Intracerebral hemorrhage (ICH), besides the damage it induces through an increase in intracranial pressure derived from a sudden accumulation of spilled blood in the brain parenchyma, brings about toxic effects produced by substances of the leaked blood [8,9]. In particular, the breakdown of erythrocytes leads to the release of hemoglobin, from which heme and, ultimately, high amounts of iron are released to the cerebral parenchyma [10–12]. These compounds lead to oxidative stress, blood–brain barrier disruption, and the activation of different death pathways in the hematoma and perihematomal regions that lead to neuronal death [13,14].

Ferroptosis, a non-apoptotic and iron-dependent programmed cell death [15], has been described as playing a crucial role, especially at early time points, in the ICH model induced by collagenase [16]. Nevertheless, contrasting results have been reported regarding the effect of ICH on the expression of some iron- and classical ferroptosis-related proteins [17–19]. Such discrepancies might be due, at least in part, to the severity of the model and experimental design/time course or the brain region analyzed. Alternatively, beyond the classical ferroptotic mechanisms directly linked to iron and loss of reactive oxygen species (ROS) detoxifying potential, the ferroptosis field is evolving and the most recently discovered ferroptotic pathways might have specific roles that have not yet been identified.

To date, the whole picture of the mechanisms driving hemorrhagic stroke damage is still far from complete. Specifically, the therapeutic potential and safety profile of Tf in hemorrhagic stroke is not known, although ferroptosis, an iron-mediated type of cell death, has been previously suggested to be implicated [16]. We hypothesized that Tf, which has demonstrated benefits in ischemic stroke, could reduce the detrimental consequences of ICH and, thus, is a potential pre-hospital and pre-triage frontline treatment for stroke patients. The present work aimed to investigate (1) the effect of early treatment with Tf on the hematoma size, antioxidant status, and neurological outcome in a mouse model of ICH, and (2) the effect of ICH and Tf on the levels and expression of iron- and ferroptosis-related molecules relevant in stroke.

2. Materials and Methods

2.1. Animals

Adult 9-week-old male C57BL/6J mice purchased from Charles River Laboratories were used in this study. They were housed in controlled standard conditions of temperature, humidity, and photoperiod, and had food and water ad libitum. The animal experiments were approved by the Animal Research Ethics Committee (CEEA) of the Germans Trias i Pujol Research Institute (IGTP) and the Catalan Government (references 11182 and 11131) and were conducted in a randomized manner and according to international guidelines (EU Directive 2010/63/EU) at the Comparative Medicine and Bioimage Centre of Catalonia (CMCIB). We followed the ARRIVE guidelines and were committed to the 3Rs of laboratory animal research. As postoperative care and until complete recovery, the operated animals were placed onto a heating pad and 0.8 mL subcutaneous sterile saline was injected. Euthanasia was performed by cervical dislocation after completion of the experiments.

2.2. Hypoxic/Ischemic Stroke Model (IS)

The mice (n = 12) were exposed to transient unilateral brain ischemia followed by a global hypoxia procedure adapted from Guan *et al.* [20]. In brief, the mice were anesthetized with isoflurane

(4% for induction and 1.5% for maintenance) in a 30–70% mixture of oxygen (O₂) and nitrous oxide (N₂O) and the right common carotid artery (CCA) was transiently occluded by ligature (using a 5-0, black braided silk non-absorbable suture) (Ethicon, LLC.; San Lorenzo, Puerto Rico). The mice were allowed to recover with free access to food and water for 2 h and then placed in a hypoxia chamber at 35.5 °C for 20 min, ventilated with a humidified gas mixture of 8% O₂/92% N₂ at an airflow rate of 1 L/min. Then, under general anesthesia with isoflurane, the suture occluding the CCA was removed, blood flow restoration in the CCA was verified *de visu*, and the wound was sutured with a 4-0, black braided silk non-absorbable suture (Silkam, B.Braun; Rubí, Spain).

2.3. Intracerebral Hemorrhage Stroke Model (ICH)

The ICH procedure was adapted from Klebe *et al.* [21]. Briefly, the mice were anesthetized with isoflurane (4% for induction and 1.5% for maintenance) in a 30/70 mixture of O₂/N₂O and placed in a stereotaxic frame (Model 940 Small animal; Kopf instruments, Tujunga, CA, USA) for the intrastratial injection of sterile bacterial collagenase type VII-S (collagenase from Clostridium histolyticum Type VII-S; Sigma-Aldrich, Saint Louis, MO, USA). Using a microinjection pump (Model UMP3T-A; Kopf Instruments, Tujunga, CA, USA) and a NanoFil 26 G syringe (World Precision Instruments; Sarasota, FL, USA), 0.06 U of collagenase in 0.4 µL sterile saline was injected into the right striatum at a rate of 200 nL/min. The coordinates from Bregma for the stereotaxic injection were 0.5 mm anterior, 1.7 mm lateral, and 3.0 mm ventral. After the infusion and before syringe withdrawal, the needle was left in place for 10 min and the isoflurane was decreased to 1%. The syringe was removed at a rate of 1 mm/min in order to avoid retrograde flow, and the cranial burr hole was sealed with bone wax (B.Braun Vertcare; Rubí, Spain). The animals of the sham group received the same surgical procedure and were injected with 0.4 µL vehicle. Once the common iron-related protein response in ischemic (n = 12) and hemorrhagic (n = 7) stroke models was established, the effect of hATf was tested in experimental ICH. The mice were randomly assigned to the groups ICH-vehicle (sterile saline) and ICH-human apotransferrin (hATf; Sigma-Aldrich, Saint Louis, MO, USA) at the dose of 230 mg/kg (n = 8 in each group). Exogenous hATf was used to be able to distinguish it from endogenous mouse ATf. Forty minutes after collagenase administration, vehicle or hATf was administered intravenously

2.4. Tail Bleeding Test

Nine male C57BL/6J mice were used to test a putative effect of exogenously administered hATf on coagulation (vehicle n = 5, hATf n = 4). Ten minutes after an i.v. administration of sterile saline or 230 mg/kg hATf, the tip of the tail was cut, the tail was submerged in physiological saline at 37 °C to ease bleeding, and the time elapsed until the tail stopped bleeding was measured.

2.6. Blood and Brain Sampling and Processing

Blood samples were obtained using EDTA-K or lithium heparin tubes (Microvette CB 300 EDTA or Microvette CB 300 lithium heparin; Sarstedt, Nümbrecht, Germany) before surgery, after the i.v. injection, and 24 h after the ICH induction. The plasma obtained after centrifugation was stored at –20 °C.

Three days after the treatments, the mice were euthanized via cervical dislocation, and the brains were quickly obtained and cut into 2 mm thick slices using a coronal mouse brain slicer matrix. Then, the slices were photographed on both sides. For Western blot and qPCR, the third fronto-caudal brain slice, the one showing the highest level of infarct or hematoma in the ischemic or hemorrhagic stroke models, respectively, was divided and saved separately into ipsilateral and contralateral hemispheres, flash-frozen in liquid N₂, and stored at –80 °C. Further, the samples were lyophilized (Freeze Dryer; B.Braun Biotech; Melsungen, Germany) following Aliena-Valero *et al.*'s protocol [22] and stored at –80 °C until analysis. This way, we obtained a bias-free selection of the tissue for both WB and qPCR analyses. We chose this conservative procedure, despite it potentially underestimating the molecular changes in the ipsilateral hemisphere due to it also containing healthy tissue, as it allows for an objective standardization of the tissue collected for analyses. For immunohistochemistry, the second rostro-caudal 2 mm thick slice obtained from the brain slicer matrix was preserved and stored

at -80°C . The most caudal side of this 2 mm slice, adjacent to the tissue used for qPCR and Western blot, was sliced using a cryostat into 15 μm thick slices to be used to detect 4-HNE and NeuN.

2.7. Assessment of the Ischemic Infarct Volume in the IS Model, Hemorrhage Volume, and Brain Hemoglobin and Heme Concentration in the ICH Model

The infarct volume and hemorrhage volume were quantified 72 h after treatments by measuring the 2,3,5-triphenyltetrazolium chloride (TTC)-unstained area or the hematoma area, respectively, in 2 mm thick coronal slices using ImageJ v1.53 (Wayne Rasband; NIH; Bethesda, MD, USA) and calculated as previously reported [23]. The brain hemoglobin and heme levels were measured using colorimetric detection assay kits (QuantiChrom Hemoglobin Assay Kit and QuantiChrom Heme Assay Kit; BioAssay Systems; Hayward, CA, USA) following the manufacturers' instructions.

2.8. RT-qPCR

A miRNeasy Tissue/Cells Advanced Mini Kit (Qiagen; Hilden, Germany) was used for RNA isolation. Briefly, lyophilized brain tissue samples (ipsi and contralateral hemispheres separately) were resuspended in the supplied lysis buffer with 0.01% β -mercaptoethanol and homogenized by passing the lysate through a 21 G needle at least 5 times in order to isolate the RNA. The RNA was finally recovered in RNase-free water and its concentration and purity were assessed using a NanoDrop ND-1000 Spectrophotometer (NanoDrop; Thermo Fisher Scientific; Waltham, MA, USA). The same amount of RNA was used for the reverse transcription of each sample following QuantiTect Reverse Transcription Kit (Qiagen; Hilden, Germany) instructions. The samples were first incubated with a gDNA elimination reaction for 2 min at 42°C and immediately placed on ice. The reverse transcription reaction was performed at 42°C for 15 min, followed by inactivation at 95°C for 3 min. A no-reverse transcription control was also prepared by replacing the reverse transcriptase with water. The obtained cDNA was then mixed with LightCycler 480 SYBR Green I Master (Roche Applied Science; Penzberg, Germany) and PrimeTime® qPCR Primers for different genes (Integrated DNA Technologies; Coralville, IA, USA). Real-time PCR was performed in a Real-Time PCR Roche LightCycler 480 I (Roche Applied Science; Penzberg, Germany). The reaction was initiated using a pre-incubation step of 5 min at 95°C , followed by 45 cycles of amplification at 95°C for 10 s, 60°C for 10 s, and 72°C for 10 s. Triplicates of the samples and melting curve analysis were also performed. A no-template control was included, replacing the sample cDNA with RNase-free water, as well as a positive control using Universal Mouse Reference RNA (Invitrogen; Waltham, MA, USA). Data analysis was performed using the $\Delta\Delta\text{Cp}$ method and GAPDH was utilized as a house-keeping gene. Commercial proprietary predesigned qPCR forward and reverse primers obtained from IDT (Integrated DNA Technologies; Coralville, IA, USA) were used (Table S1).

2.9. Western Blot (WB)

Lyophilized brain samples were reconstituted in the same lysis buffer used for the hemoglobin and heme quantification. The protein content of the reconstituted samples was determined using a Pierce™ BCA Protein Assay Kit (Thermo Fisher Scientific; Waltham, MA, USA). Then, 30 μg of total protein from the brain was loaded in Precast NuPAGE Midi 10% Bis-Tris (Thermo Fisher Scientific; Waltham, MA, USA). A molecular weight marker (Precision Plus Protein™ Standards; Bio-Rad; Hercules, CA, USA) was included in the gels and GAPDH was used as a tissue sample loading control.

For the TSAT assessment, 0.15 μL of plasma sample was loaded in Precast 6% TBE urea gels (U-PAGE) (Thermo Fisher Scientific; Waltham, MA, USA). These gels included human apotransferrin and human holotransferrin (hHTf) (Sigma-Aldrich; Saint Louis, MO, USA), as well as in-lab prepared mouse ATf and HTf standards, which were prepared following the methods described in Byrne S *et al.* and Nagaoka MH *et al.* [24,25]. PVDF-LF membranes (Millipore; Burlington, VT, USA) were used for the electroblotting of the gels, which were blocked with Intercept® Blocking Buffer (Li-COR Biosciences; Lincoln, NE, USA) for 1 h. Then, the membranes were incubated overnight at 4°C with the specific primary antibodies. After that, they were incubated with NIR-conjugated secondary antibodies. The bands were measured using an Odyssey Imaging system and

Image Studio Lite software v5.2 (Li-COR Biosciences; Lincoln, NE, USA). The values were measured in terms of mean integrated density (ID) in arbitrary units ((mean optical density of pixels of the specific signal) – (mean background optical density)). Then, for each protein, 1.00 was assigned to the ID of the contralateral brain hemisphere and the ID of the ipsilateral hemisphere was expressed in terms of the fold-change of that of the contralateral hemisphere.

2.10. Determination of 4-Hydroxynonenal (4-HNE) Using Immunohistochemistry (IHC)

In this stage, 15 μ m thick brain slices from frozen tissue were obtained using a cryostat (Leica CM1950; Leica Biosystems; Deer Park, TX, USA) on poly-L-lysine-coated glass slides and fixed in 4% paraformaldehyde. They were exposed to antigen retrieval (90–95° in 0.01 mol/L citrated buffer, pH 6.0, for 20 min), incubated overnight with the primary antibodies at 4 °C, and then with the secondary antibodies and Hoechst (33342; Thermo Fisher Scientific; Waltham, MA, USA). Fluoromount (Sigma-Aldrich F4680; Saint Louis, MO, USA) was used as the mounting medium. Images were obtained using an AxioOberver Z1 microscope (Carl Zeiss; Oberkochen, Germany) in the Microscopy Platform Core Facility at the IGTP and analyzed using ImageJ. NeuN immunohistochemistry was macroscopically imaged on an Odyssey Imaging System. In brief, the 15 μ m thick brain slice that preceded the slice used for microscopy studies was subsequently incubated with anti-NeuN antibody and with an NIR-conjugated secondary antibody for Odyssey imaging. Due to the loss of neurons, almost no NeuN staining was observed within the hematoma in the whole picture of the Odyssey-imaged brain slice. The cortical areas neighboring the hematoma had neurons potentially exposed to ICH-produced toxic compounds. Under the microscope, the areas devoid of NeuN, which are hematoma, together with the anatomical brain references easily identified in the slice under the microscope (e.g., *corpus callosum*, ventricles), enabled us to identify periinfarct areas of interest in the nearby cortex. Several different series of images were obtained and 4-HNE was detected and quantified in NeuN-positive neurons in the areas of interest.

2.11. TSAT Assessment

Basal TSAT levels were determined before the onset of the experimental stroke procedures to check that mice had TSAT levels similar to those in the human population (<40%), and 24, 48, and 72 h after ICH induction.

The U-PAGE gels mentioned above separate transferrin into ATf (Tf devoid of iron), monoferric Tf (mFe, an Fe atom in the C-terminal region or in the N-terminal region) and diferric Tf (diFe, holotransferrin, HTf), giving different bands according these Tf isoforms. The % TSAT was calculated using the measurement of the bands from the U-PAGE gels and the TSAT formula previously used by us and others [3,26]:

$$\text{TSAT}(\%) = \left(\frac{1}{2} \times \text{mFe}\cdot\text{Tf} + \text{diFe}\cdot\text{Tf} \right) \times 100 / (\text{ATf} + \text{mFe}\cdot\text{Tf} + \text{diFe}\cdot\text{Tf})$$

2.12. Antibodies

The primary and secondary antibodies used for WB and IHC (see Table S2) were from Thermo Fisher Scientific (Waltham, MA, USA), Abcam (Cambridge, UK), Novus Biologicals (Centennial, CO, USA), Santa Cruz Biotechnology (Dallas, TX, USA), Green Mountain Antibodies (Burlington, VT, USA), Cappel, ICN Pharmaceuticals (Costa Mesa, CA, USA), and Sigma-Aldrich (Saint Louis, MO, USA), Li-COR Bioscience (Lincoln, NE, USA) and Thermo Fisher Scientific (Waltham, MA, USA).

2.13. Statistics

Original or log-transformed data were analyzed using GraphPad Prism 9. A paired or unpaired Student's *t*-test or independent or repeated-measures one-way ANOVA followed by the multiple comparisons Tukey's test were used, as appropriate. Statistical significance was considered at *p* < 0.05. Data are presented as the mean and SEM.

3. Results

3.1. Gross Differences and Commonalities between Ischemic and Hemorrhagic Stroke Models

The nature, extent, and location of the brain regions affected by stroke differ between the two stroke models. There is a large corticostratal infarct in ischemia, and smaller, mainly striatal, hemorrhage in ICH (Figure 1B,F). Despite this, body weight loss followed the same pattern in both ischemic and ICH mice (Figure 1E,I), and the same applied for edema (Figure 1C,G) and the cerebral midline shift induced by the ipsilateral hemisphere enlargement (Figure 1D,H).

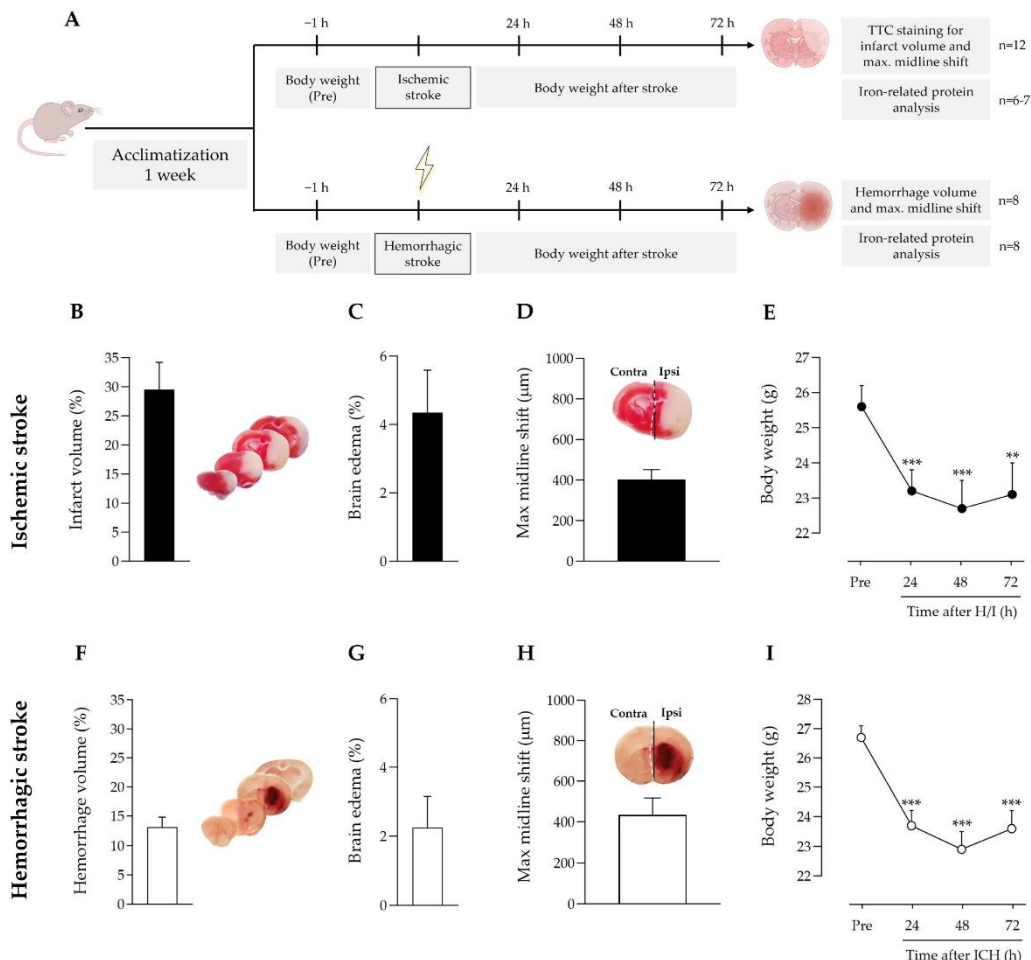


Figure 1. (A) Timeline scheme of the experimental groups and procedures. Effect of (B–E) ischemic stroke and (F–I) intracerebral hemorrhage on (B,F) infarct or hemorrhage volume, (C,G) edema, (D,H) stroke-induced maximum hemispheric midline shift (broken white line) vs. the theoretical midline (solid black line), and (E,I) body weight loss; ** $p < 0.01$ and *** $p < 0.005$ vs. pre-stroke (repeated measures one-way ANOVA and Tukey's test). Data are represented as the mean and SEM. Contra: contralateral; ipsi: ipsilateral. Representative images of ischemic regions (regions in white in the brain slices in (B) and hemorrhagic regions (reddish areas in the brain slices in (F) in coronal brain slices are shown and were used to quantify ischemic infarct volume and hemorrhagic stroke volume, respectively.

3.2. Ischemic and Hemorrhagic Stroke Share a Common Profile of Iron-Binding, Ferroptosis-Related Proteins in the Ipsilateral Brain Hemisphere 72 h after Stroke Induction

Importantly, compared with the contralateral brain hemisphere, both ischemic and hemorrhagic stroke increased the protein levels of iron-storage ferritin and the iron-binding and carrier transferrin in the ipsilateral hemisphere (Figure 2A,B). A modest increase in the levels of divalent metal transporter 1 (DMT1), which imports ferrous iron to the cytosol, was observed in the ipsilateral hemisphere of the ischemic stroke mice only (Figure 2A); no changes were observed in the levels of transferrin receptor (TfR) (Figure 2A,B), which plays a pivotal role as the main gate for iron entry into the endothelial cells of the brain capillaries and into neurons; also, TfR has recently been identified as a ferroptosis biomarker [27].

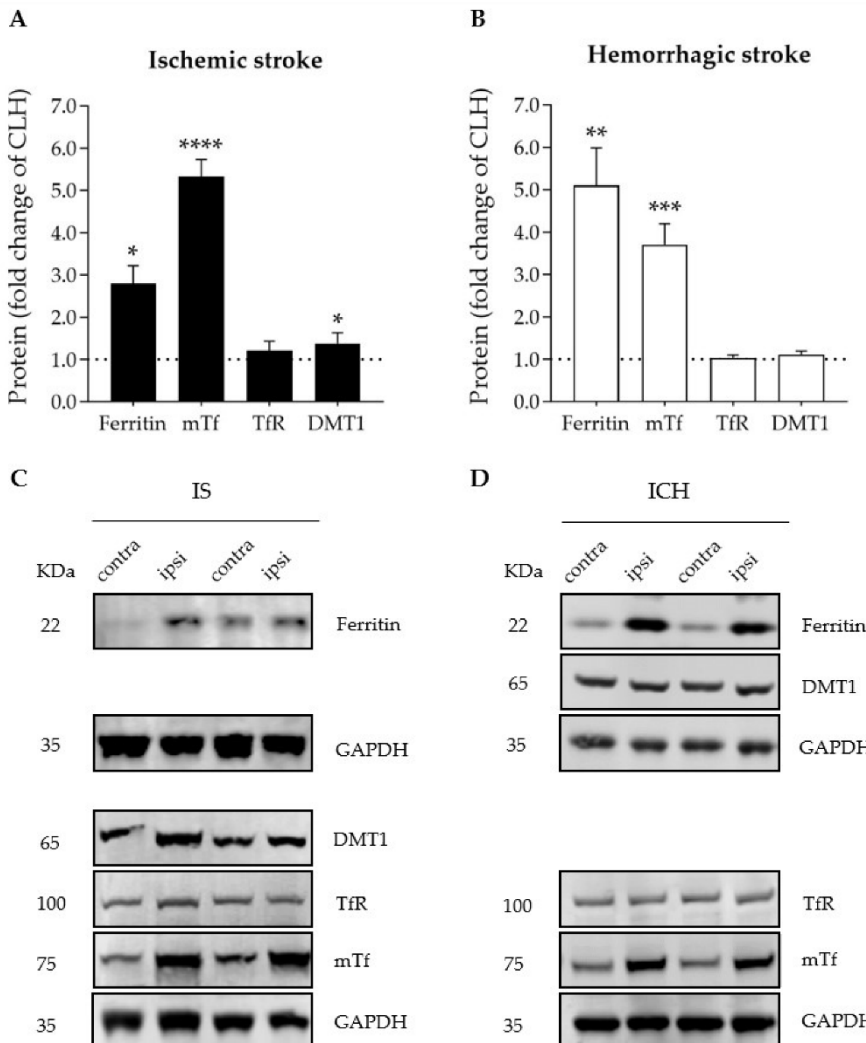


Figure 2. Graphs depicting the effect of (A) ischemic stroke and (B) intracerebral hemorrhage on ipsilateral brain levels of iron- and ferroptosis-related proteins 72 h after stroke onset, expressed as fold change of those of the contralateral hemisphere (CLH, mean represented by the dotted line at y = 1.0); * $p < 0.05$, ** $p < 0.01$, *** $p < 0.005$, and **** $p < 0.0001$ vs. contralateral hemisphere (paired t test), $n = 6\text{--}7$. Mean and SEM are shown. (C,D) Representative WB of the bands of the proteins of interest in the contralateral (contra) and ipsilateral (ipsi) hemispheres of (C) ischemic stroke (IS) and (D) intracerebral hemorrhage (ICH). DMT1: divalent metal transporter 1; GAPDH: glyceraldehyde3-

phosphate dehydrogenase; mTf: mouse transferrin; TfR: transferrin receptor. GAPDH was used as the housekeeping protein and is shown in the figure as the bottom row in each one of the four representative membranes depicted (no more than four antibodies were tested in the same membrane).

3.3. Early Peripheral Administration of hATf into the Bloodstream after ICH Induction Does Not Reduce Parenchymal Hemorrhage

The common iron-binding, ferroptosis-related protein signature we observed in both the ischemic and the hemorrhagic models above, together with the fact that our group has previously demonstrated that ATf exerts neuroprotection in ischemic stroke models in rats [3], provided the rationale to study the neuroprotective potential of iron-devoid ATf in the ICH mouse model. We administered i.v. human ATf (hATf) to be able to distinguish it from endogenous mouse ATf in the WB, using the appropriate gel conditions and the specific species antibodies already tested in our lab [3].

Figure 3C shows that ICH itself did not alter blood transferrin saturation with iron, also known as TSAT, which remained at around 40% before, and 45 min and 24 h after ICH induction. By contrast, hATf reduced TSAT to approximately half the pre-ICH values 5 min after administration (hence, 45 min after ICH induction), and TSAT remained low in these animals 24 h later. These observations are very similar to those we reported in ischemic stroke models in rats [3].

On the other hand, blood extravasation in the ipsilateral hemisphere in both ICH-vehicle and ICH-hATf mice was evident and of comparable magnitude in the gross histology (Figure 3D), and no significant difference was observed in the hemorrhagic volume 72 h after ICH onset (Figure 3E), or in terms of hemoglobin (Figure 3F) or heme levels (Figure S2). In the WB, hATf was not detected in the cerebral hemisphere of the mice administered the vehicle, as expected, and the hATf signal was very low in the contralateral hemisphere and high in the ipsilateral hemisphere of the mice given hATf (Figure 3G,H). Also, hATf treatment altered neither body weight loss (Figure 3B) nor the tail bleed clotting time (Figure 3I).

3.4. hATf Reduces ICH-Induced Sensorimotor Impairment in the Adhesive Tape Detection and Removal Test

As expected, ICH considerably increased the time the mice took to detect (Figure 4A) and to remove (Figure 4B) the tape from the contralateral paw compared to the training session prior to ICH induction. The administration of hATf after ICH induction progressively reduced the ICH-induced sensorimotor impairment, reducing the time required to detect the tape at 48 and 72 h and to remove the tape at 72 h (ns: non-significant) compared with their performance before ICH (training). ICH mice treated with hATf also showed significant improvement at 72 h when compared with their post-ICH performance at 24 h (# p < 0.05). Vehicle-treated, but not ATf-treated, ICH animals had increased 4-HNE levels in the perihematomal tissue of the ipsilateral hemisphere, as determined by immunohistochemistry (Figure 4C,D).

3.5. Effect of hATf on Iron Storage/Transport-Related mRNA and Protein Levels in ICH Mice

As shown in Figure 5, ICH plus either vehicle or hATf increased ferritin and endogenous transferrin mRNA and protein levels in the ipsilateral hemisphere compared with the respective contralateral hemisphere (CLH) and with sham mice. However, the increases in mouse transferrin mRNA and protein levels were of less magnitude in the hATf-treated mice than they were in the vehicle mice.

3.6. Effects of hATf on Classical Key Ferroptosis mRNA and Protein Levels in ICH Mice

No statistically significant effects of ICH were found in glutathione peroxidase 4 (GPX4) mRNA and protein levels. Nonetheless, GPX4 mRNA levels showed a trend of being lower in the ipsilateral hemisphere of the ICH mice when compared with sham animals (p = 0.0624 in ICH-vehicle and p = 0.0681 in ICH-hATf mice) (Figure 6). ICH increased system xc- gene expression (Slc3a2 mRNA) irrespective of the treatment; at the protein level (xCT), it did not reach statistical significance (Figure 6). ICH induced a similar decrease in TfR mRNA levels in both vehicle and hATf mice, but only hATf provoked a concomitant decrease in TfR at the protein level.

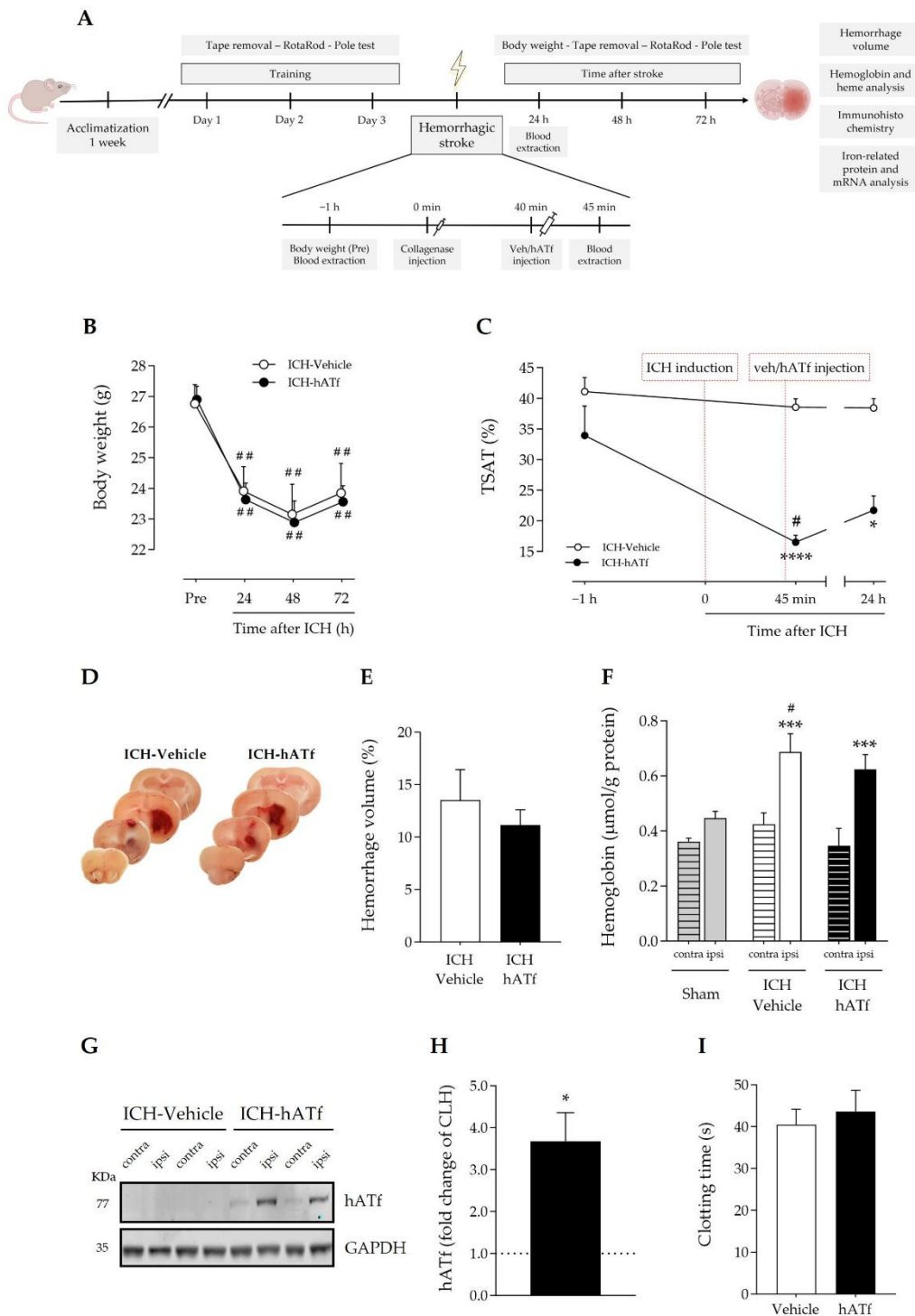


Figure 3. (A) Timeline scheme of the experimental groups and procedures to determine the effect of hATf administration in ICH mice. (B) Body weight loss; ## $p < 0.01$ vs. respective Pre (repeated-measures (RM) one-way ANOVA and Tukey's test). (C) Time course of %TSAT before and after

ICH induction and i.v. administration of vehicle or hATf; * $p < 0.05$ and *** $p < 0.0001$ vs. pre-administration (-1 h) measure (RM one-way ANOVA and Tukey's test), # $p < 0.05$ vs. ICH-Vehicle (*t* test). (D) Representative images of hemorrhage in coronal brain slices and (E) quantification of the hemorrhage volume. (F) Hemoglobin levels in the contralateral (contra) and the ipsilateral (ipsi) hemispheres of ICH mice given vehicle or hATf; a group of sham mice was included; *** $p < 0.005$ vs. respective contra (paired *t* test), # $p < 0.05$ vs. Sham-ipsi (*t* test). (G) Representative WB showing hATf levels in the contralateral (contra) and the ipsilateral (ipsi) hemispheres of ICH mice administered vehicle or hATf and (H) its quantification; * $p < 0.05$ versus contralateral (CLH, mean represented by the dotted line at $y = 1.0$; paired *t* test). (I) Tail bleed clotting time in mice given vehicle or hATf. Mean and SEM are shown.

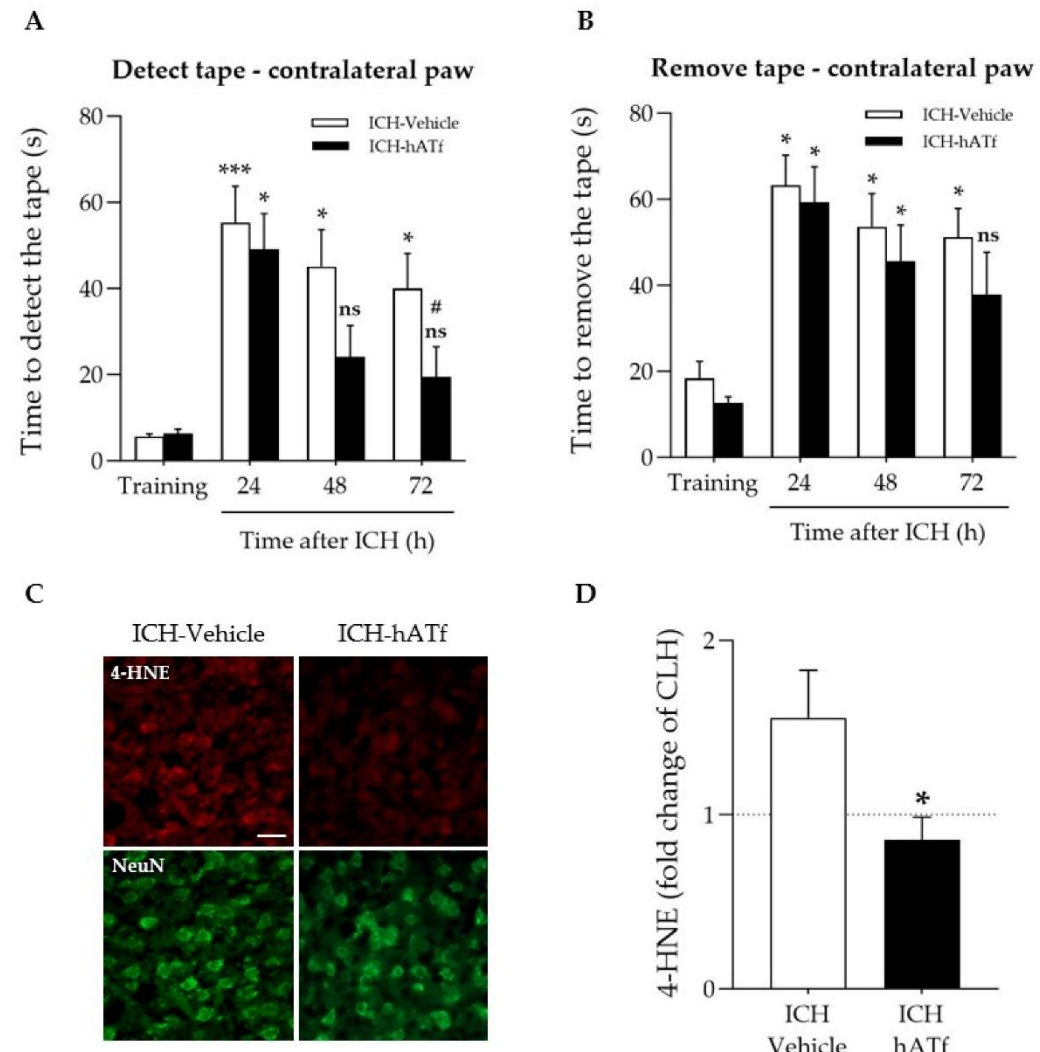


Figure 4. Effect of ICH and hATf on the neurobehavioral performance and brain 4-HNE levels. (A,B) Graphs depicting the hATf-induced improvement in the adhesive tape detection/removal test of the contralateral paw showing (A) time to detect and (B) the time to remove the tape at 24, 48, and 72 h post-ICH. * $p < 0.05$ and *** $p < 0.0001$ vs. respective training; ns means non-significant versus training (mice performance before being exposed to ICH), # $p < 0.05$ vs. respective 24 h (repeated-

measures one-way ANOVA and Tukey's test). **(C)** Representative immunohistofluorescence images of 4-hydroxynonenal (4-HNE) and NeuN in the perihematomal cortical area of the ipsilateral hemisphere of ICH-Vehicle and ICH-hATf mice; scale bar, 20 μ m. **(D)** Graph depicting 4-HNE levels in neurons in the perihematomal cortical area in fold change of mirror areas of the CLH (mean represented by the dotted line at y = 1.0). * p < 0.05 vs. vehicle. Mean and SEM are shown.

3.7. Effect of hATf on the mRNA Expression of Newly Reported Key Ferroptosis Players AIFM2/FSP1 and PCBP2 in ICH Mice

Neither ICH nor hATf changed the mRNA expression of apoptosis-inducing factor 2 (AIFM2, also known as ferroptosis suppressor protein 1, FSP1), a newly identified ferroptosis player (Figure 7A). We found a slight decrease in the mRNA levels of the cytosolic iron chaperone poly (rC)-binding protein 2 (PCBP2) in the ICH-vehicle animals that was no longer observed in the ICH-hATf-treated animals (Figure 7B).

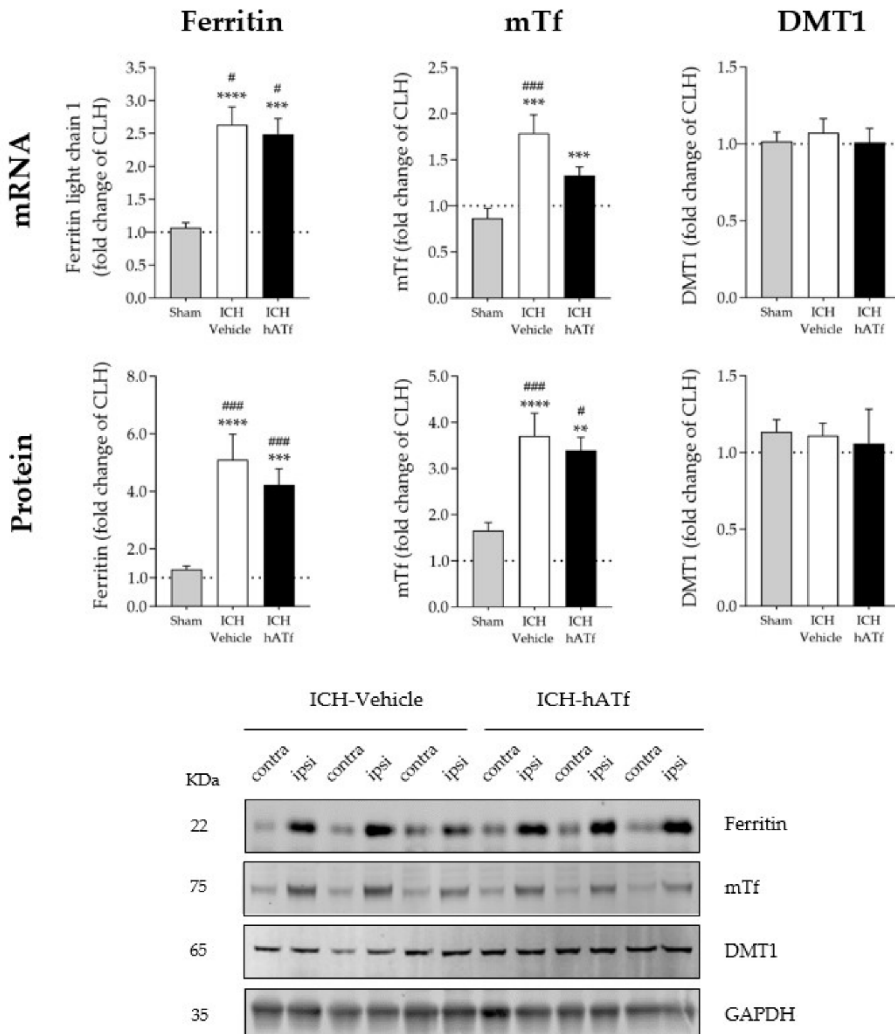


Figure 5. Graphs showing the effect of ICH and hATf on mRNA (top) and protein (bottom) levels of ferritin, endogenous mouse transferrin (mTf), and divalent metal transporter 1 (DMT1) in the ipsilateral cerebral hemisphere 72 h after ICH induction, expressed as fold change of the contralateral

hemisphere (CLH, mean represented by a dotted line at $y = 1.0$). ** $p < 0.01$, *** $p < 0.005$, and **** $p < 0.0001$ vs. CLH (paired t test); # $p < 0.05$, and ### $p < 0.005$ vs. sham (one-way ANOVA and Tukey's test). Mean and SEM are shown. Bottom panel: representative WB of the contralateral (contra) and ipsilateral (ipsi) hemispheres; glyceraldehyde-3-phosphate dehydrogenase (GAPDH) was used as the housekeeping protein.

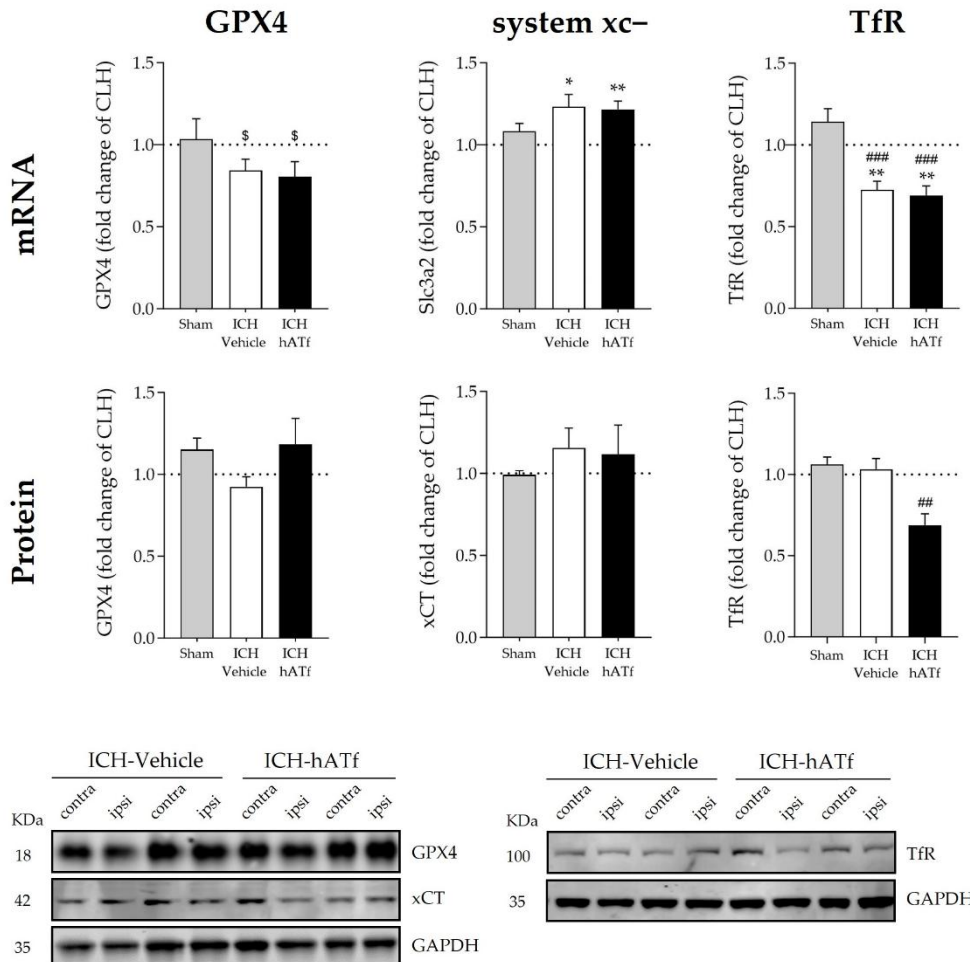


Figure 6. Graphs showing the effect of ICH and hATf on mRNA (**top**) and protein (**bottom**) levels of glutathione peroxidase 4 (GPX4), Tf receptor (TfR), and the cysteine/glutamate antiporter system xc- in the ipsilateral cerebral hemisphere 72 h after ICH induction, expressed as fold change of the contralateral hemisphere (CLH, mean represented by a dotted line at $y = 1.0$). * $p < 0.05$ and ** $p < 0.01$ vs. contralateral hemisphere (paired t test), ## $p < 0.01$ vs. sham and ICH-vehicle (TfR protein), ### $p < 0.005$ vs. sham (TfR mRNA) (one-way ANOVA and Tukey's test), \$ $0.06 < p < 0.07$ vs. contralateral hemisphere (GPX4 mRNA) (paired t test). Mean and SEM are shown. Representative WB of GPX4, xCT, and TfR in the contralateral (contra) and ipsilateral (ipsi) hemispheres of vehicle and hATf-treated mice are shown; glyceraldehyde-3-phosphate dehydrogenase (GAPDH) was used as the housekeeping protein.

3.8. hATf Reduces ICH-Induced Caspase 2 Activation

ICH increased the levels of cleaved Casp2 p18 form, which was partly prevented by the administration of hATf (Figure 8A).

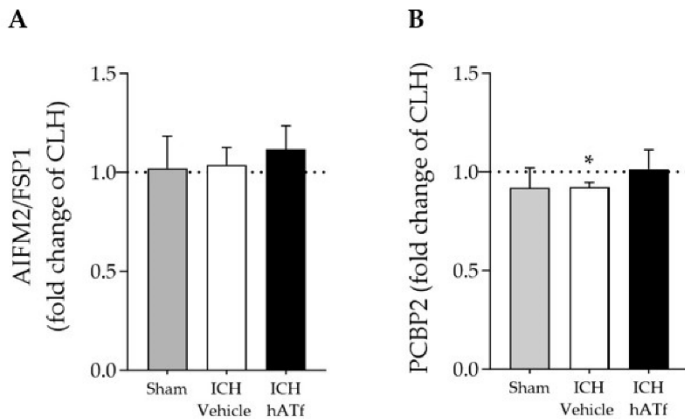


Figure 7. Effect of ICH and hATf on mRNA levels of (A) ferroptosis-related apoptosis-inducing factor 2 (AIFM2/FSP1) and (B) the iron chaperone poly(rC)-binding protein 2 (PCBP2) in the ipsilateral cerebral hemisphere 72 h after ICH induction, expressed as fold change of the contralateral hemisphere (CLH, mean represented by a dotted line at $y = 1.0$). * $p < 0.05$ vs. contralateral hemisphere (paired t test). Mean and SEM are shown.

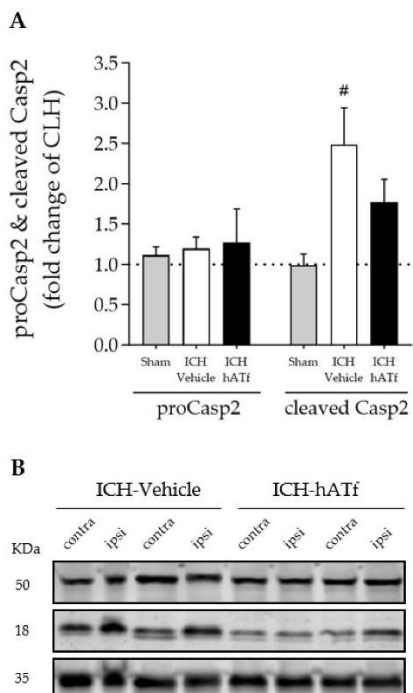


Figure 8. (A) Effect of ICH and hATf on brain caspase-2 (proCasp2) activation by cleavage into the p18 form (cleaved p18) in the ipsilateral cerebral hemisphere 72 h after ICH induction, expressed as

fold change of the contralateral hemisphere (CLH, mean represented by a dotted line at $y = 1.0$). (B) Representative WB showing proCasp2 and cleaved Casp2 in the contralateral and ipsilateral hemispheres of vehicle- and hATf-treated mice. # $p < 0.05$ vs. respective sham (one-way ANOVA and Tukey's test). Mean and SEM are shown.

4. Discussion

Here we demonstrate, in an *in vivo* collagenase-induced ICH model in mice, that a single intravenous administration of hATf shortly after stroke induction is not only safe, but shows efficacy in reducing the sensorimotor impairment of the affected forepaw (Figure 4). The results of the study also suggest that the benefits of the hATf treatment might be exerted through an antiferroptotic mechanism independent of the canonical inhibitor of the ferroptosis system xc-/GPX4 axis.

Our results show that both stroke models, ischemic and hemorrhagic, provoked similar body weight loss, and swelling and a shift of the ipsilateral brain hemisphere beyond the sagittal midline (Figure 1). We also observed similar effects in both stroke models (a 2.8- to 5.3-fold increase) in the levels of the main iron storage and transport proteins, ferritin and endogenous mouse Tf, respectively, in the ipsilateral hemisphere with a minor effect, or none at all, of ICH on the levels of the main molecular gates for iron passage into the cytosol: TfR at the cell membrane and DMT1 (also known as SLC11A2, DCT1, or Nramp2) as the lysosome-to-cytosol gate (Figure 2). This points to a common picture of iron dyshomeostasis with the need to safely store excess cellular iron in the intracellular iron-storage protein ferritin in stroke arising from both etiologies, which is in agreement with previous literature on the issue [3,11,28–31]. Therefore, molecules with the ability to prevent iron overload in neurons would be good putative candidates to alleviate stroke-induced neurodegeneration, as has also been previously reported for deferoxamine in ICH or ischemic stroke patients [4,32]. Our group has also already reported the protective effect for hATf in ischemic stroke models [3].

The clearance and iron status in the blood of the hATf administered in ICH mice is similar to that previously reported in ischemic stroke in rats [3]. Thus, hATf administration immediately reduced plasma TSAT compared to mice given the vehicle (as assessed 5 min later), an effect that lasted for at least 24 h post-ICH (Figure 3C). Also, exogenous hATf reached and remained in the brain, as assessed at 72 h, at higher levels in the ipsilateral than in the contralateral hemisphere (Figure 3G,H). Of note, the presence of hATf in the brain parenchyma is associated with a reduction in the neuronal levels of 4-HNE in the ICH-affected perihematomal areas of the hemisphere (Figure 4C,D). Interestingly, previous work demonstrates that the addition of hATf *in vitro* to the extracellular medium of excitotoxically challenged neurons in culture, being equivalent to lowering TSAT *in vivo*, decreases neuronal oxidative stress [3], whereas the addition of iron-loaded transferrin (holotransferrin, HTf) to ischemic or excitotoxically challenged neurons increases ROS production and harmful neuronal iron uptake [3]. As for the neurological outcome, we found that treatment with hATf induced better performance in the sensory aspects of the adhesive tape removal test when compared to placebo mice. The hATf-treated ICH mice regained sensorimotor skills in this test, which measured front paw tasks (Figure 4A), although they did not regain general coordination (Figure S1). There was no statistical difference in the contralateral paw detection performance of hATf-treated mice at 48 and 72 h, nor in the time taken to remove the tape 72 h after the ICH onset compared to the results from pre-ICH training sessions. This was different to mice given the vehicle, and, thus, hATf-treated mice show an improvement in their post-ICH performance in a complex task requiring sensory, motor, and coordination skills.

While searching for other underlying mechanisms through which hATf provides sensorimotor improvement in ICH mice, we investigated the effects of hATf administration on: (1) the size of the brain hematoma and changes in blood coagulation, and (2) iron- and ferroptosis-related molecules relevant to stroke.

Regarding the size of the hematoma, despite hATf reaching the hemorrhagic brain hemisphere, it did not reduce the ICH-induced hemorrhage volume, the edema, or the hemoglobin and heme concentration in the ipsilateral hemisphere when administered in a relevant time window (40 min post-collagenase) (Figures 3 and S2). In addition, we did not find any effect of hATf treatment on the clotting time assessed in the tail-bleeding time test in the systemic circulation in healthy mice

(Figure 3I). Moreover, there was no any significant alteration in the parameters of the coagulation cascade when hATf was incubated *in vitro* with freshly obtained human blood in experimental *in vitro* conditions that mimic as closely as possible (1) the concentration of hATf in blood, and (2) the blood dilution produced when adding the treatment volume in the mice blood (Figure S3). Of note, we tested these parameters and obtained these negative results in two species, in physiological conditions, and in acute scenarios, all of which presented as very relevant for stroke. However, other studies tested the effects of transferrin on coagulation in other conditions, reporting either procoagulant effects, e.g., chronically elevated transferrin levels or blood processed much further than we did [33,34] or, in contrast, higher transferrin associated with protection from thrombosis [35].

Regarding the iron- and classical ferroptosis-related molecules relevant to stroke, we found no significant effect of ICH, suggesting that a physiological attempt to maintain normal GPX4 protein levels and to provide enough supply of cystine, through system xc, cysteine, and, ultimately, the GPX4 cofactor GSH to reduce the ICH-induced lipid peroxidation is taking place. Neither ICH nor hATf altered the protein levels of GPX4 or xCT (SLC7A11), although GPX4 mRNA levels showed a trend of being reduced ($0.06 < p < 0.07$) and the mRNA levels of the heavy-chain subunit of the system xc- (Slc3a2) were increased in the ipsilateral hemisphere of the ICH mice, irrespective of whether they had received vehicle or hATf (Figure 6). Neither ICH nor hATf altered the mRNA levels of ferroptosis suppressor protein 1 (FSP1 or AIFM2) (Figure 7), which stands for another key ferroptosis axis, the FSP1/CoQ10/NAD(P)H pathway, which has only received attention very recently [36,37]. Interestingly, ICH reduced the mRNA levels of the cytosolic iron chaperone PCBP2; this reduction was prevented by hATf treatment and is relevant, since knocking down PCBP2 has been recently reported to promote ferroptosis [38].

In addition, and of special interest regarding a putative anti-ferroptotic effect of hATf, ICH decreased Tfr1 mRNA levels in both vehicle- and hATf-injected mice, whereas only the hATf-treated animals showed a concomitant reduction in Tfr protein levels (Figure 6), which, as the main membrane cellular gate of iron entry into the cell, might be directly implicated in the benefit induced by hATf treatment. Tfr1 abundance, especially at the cell membrane, is a known hallmark promotor of ferroptosis [27,39]. This is in line with a recent report that shows that the knockdown of Tfr1 inhibits ischemia/reperfusion-induced ferroptosis in the rat heart through the inactivation of the p53/Tfr1 pathway [40]. Another recent study reports that ferroptosis in the hippocampus and cognitive dysfunction induced by the i.c.v. injection of lipopolysaccharide are prevented by the downregulation/suppression of Tfr1 expression [41,42]. Of note, the reduction in the Tfr mRNA levels observed in ICH would be in accordance with the reported *in vitro* effect of hemin as an epigenetic negative regulatory factor upon transcription of the transferrin receptor gene [43].

The effect of ICH on the parenchymal levels of the key molecule involved in ferroptosis GPX4 is controversial, with some authors reporting no changes at 72 h [18,19], whereas others report reductions in mRNA and protein expression at 72 h [17,43–45]. Our results, which only show a trend of reduction in the mRNA levels, added to the disparities in the literature. It is plausible that the differences in the methodology of the few studies carried out to date on this issue may account for the discrepancies. With regard to this, we found large differences in the GPX4 levels present in young/undifferentiated neurons in culture compared to differentiated ones, with young neurons containing low levels of GPX4 being more susceptible to ferroptosis (Figure S4). Moreover, isoflurane has been reported to have either neuroprotective or neurotoxic effects [46], and it has been recently reported to reduce hippocampal GPX4 levels after long exposures (1.5% for more than 2h) [47]. In the present experiments, although no mice were exposed to more than 1 h isoflurane, we cannot rule out that an isoflurane-induced reduction in GPX4 levels in both hemispheres might have masked the ICH-induced effect in the ipsilateral hemisphere to some degree.

Wang *et al.* reported that the restoration of GPX4 and FSP1/AIFM2 levels through the early administration of the antioxidant dexamipexole maintains white matter integrity and improves locomotion and motor coordination in the model of ICH induced by the injection of autologous blood in the striatum [48]. Our results here suggest that even when the two pathways mentioned are not significantly affected, iron-burden-dependent ferroptosis is occurring, and this could take place mainly through the p53/Tfr1 pathway. This fits the recent understanding of ferroptosis as a flexible process

under the regulation of many different functionally related molecules. The fact that hATf binding to the remaining TfR1 exerts a competitive effect on the iron-loaded transferrin binding and internalization through this receptor suggests that exogenous hATf plays a decisive role in preserving brain parenchyma and neuronal iron homeostasis. The recent identification of a novel lncRNA that constitutively represses p53 and apoptosis in cooperation with PCBP2 [49] provides a nexus between the p53/TfR1 pathway, PCBP2, and apoptosis, and strongly suggests that there is crosstalk between the pathways driving to apoptosis and to ferroptosis. Since, *in vitro*, PCBP2-specific siRNA-transfected neurons show a significant decrease in apoptosis following glutamate stimulation [50], we investigated the effect of ICH and hATf treatment on the activation of caspase-2, one of the upstream caspase effectors. We observed that the ICH-induced cleavage of procaspase-2 that renders an increase in active caspase-2 was abrogated by treatment with hATf (Figure 8). The fact that PCBP2 knockdown significantly increases the sensitivity to erastin-induced ferroptosis in cancer cells, whereas it reduces glutamate-induced apoptosis in neurons [38,50], points to a prominent dual antiferroptotic and proapoptotic role of PCBP2; the balance between the two processes probably depends on the cell type and its physiological status, with all of these together finally determining the cell fate.

The mechanisms that finally underlie the improvement in the sensorimotor abilities of ICH mice treated with hATf are likely to be multifactorial and related to its effect on ferroptosis players, such as TfR1 and PCBP2, and on the inactivation of caspase-2. In addition, the previously reported effects of ATf increasing the proliferation and maturation of remyelinating oligodendrocytes and on myelin deposition [51] might also contribute.

In summary, ATf administration is safe and provides sensorimotor improvement to mice exposed to experimental ICH. The present results, together with the benefit previously demonstrated for ATf in experimental ischemic stroke, allow the proposal of ATf as a pre-hospital frontline treatment that could be administered to patients very early on, even en route to an accurate in-hospital differential diagnostic.

Supplementary Materials: The following supporting information can be downloaded at: <https://www.mdpi.com/article/10.3390/antiox12111945/s1>: Table S1: Commercial proprietary predesigned qPCR forward and reverse primers used; Table S2: Antibodies used for WB and immunohistochemistry (IHC); Figure S1: Effect of ICH and hATf on the neurobehavioral performance of mice in the pole test and the rotarod; Figure S2: Heme levels in the contralateral and the ipsilateral hemispheres of ICH mice given vehicle or hATf; Figure S3: Effect of human ATf and human HTf on human blood coagulation; Figure S4: Effect of erastin on neuronal viability *in vitro* and levels of GPX4 and xCT along neuronal maturation; Figure S5: Body weight of sham H/I and sham ICH mice over the course of the experimental period; Gels S1–S6: Original full WB gels.

Author Contributions: Conceptualization, T.G. and O.M.-S.; writing—original draft preparation, A.G.-S., O.M.-S. and T.G.; *in vivo* experiments, A.G.-S. and M.M.-S.; *in vitro* experiments, A.G.-S., J.O., N.D.-R. and K.O.; supervision, O.M.-S. and T.G.; funding acquisition, T.G. and O.M.-S. All authors have read and agreed to the published version of the manuscript.

Funding: This study was supported by grants from the Agency for Management of University and Research Grants (AGAUR) Catalan Research Group (SGR) 2021SGR00925 and 2019PROD00120, and by the Fondo de Investigaciones Sanitarias–Instituto de Salud Carlos III projects PI18/01813 and PI21/01925, RICORS RD21/0006/0024, that were susceptible to be co-financed by FEDER/FSE funds. MMS was supported by a PFIS contract from the ISCIII (FI19/00174), and AGS was supported by contracts associated with 2019PROD00120 and PI18/01813. The IGTP is a Research Center of Catalonia of the CERCA Program/Government of Catalonia. The group has received funding from “la Caixa” CI15-00009 from the European Institute of Innovation and Technology (EIT) PoC-2016- SPAIN-04, which receives support from the European Union’s Horizon 2020 research and innovation program; and from the Fundación para la Innovación y la Prospectiva en Salud en España (FIPSE) program 3594-18.

Institutional Review Board Statement: The animal study protocol was approved by the Institutional Review Board (or Ethics Committee) of the Research Institute Germans Trias i Pujol (IGTP) and the Catalan Government (references 11182 (FUE-2020-01734578 and ID YXVFPXYJ4), 11131 (FUE-2020- 01691361 and ID HYNMX7RXG), and 10407 (FUE-2018-00928437 and ID 0JW23H9GS) on 17 December 2020, 17 December 2015, and 22 February 2019, respectively).

Data Availability Statement: Data are available upon reasonable request.

Acknowledgments: The authors thank the Germans Trias i Pujol Hospital Hematology-Core section from the Clinic Analysis and Biochemistry Service for its contribution in performing the blood coagulation tests, the IGTP Microscopy Platform Core Facility and staff, and the CMCiB at IGTP staff in securing the welfare of the animals throughout all of the experimental procedures.

Conflicts of Interest: The authors declare no conflict of interest.

References

1. Hanson, L.R.; Roeytenberg, A.; Martinez, P.M.; Coppes, V.G.; Sweet, D.C.; Rao, R.J.; Marti, D.L.; Hockman, J.D.; Matthews, R.B.; Frey, W.H., 2nd; *et al.* Intranasal deferoxamine provides increased brain exposure and significant protection in rat ischemic stroke. *J. Pharmacol. Exp. Ther.* 2009, 330, 679–686. [\[CrossRef\]](#) [\[PubMed\]](#)
2. Freret, T.; Valable, S.; Chazalviel, L.; Saulnier, R.; Mackenzie, E.T.; Petit, E.; Bernaudin, M.; Boullouard, M.; Schumann-Bard, P. Delayed administration of deferoxamine reduces brain damage and promotes functional recovery after transient focal cerebral ischemia in the rat. *Eur. J. Neurosci.* 2006, 23, 1757–1765. [\[CrossRef\]](#) [\[PubMed\]](#)
3. DeGregorio-Rocasolano, N.; Martí-Sistac, O.; Ponce, J.; Castelló-Ruiz, M.; Millán, M.; Guirao, V.; García-Yébenes, I.; Salom, J.B.; Ramos-Cabrera, E.A.; Lizasoain, I.; *et al.* Iron-Loaded transferrin (Tf) is detrimental whereas iron-free Tf confers protection against brain ischemia by modifying blood Tf saturation and subsequent neuronal damage. *Redox Biol.* 2018, 15, 143–158. [\[CrossRef\]](#) [\[PubMed\]](#)
4. Millán, M.; DeGregorio-Rocasolano, N.; Pérez de la Ossa, N.; Reverté, S.; Costa, J.; Giner, P.; Silva, Y.; Sobrino, T.; Rodríguez-Yáñez, M.; Nombela, F.; *et al.* Targeting Pro-Oxidant Iron with Deferoxamine as a Treatment for Ischemic Stroke: Safety and Optimal Dose Selection in a Randomized Clinical Trial. *Antioxidants* 2021, 10, 1270. [\[CrossRef\]](#)
5. Chen-Roetling, J.; Chen, L.; Regan, R.F. Apotransferrin protects cortical neurons from hemoglobin toxicity. *Neuropharmacology* 2011, 60, 423–431. [\[CrossRef\]](#)
6. Foster, L.; Robinson, L.; Yeatts, S.D.; Conwit, R.A.; Shehadah, A.; Lioutas, V.; Selim, M.; i-DEF Investigators. Effect of Deferoxamine on Trajectory of Recovery After Intracerebral Hemorrhage: A Post Hoc Analysis of the i-DEF Trial. *Stroke* 2022, 53, 2204–2210. [\[CrossRef\]](#)
7. Wei, C.; Wang, J.; Foster, L.D.; Yeatts, S.D.; Moy, C.; Mocco, J.; Selim, M.; i-DEF Investigators. Effect of Deferoxamine on Outcome According to Baseline Hematoma Volume: A Post Hoc Analysis of the i-DEF Trial. *Stroke* 2022, 53, 1149–1156. [\[CrossRef\]](#)
8. Xi, G.; Keep, R.F.; Hoff, J.T. Mechanisms of brain injury after intracerebral haemorrhage. *Lancet Neurol.* 2006, 5, 53–63. [\[CrossRef\]](#)
9. Koeppen, A.H.; Dickson, A.C.; McEvoy, J.A. The cellular reactions to experimental intracerebral hemorrhage. *J. Neurol. Sci.* 1995, 134, 102–112. [\[CrossRef\]](#)
10. Xi, G.; Keep, R.F.; Hoff, J.T. Erythrocytes and delayed brain edema formation following intracerebral hemorrhage in rats. *J. Neurosurg.* 1998, 89, 991–996. [\[CrossRef\]](#)
11. Wu, J.; Hua, Y.; Keep, R.F.; Nakamura, T.; Hoff, J.T.; Xi, G. Iron and iron-handling proteins in the brain after intracerebral hemorrhage. *Stroke* 2003, 34, 2964–2969. [\[CrossRef\]](#) [\[PubMed\]](#)
12. Huang, F.P.; Xi, G.; Keep, R.F.; Hua, Y.; Nemoianu, A.; Hoff, J.T. Brain edema after experimental intracerebral hemorrhage: Role of hemoglobin degradation products. *J. Neurosurg.* 2002, 96, 287–293. [\[CrossRef\]](#) [\[PubMed\]](#)

13. Zille, M.; Karuppagounder, S.S.; Chen, Y.; Gough, P.J.; Bertin, J.; Finger, J.; Milner, T.A.; Jonas, E.A.; Ratan, R.R. Neuronal Death After Hemorrhagic Stroke *In Vitro* And *In Vivo* Shares Features of Ferroptosis and Necroptosis. *Stroke* 2017, 48, 1033–1043. [\[CrossRef\]](#) [\[PubMed\]](#)
14. Xi, G.; Hua, Y.; Bhasin, R.R.; Ennis, S.R.; Keep, R.F.; Hoff, J.T. Mechanisms of edema formation after intracerebral hemorrhage: Effects of extravasated red blood cells on blood flow and blood-brain barrier integrity. *Stroke* 2001, 32, 2932–2938. [\[CrossRef\]](#)
15. Dixon, S.J.; Lemberg, K.M.; Lamprecht, M.R.; Skouta, R.; Zaitsev, E.M.; Gleason, C.E.; Patel, D.N.; Bauer, A.J.; Cantley, A.M.; Yang, W.S.; *et al.* Ferroptosis: An iron-dependent form of nonapoptotic cell death. *Cell* 2012, 149, 1060–1072. [\[CrossRef\]](#)
16. Wang, Y.; Wu, S.; Li, Q.; Sun, H.; Wang, H. Pharmacological Inhibition of Ferroptosis as a Therapeutic Target for Neurodegenerative Diseases and Strokes. *Adv. Sci.* 2023, 10, e2300325. [\[CrossRef\]](#)
17. Duan, L.; Zhang, Y.; Yang, Y.; Su, S.; Zhou, L.; Lo, P.C.; Cai, J.; Qiao, Y.; Li, M.; Huang, S.; *et al.* Baicalin Inhibits Ferroptosis in Intracerebral Hemorrhage. *Front. Pharmacol.* 2021, 12, 629379. [\[CrossRef\]](#)
18. Han, R.; Wan, J.; Han, X.; Ren, H.; Falck, J.R.; Munnuri, S.; Yang, Z.J.; Koehler, R.C. 20-HETE Participates in Intracerebral Hemorrhage-Induced Acute Injury by Promoting Cell Ferroptosis. *Front. Neurol.* 2021, 12, 763419. [\[CrossRef\]](#)
19. Zhang, Z.; Wu, Y.; Yuan, S.; Zhang, P.; Zhang, J.; Li, H.; Li, X.; Shen, H.; Wang, Z.; Chen, G. Glutathione peroxidase 4 participates in secondary brain injury through mediating ferroptosis in a rat model of intracerebral hemorrhage. *Brain Res.* 2018, 1701, 112–125. [\[CrossRef\]](#)
20. Guan, J.; Williams, C.; Gunning, M.; Mallard, C.; Gluckman, P. The effects of IGF-1 treatment after hypoxic-ischemic brain injury in adult rats. *J. Cereb. Blood Flow Metab.* 1993, 13, 609–616. [\[CrossRef\]](#)
21. Klebe, D.; Inighe, L.; Burchell, S.; Reis, C.; Akyol, O.; Tang, J.; Zhang, J.H. Intracerebral hemorrhage in mice. *Methods Mol. Biol.* 2018, 1717, 83–91. [\[CrossRef\]](#) [\[PubMed\]](#)
22. Aliena-Valero, A.; Rius-Pérez, S.; Pérez, S.; Torregrosa, G.; Salom, J.B. Optimised lyophilisation-based method for different biomolecule single-extractions from the same rat brain sample: Suitability for RNA and protein expression analyses after ischemic stroke. *J. Neurosci. Methods.* 2019, 327, 108402. [\[CrossRef\]](#)
23. Zhang, Y.; Zhang, X.; Wee Yong, V.; Xue, M. Vildagliptin improves neurological function by inhibiting apoptosis and ferroptosis following intracerebral hemorrhage in mice. *Neurosci. Lett.* 2022, 776, 136579. [\[CrossRef\]](#) [\[PubMed\]](#)
24. Byrne, S.L.; Mason, A.B. Human serum transferrin: A tale of two lobes. Urea gel and steady state fluorescence analysis of recombinant transferrins as a function of pH, time, and the soluble portion of the transferrin receptor. *J. Biol. Inorg. Chem.* 2009, 14, 771–781. [\[CrossRef\]](#) [\[PubMed\]](#)
25. Nagaoka, M.H.; Maitani, T. Differed preferential iron-binding lobe in human transferrin depending on the presence of bicarbonate detected by HPLC/high-resolution inductively coupled plasma mass spectrometry. *Biochim. Biophys. Acta* 2000, 1523, 182–188. [\[CrossRef\]](#)
26. Agarwal, R. Transferrin saturation with intravenous irons: An *in vitro* study. *Kidney Int.* 2004, 66, 1139–1144. [\[CrossRef\]](#)
27. Feng, H.; Schorpp, K.; Jin, J.; Yozwiak, C.E.; Hoffstrom, B.G.; Decker, A.M.; Rajbhandari, P.; Stokes, M.E.; Bender, H.G.; Csuka, J.M.; *et al.* Transferrin Receptor Is a Specific Ferroptosis Marker. *Cell Rep.* 2020, 30, 3411–3423.e7. [\[CrossRef\]](#)
28. Wang, G.; Hu, W.; Tang, Q.; Wang, L.; Sun, X.G.; Chen, Y.; Yin, Y.; Xue, F.; Sun, Z. Effect Comparison of Both Iron Chelators on Outcomes, Iron Deposit, and Iron Transporters After Intracerebral Hemorrhage in Rats. *Mol. Neurobiol.* 2016, 53, 3576–3585. [\[CrossRef\]](#)
29. Yang, G.; Qian, C.; Zhang, C.; Bao, Y.; Liu, M.Y.; Jiang, F.; Li, W.; Liu, Y.; Ke, Y.; Qian, Z.M. Hepcidin attenuates the iron-mediated secondary neuronal injury after intracerebral hemorrhage in rats. *Transl. Res.* 2021, 229, 53–68. [\[CrossRef\]](#)
30. Hatakeyama, T.; Okauchi, M.; Hua, Y.; Keep, R.F.; Xi, G. Deferoxamine reduces neuronal death and hematoma lysis after intracerebral hemorrhage in aged rats. *Transl. Stroke Res.* 2013, 4, 546–553. [\[CrossRef\]](#)

31. Ding, H.; Yan, C.Z.; Shi, H.; Zhao, Y.S.; Chang, S.Y.; Yu, P.; Wu, W.S.; Zhao, C.Y.; Chang, Y.Z.; Duan, X.L. Hepcidin is involved in iron regulation in the ischemic brain. *PLoS ONE* 2011, 6, e25324. [\[CrossRef\]](#) [\[PubMed\]](#)

32. Selim, M.; Foster, L.D.; Moy, C.S.; Xi, G.; Hill, M.D.; Morgenstern, L.B.; Greenberg, S.M.; James, M.L.; Singh, V.; Clark, W.M.; *et al.* Deferoxamine mesylate in patients with intracerebral haemorrhage (i-DEF): A multicentre, randomised, placebo-controlled, double-blind phase 2 trial. *Lancet Neurol.* 2019, 18, 428–438. [\[CrossRef\]](#)

33. Tang, X.; Zhang, Z.; Fang, M.; Han, Y.; Wang, G.; Wang, S.; Xue, M.; Li, Y.; Zhang, L.; Wu, J.; *et al.* Transferrin plays a central role in coagulation balance by interacting with clotting factors. *Cell Res.* 2020, 30, 119–132. [\[CrossRef\]](#) [\[PubMed\]](#)

34. Tang, X.; Fang, M.; Cheng, R.; Zhang, Z.; Wang, Y.; Shen, C.; Han, Y.; Lu, Q.; Du, Y.; Liu, Y.; *et al.* Iron-deficiency and estrogen are associated with ischemic stroke by up-regulating transferrin to induce hypercoagulability. *Cir. Res.* 2020, 127, 651–663. [\[CrossRef\]](#) [\[PubMed\]](#)

35. Shah, B.N.; Zhang, X.; Sergueeva, A.I.; Miasnikova, G.Y.; Ganz, T.; Prchal, J.T.; Gordeuk, V.R. Increased transferrin protects from thrombosis in Chuvash erythrocytosis. *Am. J. Hematol.* 2023, 98, 1532–1539. [\[CrossRef\]](#) [\[PubMed\]](#)

36. Doll, S.; Freitas, F.P.; Shah, R.; Aldrovandi, M.; da Silva, M.C.; Ingold, I.; Goya Grocin, A.; Xavier da Silva, T.N.; Panzilius, E.; Scheel, C.H.; *et al.* FSP1 is a glutathione-independent ferroptosis suppressor. *Nature* 2019, 575, 693–698. [\[CrossRef\]](#)

37. Bersuker, K.; Hendricks, J.M.; Li, Z.; Magtanong, L.; Ford, B.; Tang, P.H.; Roberts, M.A.; Tong, B.; Maimone, T.J.; Zoncu, R.; *et al.* The CoQ oxidoreductase FSP1 acts parallel to GPX4 to inhibit ferroptosis. *Nature* 2019, 575, 688–692. [\[CrossRef\]](#)

38. Yue, L.; Luo, Y.; Jiang, L.; Sekido, Y.; Toyokuni, S. PCBP2 knockdown promotes ferroptosis in malignant mesothelioma. *Pathol. Int.* 2022, 72, 242–251. [\[CrossRef\]](#)

39. Jin, J.; Schorpp, K.; Samaga, D.; Unger, K.; Hadian, K.; Stockwell, B.R. Machine Learning Classifies Ferroptosis and Apoptosis Cell Death Modalities with TfR1 Immunostaining. *ACS Chem. Biol.* 2022, 17, 654–660. [\[CrossRef\]](#)

40. Tang, L.J.; Zhou, Y.J.; Xiong, X.M.; Li, N.S.; Zhang, J.J.; Luo, X.J.; Peng, J. Ubiquitin-specific protease 7 promotes ferroptosis via activation of the p53/Tfr1 pathway in the rat hearts after ischemia/reperfusion. *Free Radic. Biol. Med.* 2021, 162, 339–352. [\[CrossRef\]](#)

41. Du, L.; Wu, Y.; Jia, Q.; Li, J.; Li, Y.; Ma, H.; Fan, Z.; Guo, X.; Li, L.; Peng, Y.; *et al.* Autophagy Suppresses Ferroptosis by Degrading TFR1 to Alleviate Cognitive Dysfunction in Mice with SAE. *Cell Mol. Neurobiol.* 2023, 43, 3605–3622. [\[CrossRef\]](#) [\[PubMed\]](#)

42. Lan, T.; Hu, L.; Sun, T.; Wang, X.; Xiao, Z.; Shen, D.; Wu, W.; Luo, Z.; Wei, C.; Wang, X.; *et al.* H3K9 trimethylation dictates neuronal ferroptosis through repressing Tfr1. *J. Cereb. Blood Flow Metab.* 2023, 43, 1365–1381. [\[CrossRef\]](#) [\[PubMed\]](#)

43. Wang, F.; Li, W.L.; Shen, L.J.; Jiang, T.T.; Xia, J.J.; You, D.L.; Hu, S.Y.; Wang, L.; Wu, X. Crocin Alleviates Intracerebral Hemorrhage-Induced Neuronal Ferroptosis by Facilitating Nrf2 Nuclear Translocation. *Neurotox. Res.* 2022, 40, 596–604. [\[CrossRef\]](#) [\[PubMed\]](#)

44. Feng, L.; Wang, L.; Wu, G. Mechanism of RNA-binding protein Lin28 in neuronal ferroptosis after intracerebral haemorrhage. *Folia Neuropathol.* 2022, 60, 35–47. [\[CrossRef\]](#)

45. Zhang, H.; Wen, M.; Chen, J.; Yao, C.; Lin, X.; Lin, Z.; Ru, J.; Zhuge, Q.; Yang, S. Pyridoxal Isonicotinoyl Hydrazone Improves Neurological Recovery by Attenuating Ferroptosis and Inflammation in Cerebral Hemorrhagic Mice. *Biomed. Res. Int.* 2021, 2021, 9916328. [\[CrossRef\]](#)

46. Neag, M.-A.; Mitre, A.-O.; Catinean, A.; Mitre, C.-I. An Overview on the Mechanisms of Neuroprotection and Neurotoxicity of Isoflurane and Sevoflurane in Experimental Studies. *Brain Res. Bull.* 2020, 165, 281–289. [\[CrossRef\]](#)

47. Liu, P.; Yuan, J.; Feng, Y.; Chen, X.; Wang, G.; Zhao, L. Ferroptosis contributes to isoflurane-induced neurotoxicity and learning and memory impairment. *Cell Death Discov.* 2021, 7, 72. [\[CrossRef\]](#)

48. Wang, B.; Zhang, X.; Zhong, J.; Wang, S.; Zhang, C.; Li, M.; Hu, Q.; Wang, S.; Chen, L.; Chen, W.; *et al.* Dexpramipexole Attenuates White Matter Injury to Facilitate Locomotion and Motor

Coordination Recovery via Reducing Ferroptosis after Intracerebral Hemorrhage. *Oxid. Med. Cell. Longev.* 2022, 2022, 6160701. [[CrossRef](#)]

49. Iwai, M.; Kajino, T.; Nakatuchi, M.; Yanagisawa, K.; Hosono, Y.; Isomura, H.; Shimada, Y.; Suzuki, M.; Taguchi, A.; Takahashi, T. Long non-coding RNA TILR constitutively represses TP53 and apoptosis in lung cancer. *Oncogene* 2023, 42, 364–373. [[CrossRef](#)]

50. Mao, X.; Liu, J.; Chen, C.; Zhang, W.; Qian, R.; Chen, X.; Lu, H.; Ge, J.; Zhao, C.; Zhang, D.; *et al.* PCBP2 Modulates Neural Apoptosis and Astrocyte Proliferation After Spinal Cord Injury. *Neurochem. Res.* 2016, 41, 2401–2414. [[CrossRef](#)] [[PubMed](#)]

51. Rosato-Siri, M.V.; Marziali, L.N.; Mattera, V.; Correale, J.; Pasquini, J.M. Combination therapy of apo-transferrin and thyroid hormones enhances remyelination. *Glia* 2021, 69, 151–164. [[CrossRef](#)] [[PubMed](#)]

Disclaimer/Publisher’s Note: The statements, opinions and data contained in all publications are solely those of the individual author(s) and contributor(s) and not of MDPI and/or the editor(s). MDPI and/or the editor(s) disclaim responsibility for any injury to people or property resulting from any ideas, methods, instructions or products referred to in the content.

Targeting Pro-Oxidant Iron with Exogenously Administered Apotransferrin Provides Benefits Associated with Changes in Crucial Cellular Iron Gate Protein TfR in a Model of Intracerebral Hemorrhagic Stroke in Mice

Alexia García-Serran ¹, Jesús Ordoño ¹, Núria DeGregorio-Rocasolano ¹, Marc Melià-Sorolla ¹, Karla Odendaal ^{1,2}, Octavi Martí-Sistac ^{1,3,*} and Teresa Gasull ^{1,*}

Supplementary Materials

Neurobehavioral tests

In the pole test, the mouse was placed head up on the top of a pole (55 cm high and 1 cm diameter) and the time that the mice required to turn around and go down was measured. In the rotarod test the mice was placed on an accelerating rod (Rota Rod LE8200; Harvard Apparatus, Holliston, USA), and the amount of time the mouse spent on the accelerating rod before it fell down was measured. In each session (at 24, 48 or 72 h post ICH), the test was repeated thrice and mean value was depicted. Mice received a 2-3-day training in the test before ICH induction.

Coagulation tests of human blood

Coagulation tests in human blood were performed by the Hematology service of the Germans Trias i Pujol Hospital using 1.8 mL BDTM VacutainerTM Citrate Tubes (Thermo Fisher Scientific; Waltham, USA). A total amount of 129 µL of hATf (Sigma-Aldrich, Saint Louis, USA) or hHTf (Sigma-Aldrich, Saint Louis, USA) at a concentration of 50 mg/mL was placed in the tubes. Physiological saline serum was used as a control. For the test *in vitro* in human blood samples, we performed the experiment as close as possible to the *in vivo* conditions by adding the same amount, concentration, and relative volume of hATf to the freshly extracted human blood plasma samples that ought to be in the blood of mice minutes/hours after the treatment.

Neuronal cell culture

Neuronal cultures were obtained from rat-fetuses (Sprague-Dawley rats from Envigo/Harlan)-cortical neurons and prepared as previously described [3]. At 3 and 11 days-*in-vitro* (DIV), cultures were exposed to either Erastin 20 μ M (MedChem Express; Quimigen; Madrid, Spain) or vehicle (DMSO 0.5%) (Quimigen; Madrid, Spain) for 48 h. Viability was determined using a 3-(4,5-dimethylthiazol-2-yl)-2,5-diphenyltetrazolium bromide colorimetric assay (MTT #M2128; Sigma-Aldrich; Saint Louis, USA) which measures the conversion of the MTT to formazan, a compound that can be quantified by light absorbance at a specific wavelength (490 nm) using a spectrophotometer (Varioskan flash reader; Thermo Fisher Scientific; Waltham, USA). Three experimental replicates for each treatment, or condition were made, in three or four biological replicates (each primary culture comes from a different gestation).

To detect and analyze GPX4 and xCT in WB total protein was isolated from the cortical cultures at different time points of maturation (3, 6, 10 and 13 DIV). Ten μ g of protein were loaded to 4–15% precast polyacrylamide gel (Mini-PROTEAN TGX Precast Protein Gels; Bio-Rad; Hercules, USA) with a molecular weight marker (Precision Plus ProteinTM Standards; Bio-Rad; Hercules, USA) and blotted onto PVDF-LF membranes (Millipore; Burlington, USA). Blocking, incubation and band measurements procedures were made as described in Material and methods section.

Table S1. Commercial proprietary predesigned qPCR forward and reverse primers obtained from IDT

Gene	Encoded protein	Commercial primer name	Sequence
Trf	Endogenous transferrin	Mm.PT.58.23794874	forward: 5'-AGATAGAGTGTGAGTCAGCAGA-3' reverse: 5'-TCTCGTAGTACTCTGCCATGA-3'
Aifm2	Ferroptosis Suppressor Protein 1	Mm.PT.58.30983091	forward: 5'-GACCTTCTCATCTCCACAAGC-3' reverse: 5'-GCCTCTTCCACAGTTAACCC-3'
Gpx4	Glutathione Peroxidase 4	Mm.PT.58.5454337	forward: 5'-CACTGTGAAATGGATGAAAGTC-3' reverse: 5'-CGCAGCCGTCTTATCAATG-3'
Ftl1	Ferritin light chain	Mm.PT.58.32413506.g	forward: 5'-GACTTAGAGCAGCGCCTG-3' reverse: 5'-GAAGCGAGTACAGTGGAAATC-3'
Slc3a2	Solute Carrier Family 3 Member 2	Mm.PT.58.41156435	forward: 5'-ACCTCACTCCAACTACCA-3' reverse: 5'-CATTCATCAGCTTCCCACATC-3'
Slc11a2	Divalent Metal Transporter 1	Mm.PT.58.16122997	forward: 5'-GCTTGCATCTGCTGAAGTATG-3' reverse: 5'-CATGTCAGAACCAATGATTGCC-3'
Tfrc	Transferrin receptor	Mm.PT.39a.22214833.g	forward: 5'-TCAAGCCAGATCAGCATTCTC-3' reverse: 5'-AGCCAGTTCATCTCCACATG-3'
Gapdh	Glyceraldehyde 3-phosphate dehydrogenase	Mm.PT.39a.1	forward: 5'-AATGGTGAAGGTCGGTGTG-3' reverse: 5'-GTGGAGTCATACTGGAACATGTAG-3'
Pcbp2	Poly(RC) Binding Protein 2	Mm.PT.58.7663496	forward: 5'-CATTCCACAGCCAGATTGAC-3' reverse: 5'-CATGAGAAGTAGTTGAGCAGATG-3'

Table S2. Antibodies used for WB and immunohistochemistry (IHC)

Primary antibody	Dilution	Method	RRID/Ref.	Company
Mouse anti-Transferrin receptor (H68.4) (Tfr)	1:1000	WB	AB_2533029	Thermo Fisher Scientific
Mouse anti-glyceraldehyde-3-phosphate dehydrogenase (GAPDH)	1:2000	WB	AB_2536381	
Rabbit anti-ferritin light chain	1:1000	WB	AB_1523609	
Rabbit anti-Glutathione Peroxidase 4 (GPX4)	1:2000	WB	AB_10973901	
Rabbit anti-4 hydroxynonenal (4-HNE)	1:100	IHC	AB_722490	Abcam
Goat anti-mouse Transferrin (mTf)	1:1000	WB	AB_1147328	
Rabbit anti-xCT complex (SLC7A11 subunit – Solute Carrier Family 7 Member 11)	1:1000	WB	AB_2239445	Novus Biologicals
Mouse anti-Neuronal Nuclei (NeuN)	1:100	IHC	AB_2298772	
Mouse anti-NRAMP 2 (G-5), so called divalent metal transporter 1 (DMT1)	1:200	WB	AB_10610255	Santa Cruz Biotechnology
Mouse anti-human Tf (GMA-099)	1:250	WB	Lot#109052B	Green Mountain Antibodies
Rabbit anti-rat Tf	1:150	WB	Cat#55729	Cappel, ICN Pharmaceuticals
Secondary antibody	Dilution	Method	RRID	Company
IRDye-800CW donkey anti-mouse	1:25,000	WB	AB_2716622	Li-COR Bioscience
IRDye-680RD donkey anti-rabbit	1:15,000	WB	AB_2716687	
IRDye-680RD donkey anti-goat	1:10,000	WB	AB_2650427	
Donkey anti-rabbit IgG (H+L) Alexa Fluor 555	1:500	IHC	AB_162543	Thermo Fisher Scientific
Donkey anti-mouse IgG (H+L) Alexa Fluor 555	1:500	IHC	AB_141607	

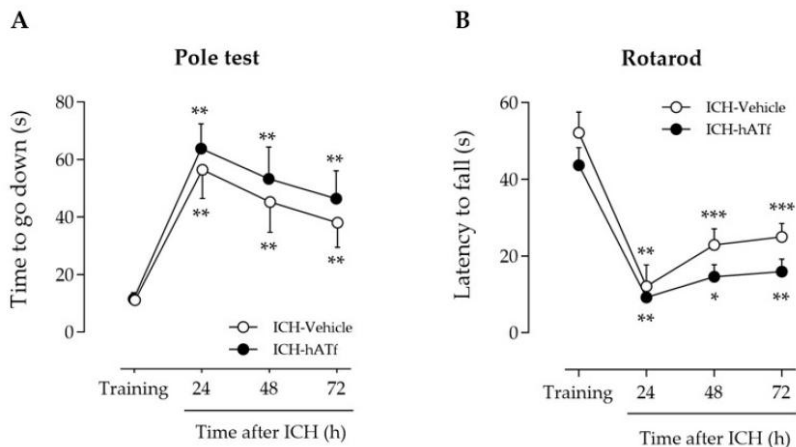
Figure S1

Figure S1. Effect of ICH and treatment with vehicle or hATf on the neurobehavioral performance of mice at 24, 48 and 72 h post-ICH induction in (A) the pole test and (B) the rotarod. * $p<0.05$, ** $p<0.01$ and *** $p<0.005$ vs respective training (repeated measures one-way ANOVA and Tukey's test). Mean and SEM are shown.

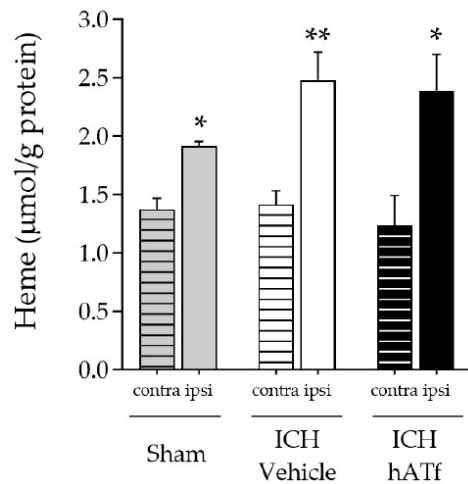
Figure S2

Figure S2. Heme levels in homogenates of the contralateral (contra) and the ipsilateral (ipsi) hemispheres of ICH mice treated with vehicle or hATf; a group of sham mice was included to determine the effect of the surgery associated to the administration of collagenase i.c.v.; * $p<0.05$ and ** $p<0.01$ vs respective contra (paired t -test).

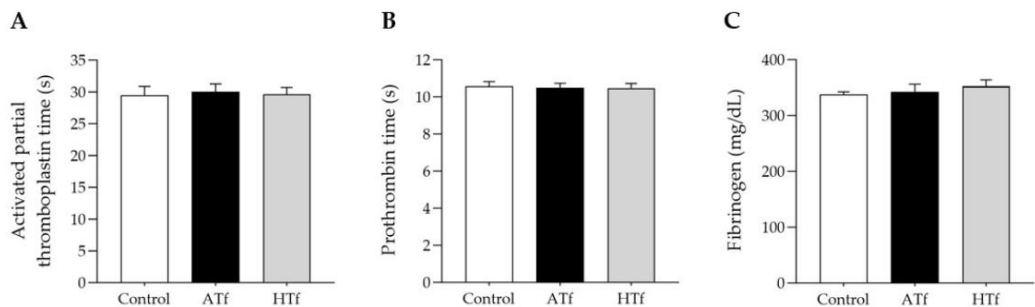
Figure S3

Figure S3. Effect of the addition of human ATf or human HTf on coagulation parameters of freshly obtained human blood: (A) activated partial thromboplastin time, (B) prothrombin time, and (C) fibrinogen. No significant differences were found (one-way ANOVA and Tukey's test).

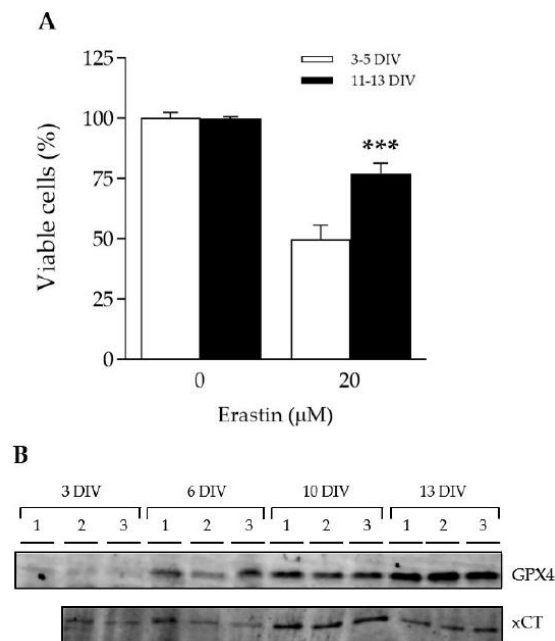
Figure S4

Figure S4. (A) Effect of the ferrostatin inducer erastin on neuronal viability *in vitro*. Young/undifferentiated (3-5 days-*in-vitro*/DIV) and differentiated (11-13 DIV) cell cultures were treated with 0 or 20 μ M erastin for 48 h, and MTT levels were measured to determine % of viable cells. (B) Representative Western Blot images of triplicate wells showing the levels of glutathione peroxidase 4 (GPX4) and cysteine/glutamate antiporter xCT in undisturbed neuronal primary cell cultures at different days *in vitro* (DIV). *** $p < 0.005$ vs 3-5 DIV (*t* test).

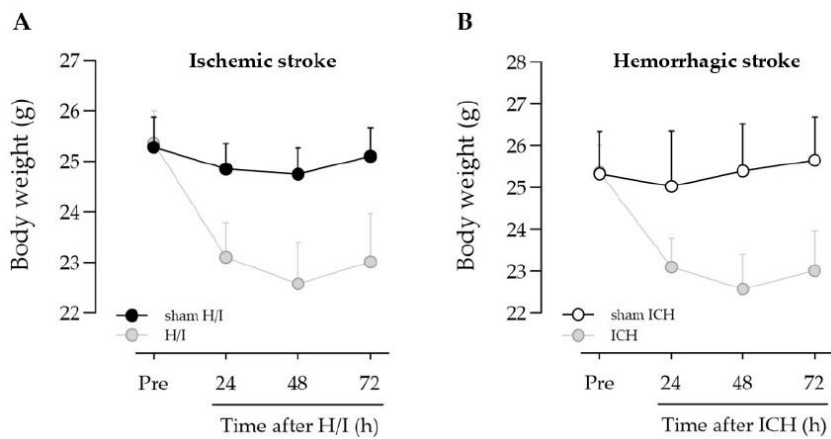
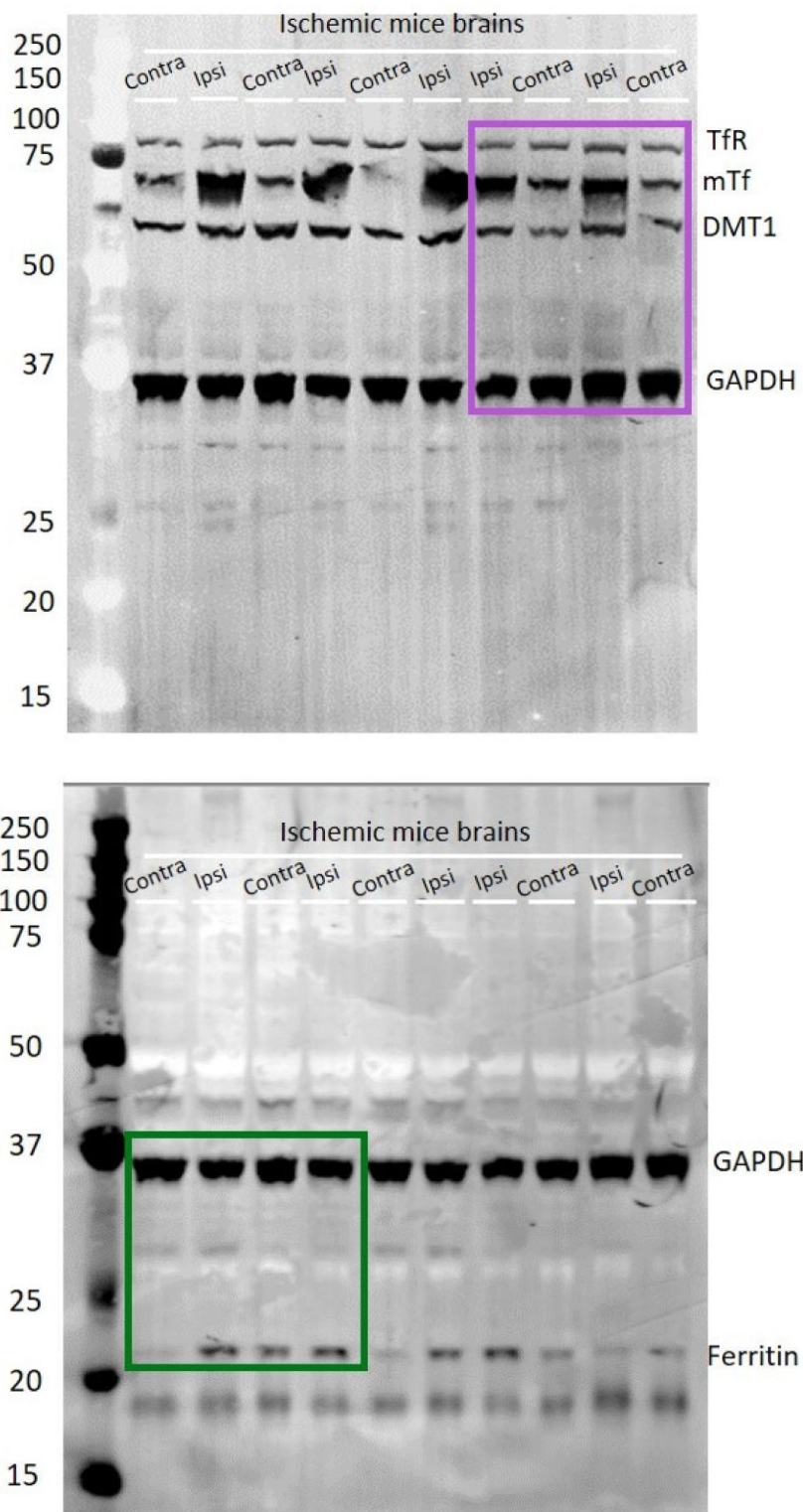
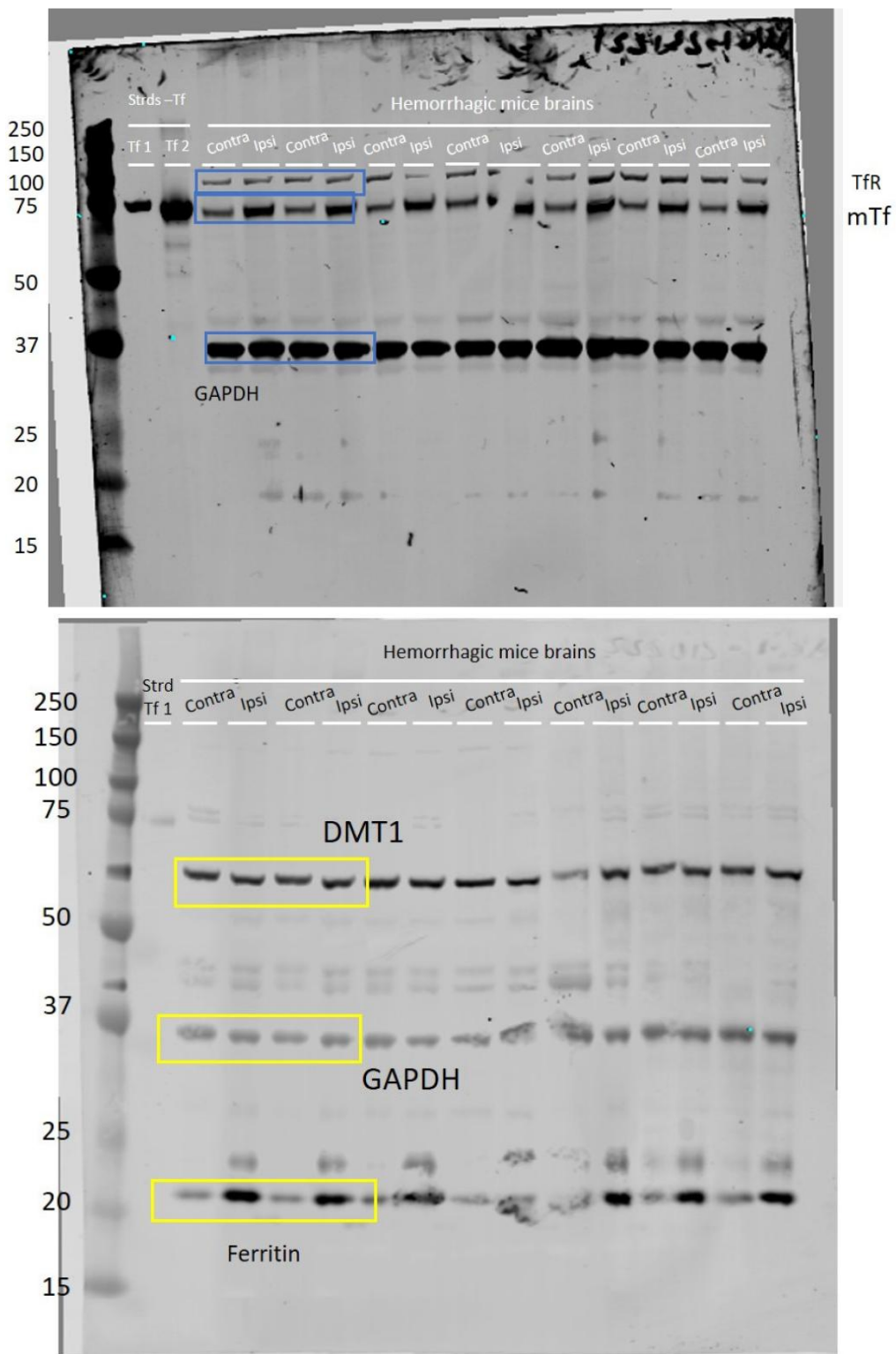
Figure S5

Figure S5. Body weight of (A) sham H/I (n=4) and (B) sham ICH (n=4) mice over the course of the experimental period; no statistically significant changes were observed. For the purpose of comparison, body weight loss of (A) H/I and (B) ICH mice are also depicted in pale gray.

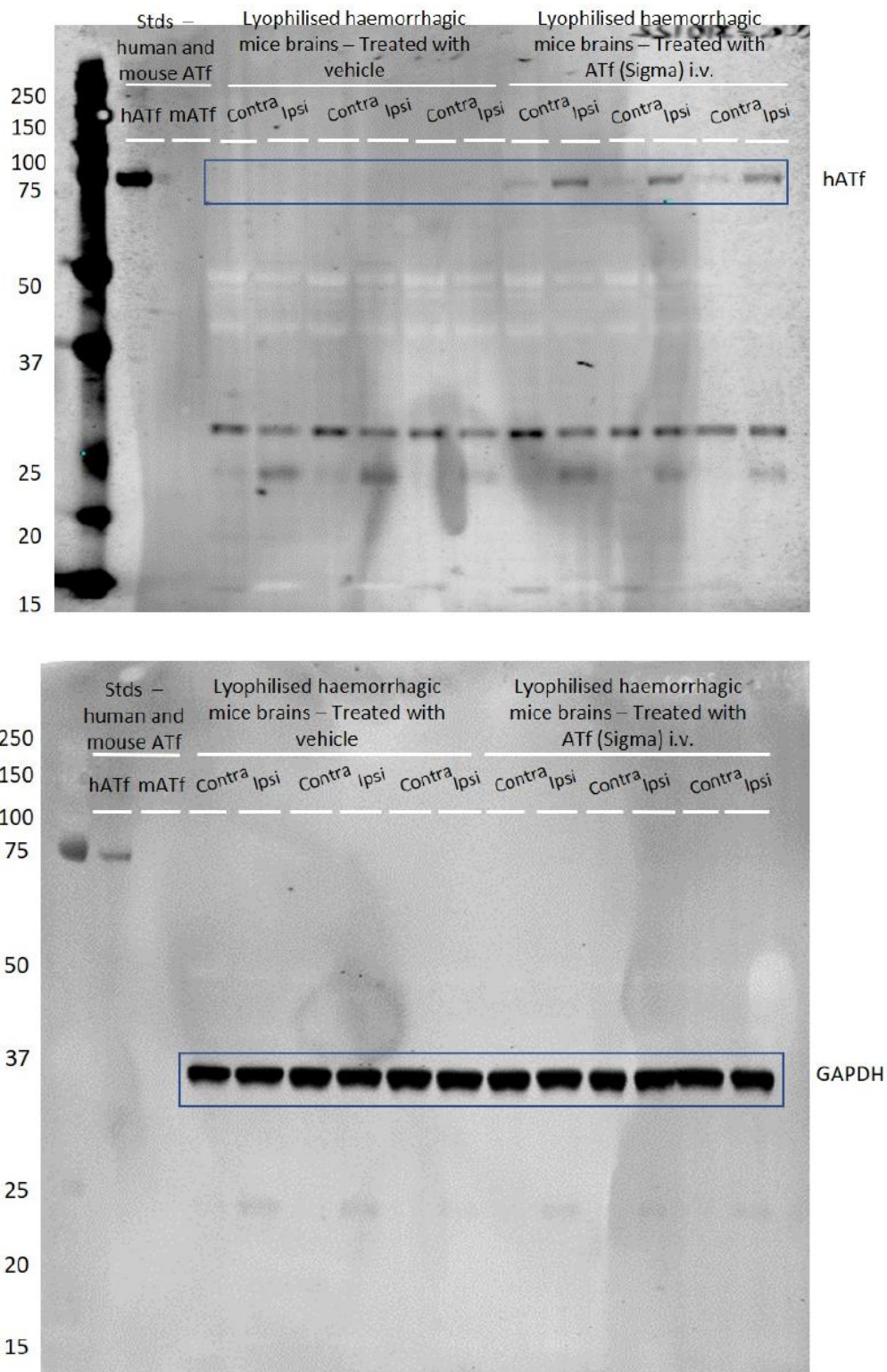
Membrane S1 (Figure 2C)



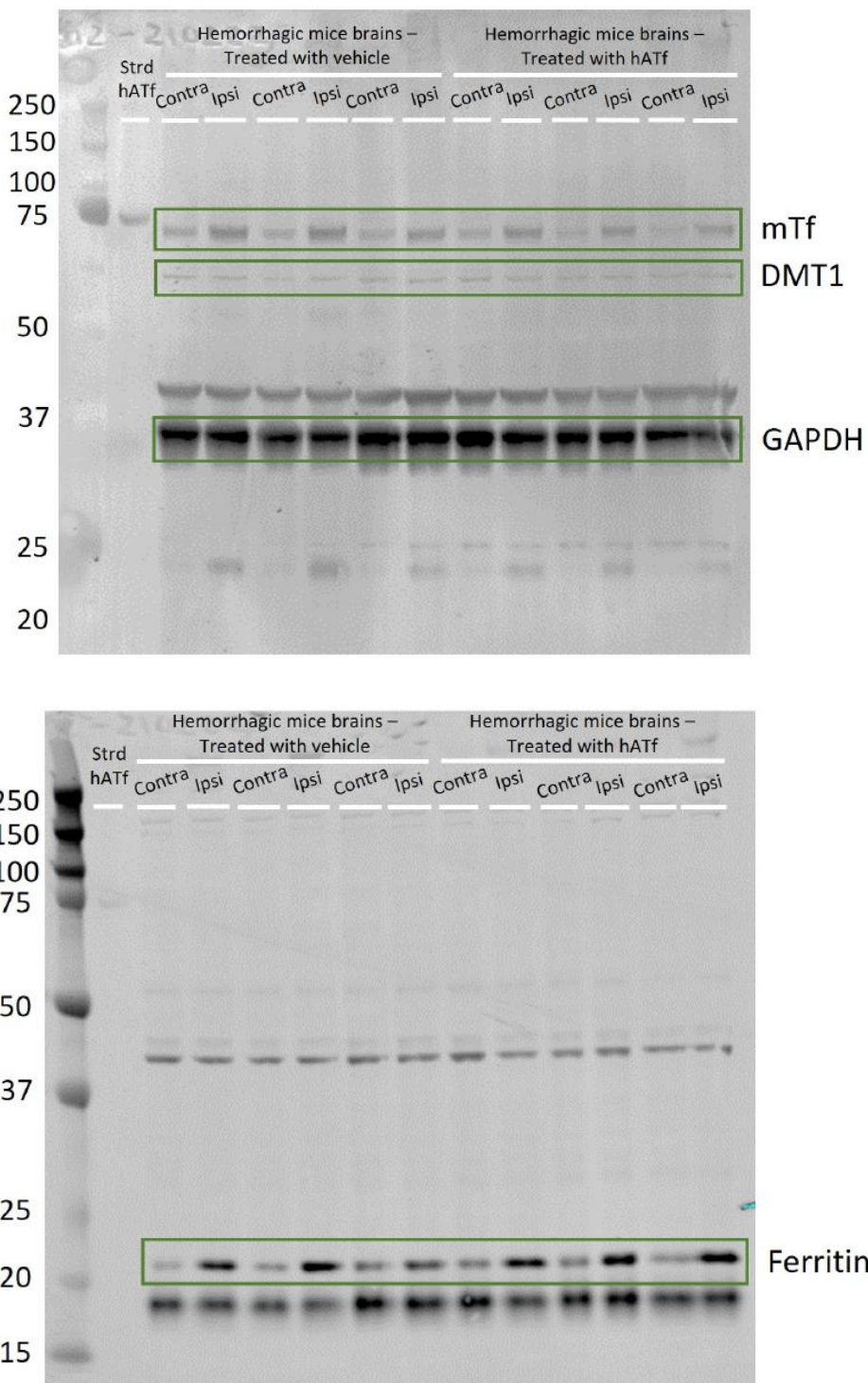
Membrane S1 (Figure 2D)



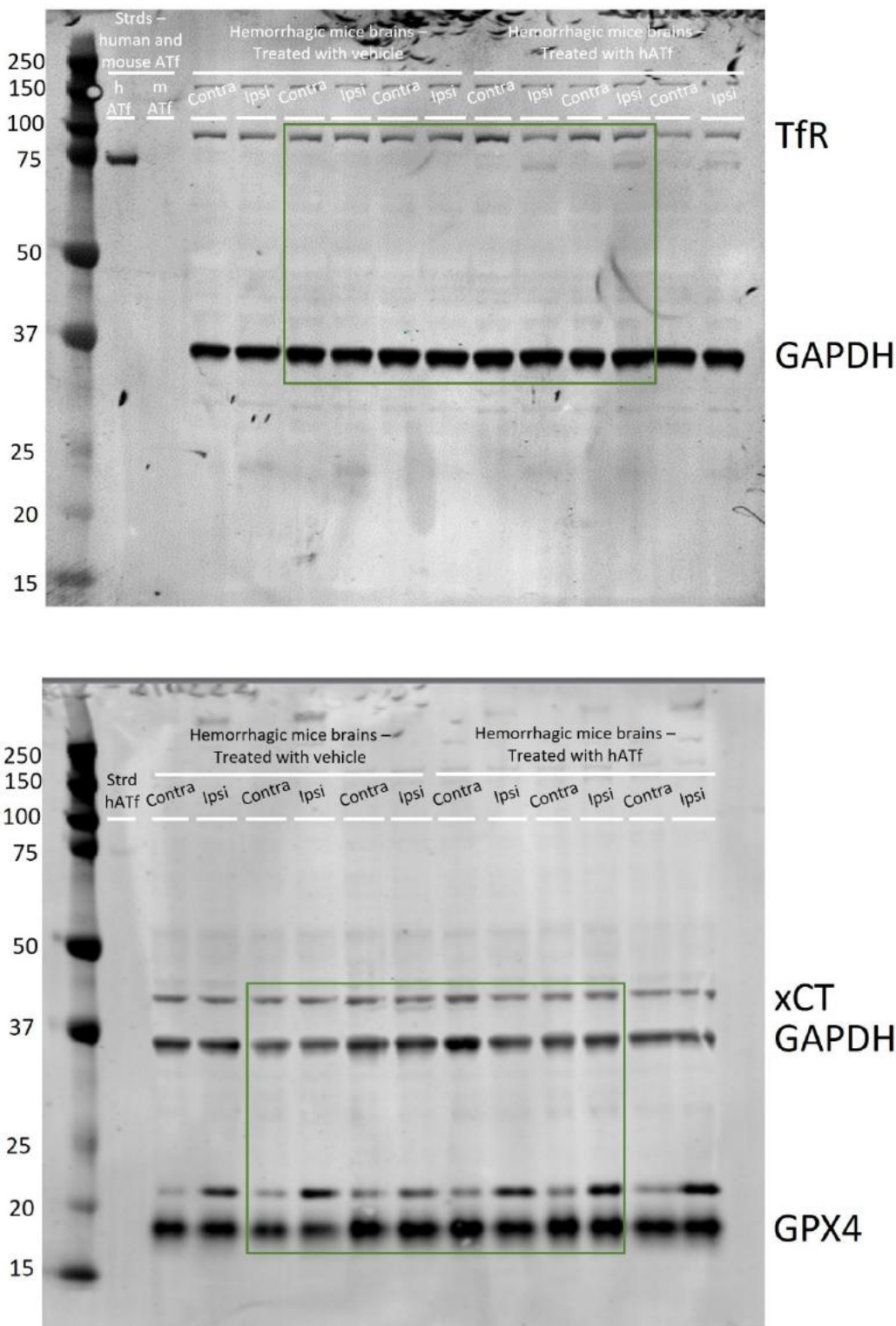
Membrane S3 (Figure 3G)



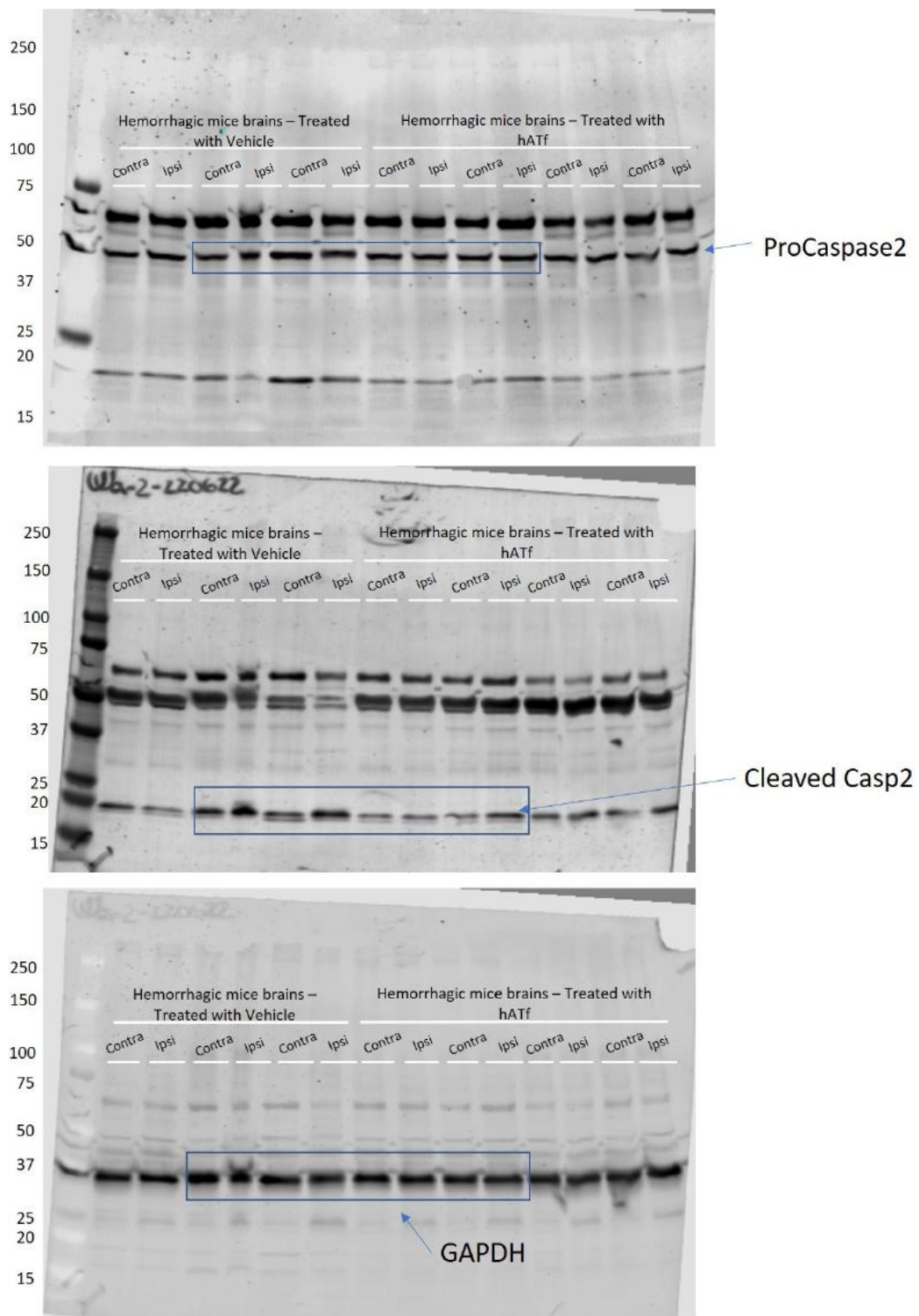
Membrane S4 (Figure 5)



Membrane S5 (Figure 6)



Membrane S6 (Figure 8B)



ANNEX MANUSCRIPT I

Targeting Pro-Oxidant Iron with Exogenously Administered Apotransferrin Provides Benefits Associated with Changes in Crucial Cellular Iron Gate Protein TfR in a Model of Intracerebral Hemorrhagic Stroke in Mice

Alexia García-Serran ¹, Jesús Ordoño ¹, Núria DeGregorio-Rocasolano ¹, Marc Melià-Sorolla ¹, Karla Odendaal ^{1,2}, Octavi Martí-Sistac ^{1,3,*} and Teresa Gasull ^{1,*}

Imaging Techniques

At the time of the manuscript submission, we had tried unsuccessfully to see the hemorrhage expansion at the MicroCT (SkyScan 1076; Bruker; Kontich, Belgium) available in our facilities using the iodine contrast used in the clinics (Iodixanol; VisipaqueTM 320 mg/mL; GE Healthcare; Chicago, IL, USA). This microCT system, in contrast with clinical used CTs, does not detect hematoma blood or low-performance contrasts, e.g. Iodixanol.

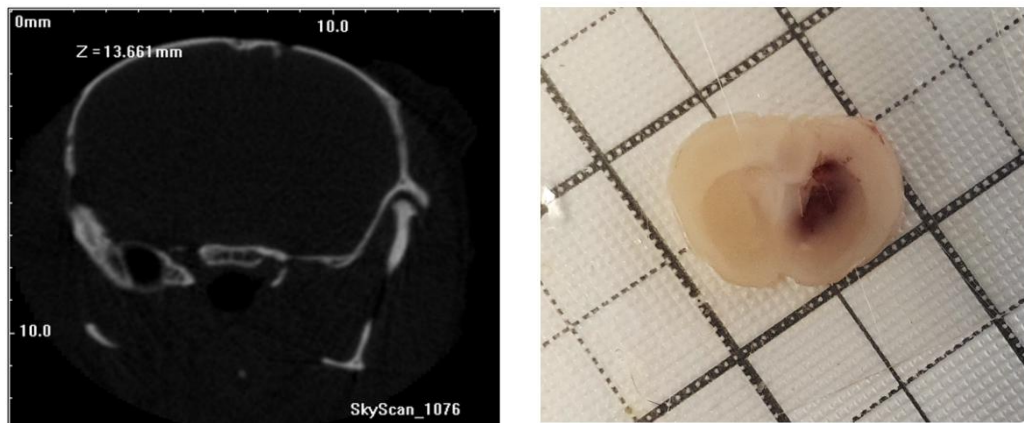
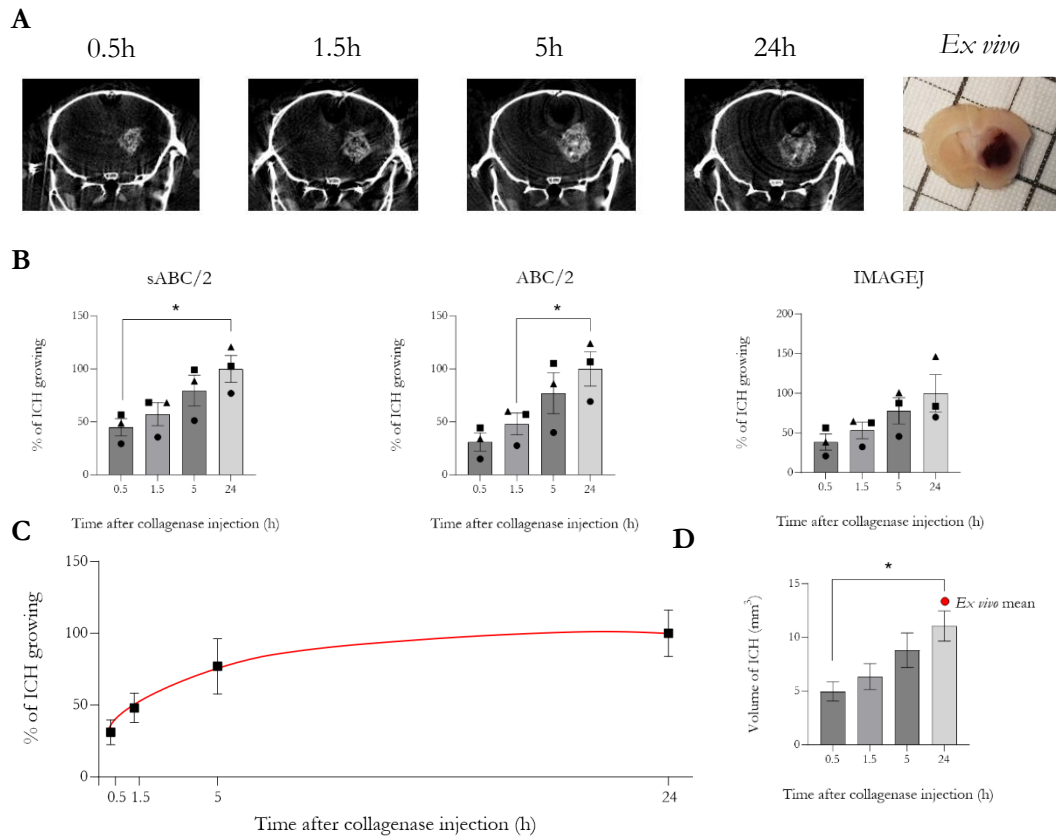


Figure AP1. Coronal section of a mouse brain acquired via MicroCT scan. The same image was observed with and without contrast administration. Proper contrast delivery was verified *de visu* by confirming its presence in the bladder and kidneys. **(Left)** Reconstructed MicroCT image. **(Right)** *Ex vivo* slice of the brain imaged on the MicroCT showing the corresponding hemorrhagic lesion.

After the manuscript was accepted, we tested a preclinical-high-performance contrast (ExiTronTM nano 12000 CT contrast agent; Viscover; Berlin, Germany) injected in the blood of the mice shortly after the surgical collagenase-ICH procedure finished. We were finally able to detect the bleeding in the intracerebral parenchyma in MicroCT images starting 30 min, 1.5 hours, 5 hours and 24 hours after collagenase injection. The hemorrhage volume calculated *in vivo* on the CT images at 24 hours and that measured *ex vivo* at 24 hours was similar.

The measurement of the hemorrhage was made using the simplified ABC/2 formula, the ABC/2 formula as well as in Image J software (all methods explained in **Materials and Methods, Section 2.8.2.1.**).



Results

Figure AP2. Coronal sections of a mouse brain acquired via MicroCT scan with ExiTron™ nano 12000 CT contrast agent. **(A)** Reconstructed MicroCT images at different time points after ICH-collagenase induction with the corresponding *ex vivo* brain slice 24h after collagenase administration. **(B)** Hemorrhagic measurements using different formulas. **(C)** Percentage of growing respect to the mean at 24 hours calculated with the sABC/2 formula. **(D)** Volume of ICH at different time points calculated from MicroCT images with the sABC/2 formula compared to the *ex vivo* ICH volume mean; *ex vivo* mean ICH volume is depicted as a red dot.

Hemorrhage volume

During the *ex vivo* hemorrhage quantification in the different experiments, we could see two different regions in the hemorrhagic area; that we called the hemorrhagic core and the hemorrhagic extension.

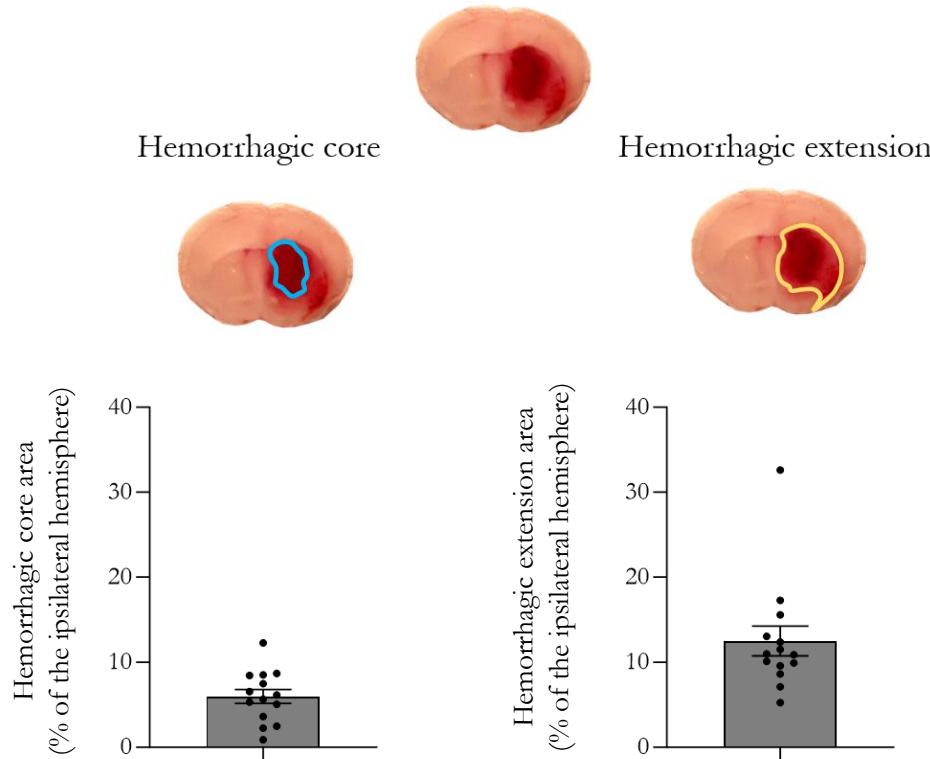


Figure AP3. Differences in the hemorrhagic areas when considering a restrictive or a less restrictive criterion. Coronal sections of a mouse brain and the measurement of the hemorrhagic core and hemorrhagic extension areas in 14 animals. We defined the hemorrhagic core area as the darker zone of the hemorrhage. The hemorrhage extension is all the area in which blood was visible.

MANUSCRIPT II

Machine learning analysis of behavior-related data from a single neurobehavioral test predicts the occurrence and severity of stroke in mice

Currently under submission (2025)

Machine/Deep Learning from Neurobehavioral Data Predicts Stroke Occurrence and Severity in Mice

Alexia García-Serran^{a,1} , Núria Mercadé Besora^{b,c,d,1} , Marina Mas-Argemí^{b,e} , Núria De-Gregorio-Rocasolano^a , Marc Melià-Sorolla^a , Marta Alcalde-Herraiz^{b,c}, Clara Prats^c, Teresa Gasull^{a,2} , Martí Català^{d,*}, Octavi Martí-Sistac^{a,f,*} 

^a Cellular and Molecular Neurobiology Research Group, Fundació Institut d'Investigació en Ciències de la Salut Germans Trias i Pujol (IGTP), Universitat Autònoma de Barcelona (UAB), Badalona, Catalonia, Spain

^b Comparative Medicine and Bioimage Centre of Catalonia (CMCIB-IGTP), Badalona, Catalonia, Spain

^c Department of Physics, Universitat Politècnica de Catalunya (UPC-BarcelonaTech), Barcelona, Catalonia, Spain

^d Centre for Statistics in Medicine, Nuffield Department of Orthopaedics, Rheumatology, and Musculoskeletal Sciences (NDORMS), University of Oxford, Oxford, United Kingdom

^e Medicine and health science faculty, University of Barcelona (UB), Barcelona, Catalonia, Spain

^f Department of Cellular Biology, Physiology and Immunology, UAB, Bellaterra, Catalonia, Spain

ARTICLE INFO

Keywords:

Machine learning
Experimental stroke
Neurobehavioral performance
Computational method
DeepLabCut
Prediction
3R animal research

ABSTRACT

Background and objective: Stroke-induced neurological impairment is commonly assessed with researcher-annotated, semiquantitative scoring methods, which are prone to bias. This study aimed to develop computational algorithms to automatically detect and grade experimental strokes in mice using video recordings by: 1) quantifying neurobehavioral variables, and 2) using these data to build models to predict stroke presence and severity in each mouse.

Methods: Adult C57BL/6J mice were subjected to hypoxia/ischemia (H/I) to generate a range of stroke severities. Performance in neurobehavioral tests, including the tape removal (TR) test, was recorded before and after stroke and visually assessed. Infarct volume was determined *ex vivo*. Body part positions in TR test videos were tracked with DeepLabCut (DLC). Data were processed in MATLAB, and predictive variables were selected by LASSO regression to train models for stroke detection and severity grading. The model was also tested in a second experiment with collagenase-induced intracerebral hemorrhage (ICH), in which hematoma burden was determined *ex vivo*.

Results: Infarcted mice, especially with severe lesions, showed significant neurobehavioral decline compared to non-infarcted controls in classical scores. The TR test provided the highest suitability for computational analysis. Several DLC-derived variables related to posture, motor control, and performance in the TR test correlated with stroke presence and severity. DLC-based models predicted stroke with high accuracy: 96% in ischemic stroke and 90% in ICH, and classified mice by severity.

Conclusions: We have developed an objective, quantitative, and time-efficient deep learning method for consistent behavioral assessment across time points and stroke subtypes. This approach improves preclinical research by: 1) standardizing outcome evaluation, and 2) enabling exclusion of animals predicted not to develop stroke damage before treatment allocation.

Corresponding author

E-mail address: tgasull@igtp.cat or teresagasull@yahoo.com (T.G.).

¹These authors contributed equally as co-first authors.

*These authors contributed equally

1. Introduction

Each year, more than 12 million people suffer a stroke, with 4 million deaths, and one-third of the stroke survivors having long-term cognitive impairment [1]. Animal disease modelling is essential in preclinical stroke research. It contributes to shed light on pathophysiological hallmarks of the disease and is required to test new treatments [2]. An ischemic stroke modelling in rodents with minimal surgical procedure (no invasion of the brain, only using systemic procedures) was first developed several decades ago by inducing a brain hemisphere ischemia by unilateral common carotid artery occlusion followed by inhalational hypoxia in adult rats, that was coined the hypoxic/ischemic (H/I) method [3] and later adapted to adult mice [4,5]. When using moderate periods of hypoxic exposure, a high inter-individual variability to develop lesion is observed in this method, from no infarct to large lesions, as compared with other stroke-inducing procedures [4]. This variability mimics what is observed in the stroke outcome in human populations, being of interest to test the effectiveness of a prediction/classification method for stroke outcome assessment in mice.

In the clinical arena, the assessment of the neurological impairment caused by stroke uses stroke rating scales based on nominal or ordinal data. This involves clinical judgments that can introduce a degree of subjectivity, depending on the observer's experience and interpretation. Similar scoring systems, not devoid of possible unintended subjective bias/error and semiquantitative as well, are used in most preclinical experimental set-ups of stroke in rodents [6,7], although some other neurobehavioral tests rely in researcher-annotated quantitative data [8,9,10]. Then, an accurate assessment of post-stroke deficits is crucial in experimental research. The implementation of quantitative, objective, and automated methods to assess the neurological dysfunction is a must to: 1) provide consistent data collection over extended timeframes, through multiple observations, and across

different laboratories in order to set up multicentric high quality preclinical studies, and 2) test neurological benefits provided by new treatments or rehabilitation programs in pre-clinical studies to select the best treatment options to go into clinical trials. In this regard, the state-of-the-art algorithm DeepLabCut (DLC) provides an opportunity for non-invasive animal tracking [11,12] by obtaining the coordinates of predefined body parts of the animal from video recordings in different species [11-14], which is useful for assessing motor deficits. This neural network model is based on transfer learning, thus requiring little training to later assess multiple and challenging behaviors.

We aimed to develop a machine learning-based predictive method to: objectively detect, quantify, and analyze the abnormal neurobehavior of mice exposed to experimental stroke; to infer the occurrence of cerebral damage from these anomalies; and to classify each mouse according to stroke severity, without requiring costly imaging equipment (e.g. MRI). We used DLC on video recordings of freely moving mice in a single neurobehavioral test, the tape removal (TR) test, and developed machine learning (ML) algorithms to create a quantitative, objective, time-efficient, and predictive system. This system enabled the identification of mice without brain ischemic damage, and the classification of each mouse as having no infarct, mild infarct, or severe infarct after exposure to hypoxia/ischemia (H/I). The system was also tested in a collagenase-induced intracerebral hemorrhage (ICH) mouse model, and the tool also predicted neurological impairment in these mice. Ultimately, this innovation offers a novel computational tool to improve the quality of preclinical trials and to quantify the benefits of potential neuroprotective or neurorepair treatments in preclinical stroke research.

2. Materials and methods

2.1. Animals

A total of 73, 9-10-week-old, C57BL/6J male mice were used in the whole study. Fifty

six of them were exposed to cerebral H/I and were used to: 1) in the initial experiments, to find the optimal time of H/I exposure providing a good percentage of mice with infarct, low mortality, and high inter-individual variability; 2) to assess the adequacy of the TR test to properly correlate with the infarct volume; and 3) in the main experiment to develop the predictive model (see [Supplementary Table 1](#), [Figure S1](#) and [Figure S2](#)). Seventeen mice were exposed to ICH, and fifteen underwent the evaluation of the model's performance in this stroke subtype.

The procedures used to induce stroke, to perform and video record the neurological tests, to determine infarct/hematoma volume, and the timings to assess neurological impairment in the video recordings are explained in detail in [Supplementary materials](#) and schematically depicted in [Figure 1](#) [10]. It should be noted that the total sample size of mice to be exposed to the H/I protocol in the main experiment was calculated based on previous data from the group, in order to ensure a sufficient number of animals in each experimental group for meaningful statistical comparisons.

After the H/I experiment, mice were categorized into groups based on *ex vivo* infarct assessment by 2,3,5-triphenyltetrazolium chloride (ITC) staining, according to the percentage of brain volume affected, as follows: no stroke (NS) (considered sham or controls) and stroke (S), which was further divided into mild stroke (MS) and severe stroke (SS). Each mouse was considered an experimental unit, and no randomization was required. The sample size (n) of each experimental group is reported in [Supplementary Table S4](#). The *ex vivo* hematoma assessment after the ICH experiment can be assessed by delineating either deep red areas (DR) or extensive red areas (ER) (see [Supplementary material](#)).

After the stroke induction, neurological impairment was assessed by several neurobehavioral tests as explained in the [Supplementary material](#). From them, the TR test was selected, and video recordings of the

performance of mice in it were used. In brief, in each TR test, a small piece of adhesive tape was placed on the mouse's forepaw, and the time taken to remove it (TR time) was assessed.

2.2. *Computational assessment of the neurological impairment*

Detailed methods for applying DLC machine learning to video recordings, MATLAB post-processing for *in vivo* pose estimation, and the development of predictive ML models are provided in the [Supplementary Materials](#). Two models were generated: one to predict the occurrence of stroke and another to predict its severity.

In each video of the test, DLC was used to track predefined body parts, including the tape, and MATLAB processing of the resulting datasets yielded up to 22 behavioral variables such as distances, velocities, TR time, and turning bias ([Supplementary Video S1, S2](#); [Supplementary Table S2](#)). Among them, TR time emerged as a key variable because of its correlation with brain injury. TR time was estimated computationally based on the positions and velocities of the paws, nose, and the tape (see [Supplementary Figures S3 and S4](#)). It was also found to increase after ICH. To avoid tracking errors caused by the researcher's hand, the first analyzable frame was automatically detected, and incoherent distance estimates between body parts were pre-established using preset thresholds (see [Supplementary Figure S6 and Table S3](#)).

For quality control, computational TR times were validated against expert annotations in rodent neurobehavior. Differences of ≤ 2 s were considered acceptable, as similar variability occurs between independent human raters. For model construction, a set of potential predictors derived from DLC variables was introduced into Least Absolute Shrinkage and Selection Operator (LASSO) regressions. A logistic LASSO regression was used to identify predictors of stroke occurrence, while a linear LASSO regression was applied to predict stroke severity.

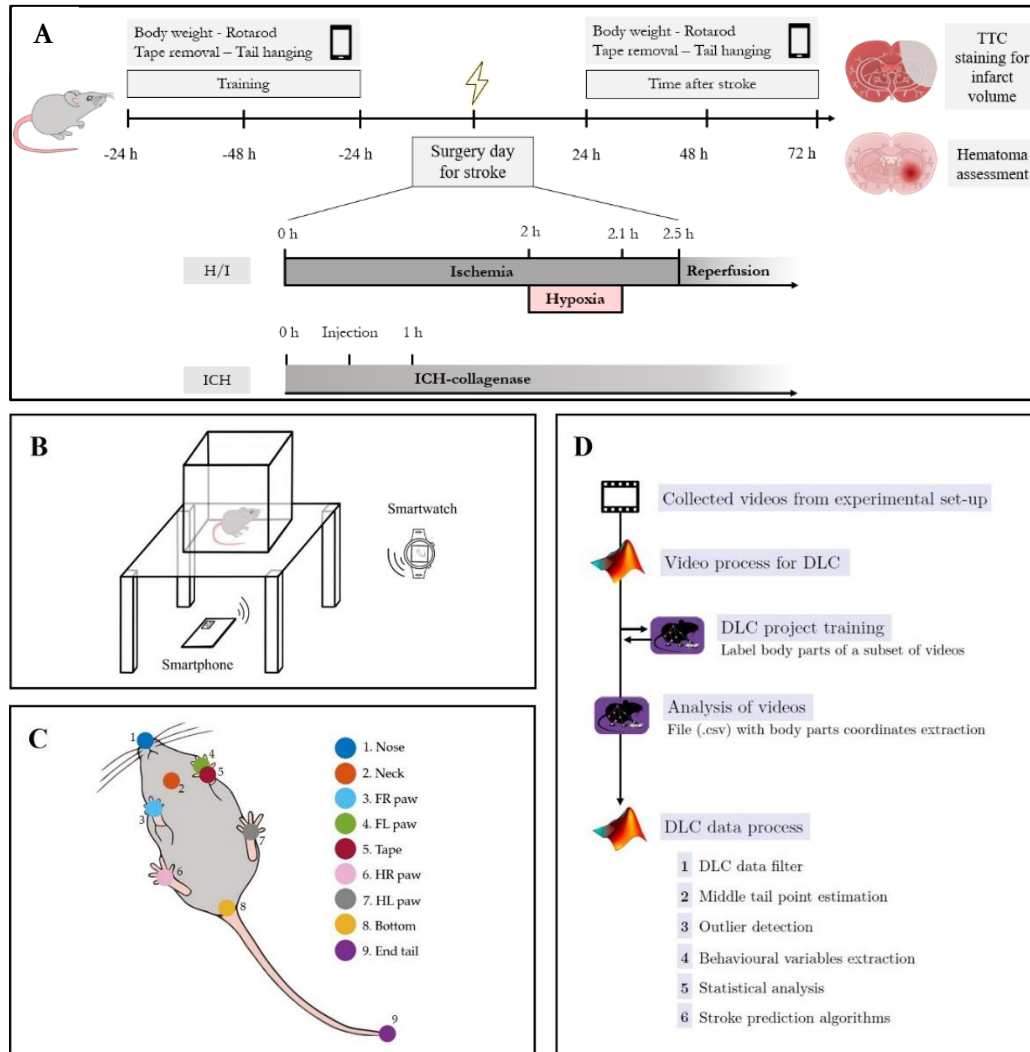


Figure 1. Infographics of the experimental and computational workflow. (A) Chronological sequence of experimental interventions on mice over the course of the experiment; mice performance in the neurobehavioral tests was recorded using a smartphone at different time points pre- and post-stroke induction. (B) Scheme of the experimental setup; the mice performance in a transparent box in the tape removal test was recorded with a smartwatch-controlled smartphone (video of the behaviour test methodology and target body parts virtual labelling are shown in the [Supplementary Video S1](#)). (C) Overview of the body parts selected to be labelled in each mouse in the DLC project training. (D) Flowchart depicting the steps of DLC video processing and subsequent data analysis of mice neurobehavior in the tape removal test; quality controls were implemented along the procedure. TTC: 2,3,5-triphenyltetrazolium chloride, FR paw: front right paw, FL paw: front left paw, HR paw: hind right paw, HL paw: hind left paw, DLC: DeepLabCut.

2.3. Statistics

Sample size (n), and mean, SD, and SEM of each experimental group and time point are depicted in [Table S4 and S5 in Supplementary materials](#). Original or log-transformed data were normally distributed (Kolmogorov-Smirnov test) and showed homoscedasticity of variances (F-test of Bartlett test). Data, either measured de visu or obtained computationally, were analyzed with *t*-test or one-way ANOVA using MATLAB or GraphPad Prism. Data are shown in the graphs as Mean \pm SEM; statistical significance was considered at $p<0.05$. LASSO regression used to select the best predictor variables and to construct the computational predictive models was implemented in MATLAB.

The analytical code for DLC data is publicly available on the internet at https://github.com/nmrcadeb/DeepLabCut_to_predict_stroke_on_mice.

3. Results

3.1. Automated DLC video processing and subsequent data analysis

A total of 562 videos were generated in the main H/I experiment that were pre-processed by resizing them to 900x900 pixels, processing only the ROI (within the box perimeter), trimming the start frame, and selecting, based on k-means algorithm, the frames used to carry out the initial DLC training. Once DLC was trained, videos were analyzed automatically by DLC; this provided for each video a large csv file with the coordinates of each one of the selected body parts of the mouse along all the duration of the tape removal test (see flowchart in [Figure 1D](#)). These data were converted into 22 neurobehavioral features/variables ([Figure 1D, DLC data process, step 4](#)) which were statistically evaluated as predictive of stroke occurrence or severity as compared with the same variables pre-stroke induction.

Only the videos post-stroke induction (50% of the videos recorded) were used for the individual prediction of the stroke occurrence

and infarct outcome (i.e., infarct volume) in each mouse ([Figure 1D, DLC data process, step 6](#)). The 279 videos from the ICH experiment were processed similarly to extract relevant features and feed them into the prediction models.

3.2. Effects of H/I on TTC-assessed infarct size, body weight loss, and researcher-scored neurobehavioral performance in several tests. Effectiveness of the tape removal test to distinguish between stroke severity groups

In the main experiment, 12 out of 24 mice exposed to H/I developed infarct (50%), as assessed *post-mortem* using TTC staining 72h after the H/I procedure ([Figure 2A](#)). Due to the high variability intentionally introduced by the chosen experimental H/I method, the infarct volume in individual mice that developed stroke ranged from 4.1% to 56.5% of the ipsilateral (stroked) hemisphere, with a mean value of 27.8% ([Supplementary Figure S2B](#)). Half of the stroked mice (n=6) were classified as mild stroke (MS) and the other half (n=6) as severe stroke (SS), as they presented an infarct volume smaller or larger than 28%, respectively. This mean of brain infarct is similar to the mean of brain infarct observed in a population of mice after 60 minutes ischemia exposure by middle cerebral artery occlusion using the intraluminal filament method [15] or that reported for a similar procedure and exposure time in rats [16]. Despite that in our previous pilot experiment (n=12) the percentage of infarcted mice was higher (67%), in both experiments, we observed a significant correlation between infarct size and TR time ([Supplementary Figures S1B and S2C](#)).

Group comparison showed that 1) stroked (S) mice lost body weight; this effect was more pronounced and long-lasting in SS than in MS mice ([Figure 2B](#)), 2) Neurological assessment in the tail hanging test showed that SS mice doubled the % of contralateral turns as compared to themselves pre-intervention or to the non-stroke group post-intervention ([Figure 2C and 3](#)) in the rotarod test, SS mice underperformed as they stood less time onto the rotating rod at 24h ([Figure 2D](#)).

The tape removal test ([Figures 2E-F](#)) allows to statistically distinguish NS from SS, NS from MS and, interestingly, mild (MS)

from severe (SS) stroke. Thus, mice that developed infarct increased the time needed to remove the tape from the contralateral forepaw (Figure 2E); in particular, SS mice required more time than MS mice to remove the tape. In addition, SS mice also showed some impairment of the ipsilateral forepaw performance (Figure 2F). The tape removal test has been reported to be able to measure the neurological damage in the subacute phase and, interestingly, to measure the improvement after a rehabilitation program in stroke animals when assessed by human raters [17]. In addition, in our hands, the tape removal test successfully measured the neurological impairment in mice exposed to experimental intracerebral hemorrhage when measured at 24h

and up at least 3 days after the ICH induction procedure (Supplementary Figure S5).

3.3. *Following DLC training, computationally assigned labels to tape and body parts were accurately tracked in the TR test videos of H/I-exposed mice*

DLC network was trained to computationally assign labels to nine selected mice body parts of interest (and the tape); eight of them were successfully placed whereas the one at the mid-point of the tail was inconsistently placed (see Supplementary Figure S3) and was not further considered in the DLC project. The resultant trained network was applied to the 562 videos obtained at different time points pre- and post-stroke H/I

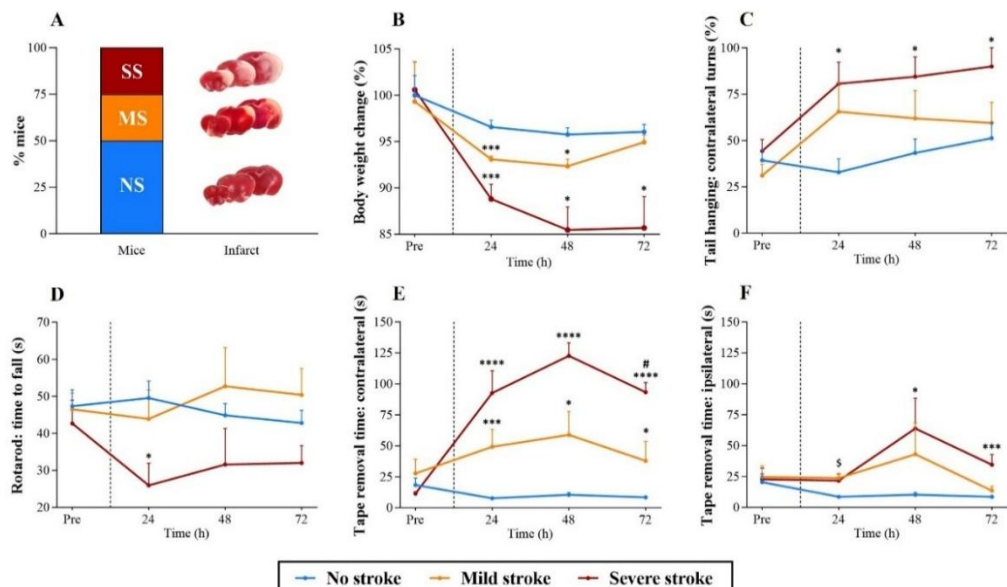


Figure 2. Researcher-scored experimental output of the H/I procedure in mice using several neurobehavioral tests indicate that the tape removal test distinguishes between different levels of stroke severity. (A) Stacked column graph showing the percentage of mice with no stroke (NS, blue), mild stroke (MS, orange) and severe stroke (SS, maroon) after exposure to H/I (left), and representative pictures of TTC-stained brain slices (right). Effect of the stroke occurrence and severity on researcher-assessed (B) body weight change, (C) percentage of contralateral turns in the tail hanging test, (D) performance in the rotarod test as determined by the time to fall from the roller, (E) contralateral stroke-induced paretic front paw performance and (F) ipsilateral front paw performance, as assessed as the time required by the mice to remove the tape from the paw. Contralateral front paw is more affected because is mainly under control of the ipsilateral (stroked) brain hemisphere. Tests were video recorded and assessed independently by 2 researchers. Mean and SEM are shown. For comparisons between the three groups of mice at the same time point: * $p<0.05$, ** $p<0.005$ and *** $p<0.001$ vs no infarct; # $p<0.05$ severe infarct vs mild infarct; \$ $p<0.05$ mild infarct vs no infarct (one-way ANOVA followed by Tukey's test).

induction. Sequential steps in DLC processing are depicted in [Figure 1D](#) and [Supplementary Video S2](#).

Manual validation of DLC raw data showed that, on average, 95.50% of all the labels (body parts and the tape) were correctly placed ([Figure 3A](#)). Most of the remaining 4.50% misplaced labels had a small likelihood, so they had a reassigned value resulting from lineal interpolation of data obtained from the closest videoframes, as explained in the DLC post-processing section in the [Supplementary](#)

[materials](#), finally reducing this misplacement to only 0.65% of the data. [Figure 3B](#) shows the Receiver Operating Characteristic (ROC) curves for each one of the labels, showing good Area Under the Curve (AUC) values.

There was a good agreement between computational and experimental tape removal time, even when considering a difference of less than 2 seconds ([Figure 3C](#)). The mean difference between computational and experimental TR time was 1.77 seconds.

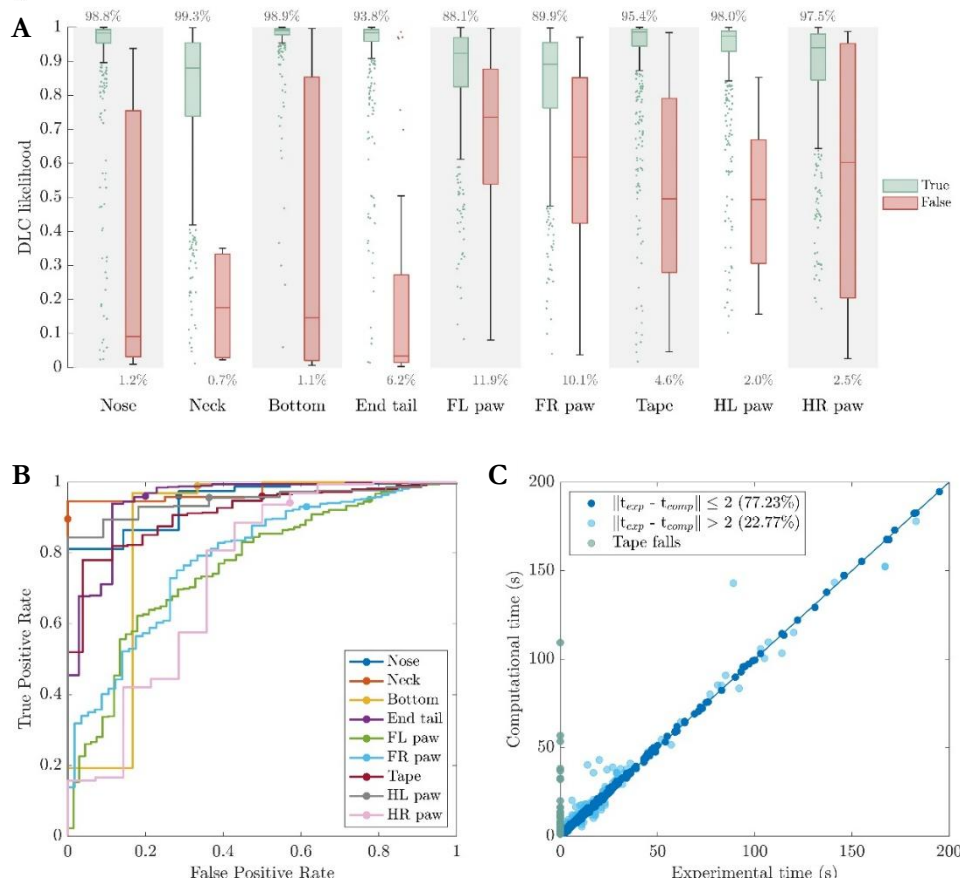


Figure 3. Evaluation of computationally-obtained results. (A) Boxcharts depicting the DLC likelihood for the tape and each one of the 8 body parts finally selected to be tracked computationally in the tape removal test to be classified as “True” (green) and “False” (rosy). The percentage of correctly placed labels are depicted on top of each body part panel. (B) ROC curves to assess the correct assignment of each DLC label. (C) Tape removal time estimated in the laboratory by researchers (experimental time) versus that calculated computationally from DLC-extracted results (computational time). FL paw: front left paw, FR paw: front right paw, HL paw: hindlimb left paw, HR paw: hindlimb right paw.

3.4. Computational identification of tracking variables most related with stroke

Values of the 22 features obtained (Supplementary Table S2) were compared in Figure 4 in two conditions: 1) pre-H/I vs post-H/I values of the same mice, and 2) between the different groups at the same time point. Figure 4 plots ANOVA test results for S, MS, and SS, as compared to NS separately. Variables showing differences between groups at the

pre-surgery time point were poorly informative and, thus, were not considered for further comparisons.

Distance travelled and tape removal time presented differences at the 3 time points post-H/I investigated when comparing NS vs S, NS vs MS or NS vs SS. Other features such as the mean velocity of the contralateral forepaw presented differences only beyond 24 h post H/I and did not differentiate NS from MS.

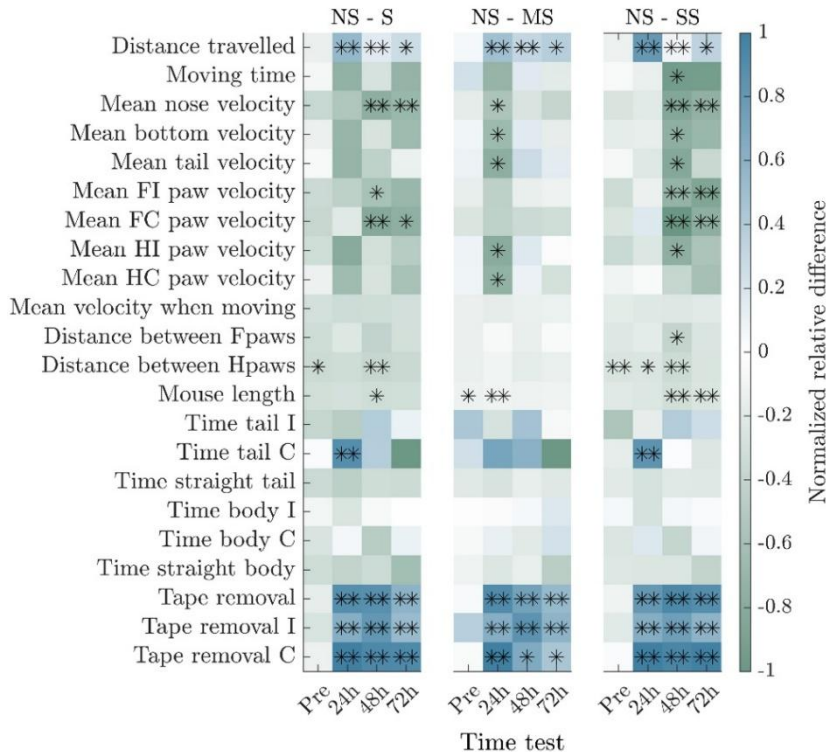


Figure 4. Colormap of the normalized relative difference (NRD) of all the computationally-extracted neurobehavioral variables. NRD was calculated as follows: $NRD = ((X - X_{NS}) / \sqrt{(X^2 + X_{NS}^2)})$, where X is the variable's median at a given time (Pre, 24, 48 or 72 h post H/I exposure, shown on the abscissas axes of the three 4-column panels) in a group of stroke mice showing ischemic brain damage (S: stroke, MS: mild stroke, and SS: severe stroke, shown on the left, middle and right panels, respectively), and X_{NS} is the median of the same variable at the same time point in the group of no stroke (NS) mice. * $p < 0.05$ and ** $p < 0.01$ for the variable indicated in the row and the time indicated in the column. F: fore, H: hind, FI paw: fore ipsilateral paw, FC paw: fore contralateral paw, this being the paretic limb in the stroked mice, HI paw: hind ipsilateral paw, HC paw: hind contralateral paw, distance between Fpaws and Hpaws: mean distance between the forepaws and hind paws, respectively, Time tail and Time body I or C means the time at which these features are turned to the ipsilateral (I) or contralateral (C) side of the lesioned hemisphere. Tape removal I, C, are the time the mice require to remove the adhesive tape that the researcher stuck to the ipsilateral or contralateral forepaw, respectively, in the tape removal test.

3.5. *Computational analysis of videos predicted the stroke condition with a 96% accuracy in H/I-exposed mice and allowed to determine severity*

Only variables showing statistically significant differences between groups at post-H/I time points and not at pre-surgery were considered mathematically for stroke prediction purposes. Therefore, according to Figure 4, the variables introduced in the LASSO

regressions were distance traveled, moving time, all body part mean velocities, distance between front paws, time with the tail curved to contralateral side, and tape removal times.

Predictor variables finally selected for the **stroke occurrence** model obtained from the logistic LASSO regression were 6: TR time in ipsilateral front paw at 24 and 48h, TR time in contralateral front paw at 48 and 72h, and distance traveled at 24 and 72h.

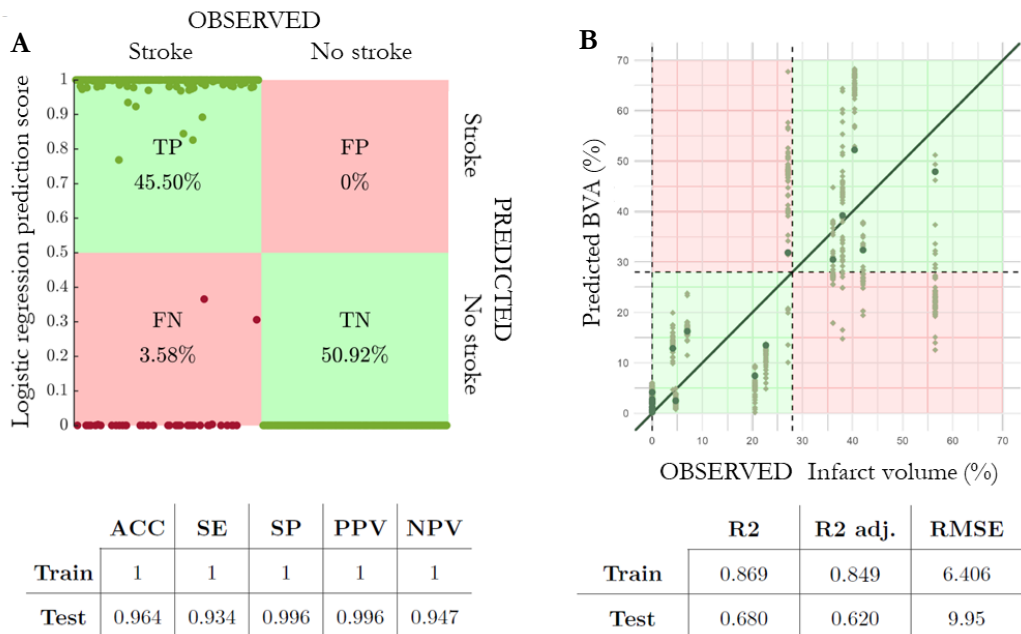


Figure 5. Confusion matrix identifying and categorizing the true prediction of stroke in the mice population exposed to the H/I condition; this condition induces infarct in half of the animals. (A) Confusion matrix uses the logistic regression prediction score threshold of 0.5 to classify as true stroke or true positive >0.5 (TP) or true no stroke or true negative <0.5 (TN) (within green areas), or false positives (FP) or false negatives (FN) (within pink areas) to assess the stroke occurrence and severity in the H/I (a condition that induces infarcts in approximately half of the animals, exhibits high inter-individual variability in brain damage, and shows a correlation between infarct volume and neurological impairment). For logistic regression prediction score, 96.4% of the cases were correctly classified, 45.5% were TP and 50.92% were TN. Each mouse underwent the process over 200 iterations as stated in [Supplementary](#). ACC: accuracy, SE: sensitivity, SP: specificity, PPV: positive predicted values, NPV: negative predicted values, RMSE: root mean square (B) Graph showing the correlation plot between the observed infarct volume using the gold standard *ex vivo* TTC staining method and the BVA (brain volume affected) predicted computationally in the H/I videos analysed. Dashed lines mark the 28% BVA threshold for MS and SS classification. Green areas allocate mice in which computational and experimental predictions are consistent with the defined thresholds.

Importantly, predictor variables finally selected for the **prediction of the brain volume affected** (BVA)/stroke severity model based on Linear LASSO regression were TR time in the contralateral front paw at 24h, and TR time in the contralateral and ipsilateral front paws at 72h.

For the stroke occurrence model, train accuracy (ACC) was 100%, and test ACC was 96.41% (Figure 5A depicts the resulting confusion matrix; in the green squares, true assignments $TP+TN= 96\%$). For the BVA stroke severity model, the R2 adjusted parameters were 0.849 and 0.620 for the train and test, respectively. Dashed lines in Figure 5B mark the 28% BVA threshold for MS and SS classification. The fully trained model successfully classified mice into MS or SS in 11 out of 12 infarcted mice (dark green dots, green squares); of note, the extent of the infarct of the animal classified incorrectly was very close

to the infarct threshold (28%) used to classify mice into mild or severe stroke.

3.6. Computational analysis of videos predicted the ICH condition with a 90% accuracy in collagenase-exposed mice and allowed to determine severity

For the ICH experiment the stroke occurrence model shows a test accuracy of 90% (Figure 6A, green squares TP 40% & TN 50%); only 3 out of 30 sets of videos were incorrectly classified, two of them corresponding to mice having the lowest hemorrhage, and being misclassified as non-ICH/non-stroke mice. When using the percentage of affected brain volume (BVA) model, trained to predict lesion volume in an ischemic scenario, the algorithm consistently predicted neurological impairment consistent with a large percentage of the brain being affected. A mean $13.43 \pm 7.991\%$ of the hemisphere was

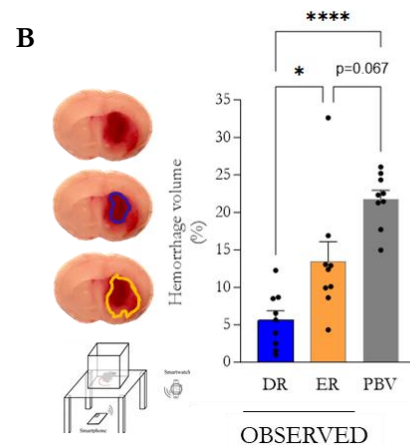
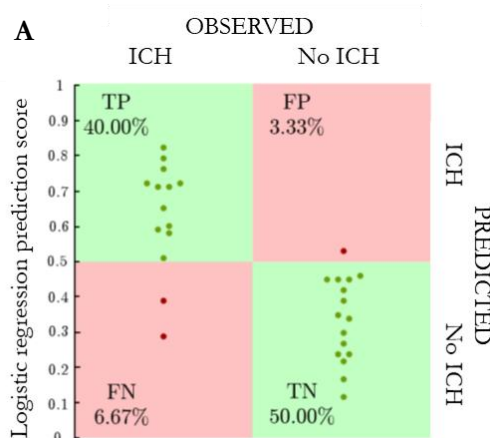


Figure 6. Confusion matrix identifying and categorizing the true prediction of stroke in the mice population naïve or exposed to ICH. (A) Confusion matrix uses the logistic regression prediction score threshold of 0.5 to classify as true stroke or true positive >0.5 (TP) or true no stroke or true negative <0.5 (TN) (within green areas) or false positives (FP) or false negatives (FN) (within pink areas). The assessment of stroke occurrence in an ICH-induced condition and in naïve mice shows that 90% (40% TP & 50% TN) of all cases (individual mice) were correctly classified. **(B)** Graph depicting the haemorrhage volume delineated as deep red (DR) (blue line & bar) or extended region with red coloration (ER) (orange line & bar). The gradation in the intensity of red introduces a subjective component when delineating as DR or ER. The grey bar shows the DLC-predicted volume affected (PVA) or BVA based on the neurological impairment. ICH-exposed mice showed computationally BVA larger than that assessed with the haemoglobin method. Mean and SEM are shown.

measured based on ER (extended region) *ex vivo*, and $21.77 \pm 3.52\%$ of the hemisphere was predicted by the BVA (Figure 6B).

4. Discussion

The present study shows that computational machine/deep learning algorithms, developed based on the performance of mice in a single neurobehavioral test, can automatically predict the occurrence of H/I ischemic stroke in individual mice with 96% accuracy. These algorithms also enable automated classification of H/I mice into groups according to stroke severity, as reflected by ischemic lesion volume. Similarly, the same algorithms predict ICH occurrence with 90% accuracy and provide assessment of ICH-induced neurological severity.

Preclinical stroke research commonly relies on researcher-annotated behavioral tests to assess impairment and recovery; however, these tests have limitations in fully capturing the extent of brain damage and could be enhanced by incorporating automated tracking-based measures. To identify test providing the most valuable information, we initially evaluated several researcher-assessed sensorimotor tests. Our results indicate impairment in the stroked mice in the TR test performance in the acute phase (Figure 2E), and the test has also been reported to be useful for measuring the protective effects of therapies or the long-term effects of rehabilitation [10,17,18]. The time to remove the tape in the TR test strongly correlates with the volume of brain damage, with $R^2 > 0.76$ (Supplementary Figures S1B and S2C) as the test may provide valuable information about 1) impairment in perceiving tactile stimulation in the affected forepaw and 2) the fine motor impairment when attempting to actively remove the tape. In contrast, the rotarod test loses its ability to differentiate between mice that develop infarcts and those that do not beyond 24 hours (Figure 2D), as highlighted in a recent systematic review and meta-analysis of post-stroke behavior in mice [19]. Additionally, the TR test statistically discriminates between MS and SS groups, whereas the rotarod and tail hanging tests do

not (Figure 2). Even with the availability of reliable tests, the inherent limitations of researcher assessments underscore the continued need for automated and objective tools to evaluate the complex changes induced by stroke. The TR test makes it possible to continuously monitor motor and behavioral parameters in freely moving mice using recent advances in automatic posture (or “pose”) estimation tools that use deep learning training of neural networks to accurately quantify a wide range of behavioral profiles from video recordings. Among the available tools, DeepLabCut (DLC) is particularly efficient for body part tracking [11-14] and was selected in this study to analyze the TR test videos. To capture detailed neurobehavioral disturbances, we initially tracked a large set of reliable body key points, eight anatomical landmarks (as shown in Figure 1C) and one external point marking the location of adhesive tape on the paw (either contralateral or ipsilateral). This allowed us to extract 22 behavioral features (see Figure 4 and Supplementary Table S2 for the complete list). Importantly, the number of labeled key points used does not affect computational inference speed, as supported by previous work. Additionally, we reduced the video frame size to optimize processing efficiency while preserving sufficient tracking accuracy, consistent with findings from prior studies [20].

DLC-based tools have been reported to detect group-level behavioral changes in both healthy and diseased mice [21], including reward-seeking behavior, obesity, dystonic features [22-24], and stroke-related impairments in gait kinematics in tests including the horizontal ladder rung walking (foot fault test), grid walking, staircase tasks in mice, and ledged beam walking tests in rats [25-27]. However, even with DLC-assisted acquisition of refined neurobehavioral data, no tool has yet been reported to be able to translate such neurobehavioral data into an accurate prediction of the percentage of brain damage following stroke induction in individual mice. This lack of prediction in previous reports might be related to the fact that, even when DLC-

dedicated data-processing toolbox such as MouseReach have been used to assess forelimb function in stroked mice, lesion volume showed only a moderate correlation $R^2 < 0,6$ with DLC-based success coefficient in the staircase test, and no correlation at all with the traditional staircase score or the slip depth [27]. In contrast, as stated above, we observed a strong correlation, providing a clear rationale for using TR test video recordings to develop an automated predictive classification tool. In our hands DLC accurately measured the time mice took to remove the tape from the front paws (Figure 3C) and allowed to determine other parameters unrelated to the tape removal activity itself, such as the mean distance between forepaws, mean velocities of previously defined body parts of interest, or % of time each mouse spent maintaining a certain pose. Once the database of the time-course longitudinal animal's body key points was obtained, we required computational support to classify complex behaviors. Although software packages such as MARS [28], SimBA [29] or BehaviorDEPOT [30] have been used to analyze the results to classify complex behaviors so far none of them has been tested in the tape removal test in stroke. We, thus, have generated here a new algorithmic tool for this purpose.

The independent assessment of the right and left forepaws' performance disclosed in silico in the present study is pivotal for the neurological evaluation of a focal damage located in one of the brain hemispheres. This pathophysiological situation represents the most common clinical presentation of stroke in humans, which is usually recapitulated in the animal studies, thereby allowing a clearer distinction between strategic compensation and true functional recovery [31]. In the H/I stroke-exposed mice, the neurobehavioral data-based computational approach was able to predict 1) infarct occurrence with a 96% accuracy (Figure 5A), and 2) the degree of infarct severity (Figure 5B). In our study, H/I mice developed ischemic strokes affecting an average of 28% of the ipsilateral hemisphere as assessed by TTC-staining, this matching

with the average 25% of the ipsilateral hemisphere damaged predicted from DLC-data-based algorithms (dark green dots in Figure 5B). Moreover, the algorithms provided estimation of the infarct volume allowing the classification of each individual mouse into no stroke, mild or severe stroke using only the video recordings. This novel tool provides researchers with a costless and time-saving method for an objective a priori allocation of mice with a computationally predicted 'stroke severity' to the placebo or treatment groups in preclinical studies without the need of MRI assessment. Moreover, we also found that both the researcher-annotated TR test (Supplementary Figure S5) and the DLC-TR-test-based computational algorithm approach (Figure 6A), effectively assessed functional impairment resulting from ICH stroke, despite the algorithm's predictive models were tailored for ischemic stroke. Based on neurological impairment, the model accurately predicted the presence or absence of hemorrhage in 90% of cases and consistently estimated larger hemorrhagic volumes than those quantified *ex vivo* using the hemoglobin-red method three days post-stroke, this recapitulating the observed in the clinic scenario. ICH-exposed mice showed hemoglobin deposition in 13% of the hemisphere but depict functional impairment comparable to that found in an ischemic scenario in which 22% of the hemisphere (BVA) was affected (Figure 6B). This, indeed has translational value since it is well known in the clinics that ischemic and hemorrhagic strokes of similar volume can produce very different patient neurological outcomes. For instance, a 70 mL lesion (approximately 10% of the brain, or 20% of one hemisphere) may result in only mild to moderate deficits in ischemic stroke, whereas a similarly sized ICH, especially if deep-seated, often causes more severe symptoms and carries a higher risk of coma or death.

Moreover, the use of a shared, automated computational tool to assess neurological damage in both ischemic and hemorrhagic stroke models could enable the development of a Neurological Impairment Equivalence

Index, which may be particularly valuable in preclinical studies of ICH. In ischemic stroke, brain damage is commonly measured using TTC staining, which determine areas where neurons have died. The size of the damaged area usually matches the level of functional impairment. In contrast, in ICH, injury severity is not based on direct signs of neuronal death. Instead, it is estimated by how far the bleeding has spread (hematoma volume) or how much blood has built up in the brain (hemoglobin density assay). Quantification of the hematoma volume is influenced by subjectivity when delineating the boundaries of the lesion (Figure 6B) or other issues (e.g. extension of hematoma into the ventricles or hematoma shrinkage in the firsts days after injury). Moreover, no correlation was found between the hemoglobin concentration in the ipsilateral hemisphere and the hemorrhage volume as determined by red-color-based delineation of brain slices (Supplementary Figure S5D); a lack of concordance between these measures has been previously reported [32]. No correlation was observed between hemoglobin levels and the degree of functional impairment predicted by the DLC model (Supplementary Figure S5C).

Our results suggest that the information obtained through this methodology is sufficient to make a computational selection of mice to be randomized into preclinical trials of new treatments in all types of stroke (ischemic and hemorrhagic), with no need for additional and/or more intrusive tests (animals that meet exclusion criteria e.g. non stroke developers can be identified and excluded). More features can be observed and measured in an objective manner that those able to be measured by expert researchers and using a method that consumes less time of the researchers. Homogenizing the criteria to enroll the experimental stroke mice in preclinical studies by being able to anticipate the severity of brain damage computationally will contribute to increase the quality of preclinical research and to reduce the number of animals as demanded by current guidelines [33,34]. This also represents one step beyond towards the

implementation of the 3R principle in animal research (Replacement, Reduction, Refinement), for the time-course evaluation of the animal's behavior with the algorithm allows a reduction of the number of animals per experiment, and the refinement of the *in vivo* procedures by reducing the distress of undergoing a battery of multiple behavioral tests.

5. Limitation of study

A limitation of the study is the relatively small sample size. A future objective will be to further train and validate the algorithm using a large cohort of stroked mice, ideally within the framework of a large, multicentrical pre-clinical study. A tool such as the one developed in this study will be pivotal for comprehensive preclinical assessment in multi-center, collaborative preclinical trials that are encouraged in the STAIR XI [35], allowing the standardization of functional outcome measures demanded [36].

Acknowledgments

This research was supported by grants PI21/01925 and PI24/00963 to TG and RI-CORS RD21/0006/0024 and RD24/0009/0015 Funded by the Carlos III Health Institute and Co-funded by the European Union, and grants from Agency for Management of University and Research Grants (AGAUR) Catalan Research Group 2021SGR00925, 2019PROD00120 and SLT036/24/000048 susceptible to be co-financed by FEDER funds. AG-S was supported by a contract associated to 2019PROD00120. The IGTP is a CERCA center of the CERCA Program/Government of Catalonia. The group has received funding from “la Caixa” CI15-00009, from the European Institute of Innovation and Technology (EIT) PoC-2016-SPAIN-04, which receives support from the European Union’s Horizon 2020 research and innovation program, and from the ‘Fundación para la Innovación y la Prospectiva en Salud en España (FIPSE)’ program 3594-18. NM, CP and MC received funding from “la Caixa” Foundation (ID 100010434), under agreement LCF/PR/GN17/50300003.

Conflict of interest

The authors have declared that no conflict of interest exists.

Supplementary data

Supplementary data to this article can be found online.

References

1. Martin SS, Aday AW, Allen NB, Almarzooq ZI, Anderson CAM, Arora P, et al. 2025 Heart Disease and Stroke Statistics: A Report of US and Global Data From the American Heart Association. *Circulation*. 2025 Feb 25;151(8):e41-e660. doi: [10.1161/CIR.0000000000001303](https://doi.org/10.1161/CIR.0000000000001303).
2. Turner RJ and Farr TD. Climbing the STAIRs to SPAN the Clinical Translation Gap: Recent Advances in Multicenter Preclinical Stroke Trials. *Stroke*. 2024; 55(9):2366-2369. doi: [10.1161/STROKEAHA.124.045998](https://doi.org/10.1161/STROKEAHA.124.045998).
3. Levine S. Anoxic-ischemic encephalopathy in rats. *Am J Pathol*. 1960;36:1-17.
4. Doyle KP, Fathali N, Siddiqui MR, Buckwalter MS. Distal hypoxic stroke: a new mouse model of stroke with high throughput, low variability and a quantifiable functional deficit. *J Neurosci Methods*. 2012; 207(1):31-40. doi: [10.1016/j.jneumeth.2012.03.003](https://doi.org/10.1016/j.jneumeth.2012.03.003).
5. Wang J, Wu C, Peng J, Patel N, Huang Y, Gao X, et al. Early-Onset Convulsive Seizures Induced by Brain Hypoxia-Ischemia in Aging Mice: Effects of Anticonvulsive Treatments. *PLoS One*. 2015; 10:e0144113. doi: [10.1371/journal.pone.0144113](https://doi.org/10.1371/journal.pone.0144113).
6. Bederson JB, Pitts LH, Tsuji M, Nishimura MC, Davis RL, Bartkowski H. Rat middle cerebral artery occlusion: evaluation of the model and development of a neurologic examination. *Stroke*. 1986; 17:472-6. doi: [10.1161/01.str.17.3.472](https://doi.org/10.1161/01.str.17.3.472).
7. Garcia JH, Wagner S, Liu KF, Hu XJ. Neurological deficit and extent of neuronal necrosis attributable to middle cerebral artery occlusion in rats. Statistical validation. *Stroke*. 1995; 26:627-634; discussion 635. doi: [10.1161/01.str.26.4.627](https://doi.org/10.1161/01.str.26.4.627).
8. Ruan J, Yao Y. Behavioral tests in rodent models of stroke. *Brain Hemorrhages*. 2020; 1:171-184. doi: [10.1016/j.hest.2020.09.001](https://doi.org/10.1016/j.hest.2020.09.001).
9. Feng L, Han CX, Cao SY, Zhang HM, Wu GY. Deficits in motor and cognitive functions in an adult mouse model of hypoxia-ischemia induced stroke. *Sci Rep*. 2020; 10(1):20646. doi: [10.1038/s41598-020-77678-8](https://doi.org/10.1038/s41598-020-77678-8).
10. García-Serran A, Ordoño J, DeGregorio-Rocasolano N, Melià-Sorolla M, Odendaal K, Martí-Sistac O, et al. Targeting Pro-Oxidant Iron with Exogenously Administered Apotransferrin Provides Benefits Associated with Changes in Crucial Cellular Iron Gate Protein TfR in a Model of Intracerebral Hemorrhagic Stroke in Mice. *Antioxidants*. 2023;12:1945. doi: [10.3390/antiox12111945](https://doi.org/10.3390/antiox12111945).
11. Mathis A, Mamidanna P, Cury KM, Abe T, Murthy VN, Mathis MW, et al. DeepLabCut: markerless pose estimation of user-defined body parts with deep learning. *Nat Neurosci*. 2018; 21:1281-1289. doi: [10.1038/s41593-018-0209-y](https://doi.org/10.1038/s41593-018-0209-y).
12. Nath T, Mathis A, Chen AC, Patel A, Bethge M, Mathis MW. Using DeepLabCut for 3D markerless pose estimation across species and behaviors. *Nat Protoc*. 2019; 14:2152-2176. doi: [10.1038/s41596-019-0176-0](https://doi.org/10.1038/s41596-019-0176-0).
13. Suryanto ME, Saputra F, Kurnia KA, Vasquez RD, Roldan MJM, Chen KH, et al. Using DeepLabCut as a Real-Time and Markerless Tool for Cardiac Physiology Assessment in Zebrafish. *Biology (Basel)*. 2022; 11:1243. doi: [10.3390/biology11081243](https://doi.org/10.3390/biology11081243).
14. Farahnakian F, Heikkonen J, Bjorkman S. Multi-pig Pose Estimation Using DeepLabCut. In *11th Int. Conf. Intell.*

Control Inf. Process., ICICIP 2021:143-148. IEEE. [doi:10.1109/ICICIP53388.2021.9642168](https://doi.org/10.1109/ICICIP53388.2021.9642168).

15. Knab F, Koch SP, Major S, Farr TD, Mueller S, Euskirchen P, *et al.* Prediction of Stroke Outcome in Mice Based on Noninvasive MRI and Behavioral Testing. *Stroke*. 2023; 54:2895-2905. [doi:10.1161/STROKEAHA.123.043897](https://doi.org/10.1161/STROKEAHA.123.043897).
16. Castelló-Ruiz M, Torregrosa G, Burguete MC, Miranda FJ, Centeno JM, López-Morales MA, *et al.* The selective estrogen receptor modulator, bazedoxifene, reduces ischemic brain damage in male rat. *Neurosci Lett*. 2014; 575:53-57. [doi:10.1016/j.neulet.2014.05.024](https://doi.org/10.1016/j.neulet.2014.05.024).
17. El Amki M, Baumgartner P, Bracko O, Luft AR, Wegener S. Task-Specific Motor Rehabilitation Therapy After Stroke Improves Performance in a Different Motor Task: Translational Evidence. *Transl Stroke Res*. 2017; 8:347-350. [doi:10.1007/s12975-016-0519-x](https://doi.org/10.1007/s12975-016-0519-x).
18. Yilmaz U, Tanbek K, Gul S, Gul M, Koc A, Sandal S. Melatonin Attenuates Cerebral Ischemia/Reperfusion Injury through Inducing Autophagy. *Neuroendocrinology*. 2023; 113:1035-1050. [doi:10.1159/000531567](https://doi.org/10.1159/000531567).
19. Boboc IKS, Rotaru-Zavaleanu AD, Calina D, Albu CV, Catalin B, Turcu-Stioliaca A. A Preclinical Systematic Review and Meta-Analysis of Behavior Testing in Mice Models of Ischemic Stroke. *Life (Basel)*. 2023; 13:567. [doi:10.3390/life13020567](https://doi.org/10.3390/life13020567).
20. Kane GA, Lopes G, Saunders JL, Mathis A, Mathis MW. Real-time, low-latency closed-loop feedback using markerless posture tracking. *Elife*. 2020; 9:e61909. [doi:10.7554/elife.61909](https://doi.org/10.7554/elife.61909).
21. Del Rosario Hernández T, Joshi NR, Gore SV, Kreiling JA, Creton R. An 8-cage imaging system for automated analyses of mouse behavior. *Sci Rep*. 2023; 13:8113. [doi:10.1038/s41598-023-35322-1](https://doi.org/10.1038/s41598-023-35322-1).
22. Iglesias AG, Chiu AS, Wong J, Campus P, Li F, Liu ZN, *et al.* Inhibition of Dopamine Neurons Prevents Incentive Value Encoding of a Reward Cue: With Revelations from Deep Phenotyping. *J Neurosci*. 2023; 43(44):7376-7392. [doi:10.1523/JNEUROSCI.0848-23.2023](https://doi.org/10.1523/JNEUROSCI.0848-23.2023).
23. Bühler D, Power Guerra N, Müller L, Wolkenhauer O, Düffer M, Vollmar B, *et al.* Leptin deficiency-caused behavioral change - A comparative analysis using EthoVision and DeepLabCut. *Front Neurosci*. 2023; 17:1052079. [doi:10.3389/fnins.2023.1052079](https://doi.org/10.3389/fnins.2023.1052079).
24. Andreoli I, Abbaszadeh M, Cao X, Cenci MA. Distinct patterns of dyskinetic and dystonic features following D1 or D2 receptor stimulation in a mouse model of parkinsonism. *Neurobiol Dis*. 2021; 157:105429. [doi:10.1016/j.nbd.2021.105429](https://doi.org/10.1016/j.nbd.2021.105429).
25. Weber RZ, Mulders G, Kaiser J, Tackenberg C, Rust R. Deep learning-based behavioral profiling of rodent stroke recovery. *BMC Biol*. 2022; 20:232. [doi:10.1186/s12915-022-01434-9](https://doi.org/10.1186/s12915-022-01434-9).
26. Ruiz-Vitte A, Gutiérrez-Fernández M, Laso-García F, Piniella D, Gómez-de Frutos MC, Díez-Tejedor E, *et al.* Ledged Beam Walking Test Automatic Tracker: Artificial intelligence-based functional evaluation in a stroke model. *Comput Biol Med*. 2025; 186:109689. [doi:10.1016/j.combiomed.2025.109689](https://doi.org/10.1016/j.combiomed.2025.109689).
27. Skrobot M, De Sa J, Walter J, Vogt A, Paulat R, Lips J, *et al.* Refined movement analysis in the staircase test reveals differential motor deficits in mouse models of stroke. *J Cereb Blood Flow Metab*. 2024; 44(9):1551-1564. [doi:10.1177/0271678X241254718](https://doi.org/10.1177/0271678X241254718).
28. Segalin C, Williams J, Karigo T, Hui M, Zelikowsky M, Sun JJ, *et al.* The Mouse Action Recognition System (MARS) software pipeline for automated analysis of social behaviors in mice. *Elife*. 2021; 10:e63720. [doi:10.7554/elife.63720](https://doi.org/10.7554/elife.63720).
29. Nilsson SR, Goodwin NL, Choong JJ, Hwang S, Wright HR, Norville ZC, *et al.* Simple Behavioral Analysis (SimBA) - an open source toolkit for computer

classification of complex social behaviors in experimental animals. *bioRxiv* [Preprint]. 2020. doi:[10.1101/2020.04.19.049452](https://doi.org/10.1101/2020.04.19.049452).

30. Gabriel CJ, Zeidler Z, Jin B, Guo C, Goodpaster CM, Kashay AQ, *et al.* BehaviorDEPOT is a simple, flexible tool for automated behavioral detection based on markerless pose tracking. *Elife*. 2022; 11:e74314. doi: [10.7554/elife.74314](https://doi.org/10.7554/elife.74314).

31. O'Neill N, Mah KM, Badillo-Martinez A, Jann V, Bixby JL, Lemmon VP. Markerless tracking enables distinction between strategic compensation and functional recovery after spinal cord injury. *Exp Neurol*. 2022; 354:114085. doi: [10.1016/j.expneurol.2022.114085](https://doi.org/10.1016/j.expneurol.2022.114085).

32. Foerch C, Arai K, Jin G, Park KP, Pallast S, van Leyen K, Lo EH. Experimental model of warfarin-associated intracerebral hemorrhage. *Stroke*. 2008 Dec;39(12):3397-404. doi: [10.1161/STROKEAHA.108.517482](https://doi.org/10.1161/STROKEAHA.108.517482).

33. Percie du Sert N, Hurst V, Ahluwalia A, Alam S, Avey MT, Baker M, *et al.* The ARRIVE guidelines 2.0: updated guidelines for reporting animal research. *BMJ Open Sci*. 2020; 4:e100115. doi: [10.1136/bmjos-2020-100115](https://doi.org/10.1136/bmjos-2020-100115).

34. Stroke Therapy Academic Industry Roundtable (STAIR). Recommendations for standards regarding preclinical neuroprotective and restorative drug development. *Stroke*. 1999; 30:2752-2758. doi: [10.1161/01.str.30.12.2752](https://doi.org/10.1161/01.str.30.12.2752).

35. Matsushita H, Hijioka M, Hisatsune A, Isohama Y, Iwamoto S, Terasawa H, *et al.* MRI-based analysis of intracerebral hemorrhage in mice reveals relationship between hematoma expansion and the severity of symptoms. *PLoS One*. 2013;8(7):e67691. doi: [10.1371/journal.pone.0067691](https://doi.org/10.1371/journal.pone.0067691).

36. Lyden P, Buchan A, Boltze J, Fisher M; STAIR XI Consortium*. Top Priorities for Cerebroprotective Studies-A Paradigm Shift: Report From STAIR XI. *Stroke*. 2021; 52:3063-3071. doi: [10.1161/STROKEAHA.121.034947](https://doi.org/10.1161/STROKEAHA.121.034947).

37. Hietamies TM, Ostrowski C, Pei Z, Feng L, McCabe C, Work LM, *et al.* Variability of functional outcome measures used in animal models of stroke and vascular cognitive impairment - a review of contemporary studies. *J Cereb Blood Flow Metab*. 2018; 38:1872-1884. doi: [10.1177/0271678X18799858](https://doi.org/10.1177/0271678X18799858).

38. Guan J, Williams C, Gunning M, Mallard C, Gluckman P. The effects of IGF-1 treatment after hypoxic-ischemic brain injury in adult rats. *J Cereb Blood Flow Metab*. 1993 Jul;13(4):609-16. doi: [10.1038/jcbfm.1993.79](https://doi.org/10.1038/jcbfm.1993.79).

Supplementary Materials for

Machine/Deep Learning from Neurobehavioral Data Predicts Stroke Occurrence and Severity in Mice

Alexia García-Serran^{a,1}, Núria Mercadé Besora^{b,c,d,1}, Marina Mas-Argemí^{b,e}, Núria DeGregorio-Roca-solano^a, Marc Melià-Sorolla^a, Marta Alcalde-Herraiz^{b,c}, Clara Prats^c, Teresa Gasull^{a,#} Martí Català^{d,*}, Octavi Martí-Sistac^{a,f,*}

MATERIALS AND METHODS

Animals

A total of 73 mice were used in the study (9- to 10-week-old C57BL/6J males; Charles River Laboratories); seven mice did not complete the follow-up, four of them in the initial pilot study when exposed to 30 min hypoxia; 1 overnight in the main H/I experiment, and 2 during the intracerebral hemorrhagic (ICH) procedure. Mice were housed under standard temperature and humidity conditions in the IGTP/CMCiB facility, 4 per cage, with nest-building materials and a shelter during the acclimatization (8–10 days), the training in the neurobehavioral tests, and the post-stroke follow-up periods. Twelve mice were exposed to 20 min cerebral hypoxia/ischemia (H/I) and completed a pilot experiment to determine the correlation between infarct volume and time to remove the tape in the tape removal test (Supplementary Figure S1) and other 19 mice were exposed to different times of H/I to determine the best option. Twenty-four mice were exposed to cerebral H/I and completed the main experiment of the machine learning analysis of behavior as predictor of the occurrence and severity of stroke (Supplementary Figure S2). Fifteen mice were exposed to ICH and completed the 72h follow-up. The experiments were designed to comply with reduction in the number of animals of the 3R principle in animal research. The total sample size used in the experiments was determined based on previous experiments conducted in our lab using this exact duration of hypoxia, which provided data on the average percentage of mice in which the H/I model did not produce brain infarction, the percentage of infarcted mice, and the individual variability of the model. The animals within each cage were labeled, and each mouse was assigned a unique identification number throughout the experiment. This number corresponded to each individual mouse as an experimental unit and, along with the date and session, was visibly displayed and verbally stated by the researcher in each recorded video for analysis. The pre-established protocol stated that only the mice that did not completed the follow-up were excluded from the study. The mice were monitored daily for inability to move limbs or complete paralysis, severe weight loss, severe dehydration, and pain/distress. Ethical requirements were followed according to EU Directive 2010/63/EU, and the study was approved by the Committee of Ethics in Animal Research of the Institut d'Investigació Germans Trias i Pujol (IGTP) and the Catalan Government (Permit numbers: reference 11131, FUE-2020-01691361 and ID HYNMX7RXG, and reference 11182, FUE-2020-01734578 and ID YXVFPXYJ4).

Cerebral hypoxia/ischemia procedure (H/I)

An initial study was performed to determine the optimal time of H/I exposure providing a good percentage of mice with infarct and producing low mortality; Table S1 indicates that 20 min exposure to hypoxia as the most convenient time. Mice were exposed to a transient single hemisphere sub-ischemic condition for 2.5 h and to an intercalated 20-min period of global hypoxia adapted from Guan *et al.* 1993 [38], as recently reported by us [10]), resulting in ischemic damage in that hemisphere in a percentage of mice and, due to decussation, an impaired function of the forepaw contralateral to the damaged hemisphere. In brief, mice were anesthetized with isoflurane and a single common carotid artery (CCA) was transiently occluded by ligature. Two hours after the CCA occlusion, mice were placed in a hypoxia chamber at 35.5°C for 20 min with 8% O₂/92% N₂ at an airflow rate of 1 L/min. Two and a half hours after initiation of ischemia, the suture occluding the CCA was removed (Figure 1A). Euthanasia was done at the completion of the experiment (72h after H/I exposure) by cervical dislocation.

Table S1. Effect of hypoxia exposure time on percentages of infarcted and non-infarcted mice, as measured by TTC (2,3,5-triphenyltetrazolium chloride) staining, and H/I-induced mortality.

Hypoxia time (min)	Mice (n)	Infarcted mice (%)	Non-infarcted mice (%)	H/I-induced mortality (%)
30	12	50	17	33
20	12	67	33	0
17	7	27	73	0

Intracerebral hemorrhage stroke model (ICH)

The ICH procedure was conducted as previously described [10]. In short, mice were anesthetized using isoflurane, and 0.06 U of collagenase type VII-S in 0.4 μ L of saline were injected into the right striatum at a rate of 200 nL/min. The coordinates for the injection were 0.5 mm anterior, 1.7 mm lateral, and 3.0 mm ventral from Bregma. After the injection, the syringe was left in place for 10 minutes before being carefully withdrawn at a rate of 1 mm/min.

Time-course evaluation of the hematoma/hemorrhagic area was conducted *in vivo* using microCT imaging with contrast agent Viscover ExiTronTM nano 12000 and indicated that the hematoma/hemorrhage area did not increase beyond 5 hours. At the end of the experiment at 72 h, brain tissue was collected, sectioned into 2 mm thick coronal slices, and the red hemorrhagic area was measured using ImageJ (Wayne Rasband, NIH, Bethesda, MD, USA) [10]. The hematoma was assessed by two blind researchers, and deep red areas (DR) or extensive red areas (ER) were measured as shown in Figure 6B.

Measurement of the actual infarct volume

At the end of the experiments, freshly excised brains were cut into 2 mm-thick coronal slices using a mouse brain slicer matrix; slices were used to calculate ischemic or hemorrhagic volume as the main outcome. H/I brain slices were immediately stained with 1% 2,3,5-triphenyltetrazolium chloride (TTC) in PBS at 37° C for 11 min; this staining method gives viable brain grey matter tissue a reddish color while leaving infarcted tissue unstained (whitish). Conversely, ICH brain slices were not stained to allow to see and measure blood-filled regions. Digital photographs of the serial slices of H/I and ICH brains were taken. Infarct volume or hemorrhage volume were measured in pictures taken from the TTC-dipped or unstained slices, respectively, using ImageJ. For each slice, the infarct/hemorrhagic (lesion) area, and the total area of the ipsilateral and the contralateral hemisphere were manually outlined and measured in mm², and the volume was calculated in mm³ by considering section thickness. The final lesion volume (mm³) resulted from the sum of the lesion volumes of all sections corrected by the ratio of the total volume of the contralateral hemisphere to that of the ipsilateral one; that is, corrected by edema. The final lesion volume results are given as % of the hemisphere. Mice exposed to H/I were assigned to stroke (S) and no stroke (NS) groups according to whether they did or did not show infarct in the post-mortem analysis. Mice in the S group were subsequently assigned to mild stroke (MS) and severe stroke (SS) if the infarct volume was under or over 28% of the brain hemisphere, respectively.

Researcher-assessed neurological impairment

Mice were weighed on a daily basis and trained in the tail hanging, rotarod, and the tape removal tests 72, 48 and 24h prior to the H/I procedure, and tested 24, 48 and 72h after H/I exposure. In the tail hanging test, the mouse was held by the tail upside down by the researcher and the side the mouse first bent within seconds, left or right, was noted down; the mouse was then gently left onto the bench. To minimize experimental error, the action was repeated 20-30 times per session to have enough trials per mouse. In the rotarod test, the amount of time a mouse spent on an accelerating spinning rod before it fell down was measured (2 trials per session for each mice). In the tape removal test of the main experiment, an open lid, 30 cm high and a squared 25x25 cm transparent bottom box (from now on, the box) was used. A round 6 mm diameter tape was adhered to the pads of the mouse's forepaws, alternating between the paw ipsilateral and the paw contralateral to the CCA occlusion. A video of each tape removal test was recorded from below the box using a smartwatch-controlled smartphone located at an orthogonal position relative to the box center ([Supplementary Video S1](#) depicts the experimental procedure), and the time the mouse took before actively removing the tape from the paw, usually by pulling it off with the mouth, was noted down as the time to remove the tape (TR time). After H/I and throughout the 72-hour follow-up, the severity of stroke damage in each individual mouse was unknown to all personnel involved in the research. Once the mice were euthanized, only the two researchers responsible for brain slice TTC staining and the team leader were aware of the mouse's infarct size. Mouse performance in the tests was video recorded, and the videos were analyzed for neurobehavioral features (main outcome) by: 1) visual inspection to annotate the tape removal time independently by two researchers trained for the task, and 2) computational analysis by experts responsible for DLC training and data extraction. All researchers involved in the acquisition of neurobehavior-related data were blinded to the final infarct volume of the mice.

Video acquisition

For the tape removal test, two sessions per forepaw per animal were performed and recorded each day. In 90% of the videos the recording stopped shortly after the mouse removed the tape, whereas for the remaining videos mice were recorded for up to 200 s.

Machine learning for labels coordinates extraction and pose estimation

DeepLabCut (DLC) was used in Anaconda environment, Python 3.8, to analyze videos of the tape removal test for pose estimation (see [Supplementary Video S1 and Video S2](#)). Before analyzing the recordings, the videos were pre-processed by resizing them to 900x900 pixels, and the external part of the box was blacked out. Then, the videos were trimmed to set the start at the frame where the body parts of the mouse to be tracked were identifiable for first time and the hand of the researcher leaving the mouse into the box was no longer visible. Although this can be done manually, we set up an automatic method to do it. [Supplementary Figure S6](#) shows the rationale and explains the mathematic formulae behind the automatic detection of the first video frame to be considered in the TR test.

To carry out the initial DLC training, frames from each one of the videos used were selected based on k-means algorithm, and the body parts of interest and the tape were further hand-labelled by a researcher. [Figure 1C](#) of the main text illustrates the tape and the eight key body points of the mouse that were finally tracked; a ninth body site of interest at the middle of the tail was not further

considered for it was inconsistently placed by DLC (Supplementary Figure S3 and Supplementary Video S1). Additionally, the sticky tape was monitored both while attached to the mouse's forepaw during movement and after being removed, when it remained stationary following the mouse's active removal (Supplementary Figure S4). After an initial evaluation of the goodness of labelling, the automatic labelling was refined manually by correcting the frames that were not visually correctly positioned, and by adding videos thought to capture challenging scenarios for pose prediction. Each labelling training consisted of 200,000 iterations, and evaluation consisted in a split of data into computing training (80%) and testing (20%) by DLC. This active-learning process was done iteratively until optimal results were achieved.

Next, all videos were analyzed with the trained neural networks. For each video, the (x, y) coordinates of each one of the labels on every frame, together with the corresponding likelihood indicating the algorithm's confidence in the prediction, were obtained. Additionally, a second network was trained to estimate the position of box edges with the aim to automatize the conversion of pixels to centimeters of the mice body parts and the tape coordinates. DLC data extraction was performed by biomedical engineering and computational and applied physics experts who were blinded to each animal's allocation into the non-stroke, mild stroke, or severe stroke groups.

DLC results from mice pose estimation were manually assessed by randomly selecting a single frame for each video and plotting the label coordinates. Each body part estimate was categorized as true or false by two investigators in an independent manner to determine if the label was correctly placed by DLC.

Post-processing for features extraction

DeepLabCut (DLC) assignment of the tail midpoint label were not satisfactory (Figure S3). Files resulting from DLC were processed and analyzed in MATLAB R2022b and R 4.2.2 as follows: 1) a coordinate with a likelihood <0.95 was excluded and instead estimated using lineal interpolation of the preceding and subsequent coordinates; 2) paw positions were relabeled (right/left and front/hind) based on the nose and bottom coordinates.

Body part positions were converted from pixels to centimeters using the results from the box vertices position extracted with DLC and the known distances between them. Then, distances between several body parts were estimated for each video and frame, and videos rendering distances between body parts above threshold limits imposed (see Supplementary Table S2) in more than 10% of the frames were excluded from subsequent analyses. Code used for processing and analyses is available at https://github.com/nmercadeb/DeepLabCut_to_predict_stroke_on_mice.

Computational prediction models

We constructed two predictive models: one to determine the occurrence of stroke, and a second one to predict the severity using a prediction of the percentage of brain volume affected (BVA).

For each mouse, the variables descriptive of its behaviour (Supplementary Table S1) were treated separately according to test recording time after H/I. Comparisons between groups and before and after H/I were done (Figure 4 in the main text) to obtain the stroke-modified behaviour measures to be used as potential predictors. Only the measures obtained 24, 48 and 72h after the H/I procedure

were run in the prediction model. The set of selected potential predictors was introduced into a Least Absolute Shrinkage and Selection Operator (LASSO) regression to select the predictor variables. For the stroke occurrence model, we used logistic LASSO regression, and for the BVA model a linear LASSO regression was used. In both cases, LASSO was performed 200 times using 5-fold cross validation. Variables that were selected in more than 75% of the iterations were chosen as predictors for the corresponding model.

Both models were evaluated by choosing randomly 80% of the mice to fit the logistic/linear regression model. This model was later used to predict the stroke/BVA outcome in the other 20% of mice. This process was repeated over 200 iterations.

The goodness of both models was assessed according to the train and test parameters obtained. Train parameters refer to the values obtained when all available data is used to train and predict, while test parameters are based on the prediction results obtained when data is repeatedly split into 80% to train and 20% to test the prediction. Reported parameters for the stroke occurrence model were accuracy (ACC), specificity (SP), sensitivity (SE), and positive and negative predicted values (PPV and NPV, respectively), while for evaluating the BVA model we used R^2 , R^2 adjusted, and the root mean square error (RMSE).

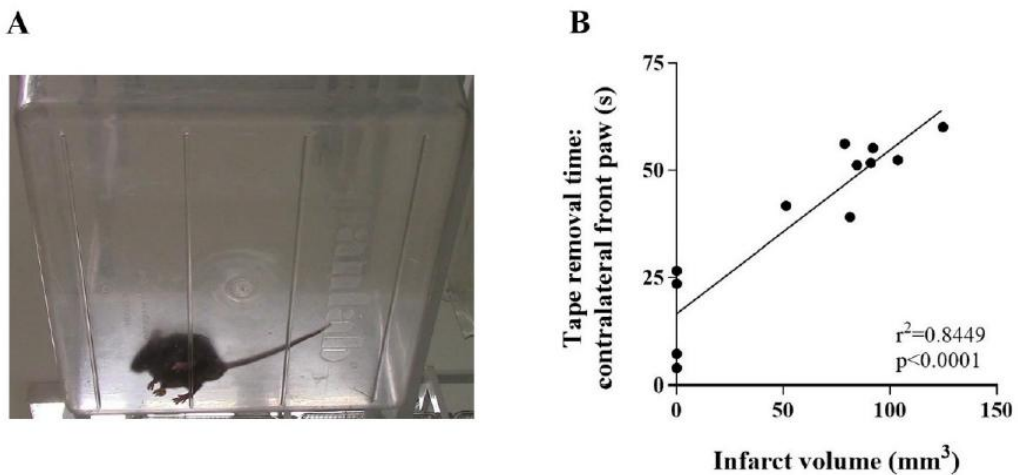


Figure S1. Pilot experiment showing correlation between infarct volume induced by H/I exposure and researcher-measured tape removal (TR) time of the contralateral forepaw.

(A) Representative frame from a video of the pilot experiment; twelve mice exposed to H/I in conditions similar to those specified in Materials & Methods were used. In this pilot experiment, mice were exposed to the TR test in a caging (translucent) box and videos were recorded (up 60 s) from below using a camera located in angle and used for researcher annotation. **(B)** A significant correlation was found between researcher-measured TR time of the contralateral forepaw and infarct volume as measured by TTC staining.

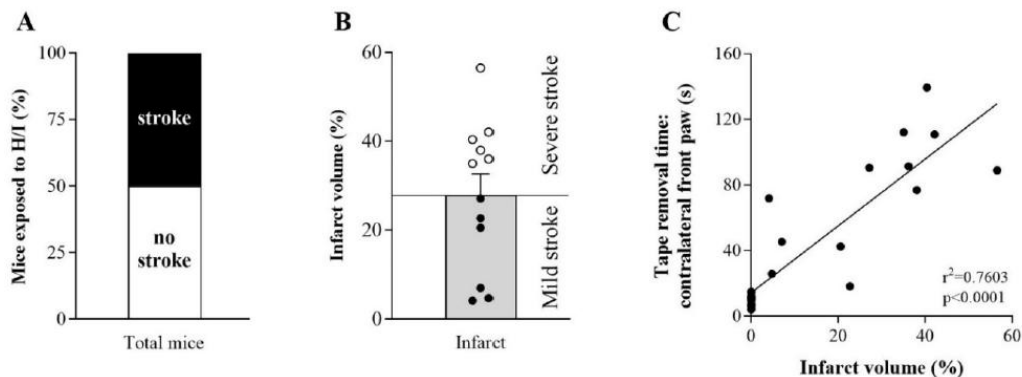


Figure S2. Infarct volume/outcome induced by H/I exposure and researcher-measured tape removal (TR) time of the contralateral forepaw in the main experiment.

(A) Stacked bar showing the percentage (%) of the H/I-exposed mice that developed stroke (50%) and those that did not (50%); these percentages are expected in this model. (B) Graph showing the variability of the individual infarct volumes induced in the mice that developed stroke; mean (SD) infarct volume was 27.8% (16.6%) (closed circles: mice assigned to mild stroke, open circles: mice assigned to severe stroke); mean and SEM is shown. (C) Significant correlation between TR time of the contralateral forepaw and infarct volume in percentage of the hemisphere (in this main experiment and to allow automated DLC-tracking, mice were exposed to the TR test in a transparent wall box and videos were recorded from below, orthogonally to the center of the box bottom; see [Supplementary Video S1](#)).

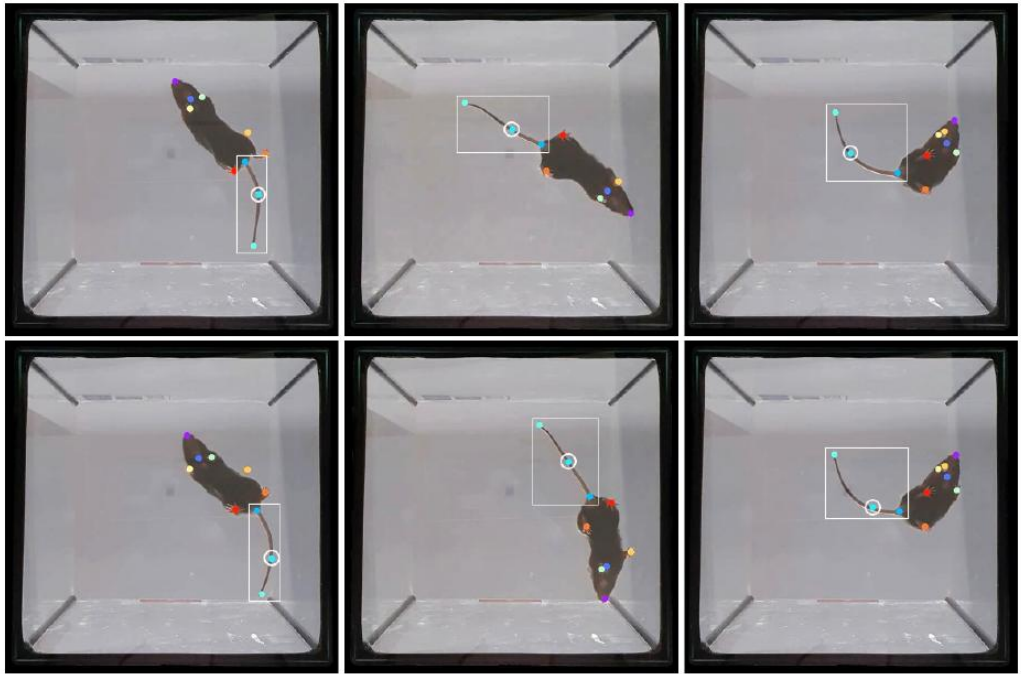


Figure S3. Representative images of the DeepLabCut (DLC) assignment of the tail midpoint label.

White rectangles enclose the tail and white circles enclose the tail midpoint label. Note that the label assignment to tail midpoint is misplaced in many frames so this reference point was not considered for further analyses.

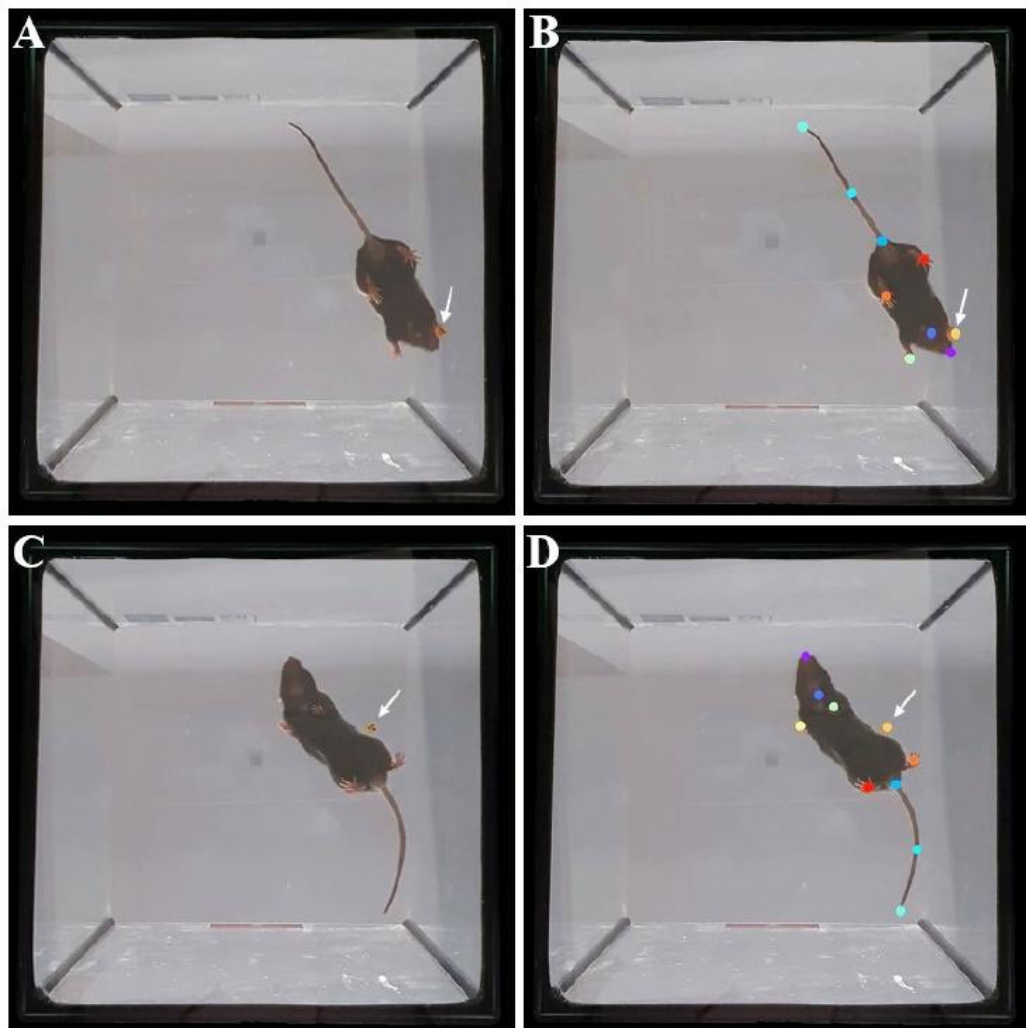


Figure S4. Representative images of the processing of videos during DeepLabCut (DLC) labelling and tracking.

Video frames of a mouse in the tape removal test; white arrows indicate the position of the adhesive tape. Top images show the mouse with the tape attached to the paw (A) before and (B) after DLC assignment of labels. Bottom images show the mouse once it has removed the tape (C) before and (D) after DLC assignment of labels. Note that on (B), the labels of the right forepaw and the tape overlap.

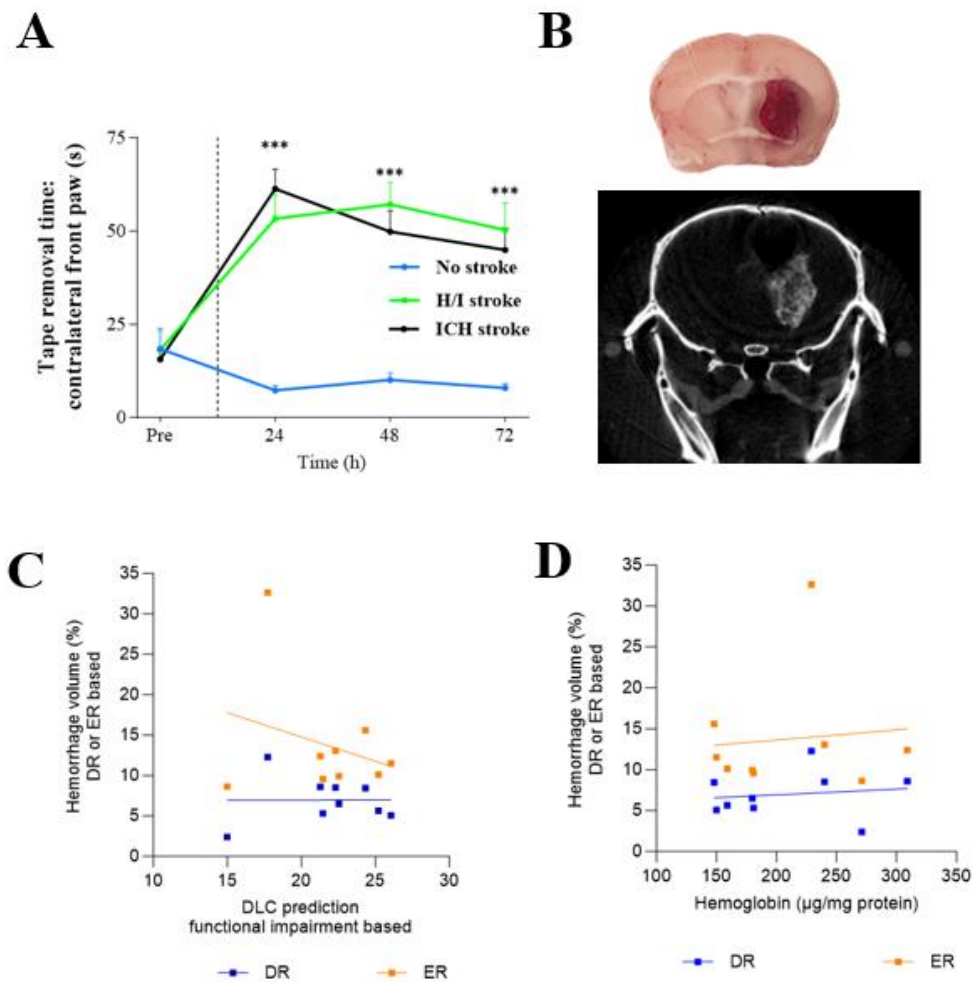


Figure S5. The tape removal (TR) test detects impairment in both ischemic and hemorrhagic stroke mice models.

(A) The tape removal (TR) test detects the neurological impairment of H/I stroked mice as compared with the no stroke mice. Interestingly, the TR test also detects the neurological deficit of mice exposed to intracerebral hemorrhagic stroke (ICH). *** $p < 0.005$ H/I and ICH stroke vs no stroke; mean and SEM are shown. **(B)** Representative images of coronal *ex vivo* (top) and MicroCT (bottom) sections of a mouse brain with ICH; hemorrhage appears red on the top image and hyperdense on the bottom image. **(C)** No correlation was found between the functional impairment-based prediction of the brain volume damaged and the volume of hemorrhage quantified based on deep red (DR) or extensive red (ER) areas. **(D)** No correlation was found between the hemoglobin concentration in homogenates of the ipsilateral hemisphere and the volume of hemorrhage quantified based on deep red (DR) or extensive red (ER) areas.

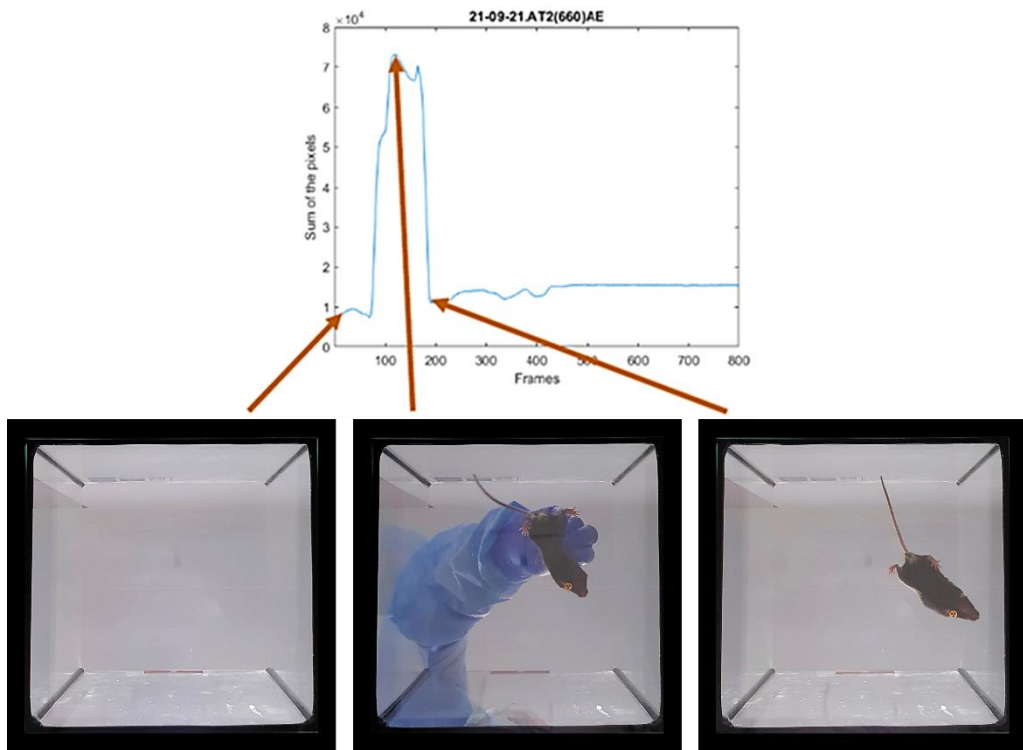


Figure S6. Method to automate the decision of which is the first frame to be analyzed by DLC.

The analysis of the pixels along the first seconds of video acquisition allows to detect automatically the frame at which the arm of the researcher is no longer seen and the frame at which the TR test counting should start.

The timelines of the tape removal test videos show the initial frames depicting only the box (left image), followed by frames depicting both the mouse and the researcher's arm when introducing the mouse in the box (middle image), and afterwards the frames when the mouse moves freely after the researcher's arm is no longer visible (right image). The peak in the Figure S6 graph represents the maximum exposure of the researcher's arm. Frames around this maximum were visualized by experienced researchers manually to decide, according to previous experience, at which frame the video should start to be processed to determine the tape removal time. The frame of choice was placed between the maximum and the first third part of the peak when decreasing. Therefore, the equation proposed to automate the first frame in the videos to be considered for further processing is the following:

$$\text{Initial Frame} = \left\lceil \frac{\text{frame(max)} - \text{frame(min)}}{3} \right\rceil + \text{frame(max)}$$

where frame(max) is the frame at which the sum of the pixels is maximum, and frame(min) is the first frame close to 0 after the maximum. A comparison of the frame chosen manually and automatically results in a mean delay of 0.1 seconds.

Table S2. Features of the mice's activity extracted computationally from the video recordings in the tape removal test

Variable	Description
Mean velocity (cm/s)	
Nose	Nose
Bottom	Bottom
Tail	Tail end point
FI paw	Ipsilateral forepaw
FC paw	Contralateral forepaw
HI paw	Ipsilateral hindpaw
HC paw	Contralateral hindpaw
When moving	Computed with the bottom part of the mouse in the frames in which it is moving
Distance (cm)	
Distance travelled	Total distance travelled by the mouse
Fpaws	Between forepaws
Hpaws	Between hindpaws
Mouse length	Nose-to-bottom distance
Time	
Moving time	% Time the mouse has been in movement
Time tail I	% Time the mouse has the tail curved to the ipsilateral side
Time tail C	% Time the mouse has the tail curved to the contralateral side
Time straight tail	% Time the mouse has the tail straight
Time body I	% Time the mouse has the body curved to the ipsilateral side
Time body C	% Time the mouse has the body curved to the contralateral side
Time straight body	% Time the mouse has the body straight
Tape removal time	Time taken to remove the tape (s)
Tape removal I	Time taken to remove the tape from ipsilateral forepaw (s)
Tape removal C	Time taken to remove the tape from contralateral forepaw (s)

Table S3. List of thresholds for the distances between body parts considered non-realistic to curate data obtained after DLC pose estimation. Exceeding these thresholds recommended to exclude either the videos or subsequent data filters. FC paw: contralateral forepaw, FI paw: ipsilateral forepaw, HC paw: contralateral hindlimb, HI paw: ipsilateral hindlimb

Distance	Threshold value (>cm)
Nose – Bottom	11
Nose – FI paw	8
Nose – FC paw	8
Bottom – HI paw	6
Bottom – HC paw	6
Bottom – End tail	12

Tables S4: Means \pm SD (SEM) in the main H/I experiment

Body weight change (%)				
	Pre	24 h	48 h	72 h
No stroke (n=12)	100.0 \pm 7.4 (2.1)	96.6 \pm 2.5 (0.7)	95.8 \pm 2.5 (0.7)	96.0 \pm 2.8 (0.8)
Mild stroke (n=6)	99.3 \pm 10.4 (4.3)	93.1 \pm 0.9 (0.4)	92.3 \pm 1.9 (0.8)	94.9 \pm 1.9 (0.8)
Severe stroke (n=6-7)	100.6 \pm 8.0 (3.0)	88.8 \pm 4.2 (1.6)	85.5 \pm 6.5 (2.5)	85.7 \pm 8.9 (3.4)

Tail hanging: contralateral turns (%)				
	Pre	24 h	48 h	72 h
No stroke (n=12)	39.3 \pm 19.6 (5.6)	32.9 \pm 25.0 (7.2)	43.3 \pm 25.6 (7.4)	51.3 \pm 29.0 (8.4)
Mild stroke (n=6)	31.1 \pm 14.9 (6.1)	65.6 \pm 38.8 (15.8)	61.9 \pm 36.7 (15.0)	59.4 \pm 27.4 (11.2)
Severe stroke (n=5-7)	44.3 \pm 16.7 (6.3)	80.7 \pm 26.0 (15.8)	84.4 \pm 26.2 (10.7)	90.0 \pm 24.5 (10.0)

Rotarod: time to fall (s)				
	Pre	24 h	48 h	72 h
No stroke (n=12)	47.3 \pm 15.2 (4.4)	49.5 \pm 15.9 (4.6)	44.9 \pm 10.9 (3.1)	42.8 \pm 11.9 (3.4)
Mild stroke (n=6)	46.5 \pm 10.8 (4.4)	43.9 \pm 19.1 (7.8)	52.7 \pm 25.6 (10.4)	50.4 \pm 17.4 (7.1)
Severe stroke (n=6-7)	42.7 \pm 16.5 (6.2)	25.9 \pm 14.6 (6.0)	31.6 \pm 23.8 (9.7)	32.0 \pm 11.4 (4.7)

Tape removal time: contralateral (s)				
	Pre	24 h	48 h	72 h
No stroke (n=11-12)	18.4 \pm 19.4 (5.6)	7.7 \pm 4.5 (1.3)	10.5 \pm 6.0 (1.7)	8.4 \pm 4.2 (1.2)
Mild stroke (n=6)	27.8 \pm 28.0 (11.4)	49.3 \pm 34.2 (14.0)	58.8 \pm 46.3 (18.9)	37.9 \pm 38.2 (15.6)
Severe stroke (n=6-7)	11.4 \pm 4.1 (1.6)	92.7 \pm 43.8 (17.9)	122.7 \pm 25.6 (10.4)	93.3 \pm 18.9 (7.7)

Tape removal time: ipsilateral (s)				
	Pre	24 h	48 h	72 h
No stroke (n=11-12)	20.4 \pm 23.4 (6.7)	8.6 \pm 4.6 (1.4)	10.2 \pm 6.4 (1.8)	8.6 \pm 4.9 (1.4)
Mild stroke (n=6)	24.8 \pm 21.5 (8.8)	23.7 \pm 9.4 (3.9)	43.0 \pm 62.3 (25.4)	13.6 \pm 8.3 (3.4)
Severe stroke (n=6-7)	22.7 \pm 24.1 (9.1)	21.7 \pm 13.0 (5.3)	63.8 \pm 59.8 (24.4)	34.5 \pm 20.5 (8.4)

Table S5: Means \pm SD (SEM) Figure S5A

Tape removal time: contralateral front paw (s)				
	Pre	24 h	48 h	72 h
No stroke (n=11-12)	18.4 \pm 19.3 (5.6)	7.3 \pm 4.4 (1.3)	10.1 \pm 6.1 (1.8)	7.9 \pm 4.2) (1.2)
H/I stroke (n=12)	18.1 \pm 17.5 (5.0)	53.3 \pm 22.4 (6.5)	57.1 \pm 20.6 (6.0)	50.3 \pm 25.2 (7.3)
ICH stroke (n=15)	15.6 \pm 8.9 (2.3)	61.3 \pm 20.4 (5.3)	49.9 \pm 21.7 (5.6)	45.0 \pm 22.8 (5.9)

MANUSCRIPT III

**Establishing an endovascular model of intracerebral hemorrhage
in swine for translational stroke research**

Article- Short communication format

Establishing an endovascular model of intracerebral hemorrhage in swine for translational stroke research

Alexia García-Serran, DVM¹✉; Carlos Castaño, MD PhD²; Marc Melià-Sorolla, PhD¹✉; Núria DeGregorio-Rocasolano, PhD¹✉; Octavi Martí-Sistac, PhD^{1,3}✉; Teresa Gasull, PhD^{1*}✉

Background: Intracerebral hemorrhage (ICH) is a devastating condition caused by the sudden spill-over of blood in the brain parenchyma. It remains among the leading causes of disability and death. Until now, most of the new experimental therapies for stroke tested in rodents have not achieved a positive result in clinics. Most ICH models require craniotomy surgeries, thus altering the intracranial blood pressure and not mimicking the human pathology. To have a successful bench-to-bedside process, it is recommended to test new therapies in big animal models with human-like characteristics, like swine models (which also develop coronary disease similar to humans). We intended to establish an alternative endovascular approach to generate a new ICH model in pigs, mammals with gyrencephalic brains, and a comparable proportion of white-to-gray matter ratio to humans.

Methods: To establish an ICH model in pigs, catheterization of the cerebral venous vasculature was performed, under angiography guidance, in order to access the thalamostriatal vein. The vein was then perforated, and 1.5 mL of arterial blood was injected. *In vivo* Magnetic Resonance Imaging (MRI) was conducted at different time points. Blood samples were collected at designated intervals, and brains were obtained at the end of the experiment. Iron-related proteins were determined by immunohistofluorescence (IHF), transferrin levels, and transferrin saturation in blood (TSAT) by Western Blot, and platelet factor 4 (PF4) by ELISA.

Results: We successfully accessed various brain regions through the pig's venous vasculature. Our ICH model reliably induced ICH in all the pigs, confirmed by contrast extravasation into the brain parenchyma on rotational angiography and by MRI sequences (FLAIR, Axial T2*, DWI, ADC) as early as 1 hour post-ICH. This minimally invasive approach enabled hemorrhage induction in different brain regions, including striatum and occipital cortex, leading to neurological impairment without hemorrhage volume increase at 24 hours nor systemic plaque activation at 1 hour post-venous perforation. Blood and brain analysis of iron-related proteins revealed a significant increase in the percentage of serum TSAT at 1 hour after ICH onset, as well as an increase in the transferrin and ferritin amount in the perihematomal area at short timepoints.

Conclusions: We have successfully developed a novel ICH model in pigs using a minimally invasive endovascular approach without using craniotomy and we have evaluated effects on iron-related parameters and platelet activation.

¹ Cellular and Molecular Neurobiology Research Group, Department of Neurosciences, Germans Trias i Pujol Research Institute (IGTP), Universitat Autònoma de Barcelona (UAB), Badalona, Spain.

² Interventional Neuroradiology Unit, University Hospital Germans Trias i Pujol, Badalona, Spain.

³ Department of Cellular Biology, Physiology and Immunology, UAB, Bellaterra, Spain.

✉ e-mail: tgasull@igtp.cat or teresagasull@yahoo.com

Introduction

Intracerebral hemorrhage (ICH) is the deadliest subtype of stroke, accounting for significant morbidity and mortality worldwide ^{1,2}. While many clinical trials focus on medical management ², only a few specifically target secondary brain injury, and most of these trials have not yielded significant improvements ³. This lack of progress is partly due to the reliance on rodent models in preclinical research, which have lissencephalic brains and a relatively high proportion of gray matter, making them less representative of the human condition ⁴. The Stroke Therapy Academic Industry Roundtable (STAIR) recommends the use of large animal models, whose brains are more similar to the human, in order to improve the translation of preclinical findings to clinical applications ⁵.

Currently, ICH stroke-pig models primarily rely on craniotomy for autologous blood or collagenase intracerebral injection to mimic human pathology ^{4,6–11}. However, these methods are invasive and can alter intracranial blood pressure ¹², posing significant limitations. Additionally, catheterizing pig cerebral arteries is challenging due to the presence of the *rete mirabile* (RM), which complicates access to the brain's vascular system ¹³. In this study, we aimed to develop an alternative, less invasive, endovascular approach to generate a novel ICH model in pigs, which are omnivorous and diurnal animals with gyrencephalic brains and have a more comparable white-to-gray matter ratio to humans than rodents. This new model will provide a more accurate platform for studying ICH pathophysiology and evaluating therapeutic interventions.

Methods

In this study, five pigs (3-month-old castrated males and females) were used to model intracerebral hemorrhage. For the neurointerventional procedure, a catheter was navigated through the transverse sinus (TS), vein of Galen (GV), and internal cerebral veins (ICV) to the thalamostriate veins (TSVs). An intracerebral hemorrhage was induced by perforating the TSV in the right hemisphere at specific locations as assessed using the digital subtraction angiography (DSA) to determine whether the catheter tip was in the venous system close

to the cortical lobe or in a deeper striatal location, followed by autologous arterial blood injection to simulate hemorrhage. Magnetic Resonance Imaging (MRI) scans were performed at several time points post-occlusion to measure hemorrhagic volumes using 3D Slicer software. Blood samples were collected before and after the ICH to assess physiological parameters and molecule levels, including the percentage of serum transferrin saturation (TSAT), transferrin (Tf), and platelet factor 4 (PF4) via Western blot and ELISA analysis.

At the end of the experiment, brain samples were collected and fixed for immunohisto-fluorescence (IHF) analysis of transferrin and ferritin.

Approval for animal experimentation and detailed descriptions of the methods can be found in the **Supplementary Material**.

Results

Reaching the brain venous system

Access to the cerebral venous system was successfully achieved in all pigs in this study via the internal jugular vein (IJV) (**Figure 1A–C** and **Supplementary video S1**), as previously described by Pasarikovski ¹⁴ and Fries ¹⁵. In 80% of the cases, access was feasible through the right IJV, while in the remaining 20%, the left IJV was used; in both cases, the right hemisphere was reached.

Consistent with previous reports, we observed that the cerebral venous system of pigs closely resembles that of humans across all animals studied, regardless of sex. Furthermore, navigation through the brain venous system was successfully performed, revealing an extensive distribution within the brain parenchyma (**Figure 1D**).

Establishment of intracerebral stroke models

After successfully accessing the cerebral venous system, we advanced the catheter into the TSV (**Figure 2A** and **Supplementary video S2**) and subsequently navigated to the targeted parenchymal region. Given that the most common intracerebral hemorrhages occur in deep brain structures ¹⁶, we aimed to replicate this distribution.

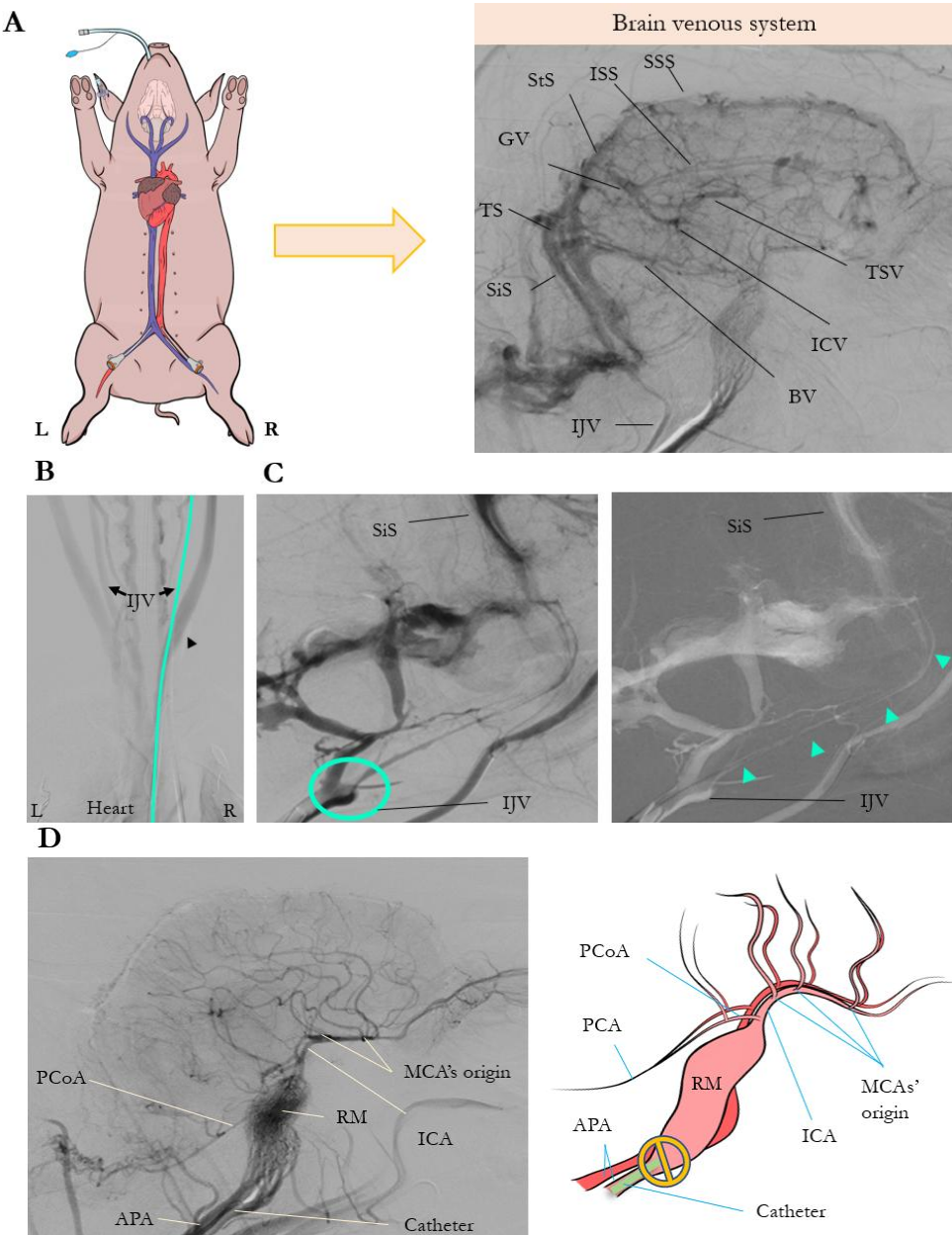


Figure 1. Endovascular access to the brain venous circulation. **(A)** digital subtraction angiography of the brain venous system. Cerebral brain vasculature exhibited similarities to that of humans, allowing identification of the superior sagittal sinus (SSS), inferior sagittal sinus (ISS), straight sinus (StS), vein of Galen (GV), transverse sinus (TS), sigmoid sinus (SiS), thalamostriate vein (TSV), internal cerebral vein (ICV), basilar vein (BV), and internal jugular vein (IJV). **(B)** Access to the cerebral venous circulation through the IJV (catheter depicted in blue for clarity), and **(C)** direct connection between the IJV and the SiS (entrance surrounded by a blue circle). **(D)** Angiography and schema of the cerebral arteries, the *rete mirabile* (RM) prevents catheter passage to the cerebral arteries. Abbreviations: posterior communicating artery (PComA), posterior cerebral artery (PCA), ascending pharyngeal artery (APA), middle cerebral arteries (MCAs), and internal cerebral artery (ICA).

While venous rupture leads to venous blood extravasation, intracerebral hemorrhage in humans typically results from arterial rupture.¹⁷ To achieve a more translationally relevant model, 1.5 mL of autologous arterial blood was injected at a rate of 0.5 mL/min in lobar or subcortical areas (**Figure 2B**).

This procedure resulted in hemorrhages corresponding to 4.85% of the ipsilateral hemisphere (**Figure 2C**), with blood accumulation observed in various locations, including lobar/cortical, striatal, subcortical, and intraventricular regions (**Supplementary Figure S1**). The autologous injected blood was clearly visible during the procedure due to contrast extravasation (**Supplementary Figure S2**) and was further confirmed by rotational angiography (computed tomography (CT)-like reconstruction) performed immediately after hemorrhage induction (**Figure 2D**).

At 90 minutes post-induction, hemorrhages were visualized across multiple MRI sequences, including fluid-attenuated inversion recovery (FLAIR), axial T2*-weighted (AxT2*), axial T2 post-gadolinium contrast (AxT2PostGd), apparent diffusion coefficient (ADC), diffusion-weighted imaging (DWI), and flow-sensitive black blood (FSBB) imaging. Among these, the AxT2* sequence provided the clearest hemorrhagic visualization (**Figure 2D** and **Figure 3B, left**).

Hemorrhage evolution

The hemorrhage was visible during all MRI scans, though its appearance changed over time (**Figure 3A**). In the hyperacute phases (90 minutes post-induction), the hemorrhage appeared as a hypointense region on MRI (**Figure 3A, 90 minutes** and **Figure 3B, left**). However, after several weeks, both hypointense and hyperintense areas were observed (**Figure 3A, 2 weeks**), especially in the pigs in which we induced subcortical hemorrhage. The hyperintense regions did not correspond to a residual blood clot (**Figure 3B, right**) but likely represented released blood components during hematoma clearance, such as hemoglobin and iron.

No evidence of hemorrhage expansion was observed in the MRI performed at 24 hours compared to the scan at 90 minutes,

suggesting that the presence of the blood that we administered into the brain parenchyma does not induce vessel damage that produces additional bleeding (**Figure 3C**).

Neurological signs

Neurological signs in pigs began to manifest at 4 hours post-ICH induction and persisted for up to 3 days. Observed symptoms included head lateralization, nystagmus, ataxia, ipsilateral circling, trembling, menace response, and head shaking. A representative video of pig behavior is provided in **Supplementary Video S3** and **Supplementary Figure S3**.

Changes in secondary brain injury-related proteins

Blood degradation products, including iron and coagulation components, are released over time. We investigated whether iron-related molecules such as transferrin (Tf), ferritin (FT), or platelet factor 4 (PF4) showed changes.

Early after the ICH induction, we observed a reduction of PF4 in all the pigs, indicating alterations in the systemic platelet response (**Figure 4C**). Other parameters of the coagulation, such as antithrombin/thrombin activity, might be difficult to assess as heparin is used in the model to prevent clot production during the endovascular approach. Pigs with ICH seem to increase Tf levels in serum in a time-course study, beginning at 24 hours and persisting up to 2 weeks post-hemorrhage (**Figure 4A**); this will be verified in the next months when increasing the cohort of pigs exposed to this model of ICH. To further assess iron parameters, we measured TSAT in blood. A significant increase in TSAT was detected in a time-course study as early as 1 hour post-ICH induction, compared to both the sham ($p<0.01$) group and the baseline sample (-1 hour) ($p<0.05$) (**Figure 4B** and **D**).

An increase in the Tf levels was also observed in perihematomal areas in the brain parenchyma (**Figure 5A**), and ferritin in NeuN+ cells in the ipsilateral hemisphere (IL) versus the contralateral hemisphere (CL).

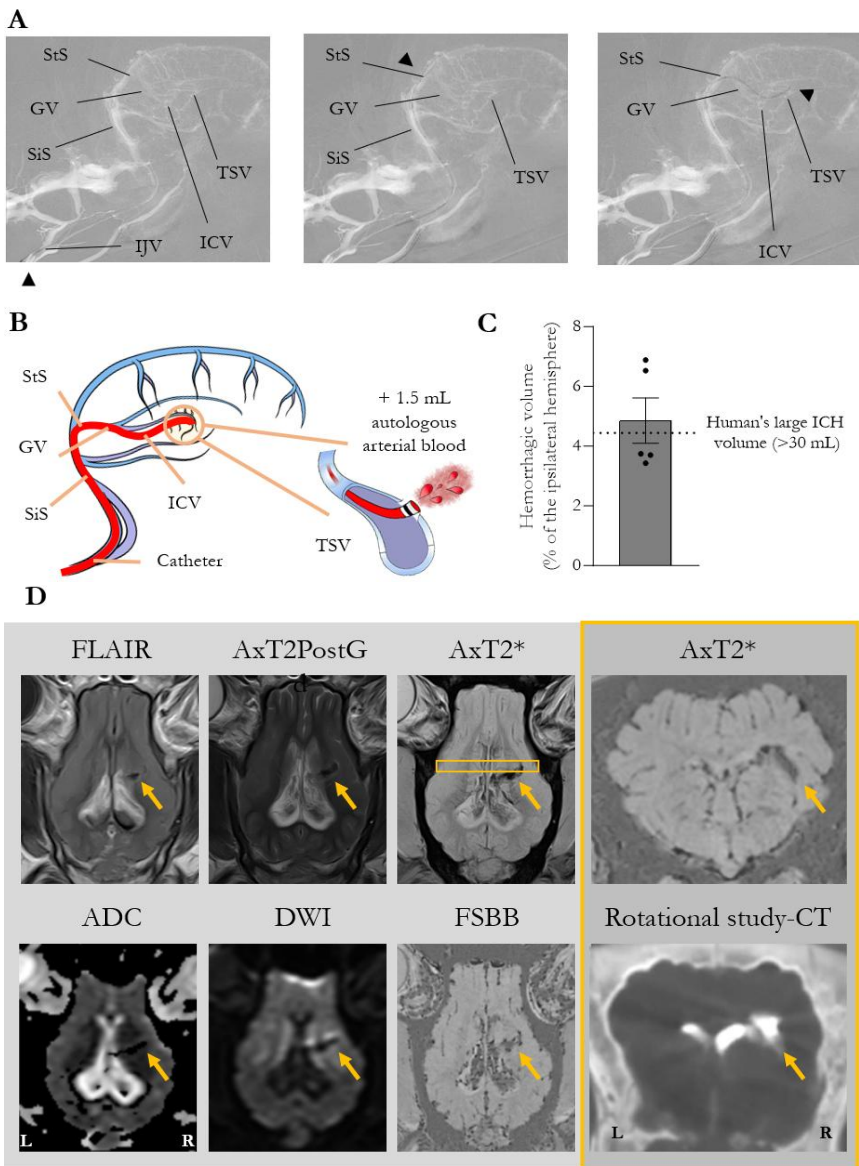


Figure 2. Development of the intracerebral hemorrhagic model. **(A)** Route of the catheter to the deep venous circulation through the sigmoid sinus (SiS), straight sinus (StS), and vein of Galen (GV) to reach the internal cerebral vein (ICV), and finally the thalamostriate veins (TSV). **(B)** Graphical representation of the rupture of the target vein and the injection of 1.5 mL of autologous arterial blood at a rate of 0.5 mL/min. **(C)** Quantification of the hemorrhagic volume (4.85% of the total brain ($n=5$)), comparable to human large hemorrhage volumes (>30 mL). **(D)** Visualization of the hemorrhage (see yellow arrows) in the rotational study performed in the angiography room and in different magnetic resonance imaging (MRI) sequences, including fluid-attenuated inversion recovery (FLAIR), axial T2-weighted post-gadolinium (AxT2PostGd), axial T2*-weighted (AxT2*), apparent diffusion coefficient (ADC), diffusion-weighted imaging (DWI), and flow-sensitive black blood (FSBB). The contrast extravasation in the coronal slide of the rotational study (**D, right-bottom**, surrounded by a yellow square) corresponded to the hemorrhage visualized in the coronal slide of the AxT2* sequence (**D, right-top**, surrounded by a yellow square).

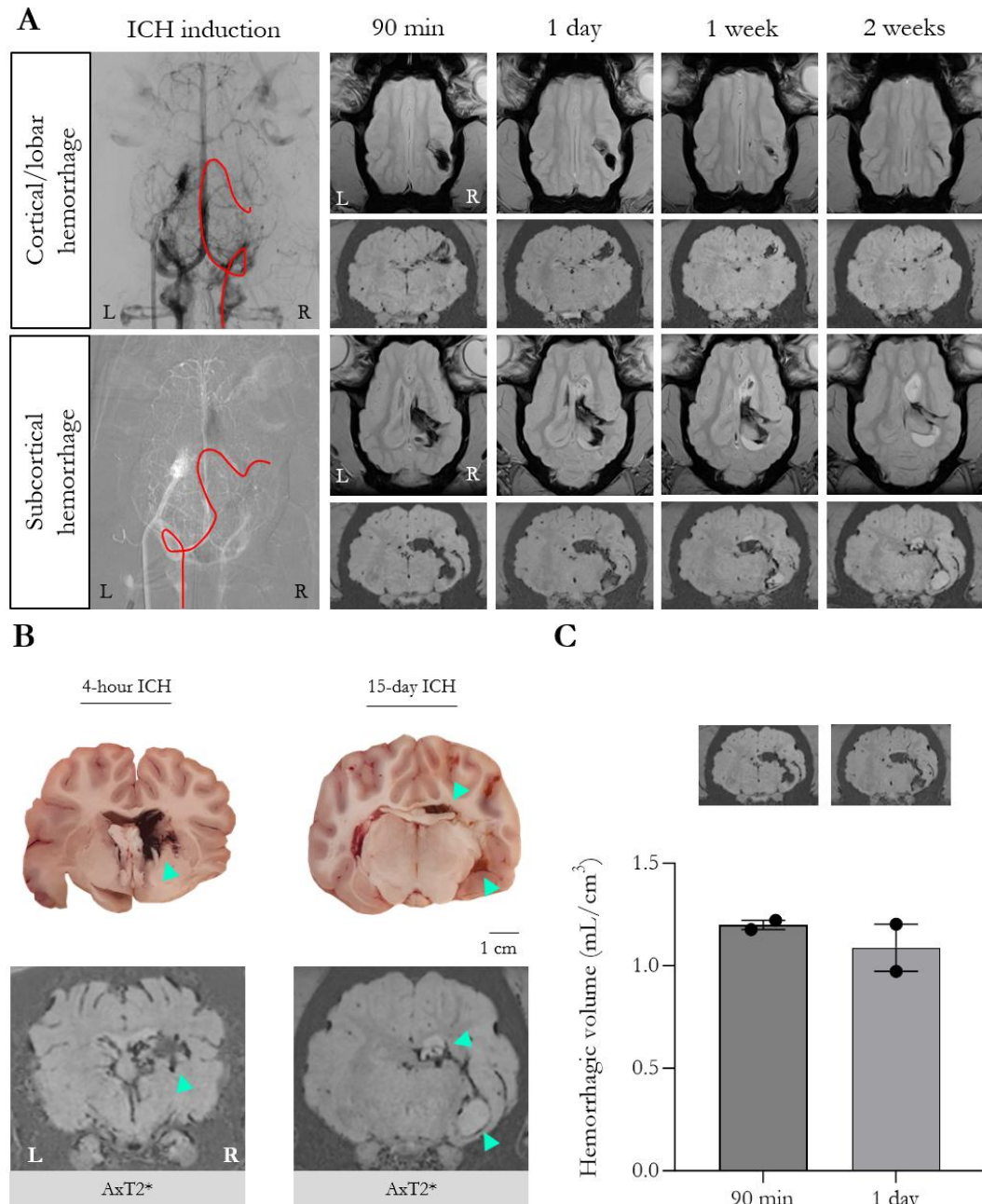


Figure 3. Hemorrhage evolution. **(A, left)** Dorsal cut angiographies of hemorrhage induction, with the catheter highlighted in red to ease visualization of the route. For cortical hemorrhage, access to the brain venous circulation was through the left internal jugular vein (IJV), while for subcortical hemorrhage, access was through the right IJV. **(A, right)** Evolution of the hemorrhages was assessed using the axial T2*-weighted (AxT2*) sequence at 90 minutes, 1 day, 1 week and 2 weeks post-ICH. **(B)** Hemorrhage (see blue arrows) at different time points (4 hours and 2 weeks post-ICH) in *ex vivo* coronal brain slices was compared with the hemorrhage visualized in the coronal brain slices from AxT2* sequence obtained just before euthanasia. **(C)** Quantification of the hemorrhagic volume at 90 minutes and 1-day post-ICH (n=2).

Discussion

Gyrencephalic swine models provide a valuable bridge for translating preclinical stroke results into clinical applications. Several porcine models of hemorrhagic stroke have been developed, most of which involve highly invasive procedures requiring specialized personnel and direct injection of autologous blood or collagenase into the brain via craniotomy, requiring a pig-specific stereotaxic frame ⁶⁻¹¹. Also, craniotomy increases the risk of infection ¹⁸ and reduces translational relevance, as it does not accurately mimic the pressure-delivered mass effect associated with the intracerebral hemorrhage in an intact skull ¹⁶. In fact, decompressive craniotomy is often used in clinical practice to reduce intracranial pressure and improve patient outcomes in cerebellar hemorrhages ¹².

We aimed to create a less invasive, endovascular pig model of ICH that better mimics human pathology, offering a more relevant platform for studying ICH mechanisms and testing treatments.

Along the literature, and also previous results from our group, demonstrate that current commercially available catheters cannot reach the circle of Willis in pigs, and thus, the intracranial arteries, due to the presence of the *rete mirabile* ¹³. However, studies by Pasarikovski and Fries showed that endovascular access to the venous brain vasculature, specifically to the SSS via the IJV, is feasible with commercially available catheters in swine (**Figure 1B**) ^{14,15}. Building on this, we successfully developed a minimally invasive porcine ICH model using endovascular access, reaching the TSV and perforating it in the desired region of the brain (**Figure 2B**). This novel approach allows for the induction of different ICH scenarios, including lobar, striatal, and intraventricular hemorrhages (IVH) (**Supplementary Figure S1**) ^{17,19}.

The method was feasible in 100% of the animals, either through the right IJC (80% of the animals) or the left (20% of the animals) (**Supplementary Video S1**). This is similar to the previous reported by Wang *et al.* describing that some swines had a narrow venous passage between the IJV and the distal spinal venous

plexus and allowing only to pass some microcatheters to reach the cerebral venous sinus ²⁰.

In clinical practice, ICH most commonly results from the rupture of an intracranial artery ^{1,19,21,22}. To recapitulate human ICH, and since venous perforation alone would induce venous bleeding, we injected 1.5 mL of autologous arterial blood at a controlled rate to better mimic clinical hemorrhagic conditions. We assessed that when only the perforation of a vein was performed, the bleeding was non-significant (**Figure 3C**) despite the use of heparin during the ICH induction procedure. This is notable considering that anticoagulation therapy has been shown to increase the risk of secondary hemorrhage ²³. Our results allow to demonstrate that ICH by endovascular approach does not increase the systemic platelet activation, as assessed by measuring levels of PF4; in fact, we found reduced levels of PF4 after the ICH, in agreement with clinical studies showing lower platelet counts in ICH patients than control patients ^{24,25}.

The severity and clinical presentation of ICH depend on hemorrhage volume and location. We found that blood deposition performed in lobar locations is contained around the initial administration area, whereas the striatally-administered blood reaches the ventricular system (IVH). In human patients, lobar hemorrhages are associated with neurological deficits such as visual neglect, hemianopia, and contralateral gaze preference ^{16,19}; these symptoms align with the findings produced by our ICH swine model. The gaze preference results in a marked circling towards the ipsilateral hemisphere that can be quantified (**Supplementary Video S3** and **Supplementary Figure S3**). Furthermore, IVH is linked to particularly high mortality rates and poor functional outcomes ^{2,16,22}. In our study, pigs with IVH exhibited severe neurological deterioration and were euthanized according to the pre-established welfare assessment threshold score within 4 hours post-ICH following MRI confirmation of hemorrhage extent.

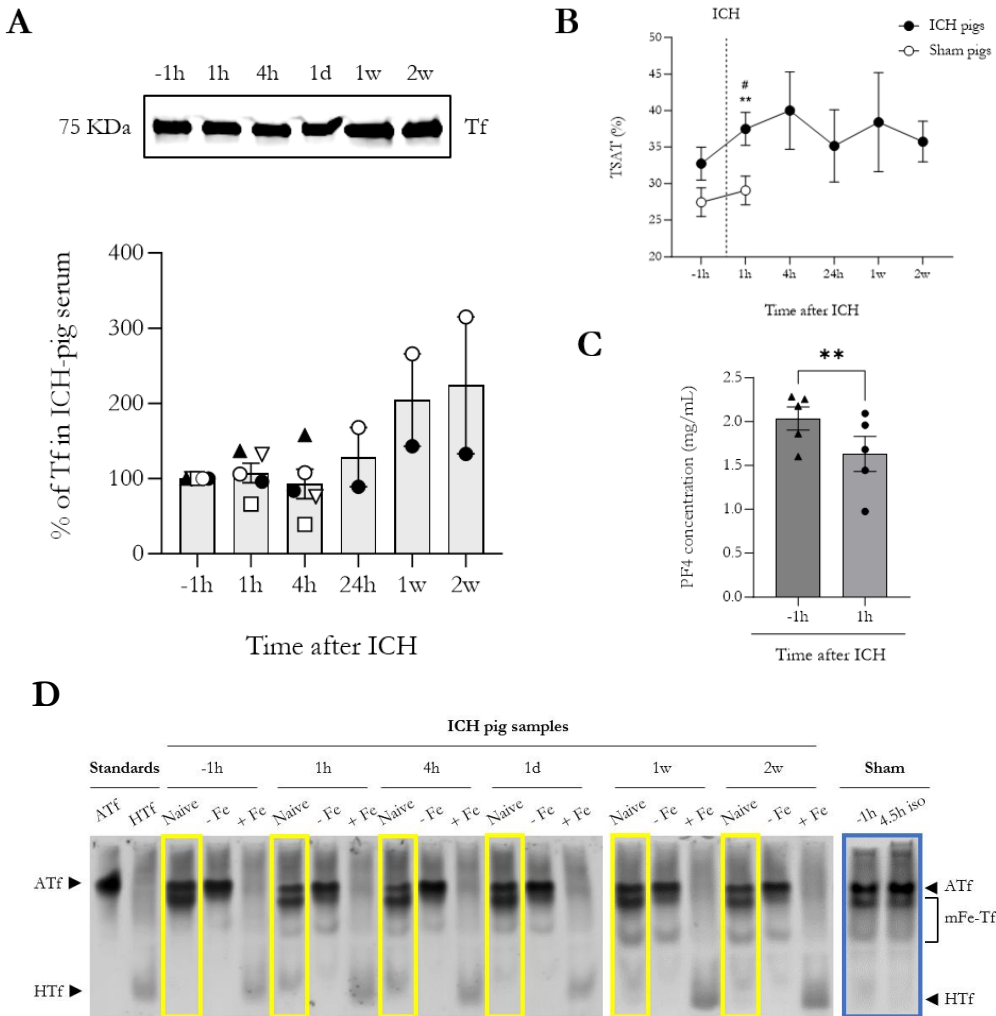


Figure 4. Changes in plasma and serum iron and coagulation-related molecules. **(A)** Representative Western Blot (WB) showing variations in transferrin (Tf) levels in serum samples at different time points post-ICH, along with its quantification. **(B)** Percentage of transferrin saturation (TSAT) over time before and after ICH induction; # $p<0.05$ vs. baseline sample (-1 hour) (repeated measures two-way ANOVA), ** $p<0.01$ vs. Sham (repeated measures two-way ANOVA). Mean and SEM are shown. **(C)** Graph showing variations in the concentration of platelet factor 4 (PFA4) in plasma samples at baseline (-1 hour) and 1 hour after ICH induction ** $p<0.01$ vs. baseline sample (-1 hour) (paired *t*-test). Mean and SEM are shown. **(D)** Representative U-PAGE/WB showing the electrophoretic pattern of transferrin isoforms (apotransferrin, ATf; monoferric transferrin, mFe-Tf; and diferric transferrin or holotransferrin, HTf) in serum pig samples at different time points post-ICH (indicated with a yellow square). In-lab prepared pig standards are loaded in the first two lanes, and each sample was loaded as naïve, with the iron removed (- Fe), and with iron loaded (+ Fe), which changes all transferrin to ATf or diFe-Tf, respectively. Representative sham samples are also shown (with a blue square), including baseline samples and those taken after 4.5 hours of anesthesia (4.5h iso), which corresponds to the 1-hour post-ICH sample. Full gels are available in the [Supplementary material](#).

During the procedure of ICH induction, contrast was used to identify the desired area of brain parenchyma to produce the hemorrhage, then the blood was injected, and expansion of contrast was visualized (Supplementary Figure S2). Subsequently, the location of the hemorrhage was confirmed using MRI (Figure 2D). Axial T2*-weighted sequences

were employed to determine hemorrhage volume, which was found to span an average of $4.85\% \pm 0.75$ of the ipsilateral hemisphere (Figure 2C). This proportion is comparable to large human hemorrhages exceeding 30 mL, which represent approximately 4.44% of the ipsilateral human brain (2.23% of the total human brain volume $\sim 1,345$ cc) [1,26](#).

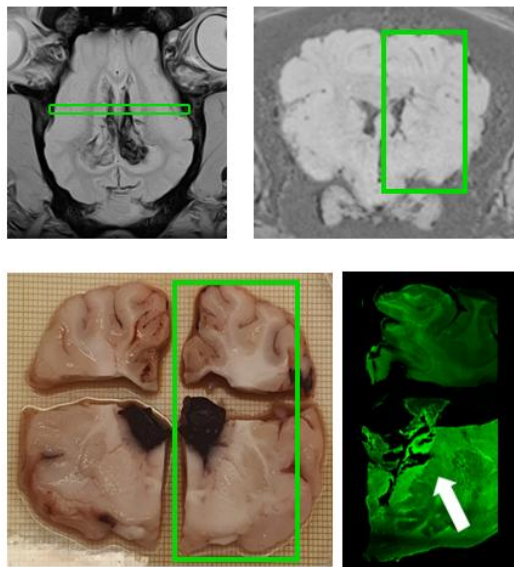
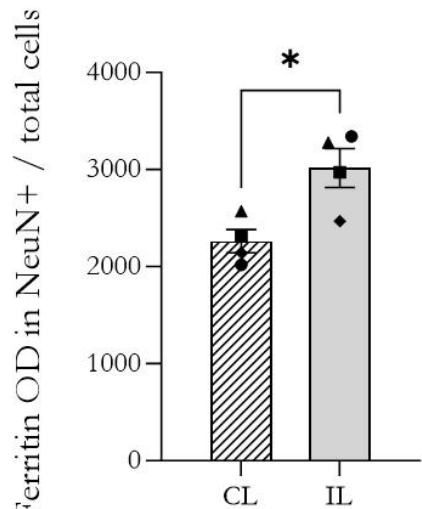
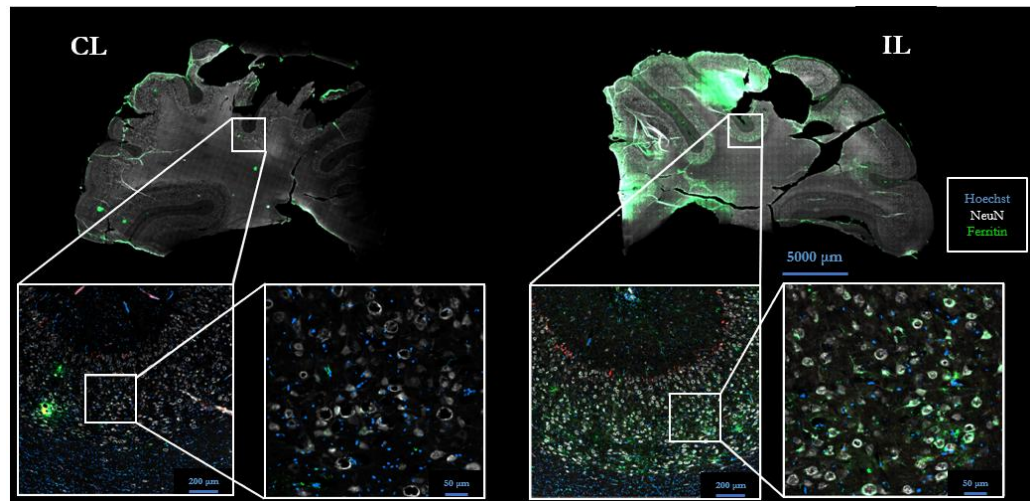
A**B****C**

Figure 5. Changes in brain iron-related molecules. (A) Representative immunohistofluorescence image expressing transferrin in an *ex vivo* coronal brain cut. The green square in the MRI and *ex vivo* images corresponds to the analyzed area. (B) Graph showing Ferritin optical density levels in NeuN+ neurons relative to the total cells. * $p < 0.05$ ipsilateral (IL) vs. contralateral (CL) (*t*-test). Mean and SEM are shown. (C) Representative immunohistofluorescence images of ROI's for analysis of ferritin expression.

MRI findings were consistent with the expected evolution of hemorrhagic lesions. In hyperacute (2-hour) and acute (1-day) phases, hemorrhages appeared hypointense on Axial T2*-weighted images. During the early subacute (1-week) and later subacute (2-week) phases, lesions show mixed hyperintense and hypointense signals, reflecting the breakdown of blood components such as hemoglobin and iron ²⁷ (**Figure 3A and B**). Remarkably, no hypointense or hyperintense regions were observed on DWI/ADC or FLAIR sequences, suggesting the absence of ischemic regions or excitotoxic damage (**Figure 2D**).

Iron metabolism plays a crucial role in secondary brain injury following ICH, showing both central and systemic changes.

Of note, the iron-related molecules, transferrin and ferritin, were also increased in the brain ipsilateral hemisphere parenchyma compared to the contralateral hemisphere of each one of the pigs in the study. This is probably due to blood extravasation, as transferrin is a protein that transports iron through the blood, and due to the vessel rupture and blood is accumulated in the perihematomal area. Iron is also one of the main components released ²². The iron accumulation in the brain parenchyma induced the expression of iron-storage proteins such as ferritin ²⁸. The increase in ferritin was observed at 4 and 2 hours after ICH.

Here, we present a new minimally invasive porcine ICH model with the potential to replicate several clinical hemorrhage location scenarios while maintaining a more clinically relevant pathophysiology. Unlike conventional craniotomy-based models, our approach preserves intracranial integrity, avoiding surgical decompression effects that could alter ICH progression. Additionally, the use of gyrencephalic, diurnal animals with a white-to-gray matter ratio closer to humans enhances the translational potential of this model.

Limitations of the study

The primary limitation of this study is the modest sample size and the use of domestic pig strains, which limits the age of the animals, requiring the use of juvenile animals. However, this limitation could be addressed in

further studies by using minipigs, which reach adult body weights of 40 kg while maintaining a cerebral vasculature comparable to domestic pigs and to humans ¹³.

Funding

This study has been supported by grants from the Instituto de Salud Carlos III FI19/00174, RICORS RD21/0006/0024 and RD24/0009/0015, PI21/01925, PI24/00963, PI18/01813, and AGAUR 2021SGR00925, susceptible to be co-financed by FEDER/FSE funds.

Disclosures/conflicts of interest

None

References

1. Martin SS, Aday AW, Allen NB, Almarzooq ZI, Anderson CAM, Arora P, *et al.* 2025 Heart Disease and Stroke Statistics: A Report of US and Global Data From the American Heart Association. *Circulation*. 2025 Feb;151(8):e41-e660. doi: 10.1161/CIR.0000000000001303.
2. Greenberg SM, Ziai WC, Cordonnier C, Dowlatshahi D, Francis B, Goldstein JN, *et al.* 2022 Guideline for the Management of Patients With Spontaneous Intracerebral Hemorrhage: A Guideline From the American Heart Association/American Stroke Association. *Stroke*. 2022 Jul;53(7):e282-e361. doi: 10.1161/STR.000000000000407.
3. Chiang PT, Tsai LK, Tsai HH. New targets in spontaneous intracerebral hemorrhage. *Curr Opin Neurol*. 2025 Feb;38(1):10-17. doi: 10.1097/WCO.0000000000001325.
4. Melià-Sorolla M, Castaño C, DeGregorio-Rocasolano N, Rodríguez-Esparagoza L, Dávalos A, Martí-Sistac O, *et al.* Relevance of Porcine Stroke Models to Bridge the Gap from Pre-Clinical Findings to Clinical Implementation. *Int J Mol Sci*. 2020 Sep;21(18):6568. doi: 10.3390/ijms21186568.
5. Stroke Therapy Academic Industry Roundtable (STAIR). Recommendations for standards regarding preclinical

neuroprotective and restorative drug development. *Stroke*. 1999 Dec;30(12):2752-8. doi: 10.1161/01.str.30.12.2752.

6. Wagner KR, Xi G, Hua Y, Kleinholtz M, de Courten-Myers GM, Myers RE, et al. Lobar intracerebral hemorrhage model in pigs: rapid edema development in perihematoma white matter. *Stroke*. 1996 Mar;27(3):490-7. doi: 10.1161/01.str.27.3.490.
7. Küker W, Thiex R, Rohde I, Rohde V, Thron A. Experimental acute intracerebral hemorrhage. Value of MR sequences for a safe diagnosis at 1.5 and 0.5 T. *Acta Radiol*. 2000 Nov;41(6):544-52. doi: 10.1080/028418500127346180.
8. Mun-Bryce S, Wilkerson AC, Papuashvili N, Okada YC. Recurring episodes of spreading depression are spontaneously elicited by an intracerebral hemorrhage in the swine. *Brain Res*. 2001 Jan;888(2):248-255. doi: 10.1016/s0006-8993(00)03068-7.
9. Rohde V, Rohde I, Thiex R, Küker W, Ince A, Gilsbach JM. The role of intraoperative magnetic resonance imaging for the detection of hemorrhagic complications during surgery for intracerebral lesions an experimental approach. *Surg Neurol*. 2001 Oct;56(4):266-74; discussion 274-5. doi: 10.1016/s0090-3019(01)00594-8.
10. Zhu H, Li F, Zou M, Xue X, Yuan J, Feng H, et al. Experimental high-altitude intracerebral hemorrhage in minipigs: histology, behavior, and intracranial pressure in a double-injection model. *Acta Neurochir (Wien)*. 2013 Apr;155(4):655-61. doi: 10.1007/s00701-013-1618-z.
11. Gerhardson T, Sukovich JR, Chaudhary N, Chenevert TL, Ives K, Hall TL, et al. Histotripsy Clot Liquefaction in a Porcine Intracerebral Hemorrhage Model. *Neurosurgery*. 2020 Mar;86(3):429-436. doi: 10.1093/neuros/nyz089.
12. Beck J, Fung C, Strbian D, Bütkofer L, Z'Graggen WJ, Lang MF, et al. Decompressive craniectomy plus best medical treatment versus best medical treatment alone for spontaneous severe deep supratentorial intracerebral haemorrhage: a randomised controlled clinical trial. *Lancet*. 2024 Jun;403(10442):2395-2404. doi: 10.1016/S0140-6736(24)00702-5. Erratum in: *Lancet*. 2024 Jun 1;403(10442):2380. doi: 10.1016/S0140-6736(24)01089-4. Erratum in: *Lancet*. 2024 Jul 6;404(10447):30. doi: 10.1016/S0140-6736(24)01355-2.
13. Castaño C, Meliá-Sorolla M, García-Serran A, DeGregorio-Rocasolano N, García-Sort MR, Hernandez-Pérez M, et al. Establishment of a reproducible and minimally invasive ischemic stroke model in swine. *JCI Insight*. 2023 Apr;8(8):e163398. doi: 10.1172/jci.insight.163398.
14. Pasarikovski CR, Ku JC, Keith J, Ramjist J, Dobashi Y, Priola SM, et al. Endovascular Cerebral Venous Sinus Imaging with Optical Coherence Tomography. *AJNR Am J Neuroradiol*. 2020 Dec;41(12):2292-2297. doi: 10.3174/ajnr.A6909.
15. Fries G, Wallenfang T, Hennen J, Velthaus M, Heimann A, Schild H, et al. Occlusion of the pig superior sagittal sinus, bridging and cortical veins: multistep evolution of sinus-vein thrombosis. *J Neurosurg*. 1992 Jul;77(1):127-33. doi: 10.3171/jns.1992.77.1.0127.
16. Sheth KN. Spontaneous Intracerebral Hemorrhage. *N Engl J Med*. 2022 Oct;387(17):1589-1596. doi: 10.1056/NEJMra2201449. Erratum in: *N Engl J Med*. 2023 Apr;388(15):1440.
17. Qureshi AI, Mendelow AD, Hanley DF. Intracerebral haemorrhage. *Lancet*. 2009 May;373(9675):1632-44. doi: 10.1016/S0140-6736(09)60371-8.
18. Kinaci A, Vaessen K, Redegeld S, van der Zwan A, van Doormaal TPC. Minimizing complications in a porcine survival craniotomy model. *Lab Anim*. 2021 Oct;55(5):435-442. doi: 10.1177/00236772211009435.
19. Qureshi AI, Tuhrim S, Broderick JP, Batjer HH, Hondo H, Hanley DF. Spontaneous intracerebral hemorrhage. *N Engl J Med*. 2001 May;344(19):1450-60. doi: 10.1056/NEJM200105103441907.
20. Wang J, Tan HQ, Li MH, Sun XJ, Fu CM, Zhu YQ, et al. Development of a new model of transvenous thrombosis in the pig superior sagittal sinus using

thrombin injection and balloon occlusion. *J Neuroradiol.* 2010 May;37(2):109-15. doi: 10.1016/j.neurad.2009.06.002.

21. Sacco RL, Kasner SE, Broderick JP, Caplan LR, Connors JJ, Culebras A, *et al.* An updated definition of stroke for the 21st century: a statement for healthcare professionals from the American Heart Association/American Stroke Association. *Stroke.* 2013 Jul;44(7):2064-89. doi: 10.1161/STR.0b013e318296aeca. Erratum in: *Stroke.* 2019 Aug;50(8):e239. doi: 10.1161/STR.0000000000000205.

22. Magid-Bernstein J, Girard R, Polster S, Srinath A, Romanos S, Awad IA, *et al.* Cerebral Hemorrhage: Pathophysiology, Treatment, and Future Directions. *Circ Res.* 2022 Apr;130(8):1204-1229. doi: 10.1161/CIRCRESAHA.121.319949

23. Schlunk F, Böhm M, Boulouis G, Qin T, Arbel M, Tamim I, Fischer P, Bacska BJ, Frosch MP, Endres M, Greenberg SM, Ayata C. Secondary Bleeding During Acute Experimental Intracerebral Hemorrhage. *Stroke.* 2019 May;50(5):1210-1215. doi: 10.1161/STROKEAHA.118.021732.

24. Ziai WC, Torbey MT, Kickler TS, Oh S, Bhardwaj A, Wityk RJ. Platelet count and function in spontaneous intracerebral hemorrhage. *J Stroke Cerebrovasc Dis.* 2003 Jul-Aug;12(4):201-6. doi: 10.1016/S1052-3057(03)00075-2.

25. Sadeghi F, Kovács S, Zsóri KS, Csiki Z, Bereczky Z, Shemirani AH. Platelet count and mean volume in acute stroke: a systematic review and meta-analysis. *Platelets.* 2020 Aug 17;31(6):731-739. doi: 10.1080/09537104.2019.1680826.

26. DeSilva J, Fannin L, Cheney I, Claxton A, Ilieş I, Kittelberger J, *et al.* Human brains have shrunk: the questions are when and why. *Front Ecol Evol.* 2023 Jun;11:1191274. doi: 10.3389/fevo.2023.1191274.

27. Rindler RS, Allen JW, Barrow JW, Pradilla G, Barrow DL. Neuroimaging of Intracerebral Hemorrhage. *Neurosurgery.* 2020 May;86(5):E414-E423. doi: 10.1093/neuros/nyaa029.

28. García-Serran A, Ordoño J, DeGregorio-Rocasolano N, Melià-Sorolla M, Oendaaal K, Martí-Sistac O, *et al.* Targeting Pro-Oxidant Iron with Exogenously Administered Apotransferrin Provides Benefits Associated with Changes in Crucial Cellular Iron Gate Protein TfR in a Model of Intracerebral Hemorrhagic Stroke in Mice. *Antioxidants (Basel).* 2023 Oct 31;12(11):1945. doi: 10.3390/antiox12111945.

Supplementary Materials for

Establishing an endovascular model of intracerebral hemorrhage in swine for translational stroke research

Alexia García-Serran, DVM¹ ; Carlos Castaño, MD PhD²; Marc Melià-Sorolla, PhD¹ ; Núria DeGregorio-Rocasolano, PhD¹ ; Octavi Martí-Sistac, PhD^{1,3} ; Teresa Gasull, PhD^{1*}

Material and methods

Animals

In this study, we utilized five 3-month-old female and castrated male Duroc x Landrace pigs with an average weight of 40.1 ± 3.3 kg from Mir Ramadera (Tona, Spain). These pigs were housed under controlled standard conditions of temperature, humidity, and photoperiod, with *ad libitum* access to food and water. Upon arrival at the Comparative Medicine and Bioimage Centre of Catalonia (CMCiB), the animals were allowed to acclimate undisturbed in their pens for a minimum of one week.

The animal experiments received were approved by both the Animal Research Ethics Committee (CEEA) of the Germans Trias i Pujol Research Institute (IGTP) and the Catalan Government (reference 10671, FUE-2019-01138108 and ID 26Q7BHRXN). The experiments were conducted in a randomized manner and adhered to international guidelines (EU Directive 2010/63/EU) at the CMCiB. Additionally, we followed the ARRIVE guidelines (<https://arriveguidelines.org/>) and adhered to the 3Rs principles (Reduce, Refine, Replace) in laboratory animal research.

Throughout all the procedures (preoperative, neurointerventional, and MRI), vital signs were continuously monitored under general anesthesia. These included electrocardiogram, heart and respiratory rates, oxygen saturation, capnography, body temperature, and non-invasive arterial blood pressure. A forced-air warmer (Bair Hugger 77514 240 V-SPA-A; Minnesota Mining and Manufacturing Company, 3M; Saint Paul, MN, USA) was used to maintain body temperature.

Preoperative procedures

The pre-neurointerventional procedures followed the protocol outlined by Castaño *et al.* 2023 ¹. Briefly, the pigs underwent a 12-hour fasting period before anesthesia administration. Premedication consisted of intramuscular (IM) administration of atropine (0.04 mg/kg), ketamine (3 mg/kg), dexmedetomidine (0.03 mg/kg), midazolam (0.3 mg/kg), and buprenorphine (0.01 mg/kg). Once sedated, corneal ointment, IM antibiotic (tulathromycin, 2.5 mg/kg), and intravenous propofol (1mg/kg) were given. Additionally, a dermal fentanyl patch (2 μ g/kg/h) was applied for analgesia.

For tracheal intubation, lidocaine spray was applied to the larynx to facilitate the procedure. After intubation, the pigs were connected to a closed mechanical ventilation system to maintain anesthesia with isoflurane (1.5 – 2%). Intravenous sterile saline solution was administered at 100 mL/h. The pigs were then transferred to either the large animal neurointerventionism room or the magnetic resonance imaging (MRI) room.

Neurointerventional procedure

The neurointerventional procedure was performed with the pig in a supine position. To prevent thrombus formation, a physiological saline containing 3,000 units of heparin was administered as a bolus during catheterization.

Using ultrasound guidance, a 7F (French) sheath introducer (Prelude® Sheath Introducer PRO-7F-11-035MT; Merit Medical; South Jordan, UT, USA) was inserted into both the right femoral vein and the left femoral artery.

For *in vivo* vascular imaging, a Canon Alphenix monoplane angiography system™ (Canon Medical Systems Corporation; Ōtawara, Tochigi, Japan) was utilized, following the approach described by Pasarikovski *et al.*² to access the pig's brain venous circulation. Briefly, a 7F Envoy guide catheter (778-256-00; Codman; Integra LifeSciences; Princeton, NJ, USA) placed in the artery was navigated into the left ascending pharyngeal artery without entering into the *rete mirabile*. Simultaneously, a second 7F guide catheter and a Terumo glidewire (RadifocusTM Guide Wire M Standard RF*GA35183M; Terumo Corporation; Shibuya, Tokyo, Japan) were introduced into the right internal jugular vein.

To visualize the interrelation between the sigmoid sinus (SiS) and the internal jugular vein (IJV), iodine contrast agent (Iodixanol; VisipaqueTM 320 mg/mL; GE Healthcare; Chicago, IL, USA) was injected through the Envoy catheter positioned in the left ascending pharyngeal artery. A second injection was administered via the catheter in the right IJV when the late-venous phase became visible.

In order to access the brain venous circulation, we navigate through the transverse sinus (TS) using a Stryker Synchro2 guidewire (Synchro2® Standard; 2641; Stryker Corporation; Kalamazoo; MI, USA) and a Microvention Headway® Duo microcatheter (Headway Duo! Microcatheter MC162156S; Terumo Corporation; Shibuya, Tokio, Japan) until reaching the superior sagittal sinus (SSS). Subsequently, we continued the navigation through the straight sinus (StS) and the vein of Galen (GV) to the internal cerebral veins (ICV) to reach the thalamostriate veins (TSV) (**Figure 2.**).

Intracerebral hemorrhage

The intracerebral hemorrhage was induced in multiple brain regions, including the lobes, striatum, putamen, and ventricles (**Supplementary Figure S1**). Once the catheter reached the intended location, a targeted venous perforation was performed in the right hemisphere, followed by an iodine contrast injection to confirm extravasation. After this, 1.5 mL of arterial blood was extracted from the same animal at that moment and subsequently injected through the Headway® duo microcatheter at a rate of 0.5 mL/min to simulate hemorrhage.

At the end of the intervention, all catheters were carefully removed. A final rotational angiography scan was performed to check the ICH. To prevent bleeding, manual pressure was applied to the femoral artery for 30 minutes before the animal was moved from the vascular radiology suite.

Magnetic resonance imaging (MRI)

MRI scans were performed on all animals using a Vantage Galan 3T (Canon Medical Systems) equipped with a 16-channel Flex SPEEDER coil. Imaging was conducted 90 min after ICH, and in cases of lobar hemorrhages, additional scans were performed at 24 hours, 1 week, and 2 weeks post-ICH. The MRI protocol included multiple sequences: diffusion tensor imaging (DTI), fluid-attenuated inversion recovery (FLAIR), T2*-weighted (T2*), 3D flow sensitive black blood (FSBB), and apparent diffusion coefficient (ADC). T2* images were used to measure hemorrhagic volume, utilizing the following parameters: TE = 12 ms, TR = 411 ms, 15 slices, slice thickness = 3 mm, inter-slice gap = 0.3 mm, in-plane resolution = 0.2 x 0.2 mm, matrix size = 320 x 256, field of view = 170 x 100 mm, and a total scan time of 7 minutes and 24 seconds.

Postoperative care, follow-up, and euthanasia

Following the neurointerventional and MRI procedures, anesthesia was reversed with an IM injection of atipamezole (0.1 mg/kg). Vital parameters, including pulse, reflexes, respiratory rate, and body temperature, were continuously monitored until they returned to normal. Once the swallowing reflex was fully restored, the pigs were extubated and transferred back to their pens for overnight recovery under continuous video monitoring.

To maintain body temperature during the early postoperative phase, pigs were initially covered with a thermal foil blanket. Later in their pens, pigs were provided with a heat lamp positioned 1.5 meters above the pen, which remained active for the first night post-surgery. Once fully alert, they had free access to food and water.

Neurological function was assessed visually by veterinarians and researchers. Blood samples to evaluate physiological status and hematological changes were collected at multiple time points: before the procedure, 1 hour post-ICH, 24 hours, 1 week, and 2 weeks post-ICH.

Comprehensive blood analyses were performed, including complete blood counts, hematocrit, platelet counts, hemoglobin, leukocyte, hemoglobin, blood urea creatinine (CRE), alkaline phosphatase (ALP), total bilirubin (TBIL), urea nitrogen (BUN), alanine aminotransferase (ALT), glucose (GLU), albumin (ALB), calcium (CA), aspartate aminotransferase (AST), total protein (TP), globulins (GLOB), and electrolytes.

At the end of the study, euthanasia was performed via IV injection of sodium pentobarbital (200 mg/kg).

Hemorrhagic volume measurement

The volume of infarcted tissue was quantified using Axial T2* MRI sequence, analysed with 3D Slicer software v5.6.1 (available at <https://www.slicer.org/>). Lesion volumes were manually delineated as hypointense regions in this sequence, taken at 90 min and 1 day post-occlusion.

Blood sampling to assess Tf in blood

Blood samples were collected from anesthetized swine from the cranial cava vein at multiple time points: prior to the ICH, and at 1 hour, 4 hours, 1 day, 1 week, and 2 weeks after ICH. The blood samples were processed to obtain serum or EDTA plasma, which were then aliquoted and stored at -80°C for future analysis.

Sham

The pigs of the sham group underwent the same preoperative procedure and were then kept anesthetized for 5 hours (n=4). Blood samples were obtained at baseline (-1 hour) and at 4.5 hours of anesthesia, which corresponds to 1 hour post-ICH.

Western Blot analysis (WB)

To assess Tf protein levels, serum samples were diluted 1:15 and loaded in Mini-PROTEAN® TGX™ precast gels (Bio-Rad; Hercules, CA, USA) alongside a molecular weight marker (precision plus protein™ standards; Bio-Rad; Hercules, CA, USA). For the percentage of transferrin saturation

(TSAT) assessment, 0.15 µL of serum sample was loaded in Precast 6% TBE urea gels (U-PAGE) (Thermo Fisher Scientific; Waltham, MA, USA). These gels included *in-lab* prepared pig apotransferrin (ATf) and holotransferrin (HTf) standards made of each sample, which were prepared following the methods described in Nagaoka MH *et al* and Byrne S *et al*.^{3, 4}

The proteins were transferred to PVDF-LF membranes (Millipore; Burlington, VT, USA) by electroblotting, followed by blocking with Intercept® blocking buffer (Li-COR Biosciences; Lincoln, NE, USA) for 1 hour. Membranes were then incubated overnight at 4°C with primary antibodies: goat anti-mouse transferrin (Tf) antibody (1:1,000; AB_1147328, Novus Biologicals) for measuring transferrin levels, and rabbit anti-rat Tf antibody (1:250; Cat#55729, Cappel, ICN Pharmaceuticals) for the TSAT assessment. Secondary antibodies: IRDye-680RD donkey anti-goat (1:10,000; AB_2650427, Li-COR Biosciences; Lincoln, NE, USA) and IRDye-680RD donkey anti-rabbit (1:15,000; AB_2716687, Li-COR Biosciences; Lincoln, NE, USA) were incubated in PVDF-LF membranes with pig serum samples in order to remove pig IgGs cross-reactivity from the secondary antibodies solution (in lab preabortion). After that, the membranes with our samples were incubated with the cleaned-NIR-conjugated secondary antibodies for 2 hours. Band intensity was quantified using the Odyssey Imaging system and Image Studio Lite software v5.2 (Li-COR Biosciences; Lincoln, NE, USA).

TSAT assessment

Basal TSAT levels were measured before the ICH induction in the pigs to confirm that the pigs had TSAT levels comparable to the human population (<40%)⁵. Subsequent TSAT assessments were performed at 1 hour, 4 hours, 1 day, 1 week, and 2 weeks after ICH onset.

The U-PAGE gels separate transferrin into 3 different bands that correspond to its isoforms: Tf without iron (apotransferrin, ATf), Tf with one Fe atom in the C-terminal or N-terminal region (monoferric Tf or mFe-Tf), and iron-loaded Tf with two Fe atoms (diferric Tf, diFe-Tf, holotransferrin, HTf). These isoforms were visualized as different bands. TSAT percentages were calculated using band intensity measurements and the formula previously used by us and others^{5, 6, 7}:

$$TSAT (\%) = \left(\frac{\frac{mFe \cdot Tf}{2} + diFe \cdot Tf}{ATf + mFe \cdot Tf + diFe \cdot Tf} \right) \times 100$$

Immunohistofluorescence (IHF)

Following euthanasia, brains were extracted and sectioned coronally into 5 mm slices using a pig brain slicer matrix. The resulting slices were fixed in 4% paraformaldehyde at 4°C for 24-48 hours. Each slice was then bisected into left and right hemispheres and trimmed into fragments. These fragments were incubated in 30% sucrose in PBS at 4°C until they sank, gently blotted dry, embedded in OCT compound (Sakura Finetek; Barcelona, Spain), snap-frozen in isopentane (Sigma-Aldrich; Saint Louis, MO, USA) pre-chilled with liquid nitrogen, and stored at -80°C. Cryosections (15 µm thick) were obtained using a Leica CM1950 cryostat (Leica Biosystems; Deer Park, TX, USA) and mounted on poly-L-lysine-coated glass slides (Thermo Fisher Scientific; Waltham, MA, USA), which were stored at -20°C until immunohistofluorescence (IHF). Prior to staining, slides were acclimated to room temperature for 15 min, then incubated at 50°C for 30 min, followed by another 15 min at room temperature. Rehydration was performed through a descending ethanol gradient.

For IHF, antigen retrieval was performed by immersing slides in citrate buffer (pH 6.0) heated to 95°C for 20 min, and blocked for 1 hour in 5% NDS, 3% BSA, 0.25% Triton before primary antibody incubation. Slides were incubated overnight at 4°C with the following primary antibodies diluted in PBS with 3% donkey serum and 0.25% Triton X-100: mouse anti-NeuN (1:100; Millipore; Sigma-Aldrich; MAB377; AB_2298772; Saint Louis, MO, USA), Rabbit anti-rat Tf (1:50; Cappel; INC Pharmaceuticals; Cat#555729; Costa Mesa, CA, USA), and Rabbit anti-pig ferritin FTH (1:50; Antibodies online; ABIN7440041; Limerick Township, PA, USA). The next day, slides were incubated for 2 hours at room temperature with the following secondary antibodies: Alexa Fluor™ 647 donkey anti-mouse IgG (1:500; Thermo Fisher Scientific; A-31571; AB_162542) and Alexa Fluor™ 488 donkey anti-rabbit IgG (1:500; Thermo Fisher Scientific; A-21206; AB_2535792) in PBS containing 1% BSA and 0.25% Triton X-100. Unbound secondary antibodies were removed with three quick PBS rinses, followed by 10 min staining with 0.4 µg/mL Hoechst (33342; Thermo Fisher Scientific; Waltham, MA, USA) in PBS. Fluoromount™ (Sigma-Aldrich F4680; Saint Louis, MO, USA) was used as a mounting medium. Imaging was performed on an AxioScan 7(Carl Zeiss; Jena, Germany) in the Advanced Microscopy Unit at the Institute Josep Carreras and analyzed using ImageJ.

Statistical analysis

All data were analyzed using GraphPad Prism 10. Statistical comparisons were performed using repeated-measures two-way ANOVA followed by Tukey's multiple comparisons test, where appropriate. Statistical significance was set at $p < 0.05$. Data are presented as mean \pm SEM.

Supplemental videos S1, S2 and S3.

Video S1. Angiography that shows the access with catheter (black arrowhead) to the cerebral venous circulation through the internal jugular vein (IJV), and the connection between the IJV and the sagittal sinus (SiS).

Video S2. Angiography that show the access with catheter (black arrowhead) to the deep venous circulation. Abbreviations: straight sinus (StS), vein of Galen (GV), sigmoid sinus (SiS), thalamostriate vein (TSV), and internal cerebral vein (ICV).

Video S3. Representative video, at increased speed, of circling behavior of pig at 48 hours post-ICH.

Supplementary references

1. Castaño C, Melià-Sorolla M, García-Serran A, DeGregorio-Rocasolano N, García-Sort MR, Hernandez-Pérez M, *et al.* Establishment of a reproducible and minimally invasive ischemic stroke model in swine. *JCI Insight*. 2023 Apr;8(8):e163398. doi: 10.1172/jci.insight.163398.
2. Pasarikovski CR, Ku JC, Keith J, Ramjist J, Dobashi Y, Priola SM, *et al.* Endovascular Cerebral Venous Sinus Imaging with Optical Coherence Tomography. *AJNR Am J Neuroradiol*. 2020 Dec;41(12):2292-2297. doi: 10.3174/ajnr.A6909.
3. Nagaoka MH, Maitani T. Differed preferential iron-binding lobe in human transferrin depending on the presence of bicarbonate detected by HPLC/high-resolution inductively coupled plasma mass spectrometry. *Biochim Biophys Acta*. 2000 Oct;1523(2-3):182-8. doi: 10.1016/s0304-4165(00)00120-3.
4. Byrne SL, Mason AB. Human serum transferrin: a tale of two lobes. Urea gel and steady state fluorescence analysis of recombinant transferrins as a function of pH, time, and the soluble portion of the transferrin receptor. *J Biol Inorg Chem*. 2009 Jun;14(5):771-81. doi: 10.1007/s00775-009-0491-y.
5. DeGregorio-Rocasolano N, Martí-Sistac O, Ponce J, Castelló-Ruiz M, Millán M, Guirao V, *et al.* Iron-loaded transferrin (Tf) is detrimental whereas iron-free Tf confers protection against brain ischemia by modifying blood Tf saturation and subsequent neuronal damage. *Redox Biol*. 2018 May;15:143-158. doi: 10.1016/j.redox.2017.11.026.
6. García-Serran A, Ordoño J, DeGregorio-Rocasolano N, Melià-Sorolla M, Odendaal K, Martí-Sistac O, *et al.* Targeting Pro-Oxidant Iron with Exogenously Administered Apotransferrin Provides Benefits Associated with Changes in Crucial Cellular Iron Gate Protein TfR in a Model of Intracerebral Hemorrhagic Stroke in Mice. *Antioxidants (Basel)*. 2023 Oct;12(11):1945. doi: 10.3390/antiox12111945.
7. Agarwal R. Transferrin saturation with intravenous irons: an *in vitro* study. *Kidney Int*. 2004 Sep;66(3):1139-44. doi: 10.1111/j.1523-1755.2004.00864.x.

Supplementary Figure 1 (S1)

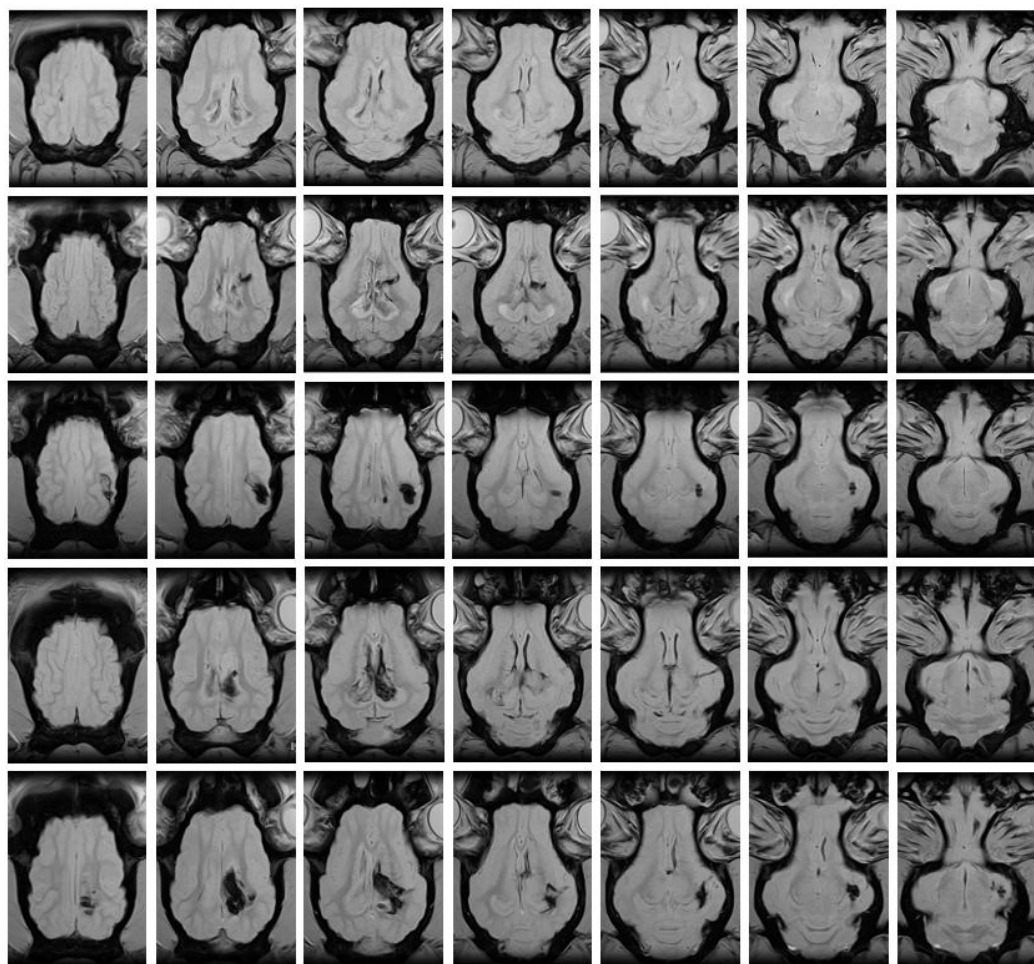


Figure S1. Dorsal sections in axial T2*-weighted sequence of the different pig brains at 90 minutes post-ICH. The hemorrhage is visible as a hypointense area.

Supplementary Figure 2 (S2)

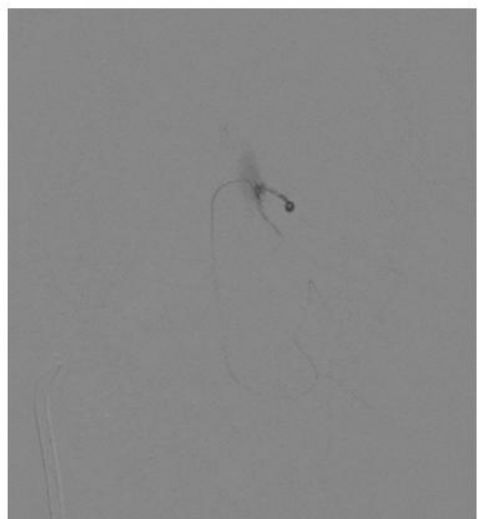
A**B**

Figure S2. (A) Angiography that shows the access with catheter (black arrowhead) to the deep cerebral venous circulation. (B) Contrast injection though the catheter to locate hemorrhage.

Supplementary Figure 3 (S3)

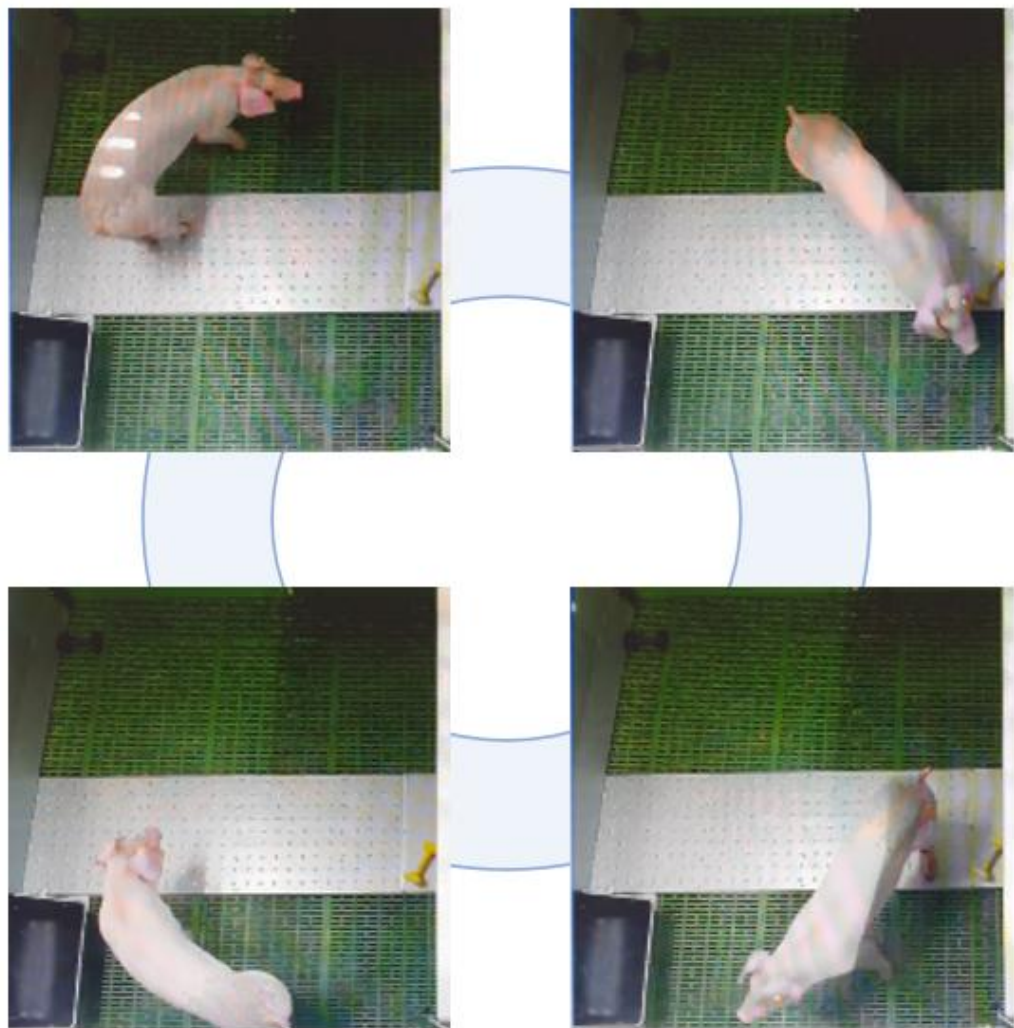
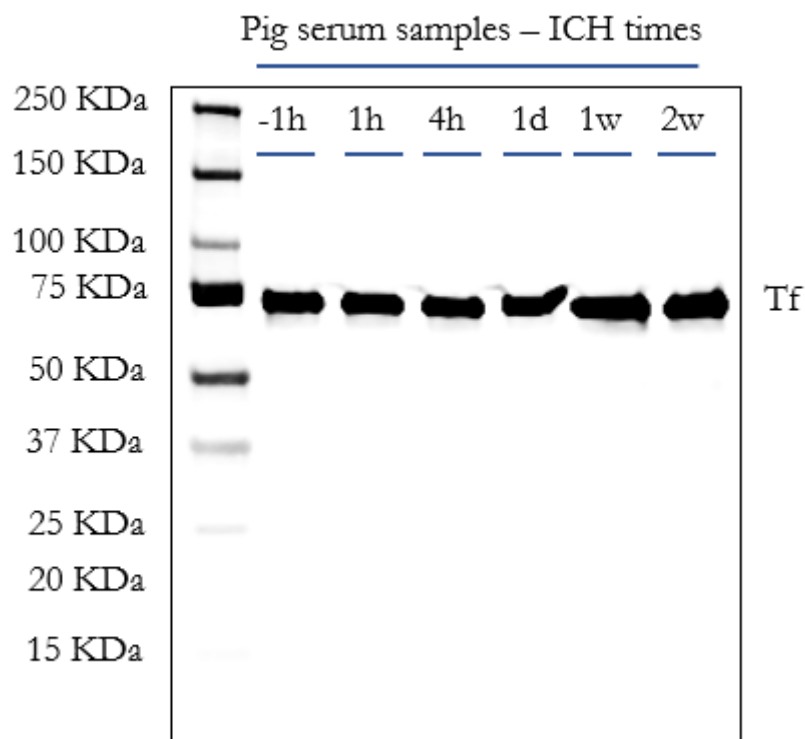
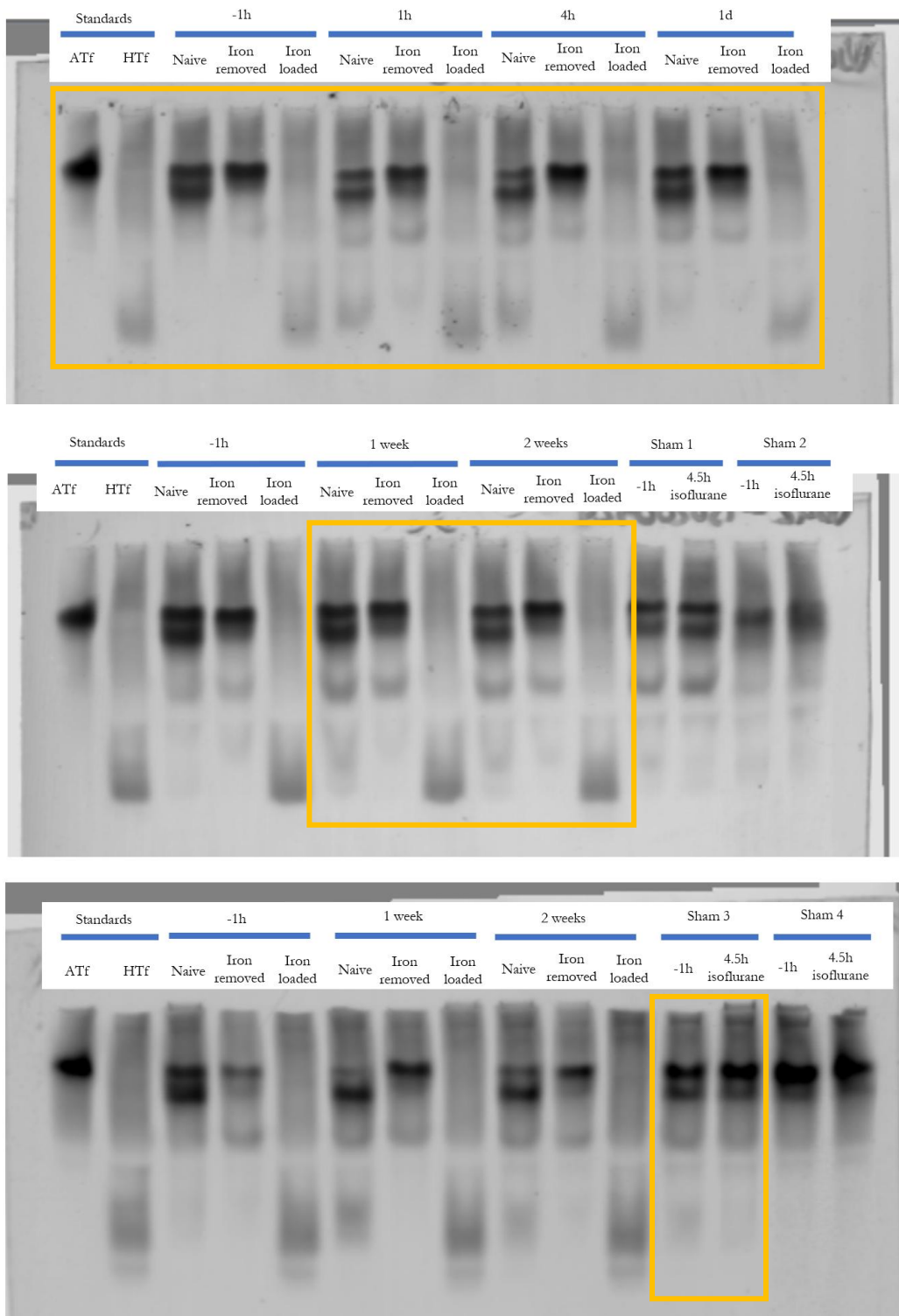


Figure S3. Screenshots of Supplementary video 3 to facilitate circling behavior visualization.

Membrane S1 (Figure 4A)

Membrane S2 (Figure 4D)

DISCUSSION

Discussion

This doctoral dissertation represents a multi-faceted contribution to the field of stroke research in ICH. It strategically integrates three critical domains: the rigorous testing of novel therapeutic agents, the development of cutting-edge automated computational methods for behavioral assessment, and the establishment of innovative translational models utilizing large animals, specifically pigs. The objective of this work is to address fundamental limitations within current preclinical stroke research paradigms, thereby accelerating the bench-to-bedside translation of promising new therapies. By fostering a more robust and clinically relevant preclinical research ecosystem, this dissertation aims to bridge the persistent gap between experimental findings and their successful application in patient care.

1. Therapeutic efficacy of hATf in ICH: Unraveling mechanisms and therapeutic potential

Manuscript I of this thesis details the investigation into the therapeutic potential of human apotransferrin (hATf) to become a good option to provide benefit in intracerebral hemorrhage (ICH). This work provides evidence for the safety and efficacy of a single intravenous administration of hATf in significantly reducing sensorimotor impairment in a well-established collagenase-induced ICH model in mice. The selection of hATf for this study was informed by prior research conducted in our laboratory, which had already demonstrated its protective effects in models of ischemic stroke, suggesting a broader neuroprotective capacity (DeGregorio-Rocasolano *et al.*, 2018). Extending these findings to ICH, a distinct and devastating form of stroke characterized by bleeding within the brain parenchyma (Sheth, 2022), was a critical next step. The precise timing of hATf administration, shortly after ICH induction and within a defined therapeutic time window is crucial for translationality. This early intervention strategy led to a statistically significant and functionally relevant reduction in sensorimotor deficits of the affected forepaw, assessed using the highly sensitive and reliable adhesive tape removal test (**Manuscript I, Figure 4.**). This improvement in a critical motor function, observed starting 48 hours after (**Manuscript 1, Figure 4.**), underscores the remarkable therapeutic potential of hATf. Of note, in general, other therapeutic options usually report some improvement starting at later time points (beyond 7 days) (Hatakeyama *et al.*, 2013). The reliability of the adhesive tape removal test, which requires fine

sensorimotor coordination, allowed for the detection of subtle yet significant neurological improvements that might be missed by less sensitive assays (O'Neill *et al.*, 2022).

Further detailed investigation into the pharmacokinetic profile of hATf in these ICH mice provided critical insights into its systemic and central nervous system disposition. The clearance and iron status dynamics of hATf were found to be remarkably consistent with prior observations in hATf-treated ischemic stroke rats (DeGregorio-Rocasolano *et al.*, 2018), suggesting a conserved mechanism of action across different stroke etiologies and species. Notably, an immediate reduction in plasma transferrin saturation (TSAT) was observed, a phenomenon that persisted for at least 24 hours post-ICH (Manuscript I, Figure 3C). Importantly, elevated levels of exogenous hATf were detected in the ipsilateral hemisphere 72 hours following a single administration (Manuscript I, Figure 3G and 3H.). This accumulation of hATf directly at the site of injury in the affected brain tissue is crucial, as it confirms its ability to cross the blood-brain barrier in a post-ICH scenario and reach the vulnerable neural tissue. The localized presence of hATf in the perihematomal region correlated strongly with a significant reduction in neuronal levels of 4-hydroxynonenal (4-HNE) in the hATf-treated animals compared to untreated controls (Manuscript I, Figure 4C and 4D.). 4-HNE is a well-established byproduct of lipid peroxidation, a key indicator of oxidative stress and cellular damage (Perluigi, Coccia and Allan Butterfield, 2012). The attenuation of this noxious process by hATf highlights a pivotal neuroprotective mechanism, suggesting that hATf directly mitigates oxidative injury following ICH.

The observed sensorimotor recovery in hATf-treated ICH mice, particularly in tasks involving forepaw dexterity as measured by the adhesive tape removal test (Manuscript I, Figure 4A.), demonstrates improvements in sensory perception, motor control, and fine coordination skills. It is important to acknowledge, however, that general coordination was not fully regained (observed in pole and rotarod tests (Manuscript I, Figure S1.), at least at these early time points (24 to 72 hours post-ICH). This nuanced outcome highlights the complexity of neurological recovery after ICH and underscores the need for comprehensive and multifaceted assessment tools to capture the full spectrum of functional improvements and residual deficits. Crucially, and perhaps one of the most significant findings, these therapeutic benefits were achieved independently of any discernible effects on hematoma size, cerebral edema, hemoglobin or heme concentration in the ipsilateral hemisphere, or systemic

blood coagulation. This is a pivotal finding, especially given the ongoing debate and some reports suggesting procoagulant effects of transferrin or processed blood under certain experimental conditions (e.g., chronically elevated transferrin levels) (Tang, Zhang and Fang, 2020; Tang, Fang and Chen, 2020). The absence of such effects in our study is paramount for the potential clinical translation of hATf, as any procoagulant activity of hATf would compromise its use in ischemic stroke patients and, thus, the potential use of ATf as an early universal treatment for all stroke patients. To further solidify this point, and subsequent to the acceptance of **Manuscript I**, we assessed the time-course of hematoma growth in the collagenase-induced ICH model. This analysis revealed that the majority of hematoma expansion occurs rapidly within the first 5 hours post-ICH induction. Since hATf was administered 40 minutes after collagenase injection, effectively hours before the hematoma reached its maximal size, our consistent observation that hATf did not reduce hematoma volume further supports the absence of procoagulant properties of hATf under our specific experimental conditions. This critical distinction demonstrates that the benefits of hATf are not derived from altering the initial bleeding or clot formation but rather through intrinsic neuroprotective and anti-inflammatory actions, making it a safer and more viable candidate for clinical translation in ICH.

2. Antiferroptotic mechanisms of hATf action: A novel pathway to neuroprotection

The intricate mechanisms underlying the therapeutic benefits of hATf in ICH appear to converge on a novel antiferroptotic pathway, operating distinctly and independently of the canonical system xCT/GPX4 axis, which is a well-recognized and intensively studied pathway in ferroptosis regulation. Our investigations revealed that neither ICH induction itself nor hATf treatment significantly altered the protein levels of key ferroptosis hallmark proteins such as GPX4 or xCT (SLC7A11), nor the mRNA levels of ferroptosis suppressor protein 1 (FSP1 or AIFM2) (**Manuscript I, Figures 6-7.**). These proteins represent the core components of both the GPX4/xCT pathway and the FSP1/CoQ10/NAD(P)H pathway, another crucial ferroptosis axis (Doll *et al.*, 2019; Bersuker *et al.*, 2019). This compelling evidence indicates that the protective effects of hATf are not merely a consequence of a broad, non-specific activation of known ferroptosis inhibitors, but rather involve distinct, nuanced, and potentially unexplored pathways within the complex landscape of iron-dependent cell

death. This specificity suggests a targeted intervention rather than a generalized cellular response.

Intriguingly, a significant finding was that hATf treatment prevented the ICH-induced reduction in the cytosolic iron chaperone PCB2 (**Manuscript I, Figure 7.**). PCB2 is an essential protein for maintaining cellular iron homeostasis, primarily by chaperoning iron to ferritin for storage. Its knockdown has been definitively shown to promote ferroptosis ([Yue et al., 2022](#)), highlighting its critical role in cellular resilience against iron-mediated damage. The preservation of PCB2 levels by hATf strongly suggests a direct role in upholding cellular iron buffering capacity and maintaining a stable iron environment within the neuron, thereby enhancing its resistance to ferroptotic insults. Furthermore, hATf-treated animals consistently exhibited a significant reduction in transferrin receptor 1 (TfR1) protein levels (**Manuscript I, Figure 6.**). TfR1 is the primary membrane cellular gate for iron entry into the cell, and its upregulation is considered a hallmark of ferroptosis, indicating increased cellular iron demand and susceptibility ([Feng et al., 2020](#); [Jin et al., 2022](#)). This reduction in TfR1 by hATf might directly explain, or at least significantly contribute to, the beneficial effects observed. By limiting the influx of iron into vulnerable cells, namely neurons, hATf can effectively mitigate the intracellular iron overload that serves as a potent trigger for ferroptosis. This suggests a direct mechanism by which hATf modulates cellular iron import, a crucial step in preventing ferroptotic cell death.

Our collective findings in **Manuscript I** strongly suggest that even in the absence of significant alterations in the primary GPX4/xCT or FSP1/CoQ10/NAD(P)H ferroptosis pathways, iron-burden-dependent ferroptosis is indeed occurring in the context of ICH, and this takes place predominantly through the p53/TfR1 pathway. This highlights a specific vulnerability in ICH pathophysiology that hATf appears to target effectively. A dual action of hATf is proposed: (1) it directly contributes to reducing the overall availability of TfR1 on the cell surface, thereby decreasing the number of potential entry points for iron, and (2) it can competitively bind to the remaining TfR1, thereby inhibiting the binding and subsequent internalization of iron-loaded transferrin through this receptor. This competitive inhibition effectively blocks the existing iron entry mechanisms. This sophisticated, two-pronged mechanism underscores the decisive role of exogenous hATf in preserving brain parenchyma function and maintaining critical neuronal iron homeostasis following the hemorrhagic

insult. By modulating both the quantity and function of TfR1, hATf provides a powerful protective strategy against iron-mediated damage.

The recent identification of a novel long non-coding RNA (lncRNA) that constitutively represses p53 and apoptosis in cooperation with PCBP2 (Iwai *et al.*, 2023) provides a compelling and insightful nexus linking the p53/TfR1 pathway, PCBP2, and apoptosis. This discovery strongly suggests a significant and intricate crosstalk between these pathways, all of which appear to be modulated by the therapeutic intervention of hATf. This finding points to a complex regulatory network that hATf effectively manipulates, indicating its ability to influence multiple interconnected cellular death pathways. Given that PCBP2-specific siRNA-transfected neurons exhibit a notable decrease in apoptosis following glutamate stimulation (Mao *et al.*, 2016), we were prompted to investigate the effect of ICH and hATf treatment on caspase-2 activation, a key initiator caspase in certain apoptotic pathways (Vigneswara and Ahmed, 2020). Our results definitively demonstrated that the ICH-induced cleavage of procaspase-2, which leads to an increase in active caspase-2, was robustly abrogated by treatment with hATf (**Manuscript I, Figure 8.**). This direct inhibition of caspase-2, a crucial mediator of programmed cell death (Vigneswara and Ahmed, 2020), provides another critical layer of neuroprotection exerted by hATf, actively preventing apoptotic cell death in the injured brain parenchyma.

Collectively, the intricate mechanisms underlying the observed improvements in sensorimotor abilities in hATf-treated ICH mice are likely linked to its multi-modal effect on key ferroptosis-related players, specifically TfR1 and PCBP2, as well as its direct influence on the inactivation of caspase-2. These three distinct but interconnected molecular targets thus represent promising novel therapeutic avenues for the design and development of future ICH treatments. The demonstration of hATf's ability to act on these diverse but functionally interconnected pathways makes it a particularly attractive and potent candidate for intervention in a complex neurological condition like ICH, where multiple pathological processes converge to cause neuronal damage.

3. Challenges in lesion assessment and its relationship with the primacy of neurobiological outcome in ICH: Time to revisit preclinical functional endpoints

Throughout the course of the rodent ICH study, we consistently encountered significant and inherent challenges in accurately and precisely delineating the "true" hemorrhagic volume affected. This difficulty is not trivial; it has profound implications for how preclinical ICH studies are designed, interpreted, and ultimately translated. In coronal sections of mouse brains, the hemorrhagic-affected areas were observed to be remarkably heterogeneous (**Figure AP3. in Annex Manuscript I**), presenting irregular boundaries and varying degrees of tissue involvement. This inherent heterogeneity makes precise volumetric measurements challenging and prone to subjective interpretation. Furthermore, conventional micro-computed tomography (MicroCT) imaging of the hemorrhage, while useful, relies on visualizing the extravasated experimental contrast agent alongside the blood. This means we are effectively observing a proxy for the hemorrhage rather than a direct, clear image of the blood/hematoma itself, precluding a direct and unequivocal volumetric measurement. While assessing brain damage volume in ischemic stroke models is relatively straightforward using *ex vivo* TTC (2,3,5-triphenyltetrazolium chloride) staining, which metabolically highlights viable tissue ([Bederson *et al.*, 1986](#)), the accurate assessment of lesion size in ICH models *ex vivo* is complicated by a continuous and indistinct color gradient. This gradient ranges from the pale pink of unaffected brain parenchyma, transitioning to a more reddish color nearby the hemorrhagic area, and culminating in an intense red in the center of the hemorrhage. Under these challenging conditions, establishing a clear and objective threshold to discriminate unaffected from lesioned tissue cannot be clearly delineated (as illustrated in the **Figure AP3. in Annex of Manuscript I**). This inherent methodological difficulty in precise volumetric assessment in ICH models underscores a critical need for alternative, more reliable, and clinically relevant outcome measures that are less dependent on subjective anatomical interpretations.

A well-established and generally accepted correlation exists between infarct size in ischemic stroke and the degree of neurological impairment. However, it is crucial to recognize that this relationship is not always strictly linear in clinical settings. Various influencing factors can modulate this correlation, such as the specific brain region affected (e.g., eloquent vs.

non-eloquent areas) (Munsch *et al.*, 2016; Sheth, 2022; Rindler *et al.*, 2020) or the presence of robust collateral circulation that can mitigate tissue damage (Ginsberg, 2018). Similarly, in patients suffering intracerebral hemorrhagic stroke, a relationship between the initial volume of the hemorrhage and the subsequent severity of neurological impairment is widely recognized (Sheth *et al.*, 2022; Magid-Bernstein *et al.*, 2022). Yet, a common and clinically significant complication, such as hemorrhage widening into the ventricles (intraventricular hemorrhage), frequently results in a far larger and disproportionate neurological impairment (Hallevi *et al.*, 2009; Balami and Buchan, 2012; Greenberg *et al.*, 2022; Magid-Bernstein *et al.*, 2022) than would be expected based solely on the initial volume of blood extravasated. This phenomenon highlights that simple volumetric measures may not fully capture the complexity of ICH pathology and its functional consequences. In the preclinical ICH setting, most experimental models attempt to standardize the hemorrhage by inducing it at specific coordinates within the mouse striatum (Sun *et al.*, 2025; Zeng *et al.*, 2020; Rodríguez *et al.*, 2017; Gong *et al.*, 2018). However, even with standardized procedures, a percentage of animals will inevitably experience some degree of hemorrhage widening into the ventricles or extension into the corpus callosum. Both of these conditions are consistently associated with significantly worse neurological outcomes (Matsushita *et al.*, 2013). Consistent with the clinical and preclinical observations explained above, a clear correlation was indeed observed between ischemic volume and neurological impairment in ischemic mice (e.g., as measured by the tape removal test in **Manuscript II, Figures S1 and S2.**). In stark contrast, and critically, no statistically significant correlation was found between hematoma volume and neurological impairment using hemoglobin-based methods in the ICH model (data not shown). This compelling lack of correlation is a pivotal finding, indicating that relying solely on hematoma volume as a primary outcome measure in preclinical ICH studies may be fundamentally misleading and could obscure true therapeutic effects. Therefore, given the consistent observation that the improvements induced by hATf treatment occurred robustly without any measurable effect on hematoma volume, neurological impairment emerges as the primary and arguably most critical outcome in preclinical studies evaluating novel treatments for ICH that are intended for clinical translation. This fundamental shift in focus from purely anatomical lesion size to robust and objective measures of functional recovery is paramount for more accurately reflecting clinical relevance and significantly enhancing the probability of successful translation of preclinical findings into effective patient therapies.

4. Automated computational behavioral assessment for enhanced preclinical stroke research: Pioneering objective and scalable endpoints

Traditional preclinical stroke research in rodents heavily relies on observing and annotating changes in behavior across a battery of different tests. These annotations, typically performed manually by trained researchers, are used to infer both the extent of neurological impairment and the trajectory of functional recovery. While valuable, this manual annotation process is inherently subjective, prone to significant inter-observer variability, time-consuming, and ultimately limits the scalability and standardization of preclinical trials. These limitations pose a substantial barrier to robust, reproducible, and translatable research. **Manuscript II** details the development of novel computational tools, specifically a machine/deep learning algorithm, designed to objectively and precisely assess mouse performance in a single, well-established neurobehavioral test: the adhesive tape removal test. This approach leverages DeepLabCut (DLC), an open-source deep-learning package for markerless pose estimation and tracking of animal body parts in motor function tests (Weber *et al.*, 2022; Ruiz-Vitte *et al.*, 2025). DLC has already demonstrated its utility in analyzing animal behavior across a diverse range of disease models, including stroke, diabetes, and dystonia (Andreoli *et al.*, 2021; Bühler *et al.*, 2023; Ruiz-Vitte *et al.*, 2025; Skrobot *et al.*, 2024; Weber *et al.*, 2022). This existing foundation of robust, validated technology provided a strong platform upon which to build our novel applications. In our study, we systematically analyzed video recordings of mice performing the adhesive tape removal test, applying DLC to precisely track predefined body parts and subsequently extract a rich array of kinematic features indicative of neurological impairment and recovery.

For our comprehensive behavioral analysis, we precisely tracked multiple anatomical points on the mice, including the nose, neck, forelimbs, hindlimbs, the base of the tail (bottom), and the very end of the tail. Crucially, we also incorporated tracking of the adhesive tape itself, which was affixed to the mice's paws. This meticulous multi-point tracking enabled not only the precise measurement of tape removal time, a standard quantitative measure of sensorimotor function (O'Neill *et al.*, 2022), but simultaneously allowed us to quantify numerous additional kinematic parameters. These included, but were not limited to, mean velocities of different body parts (e.g., forepaws, hindpaws), distances between paws (reflecting

gait and coordination), and total distance traveled (an indicator of general activity and exploration). This rich, high-dimensional dataset of kinematic features provides a far more objective and detailed characterization of behavioral performance and functional recovery compared to traditional, less informative, scoring methods. The ability to automatically extract these complex movement patterns transforms subjective observations into quantifiable, repeatable data.

Beyond merely tracking and quantifying behavior, a more ambitious objective was to explore the application of advanced machine learning techniques to directly predict stroke occurrence and severity based on these derived movement patterns. This represents a significant leap forward in preclinical assessment. Similar computational approaches have already found considerable clinical utility, with deep neural networks, random forest models, and logistic regression successfully predicting long-term stroke prognosis in human patients based on clinical parameters (Heo *et al.*, 2019). Building on this precedent, our newly developed methodology achieved a 96% accuracy in automatically predicting the occurrence of stroke for a specific mouse in the hypoxic-ischemic (H/I) model. Furthermore, it enabled the automated classification of H/I mice into distinct groups based on the severity of stroke, which correlated accurately with the ischemic lesion volume (**Manuscript II, Figure 5.**). This remarkable accuracy demonstrates the profound power of computational methods to non-invasively and objectively diagnose and grade stroke severity in experimental animals. Importantly, the same sophisticated algorithms demonstrated a highly respectable 90% accuracy in predicting ICH occurrence (**Manuscript II, Figure 6.**) and provided an objective and quantitative assessment of the ICH-derived neurological severity. This validates the broad generalizability and robustness of our computational approach across different stroke etiologies and underscores its immense potential for widespread application in preclinical research.

Our results strongly suggest that the comprehensive information obtained through this advanced computational methodology, as detailed in **Manuscript II**, is entirely sufficient to facilitate the computational selection of mice for randomization into preclinical trials of new treatments. This means that preclinical researchers can effectively screen and select animals based on objective neurological deficit metrics, entirely obviating the need for additional and/or more intrusive behavioral tests. This represents a paradigm shift, offering a

significant breakthrough in streamlining preclinical research by substantially reducing the number of animals and animal handling stress, minimizing human bias inherent in manual scoring, and significantly accelerating the screening process for novel therapeutics. We anticipate that tools such as the one developed in this study will help to standardize and improve the quality in comprehensive preclinical assessment in future multi-center, collaborative pre-clinical trials, providing, for instance, an objective tool to exclude mice that fail to develop ICH from randomization in the study. These collaborative efforts are strongly encouraged by international guidelines such as the STAIR XI recommendations (Lyden *et al.*, 2021), which advocate for more rigorous and harmonized preclinical research. By providing objective and automated measures, our tools will facilitate the much-needed standardization of functional outcome measures across different laboratories and studies (Hietamies *et al.*, 2018). Such standardization is absolutely crucial for improving the reproducibility and translatability of preclinical findings, thereby increasing confidence in moving promising candidates forward into clinical development. Furthermore, our growing experience with DeepLabCut software will prove invaluable for extending these advanced analytical capabilities to assess sensorimotor disturbances associated with stroke induction and treatment improvements when applied to large animal models of stroke. This includes ongoing evaluation of complex behaviors like pig circling after stroke, demonstrating the adaptability and scalability of our computational framework. This ability to apply these sophisticated tools across species, from rodents to larger animal models, is critical for bridging the translational gap between basic discovery and eventual human clinical trials.

5. Developing a novel translational intracerebral hemorrhage model in swine: Bridging the translational gap

A primary objective of this thesis is to strategically promote the critical actions needed to effectively transition new treatments from preclinical research to human clinical trials and ultimately to patients. This fundamental goal necessitates rigorous and comprehensive testing of therapeutic candidates in large animal models prior to initiating human clinical trials. This step is particularly vital, as rodent models, despite their utility in initial screening, often fail to fully recapitulate the complex anatomical, physiological, and pathological nuances of human neurological diseases. To address this critical need, we embarked on the ambitious endeavor of developing a novel, highly translational model of ICH in swine. **Manuscript**

III details the intricate development process and the subsequent characterization of key pathophysiological hallmarks of this innovative ICH model.

Our newly developed porcine ICH model incorporates several significant advancements. Crucially, it allows for the skull to remain intact throughout the procedure, thereby significantly minimizing parenchymal damage unrelated to the hematoma itself. This is a considerable improvement over traditional methods that often involve craniotomy and mechanical trauma during stereotaxic needle advancement for collagenase injection (Melià-Sorolla *et al.*, 2020). By reducing these confounding factors, our intact-skull approach provides a more faithful and less iatrogenic representation of spontaneous ICH as observed in humans. A cornerstone of this model is its sophisticated endovascular approach, through which we successfully accessed specific lobar and striatal areas via the pig's brain venous vasculature. This is a crucial methodological distinction and a major innovation, allowing access for the precise targeting of specific brain regions without the need for an invasive craniotomy. It is important to explicitly note, as discussed in **Manuscript III**, that there is no conventional endovascular access to the pig brain parenchyma through the arterial system, which highlights the unique anatomical considerations and the innovative nature of our chosen venous approach. Once positioned in the region of interest as assessed by digital subtraction angiography, the selected vein was carefully pierced, and ICH was induced in all pigs by injecting a precise volume of 1.5 mL of fresh autologous arterial blood after a contrast bolus. The precise location and initial morphology of the induced hematoma were immediately confirmed by real-time contrast extravasation into the brain parenchyma on rotational angiography/CT, and subsequently by various advanced MRI sequences (FLAIR, Axial T2*, DWI, ADC) as early as 1 hour post-ICH. This real-time imaging capability allows for immediate verification of the hemorrhage, provides valuable data on its initial characteristics (e.g., size, shape, location), and enables longitudinal follow-up imaging. This minimally invasive endovascular approach consistently produced discernible neurological impairment once the pig recovered from the anesthesia, a critical and highly translatable outcome for preclinical studies, while importantly showing no evidence of secondary bleeding, thereby demonstrating the safety and stability of the model. Interestingly, and somewhat counterintuitively, we observed a reduction in systemic platelet activation 1 or 24 hours post-venous perforation, a finding that warrants further detailed investigation into the intricate interplay between

localized brain injury and systemic hemostasis in this novel model. This unexpected systemic response could provide valuable insights into the broader physiological impact of ICH.

Comprehensive analysis of iron-related proteins in both blood and brain tissue provided profound insights into the dynamic iron dysregulation following ICH in this large animal model. A significant increase in the percentage of transferrin saturated with iron was observed in the blood at 1 hour after ICH onset, critically, without altering the total blood levels of transferrin. This intriguing observation could reflect a rapid drainage of free or heme-bound iron from the parenchymal hematoma into the systemic circulation, where it quickly saturates the available transferrin. This finding suggests a dynamic and rapid interplay between brain and systemic iron homeostasis following intracerebral bleeding, indicating that the systemic circulation acts as a sink for released iron. This provides valuable insights into the broader systemic response to intracerebral hemorrhage. Furthermore, levels of transferrin and ferritin, both key iron-handling proteins, significantly increased in the peri-hematomal area and the parenchyma of the ipsilateral hemisphere. Notably, ferritin signal was observed to co-localize extensively with the neuronal marker NeuN, indicating an early and robust neuronal response to iron overload and suggesting the activation of protective mechanisms within affected neurons; this is in agreement with previous reports in rodents (DeGregorio-Rocasolano *et al.*, 2018; Wu *et al.*, 2003; Wang *et al.*, 2016; Yang *et al.*, 2021; Hatakeyama *et al.*, 2013; Ding *et al.*, 2011). Critically, elevated ferritin levels in the affected parenchyma were found to persist for at least one week post-ICH induction, highlighting the prolonged nature of iron dysregulation and subsequent oxidative stress in the brain after hemorrhage. This prolonged iron burden suggests the therapeutic window and the potential for long-term interventions targeting iron metabolism to mitigate ongoing secondary injury. This characterization of iron dynamics in a large animal model provides crucial and clinically relevant insights into the pathophysiology of ICH, laying the groundwork for iron-targeting therapies.

6. Conclusion and future directions: A strategic pathway for translational stroke research

In conclusion, this doctoral dissertation presents a body of work that significantly contributes to the advancement of stroke research across multiple critical frontiers. The

demonstrated therapeutic benefits of hATf in the collagenase-induced ICH rodent model, particularly its novel antiferroptotic mechanisms of action, represent a significant stride in identifying promising pharmacological agents. Concurrently, the development and validation of advanced DeepLabCut-based methodologies for objective and automated neurological outcome assessment in rodents, with clear applicability to the newly developed pig ICH model, address a long-standing need for more standardized, efficient, and unbiased preclinical evaluation tools. Finally, the pioneering establishment of a novel, minimally invasive, and highly translational ICH model in swine, coupled with the ongoing evaluation of hATf in both ischemic and hemorrhagic large animal/pig models, collectively represents **Preclinical Strategic Advances in the Therapeutic Landscape of Intracerebral Hemorrhagic Stroke.**

The individual components of this thesis, when viewed in concert, articulate an integrated translational pipeline designed to accelerate the journey of novel therapies from laboratory discovery to clinical application. The elucidation of the precise antiferroptotic mechanisms of hATf in ICH mice provides a scientific rationale for its continued therapeutic exploration, offering a targeted approach to mitigate a key cell death pathway after hemorrhage. The development and validation of automated behavioral assessment tools directly address critical limitations inherent in traditional preclinical study designs. By providing objective, high-throughput, and reproducible measures of functional recovery, these tools pave the way for more efficient, standardized, and ultimately more predictive research outcomes in preclinical studies. Furthermore, the establishment of a novel, minimally invasive ICH model in swine represents a crucial and indispensable step towards bridging the persistent translational gap. This physiologically relevant large animal model allows for the evaluation of therapeutic efficacy and safety profiles in an anatomical and physiological context far more analogous to humans than rodent models, thereby increasing the likelihood of successful translation to human clinical trials.

We are confident that these integrated and synergistic efforts will serve as a robust and enduring foundation for the future translation of promising therapies, ultimately improving the lives and functional outcomes for stroke patients worldwide. The foundational findings from this dissertation lay compelling groundwork for further comprehensive investigations into hATf as a leading potential therapeutic agent for ICH. Concurrently, they validate cutting-

Discussion

edge advanced computational tools for robust preclinical assessment, and most importantly, they establish a valuable and clinically relevant large animal model that will significantly accelerate the development and testing of new treatments for this devastating neurological condition. This comprehensive approach, integrating novel therapeutics, advanced assessment, and translational models, sets a new standard for preclinical stroke research.

CONCLUSIONS

Conclusions

The findings of this doctoral dissertation are as follows:

Conclusions from Manuscript I – Hypotheses I and II

- Ischemic and hemorrhagic strokes share a common altered profile of iron-binding and ferroptosis-related molecules.
- The administration of apotransferrin is safe and beneficial, as assessed by a neurological sensorimotor improvement in mice exposed to experimental ICH in a complex sensorimotor neurobehavioral test, the tape removal test. This is associated with a reduction of the byproduct of lipid peroxidation 4-hydroxynonenal.
- These results, along with previously demonstrated benefits of apotransferrin in ischemic stroke, support the potential of ATf as an early, pre-hospital frontline treatment. Apotransferrin could be administered immediately, even before an accurate in-hospital differential diagnosis.
- The study of the effect of apotransferrin on brain molecules involved in iron homeostasis/ferroptosis has identified a reduction of the transferrin receptor protein levels, an increase of PCBP2, and a reduction of the cleaved, active caspase 2, and thus they are potential candidates to become targets of therapeutic intervention.
- At the doses used as a treatment, IV administration of ATf neither prevents the extension of hemorrhage nor affects the systemic coagulation.
- Neurobehavioral tests other than the tape removal test, which are more addressed at assessing slow movements, balance, and motor coordination learning, and without the sensory component (pole test or rotarod), were found inadequate to reflect the apotransferrin-induced neurological improvement.

Conclusions from Manuscript II – Hypothesis III

- We developed a machine learning model capable of the automated assessment of the tape removal time, and an algorithm able to predict individual outcomes in mice subjected to experimental stroke using only a single neurobehavioral test, the adhesive tape removal test.

Conclusions

- This computational approach is quantitative, objective, eliminates human observational error and bias, and significantly reduces time and resource consumption.
- This computational method is able to predict damage from ischemic stroke and also from intracerebral hemorrhagic stroke in rodents.
- By enhancing data accuracy while minimizing animal use and saving researchers' time, this methodology aligns with the 3Rs principle (replace, reduce, and refine) and has the potential to become the gold standard for preclinical stroke research in rodents.

Conclusions from Manuscript III – Hypotheses IV and V

- We successfully established a novel, minimally invasive, endovascular ICH model in pigs, avoiding the need for craniotomy (3R) while better replicating the clinical pathophysiology of human hemorrhagic stroke.
- This model enables the induction of hemorrhages in various pre-determined brain regions without damaging the parenchyma during the blood administration, offering a more translational approach for preclinical studies.
- Additionally, our findings reveal significant changes in serum iron-related proteins, changes in the platelet factor 4, increased ferritin in neurons and transferrin in the parenchymal areas near the hemorrhage, further supporting the role of iron metabolism in secondary brain injury following ICH in gyrencephalic brains.

REFERENCES

References

- Abid KA, Vail A, Patel HC, King AT, Tyrrell PJ, Parry-Jones AR. Which factors influence decisions to transfer and treat patients with acute intracerebral haemorrhage and which are associated with prognosis? A retrospective cohort study. *BMJ Open*. 2013 Dec 17;3(12):e003684. doi: 10.1136/bmjopen-2013-003684.
- Adam SJ, Rund LA, Kuzmuk KN, Zachary JF, Schook LB, Counter CM. Genetic induction of tumorigenesis in swine. *Oncogene*. 2007 Feb 15;26(7):1038-45. doi: 10.1038/sj.onc.1209892.
- Adams HP Jr, Bendixen BH, Kappelle LJ, Biller J, Love BB, Gordon DL, *et al*. Classification of subtype of acute ischemic stroke. Definitions for use in a multicenter clinical trial. TOAST. Trial of Org 10172 in Acute Stroke Treatment. *Stroke*. 1993 Jan;24(1):35-41. doi: 10.1161/01.str.24.1.35.
- Agarwal R. Transferrin saturation with intravenous irons: an *in vitro* study. *Kidney Int*. 2004 Sep;66(3):1139-44. doi: 10.1111/j.1523-1755.2004.00864.x.
- Akhigbe T, Okafor U, Sattar T, Rawluk D, Fahey T. Stereotactic-Guided Evacuation of Spontaneous Supratentorial Intracerebral Hemorrhage: Systematic Review and Meta-Analysis. *World Neurosurg*. 2015 Aug;84(2):451-60. doi: 10.1016/j.wneu.2015.03.051.
- Alim I, Caulfield JT, Chen Y, Swarup V, Geschwind DH, Ivanova E, *et al*. Selenium Drives a Transcriptional Adaptive Program to Block Ferroptosis and Treat Stroke. *Cell*. 2019 May 16;177(5):1262-1279.e25. doi: 10.1016/j.cell.2019.03.032.
- Alsbrook DL, Di Napoli M, Bhatia K, Biller J, Andalib S, Hinduja A, *et al*. Neuroinflammation in Acute Ischemic and Hemorrhagic Stroke. *Curr Neurol Neurosci Rep*. 2023 Aug;23(8):407-431. doi: 10.1007/s11910-023-01282-2.
- Amarenco P, Bogousslavsky J, Caplan LR, Donnan GA, Hennerici MG. Classification of stroke subtypes. *Cerebrovasc Dis*. 2009;27(5):493-501. doi: 10.1159/000210432.
- An D, Park J, Shin JI, Kim HJ, Jung DI, Kang JH, *et al*. Temporal Evolution of MRI Characteristics in Dogs with Collagenase-Induced Intracerebral Hemorrhage. *Comp Med*. 2015 Dec;65(6):517-25. PMID: 26678369; PMCID: PMC4681246.
- An SJ, Kim TJ, Yoon BW. Epidemiology, Risk Factors, and Clinical Features of Intracerebral Hemorrhage: An Update. *J Stroke*. 2017 Jan;19(1):3-10. doi: 10.5853/jos.2016.00864.
- Andaluz N, Zuccarello M, Wagner KR. Experimental animal models of intracerebral hemorrhage. *Neurosurg Clin N Am*. 2002 Jul;13(3):385-93. doi: 10.1016/s1042-3680(02)00006-2.
- Andersen OM, Bøgh N, Landau AM, Pløen GG, Jensen AMG, Monti G, *et al*. A genetically modified minipig model for Alzheimer's disease with SORL1 haploinsufficiency. *Cell Rep Med*. 2022 Sep 20;3(9):100740. doi: 10.1016/j.xcrm.2022.100740.

- Anderson CS, Huang Y, Wang JG, Arima H, Neal B, Peng B, *et al.* Intensive blood pressure reduction in acute cerebral haemorrhage trial (INTERACT): a randomised pilot trial. *Lancet Neurol*. 2008 May;7(5):391-9. doi: 10.1016/S1474-4422(08)70069-3.
- Anderson CS, Heeley E, Huang Y, Wang J, Stapf C, Delcourt C, *et al.* Rapid blood-pressure lowering in patients with acute intracerebral hemorrhage. *N Engl J Med*. 2013 Jun 20;368(25):2355-65. doi: 10.1056/NEJMoa1214609.
- Andreoli L, Abbaszadeh M, Cao X, Cenci MA. Distinct patterns of dyskinetic and dystonic features following D1 or D2 receptor stimulation in a mouse model of parkinsonism. *Neurobiol Dis*. 2021; 157:105429. doi: 10.1016/j.nbd.2021.105429.
- Ariesen MJ, Claus SP, Rinkel GJ, Algra A. Risk factors for intracerebral hemorrhage in the general population: a systematic review. *Stroke*. 2003 Aug;34(8):2060-5. doi: 10.1161/01.STR.0000080678.09344.8D.
- Arima H, Wang JG, Huang Y, Heeley E, Skulina C, Parsons MW, *et al.* Significance of perihematomal edema in acute intracerebral hemorrhage: the INTERACT trial. *Neurology*. 2009 Dec 8;73(23):1963-8. doi: 10.1212/WNL.0b013e3181c55ed3.
- Aromataro M, Torsello A, D'Errico S, Bertozzi G, Sessa F, Cipolloni L, *et al.* Traumatic Epidural and Subdural Hematoma: Epidemiology, Outcome, and Dating. *Medicina (Kaunas)*. 2021 Feb 1;57(2):125. doi: 10.3390/medicina57020125.
- Aronowski J, Zhao X. Molecular pathophysiology of cerebral hemorrhage: secondary brain injury. *Stroke*. 2011 Jun;42(6):1781-6. doi: 10.1161/STROKEAHA.110.596718.
- van Asch CJ, Luitse MJ, Rinkel GJ, van der Tweel I, Algra A, Klijn CJ. Incidence, case fatality, and functional outcome of intracerebral haemorrhage over time, according to age, sex, and ethnic origin: a systematic review and meta-analysis. *Lancet Neurol*. 2010 Feb;9(2):167-76. doi: 10.1016/S1474-4422(09)70340-0.
- Auriat AM, Silasi G, Wei Z, Paquette R, Paterson P, Nichol H, *et al.* Ferric iron chelation lowers brain iron levels after intracerebral hemorrhage in rats but does not improve outcome. *Exp Neurol*. 2012 Mar;234(1):136-43. doi: 10.1016/j.expneurol.2011.12.030.
- Aviv RI, Huynh T, Huang Y, Ramsay D, Van Slyke P, Dumont D, *et al.* An *in vivo*, MRI-integrated real-time model of active contrast extravasation in acute intracerebral hemorrhage. *AJNR Am J Neuroradiol*. 2014 Sep;35(9):1693-9. doi: 10.3174/ajnr.A3939.
- Ayre JR, Bazira PJ, Abumattar M, Makwana HN, Sanders KA. A new classification system for the anatomical variations of the human circle of Willis: A systematic review. *J Anat*. 2022 Jun;240(6):1187-1204. doi: 10.1111/joa.13616.
- Bai Q, Liu J, Wang G. Ferroptosis, a Regulated Neuronal Cell Death Type After Intracerebral Hemorrhage. *Front Cell Neurosci*. 2020 Nov 16;14:591874. doi: 10.3389/fncel.2020.591874.

- Baker EW, Kinder HA, Hutcheson JM, Duberstein KJJ, Platt SR, Howerth EW, *et al.* Controlled Cortical Impact Severity Results in Graded Cellular, Tissue, and Functional Responses in a Piglet Traumatic Brain Injury Model. *J Neurotrauma*. 2019 Jan 1;36(1):61-73. doi: 10.1089/neu.2017.5551.
- Balami JS, Buchan AM. Complications of intracerebral haemorrhage. *Lancet Neurol*. 2012 Jan;11(1):101-18. doi: 10.1016/S1474-4422(11)70264-2.
- Balkaya MG, Trueman RC, Boltze J, Corbett D, Jolkonen J. Behavioral outcome measures to improve experimental stroke research. *Behav Brain Res*. 2018 Oct 15;352:161-171. doi: 10.1016/j.bbr.2017.07.039.
- Bao H, Yang X, Huang Y, Qiu H, Huang G, Xiao H, *et al.* The neuroprotective effect of apelin-13 in a mouse model of intracerebral hemorrhage. *Neurosci Lett*. 2016 Aug 15;628:219-24. doi: 10.1016/j.neulet.2016.06.046.
- Bao WD, Zhou XT, Zhou LT, Wang F, Yin X, Lu Y, *et al.* Targeting miR-124/Ferroportin signaling ameliorated neuronal cell death through inhibiting apoptosis and ferroptosis in aged intracerebral hemorrhage murine model. *Aging Cell*. 2020 Nov;19(11):e13235. doi: 10.1111/acel.13235.
- Bederson JB, Pitts LH, Germano SM, Nishimura MC, Davis RL, Bartkowski HM. Evaluation of 2,3,5-triphenyltetrazolium chloride as a stain for detection and quantification of experimental cerebral infarction in rats. *Stroke*. 1986 Nov-Dec;17(6):1304-8. doi: 10.1161/01.str.17.6.1304.
- van den Berghe G, Wouters P, Weekers F, Verwaest C, Bruyninckx F, Schetz M, *et al.* Intensive insulin therapy in critically ill patients. *N Engl J Med*. 2001 Nov 8;345(19):1359-67. doi: 10.1056/NEJMoa011300.
- Berndt C, Alborzinia H, Amen VS, Ayton S, Barayeu U, Bartelt A, *et al.* Ferroptosis in health and disease. *Redox Biol*. 2024 Sep;75:103211. doi: 10.1016/j.redox.2024.103211.
- Bersuker K, Hendricks JM, Li Z, Magtanong L, Ford B, Tang PH, *et al.* The CoQ oxidoreductase FSP1 acts parallel to GPX4 to inhibit ferroptosis. *Nature*. 2019 Nov;575(7784):688-692. doi: 10.1038/s41586-019-1705-2.
- Bhaskar MK, Kumar R, Ojha B, Singh SK, Verma N, Verma R, *et al.* A randomized controlled study of operative versus nonoperative treatment for large spontaneous supratentorial intracerebral hemorrhage. *Neurology India*. 2017 Jul-Aug;65(4):752-758. doi: 10.4103/neuroindia.NI_151_16.
- Blacquiere D, Demchuk AM, Al-Hazzaa M, Deshpande A, Petrich W, Aviv RI, *et al.* Intracerebral Hematoma Morphologic Appearance on Noncontrast Computed Tomography Predicts Significant Hematoma Expansion. *Stroke*. 2015 Nov;46(11):3111-6. doi: 10.1161/STROKEAHA.115.010566.

- Boltze J, Förtschler A, Nitzsche B, Waldmin D, Hoffmann A, Boltze CM, *et al.* Permanent middle cerebral artery occlusion in sheep: a novel large animal model of focal cerebral ischemia. *J Cereb Blood Flow Metab.* 2008 Dec;28(12):1951-64. doi: 10.1038/jcbfm.2008.89.
- Boltze J, Ferrara F, Hainsworth AH, Bridges LR, Zille M, Lobsien D, *et al.* Lesional and perilesional tissue characterization by automated image processing in a novel gyrencephalic animal model of peracute intracerebral hemorrhage. *J Cereb Blood Flow Metab.* 2019 Dec;39(12):2521-2535. doi: 10.1177/0271678X18802119.
- Bonkhoff AK, Ullberg T, Bretzner M, Hong S, Schirmer MD, Regenhardt RW, *et al.* Deep profiling of multiple ischemic lesions in a large, multi-center cohort: Frequency, spatial distribution, and associations to clinical characteristics. *Front Neurosci.* 2022 Aug 25;16:994458. doi: 10.3389/fnins.2022.994458.
- Brea A, Laclaustra M, Martorell E, Pedragosa A. Epidemiología de la enfermedad vascular cerebral en España [Epidemiology of cerebrovascular disease in Spain]. *Clin Investig Arterioscler.* 2013 Nov-Dec;25(5):211-7. Spanish. doi: 10.1016/j.arteri.2013.10.006.
- Broderick JP, Brott TG, Duldner JE, Tomsick T, Huster G. Volume of intracerebral hemorrhage. A powerful and easy-to-use predictor of 30-day mortality. *Stroke.* 1993 Jul;24(7):987-93. doi: 10.1161/01.str.24.7.987.
- Brott T, Broderick J, Kothari R, Barsan W, Tomsick T, Sauerbeck L, *et al.* Early hemorrhage growth in patients with intracerebral hemorrhage. *Stroke.* 1997 Jan;28(1):1-5. doi: 10.1161/01.str.28.1.1.
- Brouwers HB, Greenberg SM. Hematoma expansion following acute intracerebral hemorrhage. *Cerebrovasc Dis.* 2013;35(3):195-201. doi: 10.1159/000346599.
- Bryda EC. The Mighty Mouse: the impact of rodents on advances in biomedical research. *Mo Med.* 2013 May-Jun;110(3):207-11. PMID: 23829104; PMCID: PMC3987984.
- Bühler D, Power Guerra N, Müller L, Wolkenhauer O, Düffer M, Vollmar B, *et al.* Leptin deficiency-caused behavioral change - A comparative analysis using EthoVision and DeepLabCut. *Front Neurosci.* 2023;17:1052079. doi: 10.3389/fnins.2023.1052079.
- Bullock R, Mendelow AD, Teasdale GM, Graham DI. Intracranial haemorrhage induced at arterial pressure in the rat. Part 1: Description of technique, ICP changes and neuropathological findings. *Neurol Res.* 1984 Dec;6(4):184-8. doi: 10.1080/01616412.1984.11739687.
- Byrne SL, Mason AB. Human serum transferrin: a tale of two lobes. Urea gel and steady state fluorescence analysis of recombinant transferrins as a function of pH, time, and the soluble portion of the transferrin receptor. *J Biol Inorg Chem.* 2009 Jun;14(5):771-81. doi: 10.1007/s00775-009-0491-y.

- Campbell BCV, De Silva DA, Macleod MR, Coutts SB, Schwamm LH, Davis SM, *et al.* Ischaemic stroke. *Nat Rev Dis Primers.* 2019 Oct 10;5(1):70. doi: 10.1038/s41572-019-0118-8.
- Carlsson M, Wilsgaard T, Johnsen SH, Johnsen LH, Løchen ML, Njølstad I, *et al.* The impact of risk factor trends on intracerebral hemorrhage incidence over the last two decades-The Tromsø Study. *Int J Stroke.* 2019 Jan;14(1):61-68. doi: 10.1177/1747493018789996.
- Castaño C, Melià-Sorolla M, García-Serran A, DeGregorio-Rocasolano N, García-Sort MR, Hernández-Pérez M, *et al.* Establishment of a reproducible and minimally invasive ischemic stroke model in swine. *JCI Insight.* 2023 Apr 24;8(8):e163398. doi: 10.1172/jci.insight.163398.
- Castillo J, Dávalos A, Alvarez-Sabín J, Pumar JM, Leira R, Silva Y, *et al.* Molecular signatures of brain injury after intracerebral hemorrhage. *Neurology.* 2002 Feb 26;58(4):624-9. doi: 10.1212/wnl.58.4.624.
- Chang CF, Massey J, Osherov A, Angenendt da Costa LH, Sansing LH. Bexarotene Enhances Macrophage Erythrophagocytosis and Hematoma Clearance in Experimental Intracerebral Hemorrhage. *Stroke.* 2020 Feb;51(2):612-618. doi: 10.1161/STROKEAHA.119.027037.
- Charidimou A, Boulouis G, Xiong L, Jessel MJ, Roongpiboonsopit D, Ayres A, *et al.* Cortical superficial siderosis and first-ever cerebral hemorrhage in cerebral amyloid angiopathy. *Neurology.* 2017 Apr 25;88(17):1607-1614. doi: 10.1212/WNL.0000000000003866.
- Chen B, Chen Z, Liu M, Gao X, Cheng Y, Wei Y, *et al.* Inhibition of neuronal ferroptosis in the acute phase of intracerebral hemorrhage shows long-term cerebroprotective effects. *Brain Res Bull.* 2019 Nov;153:122-132. doi: 10.1016/j.brainresbull.2019.08.013.
- Chen G, Gao C, Yan Y, Wang T, Luo C, Zhang M, *et al.* Inhibiting ER Stress Weakens Neuronal Pyroptosis in a Mouse Acute Hemorrhagic Stroke Model. *Mol Neurobiol.* 2020 Dec;57(12):5324-5335. doi: 10.1007/s12035-020-02097-9.
- Chen S, Zuo Y, Huang L, Sherchan P, Zhang J, Yu Z, *et al.* The MC4 receptor agonist RO27-3225 inhibits NLRP1-dependent neuronal pyroptosis via the ASK1/JNK/p38 MAPK pathway in a mouse model of intracerebral haemorrhage. *Br J Pharmacol.* 2019 May;176(9):1341-1356. doi: 10.1111/bph.14639.
- Chen S, Li L, Peng C, Bian C, Ocak PE, Zhang JH, *et al.* Targeting Oxidative Stress and Inflammatory Response for Blood-Brain Barrier Protection in Intracerebral Hemorrhage. *Antioxid Redox Signal.* 2022 Jul;37(1-3):115-134. doi: 10.1089/ars.2021.0072.
- Chen W, Xia M, Guo C, Jia Z, Wang J, Li C, *et al.* Modified behavioural tests to detect white matter injury- induced motor deficits after intracerebral haemorrhage in mice. *Sci Rep.* 2019 Nov 18;9(1):16958. doi: 10.1038/s41598-019-53263-6.

References

- Chen Y, Chen S, Chang J, Wei J, Feng M, Wang R. Perihematomal Edema After Intracerebral Hemorrhage: An Update on Pathogenesis, Risk Factors, and Therapeutic Advances. *Front Immunol*. 2021 Oct 19;12:740632. doi: 10.3389/fimmu.2021.740632.
- Chen-Roetling J, Regan RF. Targeting the Nrf2-Heme Oxygenase-1 Axis after Intracerebral Hemorrhage. *Curr Pharm Des*. 2017;23(15):2226-2237. doi: 10.2174/138161282266161027150616.
- Cheng Y, Xi G, Jin H, Keep RF, Feng J, Hua Y. Thrombin-induced cerebral hemorrhage: role of protease-activated receptor-1. *Transl Stroke Res*. 2014 Aug;5(4):472-5. doi: 10.1007/s12975-013-0288-8.
- Chevilly A, Lesept F, Lenoir S, Ali C, Parcq J, Vivien D. Impacts of tissue-type plasminogen activator (tPA) on neuronal survival. *Front Cell Neurosci*. 2015 Oct 16;9:415. doi: 10.3389/fncel.2015.00415.
- Chiang PT, Tsai LK, Tsai HH. New targets in spontaneous intracerebral hemorrhage. *Curr Opin Neurol*. 2025 Feb 1;38(1):10-17. doi: 10.1097/WCO.0000000000001325.
- Choi SH, Lee DY, Kim SU, Jin BK. Thrombin-induced oxidative stress contributes to the death of hippocampal neurons *in vivo*: role of microglial NADPH oxidase. *J Neurosci*. 2005 Apr 20;25(16):4082-90. doi: 10.1523/JNEUROSCI.4306-04.2005.
- Chu K, Jeong SW, Jung KH, Han SY, Lee ST, Kim M, *et al.* Celecoxib induces functional recovery after intracerebral hemorrhage with reduction of brain edema and perihematomal cell death. *J Cereb Blood Flow Metab*. 2004 Aug;24(8):926-33. doi: 10.1097/01.WCB.0000130866.25040.7D.
- Clarke E. Apoplexy in the Hippocratic writings. *Bull Hist Med*. 1963 Jul-Aug;37:301-14. PMID: 14042775.
- Cole DS, Morgan BP. Beyond lysis: how complement influences cell fate. *Clin Sci (Lond)*. 2003 May;104(5):455-66. doi: 10.1042/CS20020362.
- Combs DJ, Dempsey RJ, Kumar S, Donaldson D. Focal cerebral infarction in cats in the presence of hyperglycemia and increased insulin. *Metab Brain Dis*. 1990 Dec;5(4):169-78. doi: 10.1007/BF00997070.
- Conner ES, Lorenzo AV, Welch K, Dorval B. The role of intracranial hypotension in neonatal intraventricular hemorrhage. *J Neurosurg*. 1983 Feb;58(2):204-9. doi: 10.3171/jns.1983.58.2.0204.
- Cook DJ, Tymianski M. Nonhuman primate models of stroke for translational neuroprotection research. *Neurotherapeutics*. 2012 Apr;9(2):371-9. doi: 10.1007/s13311-012-0115-z.
- Corbett D, Carmichael ST, Murphy TH, Jones TA, Schwab ME, Jolkkonen J, *et al.* Enhancing the alignment of the preclinical and clinical stroke recovery research pipeline: Consensus-based core recommendations from the Stroke Recovery and Rehabilitation Roundtable translational

working group. *Int J Stroke*. 2017 Jul;12(5):462-471. doi: 10.1177/1747493017711814. Erratum in: *Int J Stroke*. 2018 Jan;13(1):NP1. doi: 10.1177/1747493017738693.

- Corry JJ, Asaithambi G, Shaik AM, Lassig JP, Marino EH, Ho BM, *et al.* Conivaptan for the Reduction of Cerebral Edema in Intracerebral Hemorrhage: A Safety and Tolerability Study. *Clin Drug Investig*. 2020 May;40(5):503-509. doi: 10.1007/s40261-020-00911-9.
- Cui HJ, He HY, Yang AL, Zhou HJ, Wang C, Luo JK, *et al.* Efficacy of deferoxamine in animal models of intracerebral hemorrhage: a systematic review and stratified meta-analysis. *PLoS One*. 2015 May 22;10(5):e0127256. doi: 10.1371/journal.pone.0127256.
- Crilly S, Njegic A, Parry-Jones AR, Allan SM, Kasher PR. Using Zebrafish Larvae to Study the Pathological Consequences of Hemorrhagic Stroke. *J Vis Exp*. 2019 Jun 5;(148). doi: 10.3791/59716.
- Crilly S, Withers SE, Allan SM, Parry-Jones AR, Kasher PR. Revisiting promising preclinical intracerebral hemorrhage studies to highlight repurposable drugs for translation. *Int J Stroke*. 2021 Feb;16(2):123-136. doi: 10.1177/1747493020972240.
- Dai M, Liu XC, Li HT, Xu CH, Yang B, Wang H, *et al.* EIT Imaging of Intracranial Hemorrhage in Rabbit Models Is Influenced by the Intactness of Cranium. *Biomed Res Int*. 2018 Nov 19;2018:1321862. doi: 10.1155/2018/1321862.
- Dasari R, Bonsack F, Sukumari-Ramesh S. Brain injury and repair after intracerebral hemorrhage: The role of microglia and brain-infiltrating macrophages. *Neurochem Int*. 2021 Jan;142:104923. doi: 10.1016/j.neuint.2020.104923.
- Dastur CK, Yu W. Current management of spontaneous intracerebral haemorrhage. *Stroke Vasc Neurol*. 2017 Feb 24;2(1):21-29. doi: 10.1136/svn-2016-000047.
- Deb P, Sharma S, Hassan KM. Pathophysiologic mechanisms of acute ischemic stroke: An overview with emphasis on therapeutic significance beyond thrombolysis. *Pathophysiology*. 2010 Jun;17(3):197-218. doi: 10.1016/j.pathophys.2009.12.001.
- DeGregorio-Rocasolano N, Martí-Sistac O, Ponce J, Castelló-Ruiz M, Millán M, Guirao V, *et al.* Iron-loaded transferrin (Tf) is detrimental whereas iron-free Tf confers protection against brain ischemia by modifying blood Tf saturation and subsequent neuronal damage. *Redox Biol*. 2018 May;15:143-158. doi: 10.1016/j.redox.2017.11.026.
- DeGregorio-Rocasolano N, Martí-Sistac O, Gasull T. Deciphering the Iron Side of Stroke: Neurorodegeneration at the Crossroads Between Iron Dyshomeostasis, Excitotoxicity, and Ferroptosis. *Front Neurosci*. 2019 Feb 19;13:85. doi: 10.3389/fnins.2019.00085.
- Denis C, Methia N, Frenette PS, Rayburn H, Ullman-Culleré M, Hynes RO, *et al.* A mouse model of severe von Willebrand disease: defects in hemostasis and thrombosis. *Proc Natl Acad Sci U S A*. 1998 Aug 4;95(16):9524-9. doi: 10.1073/pnas.95.16.9524.

References

- De Silva TM, Faraci FM. The DOCA-Salt Model of Hypertension for Studies of Cerebrovascular Function, Stroke, and Brain Health. *Methods Mol Biol.* 2023;2616:481-487. doi: 10.1007/978-1-0716-2926-0_34.
- Diao X, Zhou Z, Xiang W, Jiang Y, Tian N, Tang X, *et al.* Glutathione alleviates acute intracerebral hemorrhage injury via reversing mitochondrial dysfunction. *Brain Res.* 2020 Jan 15;1727:146514. doi: 10.1016/j.brainres.2019.146514.
- Díaz-Guzmán J, Egido JA, Gabriel-Sánchez R, Barberá-Comes G, Fuentes-Gimeno B, Fernández-Pérez C, *et al.* Stroke and transient ischemic attack incidence rate in Spain: the IBERICTUS study. *Cerebrovasc Dis.* 2012;34(4):272-81. doi: 10.1159/000342652.
- Diaz Diaz AC, Shearer JA, Malone K, Waeber C. Acute Treatment With Fingolimod Does Not Confer Long-Term Benefit in a Mouse Model of Intracerebral Haemorrhage. *Front Pharmacol.* 2021 Jan 8;11:613103. doi: 10.3389/fphar.2020.613103.
- Dinc R, Ardic N. Therapeutic Role of Microglia/Macrophage Polarization in Intracerebral Hemorrhage. *Clin Transl Neurosci.* 2025; 9(1):4. doi: 10.3390/ctn9010004.
- Ding H, Yan CZ, Shi H, Zhao YS, Chang SY, Yu P, *et al.* Hepcidin is involved in iron regulation in the ischemic brain. *PLoS One.* 2011;6(9):e25324. doi: 10.1371/journal.pone.0025324.
- Ding Y, Flores J, Klebe D, Li P, McBride DW, Tang J, *et al.* Annexin A1 attenuates neuroinflammation through FPR2/p38/COX-2 pathway after intracerebral hemorrhage in male mice. *J Neurosci Res.* 2020 Jan;98(1):168-178. doi: 10.1002/jnr.24478.
- Dixon SJ, Lemberg KM, Lamprecht MR, Skouta R, Zaitsev EM, Gleason CE, *et al.* Ferroptosis: an iron-dependent form of nonapoptotic cell death. *Cell.* 2012 May 25;149(5):1060-72. doi: 10.1016/j.cell.2012.03.042.
- Dixon SJ, Olzmann JA. The cell biology of ferroptosis. *Nat Rev Mol Cell Biol.* 2024 Jun;25(6):424-442. doi: 10.1038/s41580-024-00703-5.
- Doll S, Freitas FP, Shah R, Aldrovandi M, da Silva MC, Ingold I, *et al.* FSP1 is a glutathione-independent ferroptosis suppressor. *Nature.* 2019 Nov;575(7784):693-698. doi: 10.1038/s41586-019-1707-0.
- Domínguez-Oliva A, Hernández-Ávalos I, Martínez-Burnes J, Olmos-Hernández A, Verduzco-Mendoza A, Mota-Rojas D. The Importance of Animal Models in Biomedical Research: Current Insights and Applications. *Animals (Basel).* 2023 Mar 31;13(7):1223. doi: 10.3390/ani13071223.
- Duan X, Wen Z, Shen H, Shen M, Chen G. Intracerebral Hemorrhage, Oxidative Stress, and Antioxidant Therapy. *Oxid Med Cell Longev.* 2016;2016:1203285. doi: 10.1155/2016/1203285.
- Duberstein KJ, Platt SR, Holmes SP, Dove CR, Howerth EW, Kent M, *et al.* Gait analysis in a pre- and post-ischemic stroke biomedical pig model. *Physiol Behav.* 2014 Feb 10;125:8-16. doi: 10.1016/j.physbeh.2013.11.004.

- Ducruet AF, Zacharia BE, Hickman ZL, Grobelny BT, Yeh ML, Sosunov SA, *et al.* The complement cascade as a therapeutic target in intracerebral hemorrhage. *Exp Neurol.* 2009 Oct;219(2):398-403. doi: 10.1016/j.expneurol.2009.07.018.
- Durand NC, Kim HG, Patel VN, Turnbull MT, Siegel JL, Hodge DO, *et al.* Mesenchymal Stem Cell Therapy in Acute Intracerebral Hemorrhage: A Dose-Escalation Safety and Tolerability Trial. *Neurocrit Care.* 2024 Aug;41(1):59-69. doi: 10.1007/s12028-023-01897-w.
- Eckermann JM, Chen W, Jadhav V, Hsu FP, Colohan AR, Tang J, *et al.* Hydrogen is neuroprotective against surgically induced brain injury. *Med Gas Res.* 2011 May 18;1(1):7. doi: 10.1186/2045-9912-1-7.
- Fang J, Song F, Chang C, Yao M. Intracerebral Hemorrhage Models and Behavioral Tests in Rodents. *Neuroscience.* 2023 Mar 1;513:1-13. doi: 10.1016/j.neuroscience.2023.01.011.
- Feldman EA, Meola G, Zyck S, Miller CD, Krishnamurthy S, Cwikla GM, *et al.* Retrospective Assessment of Desmopressin Effectiveness and Safety in Patients With Antiplatelet-Associated Intracranial Hemorrhage. *Crit Care Med.* 2019 Dec;47(12):1759-1765. doi: 10.1097/CCM.0000000000004021.
- Feng H, Schorpp K, Jin J, Yozwiak CE, Hoffstrom BG, Decker AM, *et al.* Transferrin Receptor Is a Specific Ferroptosis Marker. *Cell Rep.* 2020 Mar 10;30(10):3411-3423.e7. doi: 10.1016/j.celrep.2020.02.049.
- Feng L, Zhang X, Li W, Wang J, Wang Q, Wang Q, *et al.* Proteomics reveals that Di Dang decoction can regulate the Jak2/Stat5 signaling pathway and inhibit apoptosis by reducing the oxidative stress response in rats with acute intracerebral hemorrhagic stroke. *J Ethnopharmacol.* 2023 Jan 30;301:115816. doi: 10.1016/j.jep.2022.115816.
- Fewel ME, Thompson BG Jr, Hoff JT. Spontaneous intracerebral hemorrhage: a review. *Neurosurg Focus.* 2003 Oct 15;15(4):E1. PMID: 15344894.
- Foster L, Robinson L, Yeatts SD, Conwit RA, Shehadah A, Lioutas V, *et al.* Effect of Deferoxamine on Trajectory of Recovery After Intracerebral Hemorrhage: A Post Hoc Analysis of the i-DEF Trial. *Stroke.* 2022 Jul;53(7):2204-2210. doi: 10.1161/STROKEAHA.121.037298.
- Fouda AY, Newsome AS, Spellacy S, Waller JL, Zhi W, Hess DC, *et al.* Minocycline in Acute Cerebral Hemorrhage: An Early Phase Randomized Trial. *Stroke.* 2017 Oct;48(10):2885-2887. doi: 10.1161/STROKEAHA.117.018658.
- Friedmann Angeli JP, Schneider M, Proneth B, Tyurina YY, Tyurin VA, Hammond VJ, *et al.* Inactivation of the ferroptosis regulator Gpx4 triggers acute renal failure in mice. *Nat Cell Biol.* 2014 Dec;16(12):1180-91. doi: 10.1038/ncb3064.

References

- Fries G, Wallenfang T, Hennen J, Velthaus M, Heimann A, Schild H, *et al.* Occlusion of the pig superior sagittal sinus, bridging and cortical veins: multistep evolution of sinus-vein thrombosis. *J Neurosurg.* 1992 Jul;77(1):127-33. doi: 10.3171/jns.1992.77.1.0127.
- Fujii Y, Takeuchi S, Sasaki O, Minakawa T, Tanaka R. Multivariate analysis of predictors of hematoma enlargement in spontaneous intracerebral hemorrhage. *Stroke.* 1998 Jun;29(6):1160-6. doi: 10.1161/01.str.29.6.1160.
- Fung C, Murek M, Z'Graggen WJ, Krähenbühl AK, Gautschi OP, Schucht P, *et al.* Decompressive hemicraniectomy in patients with supratentorial intracerebral hemorrhage. *Stroke.* 2012 Dec;43(12):3207-11. doi: 10.1161/STROKEAHA.112.666537.
- Gaasch JA, Lockman PR, Geldenhuys WJ, Allen DD, Van der Schyf CJ. Brain iron toxicity: differential responses of astrocytes, neurons, and endothelial cells. *Neurochem Res.* 2007 Jul;32(7):1196-208. doi: 10.1007/s11064-007-9290-4.
- Gao C, Jiang J, Tan Y, Chen S. Microglia in neurodegenerative diseases: mechanism and potential therapeutic targets. *Signal Transduct Target Ther.* 2023 Sep 22;8(1):359. doi: 10.1038/s41392-023-01588-0.
- Gao D, Chu X, Zhang Y, Yan H, Niu L, Jiang X, *et al.* Statins for neuroprotection in spontaneous intracerebral haemorrhage (STATIC): protocol for a multicentre, prospective and randomised controlled trial. *BMJ Open.* 2024 Jun 21;14(6):e079879. doi: 10.1136/bmjopen-2023-079879.
- García-Serran A, Ordoño J, DeGregorio-Rocasolano N, Melià-Sorolla M, Odendaal K, Martí-Sistac O, *et al.* Targeting Pro-Oxidant Iron with Exogenously Administered Apotransferrin Provides Benefits Associated with Changes in Crucial Cellular Iron Gate Protein TfR in a Model of Intracerebral Hemorrhagic Stroke in Mice. *Antioxidants (Basel).* 2023 Oct 31;12(11):1945. doi: 10.3390/antiox12111945.
- Garcia JH, Wagner S, Liu KF, Hu XJ. Neurological deficit and extent of neuronal necrosis attributable to middle cerebral artery occlusion in rats. Statistical validation. *Stroke.* 1995 Apr;26(4):627-34; discussion 635. doi: 10.1161/01.str.26.4.627.
- Garg RK, Ouyang B, Pandya V, Garcia-Cano R, Da Silva I, Hall D, *et al.* The Influence of Weather on the Incidence of Primary Spontaneous Intracerebral Hemorrhage. *J Stroke Cerebrovasc Dis.* 2019 Feb;28(2):405-411. doi: 10.1016/j.jstrokecerebrovasdis.2018.10.011.
- GBD 2019 Stroke Collaborators. Global, regional, and national burden of stroke and its risk factors, 1990-2019: a systematic analysis for the Global Burden of Disease Study 2019. *Lancet Neurol.* 2021 Oct;20(10):795-820. doi: 10.1016/S1474-4422(21)00252-0.
- Gerhardson T, Sukovich JR, Chaudhary N, Chenevert TL, Ives K, Hall TL, *et al.* Histotripsy Clot Liquefaction in a Porcine Intracerebral Hemorrhage Model. *Neurosurgery.* 2020 Mar 1;86(3):429-436. doi: 10.1093/neuros/nyz089.

- Gildersleeve KL, Hirzallah MI, Esquenazi Y, Moomaw CJ, Sekar P, Cai C, *et al.* Hemicraniectomy for Supratentorial Primary Intracerebral Hemorrhage: A Retrospective, Propensity Score Matched Study. *J Stroke Cerebrovasc Dis.* 2019 Nov;28(11):104361. doi: 10.1016/j.jstrokecerebrovasdis.2019.104361. Erratum in: *J Stroke Cerebrovasc Dis.* 2020 May;29(5):104654. doi: 10.1016/j.jstrokecerebrovasdis.2020.104654.
- Ginsberg MD. The cerebral collateral circulation: Relevance to pathophysiology and treatment of stroke. *Neuropharmacology.* 2018 May 15;134(Pt B):280-292. doi: 10.1016/j.neuropharm.2017.08.003.
- Gingrich MB, Junge CE, Lyuboslavsky P, Traynelis SF. Potentiation of NMDA receptor function by the serine protease thrombin. *J Neurosci.* 2000 Jun 15;20(12):4582-95. doi: 10.1523/JNEUROSCI.20-12-04582.2000.
- Glushakov AV, Robbins SW, Bracy CL, Narumiya S, Doré S. Prostaglandin F2 α FP receptor antagonist improves outcomes after experimental traumatic brain injury. *J Neuroinflammation.* 2013 Oct 30;10:132. doi: 10.1186/1742-2094-10-132.
- Goddard J, Lewis RM, Armstrong DL, Zeller RS. Moderate, rapidly induced hypertension as a cause of intraventricular hemorrhage in the newborn beagle model. *J Pediatr.* 1980 Jun;96(6):1057-60. doi: 10.1016/s0022-3476(80)80641-x.
- Golubczyk D, Kalkowski L, Kwiatkowska J, Zawadzki M, Holak P, Glodek J, *et al.* Endovascular model of ischemic stroke in swine guided by real-time MRI. *Sci Rep.* 2020 Oct 14;10(1):17318. doi: 10.1038/s41598-020-74411-3.
- Gong L, Manaenko A, Fan R, Huang L, Enkhjargal B, McBride D, *et al.* Osteopontin attenuates inflammation via JAK2/STAT1 pathway in hyperglycemic rats after intracerebral hemorrhage. *Neuropharmacology.* 2018 Aug;138:160-169. doi: 10.1016/j.neuropharm.2018.06.009.
- Gong Y, Li H, Cui H, Gong Y. Microglial Mechanisms and Therapeutic Potential in Brain Injury Post-Intracerebral Hemorrhage. *J Inflamm Res.* 2025 Feb 26;18:2955-2973. doi: 10.2147/JIR.S498809.
- Gong Y, Xi G, Hu H, Gu Y, Huang F, Keep RF, *et al.* Increase in brain thrombin activity after experimental intracerebral hemorrhage. *Acta Neurochir Suppl.* 2008;105:47-50. doi: 10.1007/978-3-211-09469-3_10.
- Gorelick PB. Alcohol and stroke. *Stroke.* 1987 Jan-Feb;18(1):268-71. doi: 10.1161/01.str.18.1.268.
- Goulay R, Naveau M, Gaberel T, Vivien D, Parcq J. Optimized tPA: A non-neurotoxic fibrinolytic agent for the drainage of intracerebral hemorrhages. *J Cereb Blood Flow Metab.* 2018 Jul;38(7):1180-1189. doi: 10.1177/0271678X17719180.

References

- Grabowski M, Brundin P, Johansson BB. Paw-reaching, sensorimotor, and rotational behavior after brain infarction in rats. *Stroke*. 1993 Jun;24(6):889-95. doi: 10.1161/01.str.24.6.889.
- Greenberg SM, Ziai WC, Cordonnier C, Dowlatshahi D, Francis B, Goldstein JN, *et al.* 2022 Guideline for the Management of Patients With Spontaneous Intracerebral Hemorrhage: A Guideline From the American Heart Association/American Stroke Association. *Stroke*. 2022 Jul;53(7):e282-e361. doi: 10.1161/STR.0000000000000407.
- Gregson BA, Broderick JP, Auer LM, Batjer H, Chen XC, Juvela S, *et al.* Individual patient data subgroup meta-analysis of surgery for spontaneous supratentorial intracerebral hemorrhage. *Stroke*. 2012 Jun;43(6):1496-504. doi: 10.1161/STROKEAHA.111.640284. Erratum in: *Stroke*. 2013 Jul;44(7):e82. PMID: 22511006; PMCID: PMC3419479.
- Guan J, Williams C, Gunning M, Mallard C, Gluckman P. The effects of IGF-1 treatment after hypoxic-ischemic brain injury in adult rats. *J Cereb Blood Flow Metab*. 1993 Jul; 13(4):609-16. doi: 10.1038/jcbfm.1993.79.
- Gulati S, Solheim O, Carlsen SM, Øie LR, Jensberg H, Gulati AM, *et al.* Risk of intracranial hemorrhage (RICH) in users of oral antithrombotic drugs: Nationwide pharmacoepidemiological study. *PLoS One*. 2018 Aug 23;13(8):e0202575. doi: 10.1371/journal.pone.0202575.
- Guo G, Pan C, Guo W, Bai S, Nie H, Feng Y, *et al.* Efficacy and safety of four interventions for spontaneous supratentorial intracerebral hemorrhage: a network meta-analysis. *J Neurointerv Surg*. 2020 Jun;12(6):598-604. doi: 10.1136/neurintsurg-2019-015362.
- Guo F, Xu D, Lin Y, Wang G, Wang F, Gao Q, *et al.* Chemokine CCL2 contributes to BBB disruption via the p38 MAPK signaling pathway following acute intracerebral hemorrhage. *FASEB J*. 2020 Jan;34(1):1872-1884. doi: 10.1096/fj.201902203RR.
- Guo Q, Yang S, Yang D, Zhang N, Li X, Chen T, *et al.* Differential mRNA expression combined with network pharmacology reveals network effects of Liangxue Tongyu Prescription for acute intracerebral hemorrhagic rats. *J Ethnopharmacol*. 2020 Jan 10;246:112231. doi: 10.1016/j.jep.2019.112231.
- Hakansson F, Jensen DB. Automatic monitoring and detection of tail-biting behavior in groups of pigs using video-based deep learning methods. *Front Vet Sci*. 2023 Jan 11;9:1099347. doi: 10.3389/fvets.2022.1099347.
- Hallevi H, Dar NS, Barreto AD, Morales MM, Martin-Schild S, Abraham AT, *et al.* The IVH score: a novel tool for estimating intraventricular hemorrhage volume: clinical and research implications. *Crit Care Med*. 2009 Mar;37(3):969-74, e1. doi: 10.1097/CCM.0b013e318198683a.
- Hamada R, Matsuoka H. Antithrombin therapy for intracerebral hemorrhage. *Stroke*. 2000 Mar;31(3):794-5. doi: 10.1161/01.str.31.3.791-c.

- Han R, Wan J, Han X, Ren H, Falck JR, Munnuri S, *et al.* 20-HETE Participates in Intracerebral Hemorrhage-Induced Acute Injury by Promoting Cell Ferroptosis. *Front Neurol.* 2021 Nov 12;12:763419. doi: 10.3389/fneur.2021.763419.
- Hanger HC, Geddes JA, Wilkinson TJ, Lee M, Baker AE. Warfarin-related intracerebral haemorrhage: better outcomes when reversal includes prothrombin complex concentrates. *Intern Med J.* 2013 Mar;43(3):308-16. doi: 10.1111/imj.12034.
- Hanley DF, Lane K, McBee N, Ziai W, Tuhrim S, Lees KR, *et al.* Thrombolytic removal of intraventricular haemorrhage in treatment of severe stroke: results of the randomised, multicentre, multiregion, placebo-controlled CLEAR III trial. *Lancet.* 2017 Feb 11;389(10069):603-611. doi: 10.1016/S0140-6736(16)32410-2.
- Hanley DF, Thompson RE, Rosenblum M, Yenokyan G, Lane K, McBee N, *et al.* Efficacy and safety of minimally invasive surgery with thrombolysis in intracerebral haemorrhage evacuation (MISTIE III): a randomised, controlled, open-label, blinded endpoint phase 3 trial. *Lancet.* 2019 Mar 9;393(10175):1021-1032. doi: 10.1016/S0140-6736(19)30195-3. Erratum in: *Lancet.* 2019 Apr 20;393(10181):1596. doi: 10.1016/S0140-6736(19)30859-1.
- Hatakeyama T, Okauchi M, Hua Y, Keep RF, Xi G. Deferoxamine reduces neuronal death and hematoma lysis after intracerebral hemorrhage in aged rats. *Transl Stroke Res.* 2013 Oct;4(5):546-53. doi: 10.1007/s12975-013-0270-5.
- Hayashi K, Hasegawa Y, Takemoto Y, Cao C, Mukasa A, Kim-Mitsuyama S. Enhanced oxidative stress contributes to worse prognosis and delayed neurofunctional recovery after striatal intracerebral hemorrhage in 5XFAD mice. *Eur J Neurosci.* 2020 Apr;51(8):1806-1814. doi: 10.1111/ejn.14596.
- Hemphill JC 3rd, Greenberg SM, Anderson CS, Becker K, Bendok BR, Cushman M, *et al.* Guidelines for the Management of Spontaneous Intracerebral Hemorrhage: A Guideline for Healthcare Professionals From the American Heart Association/American Stroke Association. *Stroke.* 2015 Jul;46(7):2032-60. doi: 10.1161/STR.0000000000000069.
- Heo J, Yoon JG, Park H, Kim YD, Nam HS, Heo JH. Machine Learning-Based Model for Prediction of Outcomes in Acute Stroke. *Stroke.* 2019 May;50(5):1263-1265. doi: 10.1161/STROKEAHA.118.024293.
- Herweh C, Jüttler E, Schellinger PD, Klotz E, Jenetzky E, Orakcioglu B, *et al.* Evidence against a perihemorrhagic penumbra provided by perfusion computed tomography. *Stroke.* 2007 Nov;38(11):2941-7. doi: 10.1161/STROKEAHA.107.486977.
- Herzig MC, Winkler DT, Burgermeister P, Pfeifer M, Kohler E, Schmidt SD, *et al.* Abeta is targeted to the vasculature in a mouse model of hereditary cerebral hemorrhage with amyloidosis. *Nat Neurosci.* 2004 Sep;7(9):954-60. doi: 10.1038/nn1302.

References

- Heuts SG, Bruce SS, Zacharia BE, Hickman ZL, Kellner CP, Sussman ES, *et al.* Decompressive hemicraniectomy without clot evacuation in dominant-sided intracerebral hemorrhage with ICP crisis. *Neurosurg Focus*. 2013 May;34(5):E4. doi: 10.3171/2013.2.FOCUS1326.
- Hietamies TM, Ostrowski C, Pei Z, Feng L, McCabe C, Work LM, *et al.* Variability of functional outcome measures used in animal models of stroke and vascular cognitive impairment - a review of contemporary studies. *J Cereb Blood Flow Metab*. 2018; 38:1872-1884. doi: 10.1177/0271678X18799858.
- Holste K, Xia F, Garton HJL, Wan S, Hua Y, Keep RF, *et al.* The role of complement in brain injury following intracerebral hemorrhage: A review. *Exp Neurol*. 2021 Jun;340:113654. doi: 10.1016/j.expneurol.2021.113654.
- Hu WF, Lee CH, Pang CY, Huang HY, Tsai ST, Wang PK, *et al.* Mitigating mitochondrial dysfunction and neuroinflammation by hematoma aspiration in a new surgical model for severe intracerebral hemorrhage. *Exp Neurol*. 2025 Mar;385:115098. doi: 10.1016/j.expneurol.2024.115098.
- Hua Y, Keep RF, Hoff JT, Xi G. Deferoxamine therapy for intracerebral hemorrhage. *Acta Neurochir Suppl*. 2008;105:3-6. doi: 10.1007/978-3-211-09469-3_1.
- Hua Y, Xi G, Keep RF, Hoff JT. Complement activation in the brain after experimental intracerebral hemorrhage. *J Neurosurg*. 2000 Jun;92(6):1016-22. doi: 10.3171/jns.2000.92.6.1016.
- Hua Y, Wu J, Keep RF, Nakamura T, Hoff JT, Xi G. Tumor necrosis factor-alpha increases in the brain after intracerebral hemorrhage and thrombin stimulation. *Neurosurgery*. 2006 Mar;58(3):542-50; discussion 542-50. doi: 10.1227/01.NEU.0000197333.55473.AD.
- Hua Y, Keep RF, Gu Y, Xi G. Thrombin and brain recovery after intracerebral hemorrhage. *Stroke*. 2009 Mar;40(3 Suppl):S88-9. doi: 10.1161/STROKEAHA.108.533281.
- Huang M, Wan Y, Mao L, He QW, Xia YP, Li M, *et al.* Inhibiting the Migration of M1 Microglia at Hyperacute Period Could Improve Outcome of tMCAO Rats. *CNS Neurosci Ther*. 2017 Mar;23(3):222-232. doi: 10.1111/cns.12665.
- Iglesias-Rey R, Rodríguez-Yáñez M, Arias S, Santamaría M, Rodríguez-Castro E, López-Dequidt I, *et al.* Inflammation, edema and poor outcome are associated with hyperthermia in hypertensive intracerebral hemorrhages. *Eur J Neurol*. 2018 Sep;25(9):1161-1168. doi: 10.1111/ene.13677.
- Iida S, Baumbach GL, Lavoie JL, Faraci FM, Sigmund CD, Heistad DD. Spontaneous stroke in a genetic model of hypertension in mice. *Stroke*. 2005 Jun;36(6):1253-8. doi: 10.1161/01.str.0000167694.58419.a2.
- Iwai M, Kajino T, Nakatuchi M, Yanagisawa K, Hosono Y, Isomura H, *et al.* Long non-coding RNA TILR constitutively represses TP53 and apoptosis in lung cancer. *Oncogene*. 2023 Jan;42(5):364-373. doi: 10.1038/s41388-022-02546-w.

- Iwuchukwu I, Bui C, Hsieh B, Sabharwal V, Mohammed A, McGrade H, *et al.* Decompressive hemicraniectomy in the management of subcortical spontaneous intracerebral hemorrhage. *Int J Neurosci.* 2020 Oct;130(10):965-971. doi: 10.1080/00207454.2020.1713773.
- Jauquet M, Gagnepain P, La Porte E, Thiebaut AM, Rochey A, Legros H, *et al.* Endogenous tPA levels: A biomarker for discriminating hemorrhagic stroke from ischemic stroke and stroke mimics. *Ann Clin Transl Neurol.* 2024 Nov;11(11):2877-2890. doi: 10.1002/acn3.52197.
- Jeanne M, Jorgensen J, Gould DB. Molecular and Genetic Analyses of Collagen Type IV Mutant Mouse Models of Spontaneous Intracerebral Hemorrhage Identify Mechanisms for Stroke Prevention. *Circulation.* 2015 May 5;131(18):1555-65. doi: 10.1161/CIRCULATIONAHA.114.013395.
- Jenkins A, Maxwell WL, Graham DI. Experimental intracerebral haematoma in the rat: sequential light microscopical changes. *Neuropathol Appl Neurobiol.* 1989 Sep-Oct;15(5):477-86. doi: 10.1111/j.1365-2990.1989.tb01247.x.
- Jeon JH, Kaiser EE, Waters ES, Yang X, Lourenco JM, Fagan MM, *et al.* Tanshinone IIA-loaded nanoparticles and neural stem cell combination therapy improves gut homeostasis and recovery in a pig ischemic stroke model. *Sci Rep.* 2023 Feb 13;13(1):2520. doi: 10.1038/s41598-023-29282-9.
- Jiang Y, Wu J, Hua Y, Keep RF, Xiang J, Hoff JT, *et al.* Thrombin-receptor activation and thrombin-induced brain tolerance. *J Cereb Blood Flow Metab.* 2002 Apr;22(4):404-10. doi: 10.1097/00004647-200204000-00004.
- Jiao Y, Ren S, Wang L, Wu G. PPAR γ /RAD21 alleviates peripheral secondary brain injury in rat cerebral hemorrhage model through promoting M2 polarization of microglial cells. *Int Immunopharmacol.* 2023 Jan;114:109572. doi: 10.1016/j.intimp.2022.109572.
- Jin J, Schorpp K, Samaga D, Unger K, Hadian K, Stockwell BR. Machine Learning Classifies Ferroptosis and Apoptosis Cell Death Modalities with TfR1 Immunostaining. *ACS Chem Biol.* 2022 Mar 18;17(3):654-660. doi: 10.1021/acschembio.1c00953.
- Jing C, Bian L, Wang M, Keep RF, Xi G, Hua Y. Enhancement of Hematoma Clearance With CD47 Blocking Antibody in Experimental Intracerebral Hemorrhage. *Stroke.* 2019 Jun;50(6):1539-1547. doi: 10.1161/STROKEAHA.118.024578.
- Kaiser EE, Poythress JC, Scheulin KM, Jurgielewicz BJ, Lazar NA, Park C, *et al.* An integrative multivariate approach for predicting functional recovery using magnetic resonance imaging parameters in a translational pig ischemic stroke model. *Neural Regen Res.* 2021 May;16(5):842-850. doi: 10.4103/1673-5374.297079.

References

- Kaiser EE, Waters ES, Yang X, Fagan MM, Scheulin KM, Snead SE, *et al.* Tanshinone IIA-Loaded Nanoparticle and Neural Stem Cell Therapy Enhances Recovery in a Pig Ischemic Stroke Model. *Stem Cells Transl Med.* 2022 Oct 21;11(10):1061-1071. doi: 10.1093/stcltm/szac062.
- Kaiser EE, West FD. Large animal ischemic stroke models: replicating human stroke pathophysiology. *Neural Regen Res.* 2020 Aug;15(8):1377-1387. doi: 10.4103/1673-5374.274324.
- Karki K, Knight RA, Han Y, Yang D, Zhang J, Ledbetter KA, *et al.* Simvastatin and atorvastatin improve neurological outcome after experimental intracerebral hemorrhage. *Stroke.* 2009 Oct;40(10):3384-9. doi: 10.1161/STROKEAHA.108.544395.
- Kathirvelu B, Carmichael ST. Intracerebral hemorrhage in mouse models: therapeutic interventions and functional recovery. *Metab Brain Dis.* 2015 Apr;30(2):449-59. doi: 10.1007/s11011-014-9559-7.
- Kazui S, Naritomi H, Yamamoto H, Sawada T, Yamaguchi T. Enlargement of spontaneous intracerebral hemorrhage. Incidence and time course. *Stroke.* 1996 Oct;27(10):1783-7. doi: 10.1161/01.str.27.10.1783.
- Keep RF, Hua Y, Xi G. Intracerebral haemorrhage: mechanisms of injury and therapeutic targets. *Lancet Neurol.* 2012 Aug;11(8):720-31. doi: 10.1016/S1474-4422(12)70104-7.
- Khan M, Baird GL, Elias R, Rodriguez-Srednicki J, Yaghi S, Yan S, *et al.* Comparison of Intracerebral Hemorrhage Volume Calculation Methods and Their Impact on Scoring Tools. *J Neuroimaging.* 2017 Jan;27(1):144-148. doi: 10.1111/jon.12370.
- Kidwell CS, Chalela JA, Saver JL, Starkman S, Hill MD, Demchuk AM, *et al.* Comparison of MRI and CT for detection of acute intracerebral hemorrhage. *JAMA.* 2004 Oct 20;292(15):1823-30. doi: 10.1001/jama.292.15.1823.
- Kim H, Lee JE, Yoo HJ, Sung JH, Yang SH. Effect of Pioglitazone on Perihematomal Edema in Intracerebral Hemorrhage Mouse Model by Regulating NLRP3 Expression and Energy Metabolism. *J Korean Neurosurg Soc.* 2020 Nov;63(6):689-697. doi: 10.3340/jkns.2020.0056.
- Kim Y, Han MH, Kim CH, Kim JM, Cheong JH, Ryu JI. Increased Short-Term Mortality in Patients with Spontaneous Intracerebral Hemorrhage and its Association with Admission Glucose Levels and Leukocytosis. *World Neurosurg.* 2017 Feb;98:503-511. doi: 10.1016/j.wneu.2016.11.087.
- Kinder HA, Baker EW, Howerth EW, Duberstein KJ, West FD. Controlled Cortical Impact Leads to Cognitive and Motor Function Deficits that Correspond to Cellular Pathology in a Piglet Traumatic Brain Injury Model. *J Neurotrauma.* 2019 Oct 1;36(19):2810-2826. doi: 10.1089/neu.2019.6405.
- Kinder HA, Baker EW, Wang S, Fleischer CC, Howerth EW, Duberstein KJ, *et al.* Traumatic Brain Injury Results in Dynamic Brain Structure Changes Leading to Acute and Chronic Motor

Function Deficits in a Pediatric Piglet Model. *J Neurotrauma*. 2019 Oct 15;36(20):2930-2942. doi: 10.1089/neu.2018.6303.

- Kinder HA, Baker EW, West FD. The pig as a preclinical traumatic brain injury model: current models, functional outcome measures, and translational detection strategies. *Neural Regen Res*. 2019 Mar;14(3):413-424. doi: 10.4103/1673-5374.245334.
- King MD, Alleyne CH Jr, Dhandapani KM. TNF-alpha receptor antagonist, R-7050, improves neurological outcomes following intracerebral hemorrhage in mice. *Neurosci Lett*. 2013 May 10;542:92-6. doi: 10.1016/j.neulet.2013.02.051.
- King MD, McCracken DJ, Wade FM, Meiler SE, Alleyne CH Jr, Dhandapani KM. Attenuation of hematoma size and neurological injury with curcumin following intracerebral hemorrhage in mice. *J Neurosurg*. 2011 Jul;115(1):116-23. doi: 10.3171/2011.2.JNS10784.
- Kitaoka T, Hua Y, Xi G, Nagao S, Hoff JT, Keep RF. Effect of delayed argatroban treatment on intracerebral hemorrhage-induced edema in the rat. *Acta Neurochir Suppl*. 2003;86:457-61. doi: 10.1007/978-3-7091-0651-8_94.
- Klatsky AL, Armstrong MA, Friedman GD. Alcohol use and subsequent cerebrovascular disease hospitalizations. *Stroke*. 1989 Jun;20(6):741-6. doi: 10.1161/01.str.20.6.741.
- Klebe D, Iniaghe L, Burchell S, Reis C, Akyol O, Tang J, et al. Intracerebral Hemorrhage in Mice. *Methods Mol Biol*. 2018;1717:83-91. doi: 10.1007/978-1-4939-7526-6_7.
- Kothari RU, Brott T, Broderick JP, Barsan WG, Sauerbeck LR, Zuccarello M, et al. The ABCs of measuring intracerebral hemorrhage volumes. *Stroke*. 1996 Aug;27(8):1304-5. doi: 10.1161/01.str.27.8.1304.
- Krafft PR, McBride DW, Lekic T, Rolland WB, Mansell CE, Ma Q, et al. Correlation between subacute sensorimotor deficits and brain edema in two mouse models of intracerebral hemorrhage. *Behav Brain Res*. 2014 May 1;264:151-60. doi: 10.1016/j.bbr.2014.01.052.
- Krenzlin H, Frenz C, Schmitt J, Masomi-Bornwasser J, Wesp D, Kalasauskas D, et al. High CSF thrombin concentration and activity is associated with an unfavorable outcome in patients with intracerebral hemorrhage. *PLoS One*. 2020 Nov 11;15(11):e0241565. doi: 10.1371/journal.pone.0241565.
- Krishnan K, Campos PB, Nguyen TN, Tan CW, Chan SL, Appleton JP, et al. Cerebral edema in intracerebral hemorrhage: pathogenesis, natural history, and potential treatments from translation to clinical trials. *Front Stroke*. 2023;2:1256664. doi: 10.3389/fstro.2023.1256664.
- Küker W, Thiex R, Rohde I, Rohde V, Thron A. Experimental acute intracerebral hemorrhage. Value of MR sequences for a safe diagnosis at 1.5 and 0.5 T. *Acta Radiol*. 2000 Nov;41(6):544-52. doi: 10.1080/028418500127346180.

- Kuramatsu JB, Biffi A, Gerner ST, Sembill JA, Sprügel MI, Leasure A, *et al.* Association of Surgical Hematoma Evacuation vs Conservative Treatment With Functional Outcome in Patients With Cerebellar Intracerebral Hemorrhage. *JAMA*. 2019 Oct 8;322(14):1392-1403. doi: 10.1001/jama.2019.13014.
- Kuramoto Y, Takagi T, Tatebayashi K, Beppu M, Doe N, Fujita M, *et al.* Intravenous administration of human adipose-derived stem cells ameliorates motor and cognitive function for intracerebral hemorrhage mouse model. *Brain Res.* 2019 May 15;1711:58-67. doi: 10.1016/j.brainres.2018.12.042.
- Kwak R, Kadoya S, Suzuki T. Factors affecting the prognosis in thalamic hemorrhage. *Stroke*. 1983 Jul-Aug;14(4):493-500. doi: 10.1161/01.str.14.4.493.
- Lai X, Xiong Y, Zhou J, Yang F, Peng J, Chen L, *et al.* Verbascoside attenuates acute inflammatory injury in experimental cerebral hemorrhage by suppressing TLR4. *Biochem Biophys Res Commun*. 2019 Nov 19;519(4):721-726. doi: 10.1016/j.bbrc.2019.09.057.
- Leclerc JL, Lampert AS, Diller MA, Doré S. Genetic deletion of the prostaglandin E2 E prostanoid receptor subtype 3 improves anatomical and functional outcomes after intracerebral hemorrhage. *Eur J Neurosci*. 2015 May;41(10):1381-91. doi: 10.1111/ejn.12909.
- Leclerc JL, Lampert AS, Loyola Amador C, Schlakman B, Vasilopoulos T, *et al.* The absence of the CD163 receptor has distinct temporal influences on intracerebral hemorrhage outcomes. *J Cereb Blood Flow Metab*. 2018 Feb;38(2):262-273. doi: 10.1177/0271678X17701459.
- Leclerc JL, Li C, Jean S, Lampert AS, Amador CL, Diller MA, *et al.* Temporal and age-dependent effects of haptoglobin deletion on intracerebral hemorrhage-induced brain damage and neurobehavioral outcomes. *Exp Neurol*. 2019 Jul;317:22-33. doi: 10.1016/j.expneurol.2019.01.011.
- Li H, Li X, Li M, Li W, Wei J, Huang Y, *et al.* Edaravone dextrose provides neuroprotective benefits by suppressing ferroptosis in experimental intracerebral hemorrhage. *Sci Rep*. 2025 May 13;15(1):16595. doi: 10.1038/s41598-025-99187-2.
- Li J, Sun Y, Qiu W, Zhou Y, Zhou D, Zhao Y, *et al.* Liangxue Tongyu prescription attenuates neuroinflammation by increasing cholecystokinin octapeptide in acute intracerebral hemorrhage rats. *Neuropeptides*. 2024 Oct;107:102452. doi: 10.1016/j.npep.2024.102452.
- Li Q, Wan J, Lan X, Han X, Wang Z, Wang J. Neuroprotection of brain-permeable iron chelator VK-28 against intracerebral hemorrhage in mice. *J Cereb Blood Flow Metab*. 2017 Sep;37(9):3110-3123. doi: 10.1177/0271678X17709186.
- Li R, Liu Z, Wu X, Yu Z, Zhao S, Tang X. Lithium chloride promoted hematoma resolution after intracerebral hemorrhage through GSK-3 β -mediated pathways-dependent microglia phagocytosis and M2-phenotype differentiation, angiogenesis and neurogenesis in a rat model. *Brain Res Bull*. 2019 Oct;152:117-127. doi: 10.1016/j.brainresbull.2019.07.019.

- Li X, Sun Z, Zhao W, Zhang J, Chen J, Li Y, *et al.* Effect of acetylsalicylic acid usage and platelet transfusion on postoperative hemorrhage and activities of daily living in patients with acute intracerebral hemorrhage. *J Neurosurg.* 2013 Jan;118(1):94-103. doi: 10.3171/2012.9.JNS112286.
- Li Z, Li M, Shi SX, Yao N, Cheng X, Guo A, *et al.* Brain transforms natural killer cells that exacerbate brain edema after intracerebral hemorrhage. *J Exp Med.* 2020 Dec 7;217(12):e20200213. doi: 10.1084/jem.20200213.
- Liang H, Sun Y, Gao A, Zhang N, Jia Y, Yang S, *et al.* Ac-YVAD-cmk improves neurological function by inhibiting caspase-1-mediated inflammatory response in the intracerebral hemorrhage of rats. *Int Immunopharmacol.* 2019 Oct;75:105771. doi: 10.1016/j.intimp.2019.105771. Erratum in: *Int Immunopharmacol.* 2023 Jun;119:110283. doi: 10.1016/j.intimp.2023.110283.
- Liddelow SA, Guttenplan KA, Clarke LE, Bennett FC, Bohlen CJ, Schirmer L, *et al.* Neurotoxic reactive astrocytes are induced by activated microglia. *Nature.* 2017 Jan 26;541(7638):481-487. doi: 10.1038/nature21029.
- Lin X, Ye H, Siaw-Debrah F, Pan S, He Z, Ni H, *et al.* AC-YVAD-CMK Inhibits Pyroptosis and Improves Functional Outcome after Intracerebral Hemorrhage. *Biomed Res Int.* 2018 Oct 16;2018:3706047. doi: 10.1155/2018/3706047.
- Liu J, Li Z, Ni J, Deng J, Cui G, Wang S, *et al.* Modeling Warfarin Associated Intracerebral Hemorrhage (ICH) in Cynomolgus Monkeys. *Blood.* 2014;124(21):2871-2871. doi: 10.1182/blood.V124.21.2871.2871.
- Liu P, Yuan J, Feng Y, Chen X, Wang G, Zhao L. Ferroptosis contributes to isoflurane-induced neurotoxicity and learning and memory impairment. *Cell Death Discov.* 2021 Apr 7;7(1):72. doi: 10.1038/s41420-021-00454-8.
- Liu T, Li X, Cui Y, Meng P, Zeng G, Wang Y, *et al.* Bioinformatics Analysis Identifies Potential Ferroptosis Key Genes in the Pathogenesis of Intracerebral Hemorrhage. *Front Neurosci.* 2021 Jun 7;15:661663. doi: 10.3389/fnins.2021.661663.
- Liu Y, Li Z, Khan S, Zhang R, Wei R, Zhang Y, *et al.* Neuroprotection of minocycline by inhibition of extracellular matrix metalloproteinase inducer expression following intracerebral hemorrhage in mice. *Neurosci Lett.* 2021 Nov 1;764:136297. doi: 10.1016/j.neulet.2021.136297.
- Lolansen SD, Rostgaard N, Barbuskaite D, Capion T, Olsen MH, Norager NH, *et al.* Posthemorrhagic hydrocephalus associates with elevated inflammation and CSF hypersecretion via activation of choroidal transporters. *Fluids Barriers CNS.* 2022 Aug 10;19(1):62. doi: 10.1186/s12987-022-00360-w.
- Lopez-Atalaya JP, Roussel BD, Levrat D, Parcq J, Nicole O, Hommet Y, *et al.* Toward safer thrombolytic agents in stroke: molecular requirements for NMDA receptor-mediated neurotoxicity. *J Cereb Blood Flow Metab.* 2008 Jun;28(6):1212-21. doi: 10.1038/jcbfm.2008.14.

- Lourbopoulos A, Mourouzis I, Xinaris C, Zerva N, Filippakis K, Pavlopoulos A, *et al.* Translational Block in Stroke: A Constructive and "Out-of-the-Box" Reappraisal. *Front Neurosci.* 2021 May 14;15:652403. doi: 10.3389/fnins.2021.652403.
- Lu F, Nakamura T, Okabe N, Himi N, Nakamura-Maruyama E, Shiromoto T, *et al.* COA-Cl, a Novel Synthesized Nucleoside Analog, Exerts Neuroprotective Effects in the Acute Phase of Intracerebral Hemorrhage. *J Stroke Cerebrovasc Dis.* 2016 Nov;25(11):2637-2643. doi: 10.1016/j.jstrokecerebrovasdis.2016.07.006.
- Lu J, Li Z, Zhao Q, Liu D, Mei YA. Neuritin improves the neurological functional recovery after experimental intracerebral hemorrhage in mice. *Neurobiol Dis.* 2021 Aug;156:105407. doi: 10.1016/j.nbd.2021.105407.
- Lu Z, Wang Z, Yu L, Ding Y, Xu Y, Xu N, *et al.* GCN2 reduces inflammation by p-eIF2 α /ATF4 pathway after intracerebral hemorrhage in mice. *Exp Neurol.* 2019 Mar;313:16-25. doi: 10.1016/j.expneurol.2018.12.004.
- Lummel N, Lutz J, Brückmann H, Linn J. The value of magnetic resonance imaging for the detection of the bleeding source in non-traumatic intracerebral haemorrhages: a comparison with conventional digital subtraction angiography. *Neuroradiology.* 2012 Jul;54(7):673-80. doi: 10.1007/s00234-011-0953-0.
- Lyden P, Brott T, Tilley B, Welch KM, Mascha EJ, Levine S, *et al.* Improved reliability of the NIH Stroke Scale using video training. NINDS TPA Stroke Study Group. *Stroke.* 1994 Nov;25(11):2220-6. doi: 10.1161/01.str.25.11.2220.
- Lyden P, Buchan A, Boltze J, Fisher M; STAIR XI Consortium*. Top Priorities for Cerebroprotective Studies-A Paradigm Shift: Report From STAIR XI. *Stroke.* 2021; 52:3063-3071. doi: 10.1161/STROKEAHA.121.034947
- Ma L, Hu X, Song L, Chen X, Ouyang M, Billot L, *et al.* The third Intensive Care Bundle with Blood Pressure Reduction in Acute Cerebral Haemorrhage Trial (INTERACT3): an international, stepped wedge cluster randomised controlled trial. *Lancet.* 2023 Jul 1;402(10395):27-40. doi: 10.1016/S0140-6736(23)00806-1. Epub 2023 May 25. Erratum in: *Lancet.* 2023 Jul 15;402(10397):184. doi: 10.1016/S0140-6736(23)01420-4.
- MacLellan CL, Auriat AM, McGie SC, Yan RH, Huynh HD, De Butte MF, *et al.* Gauging recovery after hemorrhagic stroke in rats: implications for cytoprotection studies. *J Cereb Blood Flow Metab.* 2006 Aug;26(8):1031-42. doi: 10.1038/sj.jcbfm.9600255.
- MacLellan CL, Silasi G, Poon CC, Edmundson CL, Buist R, Peeling J, *et al.* Intracerebral hemorrhage models in rat: comparing collagenase to blood infusion. *J Cereb Blood Flow Metab.* 2008 Mar;28(3):516-25. doi: 10.1038/sj.jcbfm.9600548.

- Magid-Bernstein J, Girard R, Polster S, Srinath A, Romanos S, Awad IA, *et al.* Cerebral Hemorrhage: Pathophysiology, Treatment, and Future Directions. *Circ Res*. 2022 Apr 15;130(8):1204-1229. doi: 10.1161/CIRCRESAHA.121.319949.
- Makey DG, Seal US. The detection of four molecular forms of human transferrin during the iron binding process. *Biochim Biophys Acta*. 1976 Nov 26;453(1):250-6. doi: 10.1016/0005-2795(76)90270-1.
- Mancini M, Greco A, Tedeschi E, Palma G, Ragucci M, Bruzzone MG, *et al.* Head and Neck Veins of the Mouse. A Magnetic Resonance, Micro Computed Tomography and High Frequency Color Doppler Ultrasound Study. *PLoS One*. 2015 Jun 11;10(6):e0129912. doi: 10.1371/journal.pone.0129912.
- Mao R, Zong N, Hu Y, Chen Y, Xu Y. Neuronal Death Mechanisms and Therapeutic Strategy in Ischemic Stroke. *Neurosci Bull*. 2022 Oct;38(10):1229-1247. doi: 10.1007/s12264-022-00859-0.
- Mao X, Liu J, Chen C, Zhang W, Qian R, Chen X, *et al.* PCBP2 Modulates Neural Apoptosis and Astrocyte Proliferation After Spinal Cord Injury. *Neurochem Res*. 2016 Sep;41(9):2401-14. doi: 10.1007/s11064-016-1953-6.
- Martin SS, Aday AW, Allen NB, Almarzooq ZI, Anderson CAM, Arora P, *et al.* 2025 Heart Disease and Stroke Statistics: A Report of US and Global Data From the American Heart Association. *Circulation*. 2025 Feb 25;151(8):e41-e660. doi: 10.1161/CIR.0000000000001303.
- Martini SR, Flaherty ML, Brown WM, Haverbusch M, Comeau ME, Sauerbeck LR, *et al.* Risk factors for intracerebral hemorrhage differ according to hemorrhage location. *Neurology*. 2012 Dec 4;79(23):2275-82. doi: 10.1212/WNL.0b013e318276896f.
- Masuda T, Maki M, Hara K, Yasuhara T, Matsukawa N, Yu S, *et al.* Peri-hemorrhagic degeneration accompanies stereotaxic collagenase-mediated cortical hemorrhage in mouse. *Brain Res*. 2010 Oct 8;1355:228-39. doi: 10.1016/j.brainres.2010.07.101.
- Matsushita H, Hijioka M, Hisatsune A, Isohama Y, Iwamoto S, Terasawa H, *et al.* MRI-based analysis of intracerebral hemorrhage in mice reveals relationship between hematoma expansion and the severity of symptoms. *PLoS One*. 2013;8(7):e67691. doi: 10.1371/journal.pone.0067691.
- Mayer SA, Brun NC, Begtrup K, Broderick J, Davis S, Diringer MN, *et al.* Efficacy and safety of recombinant activated factor VII for acute intracerebral hemorrhage. *N Engl J Med*. 2008 May 15;358(20):2127-37. doi: 10.1056/NEJMoa0707534.
- Mayer SA, Thomas CE, Diamond BE. Asymmetry of intracranial hemodynamics as an indicator of mass effect in acute intracerebral hemorrhage. A transcranial Doppler study. *Stroke*. 1996 Oct;27(10):1788-92. doi: 10.1161/01.str.27.10.1788.
- Mayfrank L, Kissler J, Raoofi R, Delsing P, Weis J, Küker W, *et al.* Ventricular dilatation in experimental intraventricular hemorrhage in pigs. Characterization of cerebrospinal fluid dynamics

and the effects of fibrinolytic treatment. *Stroke.* 1997 Jan;28(1):141-8. doi: 10.1161/01.str.28.1.141.

- Mehta A, Zusman BE, Shutter LA, Choxi R, Yassin A, Antony A, *et al.* The Prevalence and Impact of Status Epilepticus Secondary to Intracerebral Hemorrhage: Results from the US Nationwide Inpatient Sample. *Neurocrit Care.* 2018 Jun;28(3):353-361. doi: 10.1007/s12028-017-0489-1.
- Melià-Sorolla M, Castaño C, DeGregorio-Rocasolano N, Rodríguez-Esparragoza L, Dávalos A, Martí-Sistac O, *et al.* Relevance of Porcine Stroke Models to Bridge the Gap from Pre-Clinical Findings to Clinical Implementation. *Int J Mol Sci.* 2020 Sep 8;21(18):6568. doi: 10.3390/ijms21186568.
- Mendelow AD, Gregson BA, Fernandes HM, Murray GD, Teasdale GM, Hope DT, *et al.* Early surgery versus initial conservative treatment in patients with spontaneous supratentorial intracerebral haematomas in the International Surgical Trial in Intracerebral Haemorrhage (STICH): a randomised trial. *Lancet.* 2005 Jan 29-Feb 4;365(9457):387-97. doi: 10.1016/S0140-6736(05)17826-X.
- Mendelow AD, Gregson BA, Rowan EN, Murray GD, Ghokar A, Mitchell PM; *et al.* Early surgery versus initial conservative treatment in patients with spontaneous supratentorial lobar intracerebral haematomas (STICH II): a randomised trial. *Lancet.* 2013 Aug 3;382(9890):397-408. doi: 10.1016/S0140-6736(13)60986-1. Erratum in: *Lancet.* 2013 Aug 3;382(9890):396. Erratum in: *Lancet.* 2021 Sep 18;398(10305):1042. doi: 10.1016/S0140-6736(21)02012-2.
- Mengel A, Stefanou MI, Hadaschik KA, Wolf M, Stadler V, Poli K, *et al.* Early Administration of Desmopressin and Platelet Transfusion for Reducing Hematoma Expansion in Patients With Acute Antiplatelet Therapy Associated Intracerebral Hemorrhage. *Crit Care Med.* 2020 Jul;48(7):1009-1017. doi: 10.1097/CCM.0000000000004348.
- Middleton S, McElduff P, Ward J, Grimshaw JM, Dale S, D'Este C, *et al.* Implementation of evidence-based treatment protocols to manage fever, hyperglycaemia, and swallowing dysfunction in acute stroke (QASC): a cluster randomised controlled trial. *Lancet.* 2011 Nov 12;378(9804):1699-706. doi: 10.1016/S0140-6736(11)61485-2.
- Middleton S, Coughlan K, Mnatzaganian G, Low Choy N, Dale S, Jammali-Blasi A, *et al.* Mortality Reduction for Fever, Hyperglycemia, and Swallowing Nurse-Initiated Stroke Intervention: QASC Trial (Quality in Acute Stroke Care) Follow-Up. *Stroke.* 2017 May;48(5):1331-1336. doi: 10.1161/STROKEAHA.116.016038.
- Millán M, DeGregorio-Rocasolano N, Pérez de la Ossa N, Reverté S, Costa J, Giner P, *et al.* Targeting Pro-Oxidant Iron with Deferoxamine as a Treatment for Ischemic Stroke: Safety and

Optimal Dose Selection in a Randomized Clinical Trial. *Antioxidants (Basel)*. 2021 Aug 10;10(8):1270. doi: 10.3390/antiox10081270.

- Min H, Jang YH, Cho IH, Yu SW, Lee SJ. Alternatively activated brain-infiltrating macrophages facilitate recovery from collagenase-induced intracerebral hemorrhage. *Mol Brain*. 2016 Apr 19;9:42. doi: 10.1186/s13041-016-0225-3.
- Montaño A, Hanley DF, Hemphill JC 3rd. Hemorrhagic stroke. *Handb Clin Neurol*. 2021;176:229-248. doi: 10.1016/B978-0-444-64034-5.00019-5.
- Moullaali TJ, Wang X, Martin RH, Shipes VB, Robinson TG, Chalmers J, *et al.* Blood pressure control and clinical outcomes in acute intracerebral haemorrhage: a preplanned pooled analysis of individual participant data. *Lancet Neurol*. 2019 Sep;18(9):857-864. doi: 10.1016/S1474-4422(19)30196-6.
- Mrácsko E, Veltkamp R. Neuroinflammation after intracerebral hemorrhage. *Front Cell Neurosci*. 2014 Nov 20;8:388. doi: 10.3389/fncel.2014.00388.
- Mun-Bryce S, Wilkerson AC, Papuashvili N, Okada YC. Recurring episodes of spreading depression are spontaneously elicited by an intracerebral hemorrhage in the swine. *Brain Res*. 2001 Jan 12;888(2):248-255. doi: 10.1016/s0006-8993(00)03068-7.
- Munsch F, Sagnier S, Asselineau J, Bigourdan A, Guttmann CR, Debruxelles S, *et al.* Stroke Location Is an Independent Predictor of Cognitive Outcome. *Stroke*. 2016 Jan;47(1):66-73. doi: 10.1161/STROKEAHA.115.011242.
- Naderi Y, Panahi Y, Barreto GE, Sahebkar A. Neuroprotective effects of minocycline on focal cerebral ischemia injury: a systematic review. *Neural Regen Res*. 2020 May;15(5):773-782. doi: 10.4103/1673-5374.268898.
- Naff NJ, Hanley DF, Keyl PM, Tuhrim S, Kraut M, Bederson J, *et al.* Intraventricular thrombolysis speeds blood clot resolution: results of a pilot, prospective, randomized, double-blind, controlled trial. *Neurosurgery*. 2004 Mar;54(3):577-83; discussion 583-4. doi: 10.1227/01.neu.0000108422.10842.60.
- Nagaoka MH, Maitani T. Differed preferential iron-binding lobe in human transferrin depending on the presence of bicarbonate detected by HPLC/high-resolution inductively coupled plasma mass spectrometry. *Biochim Biophys Acta*. 2000 Oct 18;1523(2-3):182-8. doi: 10.1016/s0304-4165(00)00120-3.
- Nagatsuna T, Nomura S, Suehiro E, Fujisawa H, Koizumi H, Suzuki M. Systemic administration of argatroban reduces secondary brain damage in a rat model of intracerebral hemorrhage: histopathological assessment. *Cerebrovasc Dis*. 2005;19(3):192-200. doi: 10.1159/000083466.

References

- Nakamura T, Kuroda Y, Yamashita S, Zhang X, Miyamoto O, Tamiya T, *et al.* Edaravone attenuates brain edema and neurologic deficits in a rat model of acute intracerebral hemorrhage. *Stroke*. 2008 Feb;39(2):463-9. doi: 10.1161/STROKEAHA.107.486654.
- Navarrete-Navarro P, Hart WM, Lopez-Bastida J, Christensen MC. The societal costs of intracerebral hemorrhage in Spain. *Eur J Neurol*. 2007 May;14(5):556-62. doi: 10.1111/j.1468-1331.2007.01756.x.
- Ng WH, Yeo TT, Seow WT. Non-traumatic spontaneous acute epidural haematoma -- report of two cases and review of the literature. *J Clin Neurosci*. 2004 Sep;11(7):791-3. doi: 10.1016/j.jocn.2003.12.002.
- NICE-SUGAR Study Investigators; Finfer S, Chittock DR, Su SY, Blair D, Foster D, *et al.* Intensive versus conventional glucose control in critically ill patients. *N Engl J Med*. 2009 Mar 26;360(13):1283-97. doi: 10.1056/NEJMoa0810625.
- Nicole O, Docagne F, Ali C, Margaill I, Carmeliet P, MacKenzie ET, *et al.* The proteolytic activity of tissue-plasminogen activator enhances NMDA receptor-mediated signaling. *Nat Med*. 2001 Jan;7(1):59-64. doi: 10.1038/83358.
- Ni W, Mao S, Xi G, Keep RF, Hua Y. Role of Erythrocyte CD47 in Intracerebral Hematoma Clearance. *Stroke*. 2016 Feb;47(2):505-11. doi: 10.1161/STROKEAHA.115.010920.
- O'Donnell MJ, Xavier D, Liu L, Zhang H, Chin SL, Rao-Melacini P, *et al.* Risk factors for ischaemic and intracerebral haemorrhagic stroke in 22 countries (the INTERSTROKE study): a case-control study. *Lancet*. 2010 Jul 10;376(9735):112-23. doi: 10.1016/S0140-6736(10)60834-3.
- O'Donnell MJ, Chin SL, Rangarajan S, Xavier D, Liu L, Zhang H, *et al.* Global and regional effects of potentially modifiable risk factors associated with acute stroke in 32 countries (INTERSTROKE): a case-control study. *Lancet*. 2016 Aug 20;388(10046):761-75. doi: 10.1016/S0140-6736(16)30506-2.
- Oddo M, Schmidt JM, Carrera E, Badjatia N, Connolly ES, Presciutti M, *et al.* Impact of tight glycemic control on cerebral glucose metabolism after severe brain injury: a microdialysis study. *Crit Care Med*. 2008 Dec;36(12):3233-8. doi: 10.1097/CCM.0b013e31818f4026.
- Ogata J, Fujishima M, Tamaki K, Nakatomi Y, Ishitsuka T, Omae T. Stroke-prone spontaneously hypertensive rats as an experimental model of malignant hypertension. A pathological study. *Virchows Arch A Pathol Anat Histol*. 1982;394(3):185-94. doi: 10.1007/BF00430664.
- Oge DD, Arsava EM, Pektezel MY, Gocmen R, Topcuoglu MA. Intracerebral hemorrhage volume estimation: Is modification of the ABC/2 formula necessary according to the hematoma shape? *Clin Neurol Neurosurg*. 2021 Aug;207:106779. doi: 10.1016/j.clineuro.2021.106779.

- Ohashi SN, DeLong JH, Kozberg MG, Mazur-Hart DJ, van Veluw SJ, Alkayed NJ, *et al.* Role of Inflammatory Processes in Hemorrhagic Stroke. *Stroke*. 2023 Feb;54(2):605-619. doi: 10.1161/STROKEAHA.122.037155.
- Ohnishi M, Kai T, Shimizu Y, Yano Y, Urabe Y, Tasaka S, *et al.* Gadolinium causes M1 and M2 microglial apoptosis after intracerebral haemorrhage and exerts acute neuroprotective effects. *J Pharm Pharmacol*. 2020 May;72(5):709-718. doi: 10.1111/jphp.13235.
- Ohnishi M, Katsuki H, Fujimoto S, Takagi M, Kume T, Akaike A. Involvement of thrombin and mitogen-activated protein kinase pathways in hemorrhagic brain injury. *Exp Neurol*. 2007 Jul;206(1):43-52. doi: 10.1016/j.expneurol.2007.03.030.
- Okauchi M, Hua Y, Keep RF, Morgenstern LB, Schallert T, Xi G. Deferoxamine treatment for intracerebral hemorrhage in aged rats: therapeutic time window and optimal duration. *Stroke*. 2010 Feb;41(2):375-82. doi: 10.1161/STROKEAHA.109.569830.
- Okuyama S, Okuyama J, Okuyama J, Tamatsu Y, Shimada K, Hoshi H, *et al.* The arterial circle of Willis of the mouse helps to decipher secrets of cerebral vascular accidents in the human. *Med Hypotheses*. 2004;63(6):997-1009. doi: 10.1016/j.mehy.2003.12.055.
- O'Neill N, Mah KM, Badillo-Martinez A, Jann V, Bixby JL, Lemmon VP. Markerless tracking enables distinction between strategic compensation and functional recovery after spinal cord injury. *Exp Neurol*. 2022; 354:114085. doi: 10.1016/j.expneurol.2022.114085.
- Papanagiotou P, Ntaios G. Endovascular Thrombectomy in Acute Ischemic Stroke. *Circ Cardiovasc Interv*. 2018 Jan;11(1):e005362. doi: 10.1161/CIRCINTERVENTIONS.117.005362.
- Parcq J, Bertrand T, Baron AF, Hommet Y, Anglès-Cano E, Vivien D. Molecular requirements for safer generation of thrombolytics by bioengineering the tissue-type plasminogen activator A chain. *J Thromb Haemost*. 2013 Mar;11(3):539-46. doi: 10.1111/jth.12128.
- Parry-Jones AR, Sammut-Powell C, Paroutoglou K, Birleson E, Rowland J, Lee S, *et al.* An Intracerebral Hemorrhage Care Bundle Is Associated with Lower Case Fatality. *Ann Neurol*. 2019 Oct;86(4):495-503. doi: 10.1002/ana.25546.
- Parry-Jones AR, Stocking K, MacLeod MJ, Clarke B, Werring DJ, Muir KW, *et al.* Phase II randomised, placebo-controlled, clinical trial of interleukin-1 receptor antagonist in intracerebral haemorrhage: BLOCking the Cytokine IL-1 in ICH (BLOC-ICH). *Eur Stroke J*. 2023 Sep;8(3):819-827. doi: 10.1177/23969873231185208.
- Pasarikovski CR, Ku JC, Keith J, Ramjist J, Dobashi Y, Priola SM, *et al.* Mechanical thrombectomy and intravascular imaging for cerebral venous sinus thrombosis: a preclinical model. *J Neurosurg*. 2020 Oct 30;135(2):425-430. doi: 10.3171/2020.6.JNS201795.

References

- Passero S, Rocchi R, Rossi S, Ulivelli M, Vatti G. Seizures after spontaneous supratentorial intracerebral hemorrhage. *Epilepsia*. 2002 Oct;43(10):1175-80. doi: 10.1046/j.1528-1157.2002.00302.x.
- Peeling J, Del Bigio MR, Corbett D, Green AR, Jackson DM. Efficacy of disodium 4-[(tert-butylimino)methyl]benzene-1,3-disulfonate N-oxide (NXY-059), a free radical trapping agent, in a rat model of hemorrhagic stroke. *Neuropharmacology*. 2001 Mar;40(3):433-9. doi: 10.1016/s0028-3908(00)00170-2.
- Pensato U, Tanaka K, Ospel JM, Aviv RI, Rodriguez-Luna D, Hill MD, *et al.* Validation of the Black-&-White sign to predict intracerebral hematoma expansion in the multi-center PREDICT study cohort. *Int J Stroke*. 2025 Jul;20(6):721-730. doi: 10.1177/17474930241307466.
- Perleberg C, Kind A, Schnieke A. Genetically engineered pigs as models for human disease. *Dis Model Mech*. 2018 Jan 22;11(1):dmm030783. doi: 10.1242/dmm.030783.
- Perluigi M, Coccia R, Butterfield DA. 4-Hydroxy-2-nonenal, a reactive product of lipid peroxidation, and neurodegenerative diseases: a toxic combination illuminated by redox proteomics studies. *Antioxid Redox Signal*. 2012 Dec 1;17(11):1590-609. doi: 10.1089/ars.2011.4406.
- Polymeris AA, Karwacki GM, Siepen BM, Schaedelin S, Tsakiris DA, Stippich C, *et al.* Tranexamic Acid for Intracerebral Hemorrhage in Patients on Non-Vitamin K Antagonist Oral Anticoagulants (TICH-NOAC): A Multicenter, Randomized, Placebo-Controlled, Phase 2 Trial. *Stroke*. 2023 Sep;54(9):2223-2234. doi: 10.1161/STROKEAHA.123.042866.
- Poon MT, Bell SM, Al-Shahi Salman R. Epidemiology of Intracerebral Haemorrhage. *Front Neurol Neurosci*. 2015;37:1-12. doi: 10.1159/000437109.
- Pradilla G, Ratcliff JJ, Hall AJ, Saville BR, Allen JW, Paulon G, *et al.* Trial of Early Minimally Invasive Removal of Intracerebral Hemorrhage. *N Engl J Med*. 2024 Apr 11;390(14):1277-1289. doi: 10.1056/NEJMoa2308440.
- Prendes CF, Rantner B, Hamwi T, Stana J, Feigin VL, Stavroulakis K, *et al.* Burden of Stroke in Europe: An Analysis of the Global Burden of Disease Study Findings From 2010 to 2019. *Stroke*. 2024 Feb;55(2):432-442. doi: 10.1161/STROKEAHA.122.042022.
- Purroy F, Montalà N. Epidemiology of stroke in the last decade: a systematic review. *Rev Neurol*. 2021 Nov 1;73(9):321-336. English, Spanish. doi: 10.33588/rn.7309.2021138.
- Qian B, Rudy RF, Cai T, Du R. Cerebral Artery Diameter in Inbred Mice Varies as a Function of Strain. *Front Neuroanat*. 2018 Feb 20;12:10. doi: 10.3389/fnana.2018.00010.
- Qiu Z, Yang J, Deng G, Fang Y, Li D, Zhang S. Angiopoietin-Like 4 Attenuates Brain Edema and Neurological Deficits in a Mouse Model of Experimental Intracerebral Hemorrhage. *Med Sci Monit*. 2018 Feb 12;24:880-890. doi: 10.12659/msm.907939.

- Qureshi AI, Safdar K, Weil J, Barch C, Blwise DL, Colohan AR, *et al.* Predictors of early deterioration and mortality in black Americans with spontaneous intracerebral hemorrhage. *Stroke*. 1995 Oct;26(10):1764-7. doi: 10.1161/01.str.26.10.1764.
- Qureshi AI, Tuhrim S, Broderick JP, Batjer HH, Hondo H, Hanley DF. Spontaneous intracerebral hemorrhage. *N Engl J Med*. 2001 May 10;344(19):1450-60. doi: 10.1056/NEJM200105103441907.
- Qureshi AI, Ali Z, Suri MF, Shuaib A, Baker G, Todd K, *et al.* Extracellular glutamate and other amino acids in experimental intracerebral hemorrhage: an *in vivo* microdialysis study. *Crit Care Med*. 2003 May;31(5):1482-9. doi: 10.1097/01.CCM.0000063047.63862.99.
- Qureshi AI, Palesch YY, Foster LD, Barsan WG, Goldstein JN, Hanley DF, *et al.* Blood Pressure-Attained Analysis of ATACH 2 Trial. *Stroke*. 2018 Jun;49(6):1412-1418. doi: 10.1161/STROKEAHA.117.019845.
- Qureshi AI, Mendelow AD, Hanley DF. Intracerebral haemorrhage. *Lancet*. 2009 May 9;373(9675):1632-44. doi: 10.1016/S0140-6736(09)60371-8.
- Rahman MS, Yang J, Luan Y, Qiu Z, Zhang J, Lu H, *et al.* Attenuation of Acute Intracerebral Hemorrhage-Induced Microglial Activation and Neuronal Death Mediated by the Blockade of Metabotropic Glutamate Receptor 5 *In Vivo*. *Neurochem Res*. 2020 May;45(5):1230-1243. doi: 10.1007/s11064-020-03006-1.
- Renner S, Fehlings C, Herbach N, Hofmann A, von Waldthausen DC, Kessler B, *et al.* Glucose intolerance and reduced proliferation of pancreatic beta-cells in transgenic pigs with impaired glucose-dependent insulinotropic polypeptide function. *Diabetes*. 2010 May;59(5):1228-38. doi: 10.2337/db09-0519.
- Rindler RS, Allen JW, Barrow JW, Pradilla G, Barrow DL. Neuroimaging of Intracerebral Hemorrhage. *Neurosurgery*. 2020 May 1;86(5):E414-E423. doi: 10.1093/neuros/nyaa029.
- Rink C, Christoforidis G, Abduljalil A, Kontzialis M, Bergdall V, Roy S, *et al.* Minimally invasive neuroradiologic model of preclinical transient middle cerebral artery occlusion in canines. *Proc Natl Acad Sci U S A*. 2008 Sep 16;105(37):14100-5. doi: 10.1073/pnas.0806678105.
- Rodríguez JA, Sobrino T, López-Arias E, Ugarte A, Sánchez-Arias JA, Vieites-Prado A, de Miguel I, Oyarzabal J, Páramo JA, Campos F, *et al.* CM352 Reduces Brain Damage and Improves Functional Recovery in a Rat Model of Intracerebral Hemorrhage. *J Am Heart Assoc*. 2017 Jun 1;6(6):e006042. doi: 10.1161/JAHA.117.006042.
- Rodríguez-Yáñez M, Brea D, Arias S, Blanco M, Pumar JM, Castillo J, *et al.* Increased expression of Toll-like receptors 2 and 4 is associated with poor outcome in intracerebral hemorrhage. *J Neuroimmunol*. 2012 Jun 15;247(1-2):75-80. doi: 10.1016/j.jneuroim.2012.03.019.

References

- Roh DJ, Asonye IS, Carvalho Poyraz F, Magid-Bernstein JR, Joiner EF, Avadhani R, *et al.* Intra-ventricular Hemorrhage Expansion in the CLEAR III Trial: A Post Hoc Exploratory Analysis. *Stroke*. 2022 Jun;53(6):1847-1853. doi: 10.1161/STROKEAHA.121.037438.
- Rohde V, Rohde I, Thiex R, Ince A, Jung A, Dückers G, *et al.* Fibrinolysis therapy achieved with tissue plasminogen activator and aspiration of the liquefied clot after experimental intracerebral hemorrhage: rapid reduction in hematoma volume but intensification of delayed edema formation. *J Neurosurg*. 2002 Oct;97(4):954-62. doi: 10.3171/jns.2002.97.4.0954.
- Rohde V, Rohde I, Thiex R, Küker W, Ince A, Gilsbach JM. The role of intraoperative magnetic resonance imaging for the detection of hemorrhagic complications during surgery for intracerebral lesions an experimental approach. *Surg Neurol*. 2001 Oct;56(4):266-74; discussion 274-5. doi: 10.1016/s0090-3019(01)00594-8.
- Ruan J, Yao Y. Behavioral tests in rodent models of stroke. *Brain Hemorrhages*. 2020 Dec;1(4):171-184. doi: 10.1016/j.hest.2020.09.001.
- Ruff IM, de Havenon A, Bergman DL, Dugue R, Frontera JA, Goldstein JN, *et al.* 2024 AHA/ASA Performance and Quality Measures for Spontaneous Intracerebral Hemorrhage: A Report From the American Heart Association/American Stroke Association. *Stroke*. 2024 Jul;55(7):e199-e230. doi: 10.1161/STR.0000000000000464.
- Ruiz-Vitte A, Gutiérrez-Fernández M, Laso-García F, Piniella D, Gómez-de Frutos MC, Díez-Tejedor E, *et al.* Ledged Beam Walking Test Automatic Tracker: Artificial intelligence-based functional evaluation in a stroke model. *Comput Biol Med*. 2025; 186:109689. doi: 10.1016/j.compbio-med.2025.109689.
- Sacco RL, Kasner SE, Broderick JP, Caplan LR, Connors JJ, Culebras A, *et al.* An updated definition of stroke for the 21st century: a statement for healthcare professionals from the American Heart Association/American Stroke Association. *Stroke*. 2013 Jul;44(7):2064-89. doi: 10.1161/STR.0b013e318296aeca. Erratum in: *Stroke*. 2019 Aug;50(8):e239. doi: 10.1161/STR.000000000000205.
- Sadeghi F, Kovács S, Zsóri KS, Csiki Z, Bereczky Z, Shemirani AH. Platelet count and mean volume in acute stroke: a systematic review and meta-analysis. *Platelets*. 2020 Aug 17;31(6):731-739. doi: 10.1080/09537104.2019.1680826.
- Sallinen H, Pietilä A, Salomaa V, Strbian D. Risk Factors of Intracerebral Hemorrhage: A Case-Control Study. *J Stroke Cerebrovasc Dis*. 2020 Apr;29(4):104630. doi: 10.1016/j.jstrokecerebro-vasdis.2019.104630.
- Scaggiante J, Zhang X, Mocco J, Kellner CP. Minimally Invasive Surgery for Intracerebral Hemorrhage. *Stroke*. 2018 Nov;49(11):2612-2620. doi: 10.1161/STROKEAHA.118.020688.

- Schaar KL, Brenneman MM, Savitz SI. Functional assessments in the rodent stroke model. *Exp Transl Stroke Med.* 2010 Jul 19;2(1):13. doi: 10.1186/2040-7378-2-13.
- Scheulin KM, Jurgielewicz BJ, Spellacy SE, Waters ES, Baker EW, Kinder HA, *et al.* Exploring the predictive value of lesion topology on motor function outcomes in a porcine ischemic stroke model. *Sci Rep.* 2021 Feb 15;11(1):3814. doi: 10.1038/s41598-021-83432-5.
- Schmidt KJ, Sager B, Zachariah J, Raad BF, James EG, Fletcher JJ. Cohort analysis of desmopressin effect on hematoma expansion in patients with spontaneous intracerebral hemorrhage and documented pre-ictus antiplatelet use. *J Clin Neurosci.* 2019 Aug;66:33-37. doi: 10.1016/j.jocn.2019.05.032.
- Schreibman DL, Hong CM, Keledjian K, Ivanova S, Tsymbalyuk S, Gerzanich V, *et al.* Mannitol and Hypertonic Saline Reduce Swelling and Modulate Inflammatory Markers in a Rat Model of Intracerebral Hemorrhage. *Neurocrit Care.* 2018 Oct;29(2):253-263. doi: 10.1007/s12028-018-0535-7.
- Schutta HS, Howe HM. Seventeenth century concepts of "apoplexy" as reflected in Bonet's "Sepulchretum". *J Hist Neurosci.* 2006 Sep;15(3):250-68. doi: 10.1080/09647040500403312.
- Seddighi R, Doherty TJ. Field Sedation and Anesthesia of Ruminants. *Vet Clin North Am Food Anim Pract.* 2016 Nov;32(3):553-570. doi: 10.1016/j.cvfa.2016.05.002.
- Segal AZ, Chiu RI, Eggleston-Sexton PM, Beiser A, Greenberg SM. Low cholesterol as a risk factor for primary intracerebral hemorrhage: A case-control study. *Neuroepidemiology.* 1999;18(4):185-93. doi: 10.1159/000026210.
- Seki S, Kamide T, Tamase A, Mori K, Yanagimoto K, Nomura M. Subarachnoid and intracerebral hemorrhage from intracranial hemangiopericytoma: An uncommon cause of intracranial hemorrhage. *Neuroradiol J.* 2016 Jun;29(3):183-6. doi: 10.1177/1971400916638352.
- Selim M, Foster LD, Moy CS, Xi G, Hill MD, Morgenstern LB, *et al.* Deferoxamine mesylate in patients with intracerebral haemorrhage (i-DEF): a multicentre, randomised, placebo-controlled, double-blind phase 2 trial. *Lancet Neurol.* 2019 May;18(5):428-438. doi: 10.1016/S1474-4422(19)30069-9.
- Seyfried DM, Han Y, Yang D, Ding J, Shen LH, Savant-Bhonsale S, *et al.* Localization of bone marrow stromal cells to the injury site after intracerebral hemorrhage in rats. *J Neurosurg.* 2010 Feb;112(2):329-35. doi: 10.3171/2009.2.JNS08907.
- Shao Z, Tu S, Shao A. Pathophysiological Mechanisms and Potential Therapeutic Targets in Intracerebral Hemorrhage. *Front Pharmacol.* 2019 Sep 19;10:1079. doi: 10.3389/fphar.2019.01079.
- Sheth KN. Spontaneous Intracerebral Hemorrhage. *N Engl J Med.* 2022 Oct 27;387(17):1589-1596. doi: 10.1056/NEJMra2201449. Erratum in: *N Engl J Med.* 2023 Apr 13;388(15):1440. doi: 10.1056/NEJMx230001.

- Shoamanesh A, Patrice Lindsay M, Castellucci LA, Cayley A, Crowther M, de Wit K, *et al.* Canadian stroke best practice recommendations: Management of Spontaneous Intracerebral Hemorrhage, 7th Edition Update 2020. *Int J Stroke.* 2021 Apr;16(3):321-341. doi: 10.1177/1747493020968424.
- Skrobot M, De Sa J, Walter J, Vogt A, Paulat R, Lips J, *et al.* Refined movement analysis in the staircase test reveals differential motor deficits in mouse models of stroke. *J Cereb Blood Flow Metab.* 2024; 44(9):1551-1564. doi: 10.1177/0271678X241254718.
- da Silva-Candal A, Vieites-Prado A, Gutiérrez-Fernández M, Rey RI, Argibay B, Mirelman D, *et al.* Blood glutamate grabbing does not reduce the hematoma in an intracerebral hemorrhage model but it is a safe excitotoxic treatment modality. *J Cereb Blood Flow Metab.* 2015 Jul;35(7):1206-12. doi: 10.1038/jcbfm.2015.28.
- Sinar EJ, Mendelow AD, Graham DI, Teasdale GM. Experimental intracerebral hemorrhage: effects of a temporary mass lesion. *J Neurosurg.* 1987 Apr;66(4):568-76. doi: 10.3171/jns.1987.66.4.0568.
- Singh SD, Brouwers HB, Senff JR, Pasi M, Goldstein J, Viswanathan A, *et al.* Haematoma evacuation in cerebellar intracerebral haemorrhage: systematic review. *J Neurol Neurosurg Psychiatry.* 2020 Jan;91(1):82-87. doi: 10.1136/jnnp-2019-321461.
- Slijkhuis N, Razzi F, Korteland SA, Heijs B, van Gaalen K, Duncker DJ, *et al.* Spatial lipidomics of coronary atherosclerotic plaque development in a familial hypercholesterolemia swine model. *J Lipid Res.* 2024 Feb;65(2):100504. doi: 10.1016/j.jlr.2024.100504.
- Smiley ST, King JA, Hancock WW. Fibrinogen stimulates macrophage chemokine secretion through toll-like receptor 4. *J Immunol.* 2001 Sep 1;167(5):2887-94. doi: 10.4049/jimmunol.167.5.2887.
- Smith EE, Shobha N, Dai D, Olson DM, Reeves MJ, Saver JL, *et al.* A risk score for in-hospital death in patients admitted with ischemic or hemorrhagic stroke. *J Am Heart Assoc.* 2013 Jan 28;2(1):e005207. doi: 10.1161/JAHA.112.005207.
- Sondag L, Schreuder FHBM, Boogaarts HD, Rovers MM, Vandertop WP, Dammers R, *et al.* Neurosurgical Intervention for Supratentorial Intracerebral Hemorrhage. *Ann Neurol.* 2020 Aug;88(2):239-250. doi: 10.1002/ana.25732.
- Sosa PM, de Souza MA, Mello-Carpes PB. Green Tea and Red Tea from *Camellia sinensis* Partially Prevented the Motor Deficits and Striatal Oxidative Damage Induced by Hemorrhagic Stroke in Rats. *Neural Plast.* 2018 Aug 2;2018:5158724. doi: 10.1155/2018/5158724.
- Souza AS, Jansen J, Tempelman RJ, Mendl M, Zanella AJ. A novel method for testing social recognition in young pigs and the modulating effects of relocation. *Appl Anim Behav Sci.* 2006;99(1-2):77-87. doi: 10.1016/J.APPLANIM.2005.09.008

- Spellicy SE, Kaiser EE, Bowler MM, Jurgielewicz BJ, Webb RL, West FD, *et al.* Neural Stem Cell Extracellular Vesicles Disrupt Midline Shift Predictive Outcomes in Porcine Ischemic Stroke Model. *Transl Stroke Res.* 2020 Aug;11(4):776-788. doi: 10.1007/s12975-019-00753-4.
- Storey CE, Pols H. Chapter 27: a history of cerebrovascular disease. *Handb Clin Neurol.* 2010;95:401-15. doi: 10.1016/S0072-9752(08)02127-1.
- Stroke Therapy Academic Industry Roundtable (STAIR). Recommendations for standards regarding preclinical neuroprotective and restorative drug development. *Stroke.* 1999 Dec;30(12):2752-8. doi: 10.1161/01.str.30.12.2752.
- Sturgeon JD, Folsom AR, Longstreth WT Jr, Shahar E, Rosamond WD, Cushman M. Risk factors for intracerebral hemorrhage in a pooled prospective study. *Stroke.* 2007 Oct;38(10):2718-25. doi: 10.1161/STROKEAHA.107.487090.
- Sukumari-Ramesh S, Alleyne CH Jr. Post-Injury Administration of Tert-butylhydroquinone Attenuates Acute Neurological Injury After Intracerebral Hemorrhage in Mice. *J Mol Neurosci.* 2016 Apr;58(4):525-31. doi: 10.1007/s12031-016-0722-y.
- Sun W, Reeves W, Fagan MM, Welch CB, Scheulin KM, Snead SE, *et al.* Evaluation of Brain Function Recovery After Traumatic Brain Injury Treatment in a Porcine Model by Cross-Group Temporal-Spatial Correlation Analysis. *Neurotrauma Rep.* 2024 Jul 1;5(1):617-627. doi: 10.1089/neur.2023.0059.
- Sun Y, Zhou D, Liu A, Zhou Y, Zhao Y, Yuan Y, *et al.* Liangxue Tongyu Prescription exerts neuroprotection by regulating the microbiota-gut-brain axis of rats with acute intracerebral hemorrhage. *Brain Res Bull.* 2025 Jan;220:111186. doi: 10.1016/j.brainresbull.2024.111186.
- Taha A, Bobi J, Dammers R, Dijkhuizen RM, Dreyer AY, van Es ACGM, *et al.* Comparison of Large Animal Models for Acute Ischemic Stroke: Which Model to Use? *Stroke.* 2022 Apr;53(4):1411-1422. doi: 10.1161/STROKEAHA.121.036050.
- Tan Q, Guo P, Zhou J, Zhang J, Zhang B, Lan C, *et al.* Targeting neutrophil extracellular traps enhanced tPA fibrinolysis for experimental intracerebral hemorrhage. *Transl Res.* 2019 Sep;211:139-146. doi: 10.1016/j.trsl.2019.04.009.
- Tanaka H, Kobayashi E. Education and research using experimental pigs in a medical school. *J Artif Organs.* 2006;9(3):136-43. doi: 10.1007/s10047-006-0343-2.
- Tang LJ, Zhou YJ, Xiong XM, Li NS, Zhang JJ, Luo XJ, *et al.* Ubiquitin-specific protease 7 promotes ferroptosis via activation of the p53/TfR1 pathway in the rat hearts after ischemia/reperfusion. *Free Radic Biol Med.* 2021 Jan;162:339-352. doi: 10.1016/j.freeradbiomed.2020.10.307.

References

- Tang X, Zhang Z, Fang M, Han Y, Wang G, Wang S, *et al.* Transferrin plays a central role in coagulation balance by interacting with clotting factors. *Cell Res.* 2020 Feb;30(2):119-132. doi: 10.1038/s41422-019-0260-6.
- Tang X, Fang M, Cheng R, Zhang Z, Wang Y, Shen C, *et al.* Iron-Deficiency and Estrogen Are Associated With Ischemic Stroke by Up-Regulating Transferrin to Induce Hypercoagulability. *Circ Res.* 2020 Aug 14;127(5):651-663. doi: 10.1161/CIRCRESAHA.119.316453.
- Tao C, Li Y, An N, Liu H, Liu Z, Sun Y, *et al.* Pathological mechanisms and future therapeutic directions of thrombin in intracerebral hemorrhage: a systematic review. *Front Pharmacol.* 2024 Apr 18;15:1293428. doi: 10.3389/fphar.2024.1293428.
- Tarzami ST, Wang G, Li W, Green L, Singh JP. Thrombin and PAR-1 stimulate differentiation of bone marrow-derived endothelial progenitor cells. *J Thromb Haemost.* 2006 Mar;4(3):656-63. doi: 10.1111/j.1538-7836.2006.01788.x.
- Teasdale G, Murray G, Parker L, Jennett B. Adding up the Glasgow Coma Score. *Acta Neurochir Suppl (Wien)*. 1979;28(1):13-6. doi: 10.1007/978-3-7091-4088-8_2.
- Tejada Meza H, Artal Roy J, Pérez Lázaro C, Bestué Cardiel M, Alberti González O, Tejero Juste C, *et al.* Epidemiology and characteristics of ischaemic stroke in young adults in Aragon. *Neurologia (Engl Ed)*. 2022 Jul-Aug;37(6):434-440. English, Spanish. doi: 10.1016/j.nrl.2019.05.008.
- Teng W, Wang L, Xue W, Guan C. Activation of TLR4-mediated NF κ B signaling in hemorrhagic brain in rats. *Mediators Inflamm.* 2009;2009:473276. doi: 10.1155/2009/473276.
- Tsopanoglou NE, Maragoudakis ME. Inhibition of angiogenesis by small-molecule antagonists of protease-activated receptor-1. *Semin Thromb Hemost.* 2007 Oct;33(7):680-7. doi: 10.1055/s-2007-991535.
- Venkatasubramanian C, Mlynash M, Finley-Caulfield A, Eyngorn I, Kalimuthu R, Snider RW, *et al.* Natural history of perihematomal edema after intracerebral hemorrhage measured by serial magnetic resonance imaging. *Stroke.* 2011 Jan;42(1):73-80. doi: 10.1161/STROKEAHA.110.590646.
- Vespa PM, O'Phelan K, Shah M, Mirabelli J, Starkman S, Kidwell C, *et al.* Acute seizures after intracerebral hemorrhage: a factor in progressive midline shift and outcome. *Neurology.* 2003 May 13;60(9):1441-6. doi: 10.1212/01.wnl.0000063316.47591.b4.
- Vigneswara V, Ahmed Z. The Role of Caspase-2 in Regulating Cell Fate. *Cells.* 2020 May 19;9(5):1259. doi: 10.3390/cells9051259.
- Vrselja Z, Brkic H, Mrdenovic S, Radic R, Curic G. Function of circle of Willis. *J Cereb Blood Flow Metab.* 2014 Apr;34(4):578-84. doi: 10.1038/jcbfm.2014.7.

- Wagner KR, Xi G, Hua Y, Kleinholz M, de Courten-Myers GM, Myers RE, *et al.* Lobar intracerebral hemorrhage model in pigs: rapid edema development in perihematomal white matter. *Stroke*. 1996 Mar;27(3):490-7. doi: 10.1161/01.str.27.3.490.
- Wakisaka Y, Chu Y, Miller JD, Rosenberg GA, Heistad DD. Spontaneous intracerebral hemorrhage during acute and chronic hypertension in mice. *J Cereb Blood Flow Metab*. 2010 Jan;30(1):56-69. doi: 10.1038/jcbfm.2009.183.
- Wan J, Ren H, Wang J. Iron toxicity, lipid peroxidation and ferroptosis after intracerebral haemorrhage. *Stroke Vasc Neurol*. 2019 Jan 13;4(2):93-95. doi: 10.1136/svn-2018-000205.
- Wan S, Cheng Y, Jin H, Guo D, Hua Y, Keep RF, *et al.* Microglia Activation and Polarization After Intracerebral Hemorrhage in Mice: the Role of Protease-Activated Receptor-1. *Transl Stroke Res*. 2016 Dec;7(6):478-487. doi: 10.1007/s12975-016-0472-8.
- Wan Y, Holste KG, Hua Y, Keep RF, Xi G. Brain edema formation and therapy after intracerebral hemorrhage. *Neurobiol Dis*. 2023 Jan;176:105948. doi: 10.1016/j.nbd.2022.105948.
- Wang G, Hu W, Tang Q, Wang L, Sun XG, Chen Y, *et al.* Effect Comparison of Both Iron Chelators on Outcomes, Iron Deposit, and Iron Transporters After Intracerebral Hemorrhage in Rats. *Mol Neurobiol*. 2016 Aug;53(6):3576-3585. doi: 10.1007/s12035-015-9302-3.
- Wang J. Preclinical and clinical research on inflammation after intracerebral hemorrhage. *Prog Neurobiol*. 2010 Dec;92(4):463-77. doi: 10.1016/j.pneurobio.2010.08.001.
- Wang J, Tan HQ, Li MH, Sun XJ, Fu CM, Zhu YQ, *et al.* Development of a new model of transvenous thrombosis in the pig superior sagittal sinus using thrombin injection and balloon occlusion. *J Neuroradiol*. 2010 May;37(2):109-15. doi: 10.1016/j.neurad.2009.06.002.
- Wang YX, Yan A, Ma ZH, Wang Z, Zhang B, Ping JL, *et al.* Nuclear factor- κ B and apoptosis in patients with intracerebral hemorrhage. *J Clin Neurosci*. 2011 Oct;18(10):1392-5. doi: 10.1016/j.jocn.2010.11.039.
- Watanabe H, Sakoh M, Andersen F, Rodell A, Sørensen JC, Østergaard L, *et al.* Statistical mapping of effects of middle cerebral artery occlusion (MCAO) on blood flow and oxygen consumption in porcine brain. *J Neurosci Methods*. 2007 Feb 15;160(1):109-15. doi: 10.1016/j.jneumeth.2006.08.016.
- Weber RZ, Mulders G, Kaiser J, Tackenberg C, Rust R. Deep learning-based behavioral profiling of rodent stroke recovery. *BMC Biol*. 2022; 20:232. doi: 10.1186/s12915-022-01434-9.
- Wei J, Zhang W, Li J, Jin Y, Qiu Z. Application of the transgenic pig model in biomedical research: A review. *Front Cell Dev Biol*. 2022 Oct 17;10:1031812. doi: 10.3389/fcell.2022.1031812.
- Wei J, Tang X, Liu J, Zhang Z. Detection of Pig Movement and Aggression Using Deep Learning Approaches. *Animals (Basel)*. 2023 Sep 30;13(19):3074. doi: 10.3390/ani13193074.

References

- Wenbo Z, Wu C, Song H, Duan J, Ma Q, Li S, *et al.* Abstract 48: Effect of Remote Ischemic Conditioning on Functional Outcomes in Patients With Supratentorial Intracerebral Hemorrhage: The Final Results of RICH-2 Randomized Controlled Clinical Trial. *Stroke*. 2025;56(Suppl_1). doi: 10.1161/str.56.suppl_1.48.
- Whitelaw A. Periventricular hemorrhage: a problem still today. *Early Hum Dev*. 2012 Dec;88(12):965-9. doi: 10.1016/j.earlhumdev.2012.09.004.
- Williamson MR, Wilkinson CM, Dietrich K, Colbourne F. Acetazolamide Mitigates Intracranial Pressure Spikes Without Affecting Functional Outcome After Experimental Hemorrhagic Stroke. *Transl Stroke Res*. 2019 Aug;10(4):428-439. doi: 10.1007/s12975-018-0663-6.
- Williamson MR, Colbourne F. Evidence for Decreased Brain Parenchymal Volume After Large Intracerebral Hemorrhages: a Potential Mechanism Limiting Intracranial Pressure Rises. *Transl Stroke Res*. 2017 Aug;8(4):386-396. doi: 10.1007/s12975-017-0530-x.
- Winkler DT, Bondolfi L, Herzig MC, Jann L, Calhoun ME, Wiederhold KH, *et al.* Spontaneous hemorrhagic stroke in a mouse model of cerebral amyloid angiopathy. *J Neurosci*. 2001 Mar 1;21(5):1619-27. doi: 10.1523/JNEUROSCI.21-05-01619.2001.
- Withers SE, Parry-Jones AR, Allan SM, Kasher PR. A Multi-Model Pipeline for Translational Intracerebral Haemorrhage Research. *Transl Stroke Res*. 2020 Dec;11(6):1229-1242. doi: 10.1007/s12975-020-00830-z.
- Witsch J, Neugebauer H, Zweckberger K, Jüttler E. Primary cerebellar haemorrhage: complications, treatment and outcome. *Clin Neurol Neurosurg*. 2013 Jul;115(7):863-9. doi: 10.1016/j.clinneuro.2013.04.009.
- World Health Organization (WHO). The top 10 causes of death. 2020. Available at: <https://www.who.int/news-room/fact-sheets/detail/the-top-10-causes-of-death> (Accessed: 2 April 2025).
- World Health Organization (WHO). Cardiovascular diseases (CVDs). 2021. Available at: [https://www.who.int/news-room/fact-sheets/detail/cardiovascular-diseases-\(cvds\)](https://www.who.int/news-room/fact-sheets/detail/cardiovascular-diseases-(cvds)) (Accessed: 2 April 2025).
- World Health Organization MONICA Project (monitoring trends and determinants in cardiovascular disease): a major international collaboration. WHO MONICA Project Principal Investigators. *J Clin Epidemiol*. 1988;41(2):105-14. doi: 10.1016/0895-4356(88)90084-4.
- Wu H, Wu T, Li M, Wang J. Efficacy of the lipid-soluble iron chelator 2,2'-dipyridyl against hemorrhagic brain injury. *Neurobiol Dis*. 2012 Jan;45(1):388-94. doi: 10.1016/j.nbd.2011.08.028.
- Wu H, Wu T, Xu X, Wang J, Wang J. Iron toxicity in mice with collagenase-induced intracerebral hemorrhage. *J Cereb Blood Flow Metab*. 2011 May;31(5):1243-50. doi: 10.1038/jcbfm.2010.209.

- Wu J, Hua Y, Keep RF, Nakamura T, Hoff JT, Xi G. Iron and iron-handling proteins in the brain after intracerebral hemorrhage. *Stroke*. 2003 Dec;34(12):2964-9. doi: 10.1161/01.STR.0000103140.52838.45.
- Wu J, Yang S, Xi G, Fu G, Keep RF, Hua Y. Minocycline reduces intracerebral hemorrhage-induced brain injury. *Neurol Res*. 2009 Mar;31(2):183-8. doi: 10.1179/174313209X385680.
- Wu L, Hu Y, Jiang L, Liang N, Liu P, Hong H, et al. Zhuyu Annao decoction promotes angiogenesis in mice with cerebral hemorrhage by inhibiting the activity of PHD3. *Hum Exp Toxicol*. 2021 Nov;40(11):1867-1879. doi: 10.1177/09603271211008523.
- Xi G, Keep RF, Hua Y, Xiang J, Hoff JT. Attenuation of thrombin-induced brain edema by cerebral thrombin preconditioning. *Stroke*. 1999 Jun;30(6):1247-55. doi: 10.1161/01.str.30.6.1247.
- Xi G, Keep RF, Hoff JT. Mechanisms of brain injury after intracerebral haemorrhage. *Lancet Neurol*. 2006 Jan;5(1):53-63. doi: 10.1016/S1474-4422(05)70283-0.
- Xi G, Reiser G, Keep RF. The role of thrombin and thrombin receptors in ischemic, hemorrhagic and traumatic brain injury: deleterious or protective? *J Neurochem*. 2003 Jan;84(1):3-9. doi: 10.1046/j.1471-4159.2003.01268.x.
- Xia Z, Wu X, Li J, Liu Z, Chen F, Zhang L, et al. Minimally Invasive Surgery is Superior to Conventional Craniotomy in Patients with Spontaneous Supratentorial Intracerebral Hemorrhage: A Systematic Review and Meta-Analysis. *World Neurosurg*. 2018 Jul;115:266-273. doi: 10.1016/j.wneu.2018.04.181.
- Xu J, Chen Z, Yu F, Liu H, Ma C, Xie D, et al. IL-4/STAT6 signaling facilitates innate hematoma resolution and neurological recovery after hemorrhagic stroke in mice. *Proc Natl Acad Sci U S A*. 2020 Dec 22;117(51):32679-32690. doi: 10.1073/pnas.2018497117.
- Xu P, Hong Y, Xie Y, Yuan K, Li J, Sun R, et al. TREM-1 Exacerbates Neuroinflammatory Injury via NLRP3 Inflammasome-Mediated Pyroptosis in Experimental Subarachnoid Hemorrhage. *Transl Stroke Res*. 2021 Aug;12(4):643-659. doi: 10.1007/s12975-020-00840-x.
- Xu Z, Carlson C, Snell J, Eames M, Hananel A, Lopes MB, et al. Intracranial inertial cavitation threshold and thermal ablation lesion creation using MRI-guided 220-kHz focused ultrasound surgery: preclinical investigation. *J Neurosurg*. 2015 Jan;122(1):152-61. doi: 10.3171/2014.9.JNS14541.
- Xue M, Del Bigio MR. Acute tissue damage after injections of thrombin and plasmin into rat striatum. *Stroke*. 2001 Sep;32(9):2164-9. doi: 10.1161/hs0901.095408.
- Xue M, Del Bigio MR. Comparison of brain cell death and inflammatory reaction in three models of intracerebral hemorrhage in adult rats. *J Stroke Cerebrovasc Dis*. 2003 May-Jun;12(3):152-9. doi: 10.1016/S1052-3057(03)00036-3.

- Xue M, Yong VW. Matrix metalloproteinases in intracerebral hemorrhage. *Neurol Res.* 2008 Oct;30(8):775-82. doi: 10.1179/174313208X341102.
- Xue M, Yong VW. Neuroinflammation in intracerebral haemorrhage: immunotherapies with potential for translation. *Lancet Neurol.* 2020 Dec;19(12):1023-1032. doi: 10.1016/S1474-4422(20)30364-1.
- Yang G, Qian C, Zhang C, Bao Y, Liu MY, Jiang F, *et al.* Hepcidin attenuates the iron-mediated secondary neuronal injury after intracerebral hemorrhage in rats. *Transl Res.* 2021 Mar;229:53-68. doi: 10.1016/j.trsl.2020.09.002.
- Yang S, Song S, Hua Y, Nakamura T, Keep RF, Xi G. Effects of thrombin on neurogenesis after intracerebral hemorrhage. *Stroke.* 2008 Jul;39(7):2079-84. doi: 10.1161/STROKEAHA.107.508911.
- Yang WS, SriRamaratnam R, Welsch ME, Shimada K, Skouta R, Viswanathan VS, *et al.* Regulation of ferroptotic cancer cell death by GPX4. *Cell.* 2014 Jan 16;156(1-2):317-331. doi: 10.1016/j.cell.2013.12.010.
- Yang Y, Zhang Y, Wang Z, Wang S, Gao M, Xu R, *et al.* Attenuation of Acute Phase Injury in Rat Intracranial Hemorrhage by Cerebrolysin that Inhibits Brain Edema and Inflammatory Response. *Neurochem Res.* 2016 Apr;41(4):748-57. doi: 10.1007/s11064-015-1745-4.
- Yao Z, Ma L, You C, He M. Decompressive Craniectomy for Spontaneous Intracerebral Hemorrhage: A Systematic Review and Meta-analysis. *World Neurosurg.* 2018 Feb;110:121-128. doi: 10.1016/j.wneu.2017.10.167.
- Yassi N, Zhao H, Churilov L, Wu TY, Ma H, Nguyen HT, *et al.* Tranexamic acid versus placebo in individuals with intracerebral haemorrhage treated within 2 h of symptom onset (STOP-MSU): an international, double-blind, randomised, phase 2 trial. *Lancet Neurol.* 2024 Jun;23(6):577-587. doi: 10.1016/S1474-4422(24)00128-5.
- Yeatts SD, Palesch YY, Moy CS, Selim M. High dose deferoxamine in intracerebral hemorrhage (HI-DEF) trial: rationale, design, and methods. *Neurocrit Care.* 2013 Oct;19(2):257-66. doi: 10.1007/s12028-013-9861-y.
- Yin XP, Chen ZY, Zhou J, Wu D, Bao B. Mechanisms underlying the perifocal neuroprotective effect of the Nrf2-ARE signaling pathway after intracranial hemorrhage. *Drug Des Devel Ther.* 2015 Nov 17;9:5973-86. doi: 10.2147/DDDT.S79399.
- Yong VW, Wells J, Giuliani F, Casha S, Power C, Metz LM. The promise of minocycline in neurology. *Lancet Neurol.* 2004 Dec;3(12):744-51. doi: 10.1016/S1474-4422(04)00937-8.
- Yousufuddin M, Moriarty JP, Lackore KA, Zhu Y, Peters JL, Doyle T, *et al.* Initial and subsequent 3-year cost after hospitalization for first acute ischemic stroke and intracerebral hemorrhage. *J Neurol Sci.* 2020 Dec 15;419:117181. doi: 10.1016/j.jns.2020.117181.

- Yu HH, Zhao H, Qing YB, Pan WR, Jia BY, Zhao HY, *et al.* Porcine Zygote Injection with Cas9/sgRNA Results in DMD-Modified Pig with Muscle Dystrophy. *Int J Mol Sci.* 2016 Oct 9;17(10):1668. doi: 10.3390/ijms17101668.
- Yu H, Cao X, Li W, Liu P, Zhao Y, Song L, *et al.* Targeting connexin 43 provides anti-inflammatory effects after intracerebral hemorrhage injury by regulating YAP signaling. *J Neuroinflammation.* 2020 Oct 28;17(1):322. doi: 10.1186/s12974-020-01978-z.
- Yu J, Guo Y, Sun M, Li B, Zhang Y, Li C. Iron is a potential key mediator of glutamate excitotoxicity in spinal cord motor neurons. *Brain Res.* 2009 Feb 27;1257:102-7. doi: 10.1016/j.brainres.2008.12.030.
- Yu L, Lu Z, Burchell S, Nowrangi D, Manaenko A, Li X, *et al.* Adropin preserves the blood-brain barrier through a Notch1/Hes1 pathway after intracerebral hemorrhage in mice. *J Neurochem.* 2017 Dec;143(6):750-760. doi: 10.1111/jnc.14238.
- Yue L, Luo Y, Jiang L, Sekido Y, Toyokuni S. PCBP2 knockdown promotes ferroptosis in malignant mesothelioma. *Pathol Int.* 2022 Apr;72(4):242-251. doi: 10.1111/pin.13209.
- Zeng Z, Gong X, Hu Z. L-3-n-butylphthalide attenuates inflammation response and brain edema in rat intracerebral hemorrhage model. *Aging (Albany NY).* 2020 Jun 21;12(12):11768-11780. doi: 10.18632/aging.103342.
- Zhang L, Tang Y, Huang P, Luo S, She Z, Peng H, *et al.* Role of NLRP3 inflammasome in central nervous system diseases. *Cell Biosci.* 2024 Jun 7;14(1):75. doi: 10.1186/s13578-024-01256-y.
- Zhang N, Luo Y, He L, Zhou L, Wu W. A self-assembly peptide nanofibrous scaffold reduces inflammatory response and promotes functional recovery in a mouse model of intracerebral hemorrhage. *Nanomedicine.* 2016 Jul;12(5):1205-17. doi: 10.1016/j.nano.2015.12.387.
- Zhang W, Wu Q, Hao S, Chen S. The hallmark and crosstalk of immune cells after intracerebral hemorrhage: Immunotherapy perspectives. *Front Neurosci.* 2023 Jan 12;16:1117999. doi: 10.3389/fnins.2022.1117999.
- Zhang Y, Zhang X, Wee Yong V, Xue M. Vildagliptin improves neurological function by inhibiting apoptosis and ferroptosis following intracerebral hemorrhage in mice. *Neurosci Lett.* 2022 Apr; 17;776:136579. doi: 10.1016/j.neulet.2022.136579.
- Zhao J, Song C, Li D, Yang X, Yu L, Wang K, *et al.* Efficacy and safety of glibenclamide therapy after intracerebral haemorrhage (GATE-ICH): A multicentre, prospective, randomised, controlled, open-label, blinded-endpoint, phase 2 clinical trial. *EClinicalMedicine.* 2022 Sep 23;53:101666. doi: 10.1016/j.eclinm.2022.101666.
- Zhao X, Song S, Sun G, Strong R, Zhang J, Grotta JC, *et al.* Neuroprotective role of haptoglobin after intracerebral hemorrhage. *J Neurosci.* 2009 Dec 16;29(50):15819-27. doi: 10.1523/JNEUROSCI.3776-09.2009.

References

- Zhao Y, Wei ZZ, Zhang JY, Zhang Y, Won S, Sun J, *et al.* GSK-3 β Inhibition Induced Neuroprotection, Regeneration, and Functional Recovery After Intracerebral Hemorrhagic Stroke. *Cell Transplant.* 2017 Mar 13;26(3):395-407. doi: 10.3727/096368916X694364.
- Zheng H, Chen C, Zhang J, Hu Z. Mechanism and Therapy of Brain Edema after Intracerebral Hemorrhage. *Cerebrovasc Dis.* 2016;42(3-4):155-69. doi: 10.1159/000445170.
- Zheng Y, Hu Q, Manaenko A, Zhang Y, Peng Y, Xu L, *et al.* 17 β -Estradiol attenuates hematoma expansion through estrogen receptor α /silent information regulator 1/nuclear factor-kappa b pathway in hyperglycemic intracerebral hemorrhage mice. *Stroke.* 2015 Feb;46(2):485-91. doi: 10.1161/STROKEAHA.114.006372.
- Zhou F, Chen G, Zhang J. Edaravone reduces brain oedema and attenuates cell death after intracerebral haemorrhage in mice. *Brain Inj.* 2009 Apr;23(4):353-7. doi: 10.1080/02699050902788527.
- Zhou H, Zhang C, Huang C. Verbascoside Attenuates Acute Inflammatory Injury Caused by an Intracerebral Hemorrhage Through the Suppression of NLRP3. *Neurochem Res.* 2021 Apr;46(4):770-777. doi: 10.1007/s11064-020-03206-9.
- Zhou Y, Wang Y, Wang J, Anne Stetler R, Yang QW. Inflammation in intracerebral hemorrhage: from mechanisms to clinical translation. *Prog Neurobiol.* 2014 Apr;115:25-44. doi: 10.1016/j.pneurobio.2013.11.003.
- Zhu H, Li F, Zou M, Xue X, Yuan J, Feng H, *et al.* Experimental high-altitude intracerebral hemorrhage in minipigs: histology, behavior, and intracranial pressure in a double-injection model. *Acta Neurochir (Wien).* 2013 Apr;155(4):655-61. doi: 10.1007/s00701-013-1618-z.
- Zhu W, Gao Y, Chang CF, Wan JR, Zhu SS, Wang J. Mouse models of intracerebral hemorrhage in ventricle, cortex, and hippocampus by injections of autologous blood or collagenase. *PLoS One.* 2014 May 15;9(5):e97423. doi: 10.1371/journal.pone.0097423. Erratum in: *PLoS One.* 2021 Dec 15;16(12):e0261640. doi: 10.1371/journal.pone.0261640.
- Zhu Y, Liu C, Sun Z. Early Combined Therapy with Pharmacologically Induced Hypothermia and Edaravone Exerts Neuroprotective Effects in a Rat Model of Intracerebral Hemorrhage. *Cell Biochem Biophys.* 2015 Nov;73(2):581-587. doi: 10.1007/s12013-015-0584-x.
- Ziai WC, Carhuapoma JR. Intracerebral Hemorrhage. *Continuum (Minneapolis Minn).* 2018 Dec;24(6):1603-1622. doi: 10.1212/CON.0000000000000672.
- Ziai WC, Torbey MT, Kickler TS, Oh S, Bhardwaj A, Wityk RJ. Platelet count and function in spontaneous intracerebral hemorrhage. *J Stroke Cerebrovasc Dis.* 2003 Jul-Aug;12(4):201-6. doi: 10.1016/S1052-3057(03)00075-2.

- Zille M, Farr TD, Keep RF, Römer C, Xi G, Boltze J. Novel targets, treatments, and advanced models for intracerebral haemorrhage. *EBioMedicine*. 2022 Feb;76:103880. doi: 10.1016/j.ebiom.2022.103880.
- Zille M, Karuppagounder SS, Chen Y, Gough PJ, Bertin J, Finger J, *et al.* Neuronal Death After Hemorrhagic Stroke *de visu* and *In Vivo* Shares Features of Ferroptosis and Necroptosis. *Stroke*. 2017 Apr;48(4):1033-1043. doi: 10.1161/STROKEAHA.116.015609.
- Zou X, Wu Z, Zhu W, Chen L, Mao Y, Zhao F. Effectiveness of minocycline in acute white matter injury after intracerebral hemorrhage. *J Neurosurg*. 2017 Jun;126(6):1855-1862. doi: 10.3171/2016.5.JNS152670.



ANNEX

Curriculum Vitae

Academic background

- **PhD in Neurosciences** (2020 – ongoing) – Universitat Autònoma de Barcelona (UAB), Bellaterra (Spain).
- **Postgraduate course in technology transfer from bench to the market** (2020 – 2021) – Universitat Pompeu Fabra (UPF), Barcelona (Spain).
- **Veterinary Medicine Degree** (2015 – 2020) – Universitat Autònoma de Barcelona (UAB), Barcelona (Spain).

Background

- PhD Student – Cellular and Molecular Neurobiology Group (CMN), Institut d'Investigació en Ciències de la Salut Germans Trias i Pujol (IGTP), Badalona (Spain). 2020 – ongoing.
- Internal Project Manager and Business Developmer Manager – Anapath Research SAU, Santiga (Spain). 2024-2025.
- Research internship – Dipartimento di Scienze Mediche Veterinarie, ALMA MATER STUDIORUM - Università di Bologna, Ozzano dell'Emilia (Italy). 2024.
- Research internship – The West Laboratory. Animal and Dairy Science Department, College of Agricultural and Environmental Sciences, University of Georgia, Athens (Georgia). 2022.
- Veterinarian – Comparative Medicine and Bioimaging Centre of Catalonia (CMCIB), Institut d'Investigació en Ciències de la Salut Germans Trias i Pujol (IGTP), Badalona (Spain). 2020.
- Internship – Pathological Anatomy Department, Veterinary faculty, Universitat Autònoma de Barcelona (UAB), Bellaterra (Spain). 2019.
- Research veterinarian – Centre for Animal Biotechnology and gene Therapy (CBATEG), Universitat Autònoma de Barcelona (UAB), Bellaterra (Spain). 2018-2020.

- Internship – Grup de Recerca en Microbiologia Aplicada i Mediambiental, Universitat Autònoma de Barcelona (UAB), Bellaterra (Spain). 2015-2020.

Scientific publications – ORCID 0000-0003-1630-1302

- **García-Serran A**, Ordoño J, DeGregorio-Rocasolano N, Melià-Sorolla M, Oendaaal K, Martí-Sistac O, Gasull T. Targeting Pro-Oxidant Iron with Exogenously Administered Apotransferrin Provides Benefits Associated with Changes in Crucial Cellular Iron Gate Protein TfR in a Model of Intracerebral Hemorrhagic Stroke in Mice. *Antioxidants (Basel)*. 2023 Oct;12(11):1945. doi: 10.3390/antiox12111945.
- Castaño C, Melià-Sorolla M, **García-Serran A**, DeGregorio-Rocasolano N, García-Sort MR, Hernandez-Pérez M, Valls-Carbó A, Pino O, Grífols J, Iruela-Sánchez A, Palomar-García A, Puig J, Martí-Sistac O, Dávalos A, Gasull T. Establishment of a reproducible and minimally invasive ischemic stroke model in swine. *JCI Insight*. 2023 Apr;8(8):e163398. doi: 10.1172/jci.insight.163398.
- DeGregorio-Rocasolano N, Guirao V, Ponce J, Melià-Sorolla M, Alienà-Valero A, **García-Serran A**, Salom JB, Dávalos A, Martí-Sistac O, Gasull T. Comparative Proteomics Unveils LRRFIP1 as a New Player in the DAPK1 Interactome of Neurons Exposed to Oxygen and Glucose Deprivation. *Antioxidants (Basel)*. 2020 Nov 30;9(12):1202. doi: 10.3390/antiox9121202.

Involvelement in research projects

- Project: Enhancing the recovery with nutraceutic hydroxytyrosol in “humanized” stroke models in swine: a multiomics, neuroimaging and functional study (PI24/00963). Instituto de Salud Carlos III (ISCIII). Teresa Gasull Dalmau. 01/01/2025 – 01/01/2027. 227,500 €. Team member.
- Research Group: Redes de Investigación Cooperativa Orientadas a Resultados en Salud (RICORS)-ICTUS (RD21/0006/0024). Instituto de Salud Carlos III (ISCIII). Mònica Millán Torné. 01/01/2022 – 31/12/2024. Team member.
- Research group: Grup de Recerca de la Generalitat de Catalunya (2021 SGR 00925). Agència de Gestió d'Ajuts Universitaris i de Recerca (AGAUR). Mònica Millán Torné. 01/01/2022 – 31/12/2024. 40,000 €. Team member.

- Project for a private company: Modelo de glioblastoma intracerebral en ratón para la búsqueda de terapias. Teresa Gasull Dalmau. 03/06/2024 – 03/06/2024. 30,000 €. Team member.
- Project: Innovative biomarkers to diagnose ischaemic stroke: tge bet on miRNAs in extracellular vesicles in humanized swine models (PI21/01925). Instituto de Salud Carlos III (ISCIII). Teresa Gasull Dalmau. 01/01/2022 – 01/01/2025. 87,120 €. Team member.
- Project: Evaluation of Lung Injury as a Target against Stroke-Assocaited Pneumonia (PI21/00939). Instituto de Salud Carlos III (ISCIII). Alejandro Bustamante Rangel. 01/01/2022 – 01/01/2025. 108,900 €. Team member.
- Project: Apotransferrin to treat acute stroke as novel neuroprotector strategy (2019PROD00120). Agència de Gestió d'Ajuts Universitaris i de Recerca (AGAUR). Teresa Gasull Dalmau. 01/06/2020 – 30/11/2021. 99,795 €. Scientific entreprenour.
- Development of a humanized stroke model in pig by endovascular access for the dynamic study of infarction and cerebral reperfusion (PI18/01813). 176,962.5 €. Team member.

Congresses

- Poster: **García-Serran A**, Castaño C, Melià-Sorolla M, DeGregorio-Rocasolano N, Martí-Sistac O, Gasull T. Towards novel intracerebral haemorrhage stroke models by endovascular approach in swine. 10th Annual European Stroke Organisation Conference (ESOC 2024). 15/05/2024 – 17/05/2024. Basel (Switzerland).
- Oral communication: García-Serran A, Ordoño J, DeGregorio-Rocasolano N, Melià-Sorolla M, Odendaal K, Martí-Sistac O, Gasull T. Iron-free transferrin improves sensory function in an experimental model of intracerebral hemorrhage. 9th Neurological Disorders Summit (9th NDS). 06/05/2024 – 08/05/2024. Barcelona (Spain).
- Oral communication: **García-Serran A**, Castaño C, Melià-Sorolla M, DeGregorio-Rocasolano N, Martí-Sistac O, Gasull T. A novel intracerebral hemorrhagic stroke

model by endovascular approach in swine. 3rd IGTP Retreat. 30/11/2023 – 01/12/2023. Badalona (Spain).

- Oral communication: Melià-Sorolla M, Castaño C, **García-Serran A**, García-Sort MR, DeGregorio-Rocasolano N, Dávalos A, Martí-Sistac O, Grífols J, Capdevila S, Monté-Rubio G, Gasull T. Desarrollo de un nuevo modelo de ictus isquémico en modelo porcino, acorde a las 3Rs. SECAL 2023. 14/11/2023 – 17/11/2023. Santiago de Compostela (Spain).
- Poster: **García-Serran A**, Ordoño J, DeGregorio-Rocasolano N, Melià-Sorolla M, Odendaal K, Martí-Sistac O, Gasull T. Iron-free transferrin improves sensory function in an experimental model of intracerebral hemorrhage. 9th European Stroke Organisation Conference (ESOC 2023). 24/05/2023 – 26/05/2023. Munich (Germany).
- Oral communication: **García-Serran A**, Castaño C, Melià-Sorolla M, DeGregorio-Rocasolano N, Martí-Sistac O, Gasull T. Exogenous administration of iron-free transferrin is safe in intracerebral haemorrhagic stroke in mice. IX INc Scientific Conferences. 05/10/2022 – 07/10/2022. Sant Feliu de Guíxols (Spain).
- Oral communication: **García-Serran A**, Castaño C, Melià-Sorolla M, DeGregorio-Rocasolano N, Martí-Sistac O, Gasull T. Exogenous administration of iron-free transferrin is safe in intracerebral haemorrhagic stroke in mice. IV PhD Day. IGTP. 10/06/2022 – 10/06/2022. Badalona (Spain).
- Poster: Melià-Sorolla M, Castaño C, **García-Serran A**, García-Sort MR, DeGregorio-Rocasolano N, Dávalos A, Martí-Sistac O, Pino O, Grífols J, Iruela A, Palomar A, Puig J, Gasull T. Novel ischemic stroke model of permanent occlusion by endovascular approach in swine. 8th European Stroke Organisation Conference (ESOC 2022). 04/05/2022 – 06/05/2022. Lyon (France).
- Oral communication: DeGregorio-Rocasolano N, Odendaal K, Martí-Sistac O, Melià-Sorolla M, **García-Serran A**, Ordoño J, Dávalos A, Gasull T. Deciphering the iron side of stroke: Neurodegeneration at the crossroads between iron dyshomeostasis, excitotoxicity and ferroptosis. Spanish Stroke Network INVICTUS+ annual meeting. 18/11/2021 – 19/11/2021. Santiago de Compostela (Spain).
- Oral communication: Melià-Sorolla M, Castaño C, **García-Serran A**, García-Sort MR, DeGregorio-Rocasolano N, Dávalos A, Martí-Sistac O, Pino O, Grífols J,

Iruela A, Palomar A, Puig J, Gasull T. New humanized model of ischemic stroke by endovascular approximation in swine. VIII INc Scientific Conferences. 05/10/2021 – 07/10/2021. Sant Feliu de Guíxols (Spain).

- Poster: Melià-Sorolla M, Castaño C, **García-Serran A**, García-Sort MR, DeGregorio-Rocasolano N, Dávalos A, Martí-Sistac O, Pino O, Grífols J, Iruela A, Palomar A, Puig J, Gasull T. Anatomic study of the supraaortic vasculature and generation of an endovascular ischemic stroke model in swine. III IGTP PhD Day. 22/06/2021. Badalona (Spain).
- Poster: Odendaal K, DeGregorio-Rocasolano N, Melià-Sorolla M, García-Serran A, Martí-Sistac O, Gasull T. Characterisation of the time course expression of ferrop-tosis related proteins in neuronal cortical cell cultures undergoing maturation. III IGTP PhD Day. 22/06/2021. Badalona (Spain).

Courses

- **Course of Good Laboratory Practice (GLP) in research (2024).** Spanish Society of research Quality Assurance (SEGCIB). 2024.
- **Stroke animal models.** Redes de Investigación Cooperativa Orientadas a Resultados en Salud (RICORS)-ICTUS. Universidad Autónoma de Madrid (UAM). 2022.
- **FELASA qualifications. Training Course in Laboratory Animal Science for Scientists Responsible for the Design or Conduct of Animal Experiments.** Functions A, B, C, D, E and F according to directive EU63/2010 for mouse, rat, rabbit, ruminants, and pig. Universitat Autònoma de Barcelona (UAB) – Federation of European Laboratory Animal Science Associations (FELASA). 2020.

